

DESIGN, FABRICATION AND IMPLEMENTATION OF A VIBRATION
BASED MEMS ENERGY SCAVENGER FOR WIRELESS MICROSYSTEMS

A THESIS SUBMITTED TO
THE GRADUATE SCHOOL OF NATURAL AND APPLIED SCIENCES
OF
MIDDLE EAST TECHNICAL UNIVERSITY

BY

İBRAHİM SARI

IN PARTIAL FULFILLMENT OF THE REQUIREMENTS
FOR
THE DEGREE OF DOCTOR OF PHILOSOPHY
IN
MECHANICAL ENGINEERING

SEPTEMBER 2008

**DESIGN, FABRICATION AND IMPLEMENTATION OF A VIBRATION BASED MEMS
ENERGY SCAVENGER FOR WIRELESS MICROSYSTEMS**

submitted by **İBRAHİM SARI** in partial fulfilment of the requirements for the degree of **Doctor of Philosophy in Mechanical Engineering Department, Middle East Technical University** by,

Prof. Dr. Canan Özgen _____
Dean, Graduate School of **Natural and Applied Sciences**

Prof. Dr. Kemal İder _____
Head of Department, **Mechanical Engineering**

Prof. Dr. Tuna Balkan _____
Supervisor, **Mechanical Engineering Dept., METU**

Asst. Prof. Dr. Haluk Külah _____
Co-Supervisor, **Electrical and Electronics Engineering Dept., METU**

Examining Committee Members:

Prof. Dr. H. Nevzat Özgüven _____
Mechanical Engineering Dept., METU

Prof. Dr. Tuna Balkan _____
Mechanical Engineering Dept., METU

Prof. Dr. Sahir Arıkan _____
Mechanical Engineering Dept., METU

Prof. Dr. Tayfun Akin _____
Electrical and Electronics Engineering Dept., METU

Prof. Dr. Yücel Ercan _____
Mechanical Engineering Dept., TOBB ETU

Date: _____ 22 September 2008

I hereby declare that all information in this document has been obtained and presented in accordance with academic rules and ethical conduct. I also declare that, as required by these rules and conduct, I have fully cited and referenced all material and results that are not original to this work.

Name, Last name : Ibrahim Sarı

Signature :

ABSTRACT

DESIGN, FABRICATION AND IMPLEMENTATION OF A VIBRATION BASED MEMS ENERGY SCAVENGER FOR WIRELESS MICROSYSTEMS

Sarı, İbrahim

Ph.D., Department of Mechanical Engineering

Supervisor : Prof. Dr. Tuna Balkan

Co-Supervisor: Asst. Prof. Dr. Haluk Külah

September 2008, 196 pages

This thesis study presents the design, simulation, micro fabrication, and testing steps of microelectromechanical systems (MEMS) based electromagnetic micro power generators. These generators are capable of generating power using already available environmental vibrations, by implementing the electromagnetic induction technique. There are mainly two objectives of the study: (i) to increase the bandwidth of the traditional micro generators and (ii) to improve their efficiency at low frequency environmental vibrations of 1-100 Hz where most vibrations exist.

Four main types of generators have been proposed within the scope of this thesis study. The first type of generator is mainly composed of 20 parylene cantilevers on which coils are fabricated, where the cantilevers are capable of resonating with external vibrations with respect to a stationary magnet. This generator has dimensions of $9.5 \times 8 \times 6 \text{ mm}^3$, and it has been shown that 0.67 mV of voltage and 56 pW of power output can be obtained from a single cantilever of this design at a vibration frequency of 3.45 kHz. The second type generator aims to increase the bandwidth of the traditional designs by implementing cantilevers with varying length. This generator is sized $14 \times 12.5 \times 8 \text{ mm}^3$, and the mechanical design and

energy generation concept is similar to the first design. The test results show that by using 40 cantilevers with a length increment of 3 μm , the overall bandwidth of the generator can be increased to 1000 Hz. It has also been shown that 9 mV of constant voltage and 1.7 nW of constant power output can be obtained from the overall device in a vibration frequency range of 3.5 to 4.5 kHz. The third type is a standard large mass coil type generator that has been widely used in the literature. In this case, the generator is composed of a stationary base with a coil and a magnet-diaphragm assembly capable of resonating with vibrations. The fabricated device has dimensions of $8.5 \times 7 \times 2.5 \text{ mm}^3$, and it has been considered in this study for benchmarking purposes only. The test results show that 0.3 mV of voltage and 40 pW of power output can be obtained from the fabricated design at a vibration frequency of 113 Hz. The final design aims to mechanically up-convert low frequency environmental vibrations of 1-100 Hz to a much higher frequency range of 2-3 kHz. This type of generator has been implemented for the first time in the literature. The generator is composed of two parts; a diaphragm-magnet assembly on the top, and 20 cantilevers that have coils connected in series at the base. The diaphragm oscillates by low frequency environmental vibrations, and catches and releases the cantilevers from the tip points where magnetic nickel (Ni) areas are deposited. The released cantilevers then start decaying out oscillations that is at their damped natural frequency of 2-3 kHz. It has been shown with tests that frequency up-conversion is realized in micro scale. The fabricated device has dimensions of $8.5 \times 7 \times 2.5 \text{ mm}^3$, and a maximum voltage and power output of 0.57 mV and 0.25 nW can be obtained, respectively, from a single cantilever of the fabricated prototype at a vibration frequency of 113 Hz.

Keywords: Micro power generator, Energy harvesting, Frequency up-conversion, Microelectromechanical systems (MEMS).

ÖZ

KABLOSUZ SİSTEMLERE YÖNELİK TİTREŞİM TABANLI BİR MİKRO ENERJİ ÜRETECENİN TASARIMI, ÜRETEMİ VE UYGULANMASI

Sarı, İbrahim

Doktora, Makina Mühendisliği Bölümü

Tez Yöneticisi : Prof. Dr. Tuna Balkan

Ortak Tez Yöneticisi : Y. Doç. Dr. Haluk Külah

Eylül 2008, 196 sayfa

Bu tez çalışmasında, mikroelektromekanik sistem teknolojisi (MEMS) tabanlı elektromanyetik mikro enerji üreteçlerinin tasarım, mikro üretim ve test süreçleri sunulmuştur. Bu üreteçler, ortamda zaten varolan çevresel titreşimleri elektromanyetik indükleme tekniğiyle elektriksel enerjiye çevirebilmektedir. Bu çalışmanın iki amacı vardır: (i) geleneksel enerji üreteçlerinin bant genişliğini artırmak ve (ii) bu jeneratörlerin genelde çevresel titreşimin daha sık görüldüğü 1-100 Hz aralığındaki düşük frekanslarda daha verimli çalışmasını sağlamaktır.

Bu çalışma kapsamında temel olarak dört farklı tasarım öne sürülmüştür. Bunlardan ilki temel olarak parylene malzemesinden yapılmış 20 adet rezonans koldan oluşmaktadır. Bu kolların üzerinde metal sarımlar bulunmaktadır ve çevresel titreşimler yardımıyla sabit bir mıknatısa karşı hareket edebilmektedirler. Bu jenaratör $9.5 \times 8 \times 6 \text{ mm}^3$ büyüklüğündedir ve her bir kolundan, 3.45 kHz'lık bir titreşim frekansında, 0.67 mV'luk voltaj ve 56 pW'luk güç üretilebildiği gösterilmiştir. Öne sürülen ikinci tasarım ile farklı uzunlukta rezonans kollar kullanılarak geleneksel tasarımların bant genişliğinin artırılması hedeflenmiştir. Bu tasarım $14 \times 12.5 \times 8 \text{ mm}^3$ büyüklüğündedir ve mekanik yapısı bir önceki tasarıma

benzemektedir. Yapılan testlerle, 3 μm 'luk uzunluk artırımları kullanılarak bant genişliğinin 1000 Hz'e kadar artırılabilcecini ve 3.5 ile 4.5 kHz frekans aralığında 9 mV'luk sabit voltaj ve 1.7 nW'luk sabit güç elde edilebileceği gösterilmiştir. Çalışma kapsamında ele alınan üçüncü tasarım ise büyük kütle sarım jeneratördür. Bu tasarım literatürde daha önce sıkça incelenmiş bir tasarımdır. Bu jeneratör üzerinde metal sarım bulunan sabit bir alt parçadan ve çevresel titreşimlerle salınabilen bir mıknatıs-diyafram yapısından oluşmaktadır. Önerilen bu yapı $8.5 \times 7 \times 2.5 \text{ mm}^3$ büyüklüğündedir ve bu çalışma kapsamından karşılaşturma amacıyla incelenmiştir. Test sonuçlarına göre, üretilen bu tasarımdan, 113 Hz'lik çevresel titreşim frekansında, 0.3 mV'luk voltaj ve 40 pW'luk güç elde etmek mümkündür. Bu çalışmada önerilen son tasarımın amacı ise 1-100 Hz aralığındaki düşük frekanslı çevresel titreşimleri, 2-3 kHz aralığında daha yüksek bir frekans aralığına taşımaktır. Böyle bir tasarım literatürde ilk defa öne sürülerek incelenmiştir. Önerilen yapı iki parçadan oluşmaktadır; yukarıda bulunan diyafram-mıknatıs yapısı ve bunun hemen altında, üzerinde seri olarak bağlanmış sarımlar bulunan 20 adet rezonans koldur. Diyafram çevresel titreşimlerle salınmakta ve hemen altında ucunda nikel (Ni) manyetik alanlar bulunan kolları yakalayıp bırakmaktadır. Serbest kalan kollar, kendi sönümlü doğal frekanları olan 2-3 kHz aralığında salınımaktadır. Yapılan testlerle frekans çevriminin mikro ölçülerde gerçekleştirildiği gösterilmiştir. Üretilen bu tasarım $8.5 \times 7 \times 2.5 \text{ mm}^3$ büyüklüğündedir ve 113 Hz'lik çevresel titreşim frekansında, her bir koldan 0.57 mV'luk voltaj ve 0.25 nW'luk güç elde edilebilediği gösterilmiştir.

Anahtar kelimeler: Micro güç üreteci, Enerji toplama, Frekans çevirimi, Mikroelektromekanik sistemler (MEMS).

To the One

and

To Feriha Ayşe Kurt and Ayşe Sarı

ACKNOWLEDGMENTS

I would like thank to my supervisor Prof. Dr. Tuna Balkan for his guidance, support, and valuable comments for this thesis study. I am grateful to my co-supervisor Asst. Prof. Dr. Haluk Külah for his endless effort, support, and guidance to make this work perfect, without him this study would never come to life.

My sincere gratitude is for the METU-MET staff, and especially to Orhan Akar, who had great help and support during the micro fabrication steps. I would also like to thank to all my friends at the METU MEMS group for their valuable discussions, and help. I would especially like to thank to Ata Tuna Çiftlik for his great support during testing.

My sincere thanks are for my friends Hande and Namik Kaplan, Kutluk Bilge Arıkan, Ali Emre Turgut, Serkan Güroğlu, Bülent İrfanoğlu, Fatma Aslan, Ceylan and Ahmet Yozgatlıgil, and Almila and Yiğit Yazıcıoğlu for their kind and sincere friendships and support.

I would also like to thank to my parents in law, Şeyda and Dursun Ayık for their never ending smiling faces. My special thanks are for Şeyda Ayık for the meals she had made for me during my study.

I am grateful to my lovely parents Sevil and Osman Sarı who have always supported me in all my hard days and led me to the light with their great patience and love.

I would like to thank to my brother Burak Sarı and my sister in law Peri Sarı for their support, sincere conservations, and never ending smiling faces.

Finally, I would like to thank to my dear wife Müjde Sarı for her all support, patience, and never ending love. It is her love that makes everything possible for me.

This study is supported by the Scientific and Technological Research Council of Turkey (TÜBİTAK) under grant number 104E119.

TABLE OF CONTENTS

ABSTRACT	iv
ÖZ	vi
ACKNOWLEDGMENTS	ix
TABLE OF CONTENTS.....	x
LIST OF TABLES	xiv
LIST OF FIGURES	xvii
NOMENCLATURE.....	xxiii
CHAPTER	
1. INTRODUCTION.....	1
1.1 Batteries as an Energy Source	2
1.2 Environmental Energy Sources	3
1.3 Vibration Based Environmental Energy Sources	5
1.3.1 Electrostatic (Capacitive) Energy Scavengers.....	5
1.3.2 Piezoelectric Energy Scavengers.....	8
1.3.3 Electromagnetic (Inductive) Energy Harvesters.....	9
1.4 Review of Electromagnetic (Inductive) Energy Harvesters	10
1.5 Objective of the Thesis Study.....	19

1.6 Conclusions.....	21
2. DESIGN, MODELING, AND SIMULATION OF ELECTROMAGNETIC MICRO ENERGY HARVESTERS	22
2.1 The Array of Cantilevers (AOC) Design.....	23
2.1.1 Mathematical Modeling of the Array of Cantilevers (AOC) Design	23
2.1.2 Effect of System Parameters on Power Output	34
2.1.3 Analysis of Mechanical Stress Induced on the Cantilevers....	43
2.1.4 Optimization and Simulation of the Array of Cantilevers (AOC) Design.....	45
2.2 The Array of Cantilevers Design with Varying Natural Frequencies (AOC_FS), “The Frequency Sweeper”	49
2.3 The Array of Cantilevers Design with Varying Natural Frequencies (AOC_FS) as an Energy Harvesting Frequency Sensor	54
2.4 The Large Mass Coil (LMC) Design	56
2.5 The Frequency up-Converter (FUC) Design	61
2.6 Conclusions.....	74
3. FABRICATION OF THE MICRO GENERATORS.....	75
3.1 Properties of the Array of Cantilevers (AOC) Design.....	75
3.2 Properties of the Array of Cantilevers Design with Varying Natural Frequencies (AOC_FS).....	76
3.3 Properties of the Large Mass Coil (LMC) Design.....	77

3.4 Properties of the Frequency up-Converter (FUC) Design	78
3.5 Schematic Drawing of the Whole Wafer.....	79
3.6 Fabrication Steps of the Micro Generators	81
3.7 Conclusions.....	103
4. TEST OF THE MICRO GENERATORS	104
4.1 Test Setup	104
4.2 The Tests of the Array of Cantilever (AOC) Design.....	106
4.3 The Tests of the Array of Cantilevers Design with Varying Natural Frequencies (AOC_FS), “The Frequency Sweeper”	118
4.4 The Tests of the Array of Cantilevers Design with Varying Natural Frequencies (AOC_FS) as an Energy Harvesting Frequency Sensor.	123
4.5 The Tests of the Large Mass Coil (LMC) Design	126
4.6 The Tests of the Frequency up-Converter (FUC) Design.....	129
4.6.1 Analysis of Difference in the Natural Frequency of the Cantilevers	150
4.6.2 Analysis of Shift in Time in the Actuation of the Cantilevers	154
4.7 Conclusions.....	160
5. CONCLUSIONS AND FUTURE WORK	161
REFERENCES.....	169

APPENDICES

A. LAYOUT DRAWINGS	178
B. FABRICATION PROCESS OUTLINE	183
C. FABRICATION PROCESS FLOW	186
CURRICULUM VITAE	195

LIST OF TABLES

TABLES

Table 1.1. Comparison of energy scavenging sources [3].	4
Table 1.2. Comparison of energy generation densities [6].	7
Table 2.1. Optimized parameters of the generator.	47
Table 2.2. Optimized parameters of the generator.	53
Table 2.3. Optimized parameters of the generator.	60
Table 2.4. Optimized parameters of the generator.	68
Table 3.1. List of the masks used in micro fabrication of the micro generators.	83
Table 3.2. Process steps of the 1st parylene layer.	89
Table 3.3. Deposition and patterning of the 1st metal layer.....	91
Table 3.4. Process steps of the 2nd parylene layer.....	92
Table 3.5. Process steps of contact opening on 2nd parylene layer.	93
Table 3.6. Deposition and patterning of the 2nd metal layer.	95
Table 3.7. Process steps of the 3rd parylene layer.	96
Table 3.8. Process steps of Ni electroplating.	97
Table 3.9. Process steps of the 4th parylene layer.....	98
Table 3.10. Process steps backside through etch of Si.....	100

Table 4.1. Important properties of the shaker system.....	105
Table 4.2. Simulation and test results for a single cantilever of the AOC design..	110
Table 4.3. Necessary variation required in equivalent mass term to cause the corresponding change in natural frequency.....	118
Table 4.4. Simulation and test results for the AOC_FS design.....	120
Table 4.5. Simulation and test results for the LMC design.....	127
Table 4.6. Simulation and test results for the FUC design.....	132
Table 4.7. Comparison of the performances of the large mass coil (LMC) and the frequency up-converter (FUC) designs.	137
Table 4.8. Comparison of performances of the LMC design by Williams et al. and the FUC designs.	138
Table 4.9. Numerical test examples of shift in natural frequency.....	152
Table 4.10. Necessary variation required in equivalent stiffness term to cause the corresponding change in natural frequency.....	153
Table 4.11. Necessary variation required in equivalent mass term to cause the corresponding change in natural frequency.....	153
Table 4.12. Sample values relating time and phase shift to release height difference for a damped natural frequency of $\omega_d=1.5$ kHz and $f=100$ Hz.....	154
Table 4.13. Experimental values showing time shift, Δt and corresponding release height difference, Δz	156
Table 4.14. Necessary variation required in the equivalent stiffness term to cause corresponding time shift.....	157
Table 4.15. Results of height difference measurements under the probe station....	158

Table 5.1. Important performance parameters of the micro generators.....	163
Table C.1. Process steps of the 1 st parylene layer.....	186
Table C.2. Deposition and patterning of the 1 st metal layer.	187
Table C.3. Process steps of the 2 nd parylene layer.....	188
Table C.4. Process steps of contact opening on 2 nd parylene layer.	189
Table C.5. Deposition and patterning of the 2 nd metal layer.....	190
Table C.6. Process steps of the 3 rd parylene layer.	191
Table C.7. Process steps of Ni electroplating.	192
Table C.8. Process steps of the 4 th parylene layer.....	193
Table C.9. Process steps backside through etch of Si.....	194

LIST OF FIGURES

FIGURES

Figure 1.1. Relative improvements in laptop computing technology from 1990-2003 [5].	3
Figure 1.2. Typical types of mechanical structures of an electrostatic energy scavengers, figure courtesy of [12].	7
Figure 1.3. Schematic view of a typical piezoelectric harvester [21].	8
Figure 1.4. Schematic diagram of an electromagnetic energy generator [39].	9
Figure 1.5. Equivalent mass-spring-damper model of the generator [12].	11
Figure 1.6. Schematic diagram of the first electromagnetic micro generator [41] .	13
Figure 1.7. Electromagnetic generator proposed P.D. Mitcheson <i>et al.</i> [43].....	14
Figure 1.8. Representation of frequency up-conversion mechanism [7].	17
Figure 2.1. Schematic view of the array of cantilevers design (AOC).	23
Figure 2.2. Basic electrical model of a coil driving a resistive electrical load.....	25
Figure 2.3. Illustration of magnetic field lines and orientation of the cantilever....	26
Figure 2.4. Equivalent 2nd order mechanical model.	28
Figure 2.5. Non-dimensional power with respect to frequency ratio, r.	36
Figure 2.6. Non-dimensional power with respect to frequency ratio, q.....	37
Figure 2.7. 3-dimensional plot of power magnitude, $\zeta_{eq} = 0.2$	39

Figure 2.8. 3-dimensional plot of power for upper limit of $\omega < \omega_n$, $\zeta_{eq} = 0.2$	39
Figure 2.9. Cutlets of power magnitude for sample ω_n values, $\zeta_{eq} = 0.2$	40
Figure 2.10. 3-dimensional plot of power for upper limit of $\omega > \omega_n$, $\zeta_{eq} = 0.2$	40
Figure 2.11. Cutlets of power magnitude for sample ω values, $\zeta_{eq} = 0.2$	41
Figure 2.12. Variation of power with respect to electrical and mechanical damping ratios.....	42
Figure 2.13. Force acting on the structure.....	43
Figure 2.14. Illustration of moment on the structure.....	44
Figure 2.15. Voltage output from the generator for various values of damping.....	48
Figure 2.16. Schematic view of the array of cantilevers design with varying natural frequencies (AOC_FS).	50
Figure 2.17. Variation of natural frequency with cantilever length.....	51
Figure 2.18. Overall and individual outputs from the proposed design for various cantilever length increments.	52
Figure 2.19. Block diagram of the proposed frequency detector.....	55
Figure 2.20. Block diagram of the read out circuitry.....	56
Figure 2.21. Schematic view of the large mass coil (LMC) design.....	57
Figure 2.22. Equivalent model representation of the large mass coil (LMC) design.	57
Figure 2.23. Representation of the elastic arms and the mass for the diaphragm....	58
Figure 2.24. Schematic view of the frequency up-converter (FUC) design.	61
Figure 2.25. Equivalent mechanical model of the system.....	62

Figure 2.26. Representation of the contact force.	67
Figure 2.27. Matlab® Simulink® model used to simulate the frequency up-converter (FUC) design.....	70
Figure 2.28. Simulink® subsystem used to determine the final state of the model...	71
Figure 2.29. Relative displacements of the cantilevers and the magnet.	72
Figure 2.30 Simulated voltage output from a single cantilever of the frequency up-converter (FUC) design.	73
Figure 3.1. Schematic drawing of the AOC design.....	76
Figure 3.2. Schematic drawing of the AOC_FS design.	77
Figure 3.3. Schematic drawing of the LMC design.	78
Figure 3.4. Schematic drawing of the FUC design.	79
Figure 3.5. Schematic drawing of the whole wafer over a 4" silicon wafer.....	80
Figure 3.6. Relative positions of the masks with respect to each other.	82
Figure 3.7. Micro fabrication steps of the FUC design.	85
Figure 3.8. Photo and main components of the parylene deposition system, SCS PDS 2010, courtesy of SCS Inc.....	88
Figure 3.9. Photo of the AOC design just before release.	101
Figure 3.10. Photo of the AOC_FS design just before release.	101
Figure 3.11. Photo of the LMC design base (left) and diaphragm (right)....	102
Figure 3.12. Photo of the FUC design base (left) and diaphragm (right).	102
Figure 4.1. Block diagram of the test setup and photos of the components.....	105

Figure 4.2. Photograph of the AOC design attached to the PCB (left) with close-up view of the prototype (lower-right) and the cantilevers (upper-right).	106
Figure 4.3. Photographs of the PCB base, magnet assembly, spacers and nuts....	107
Figure 4.4. Assembling procedure of the components of the test sample.....	108
Figure 4.5. Assembled sample mounted on the shaker table.	109
Figure 4.6. Measured voltage output from 4 consecutive arms of the generator..	111
Figure 4.7. Phase angle plots for various values of damping.....	112
Figure 4.8. Close-up view of phase angle for $\zeta=0.02$	113
Figure 4.9. Voltage output of a single cantilever and 5 consecutive cantilevers. .	114
Figure 4.10. Zoomed in view of Figure 4.9 for further analysis.	115
Figure 4.11. Voltage output of a single cantilever and 5 consecutive cantilevers. .	115
Figure 4.12. Zoomed in view of Figure 4.11 for further analysis.	116
Figure 4.13. Thermal grease residues remaining on the cantilevers after release... .	117
Figure 4.14. Photograph of the AOC_FS design after release.....	119
Figure 4.15. Voltage output from 20 cantilevers and comparison of bandwidth with a single cantilever.	121
Figure 4.16. Overall voltage output from all 40 cantilevers of the AOC_FS.	122
Figure 4.17. Measured voltage output from 35 cantilevers of the AOC_FS.	122
Figure 4.18. Measured voltage output from 40 cantilevers of the AOC_FS.	123
Figure 4.19. Block diagram of the proposed frequency sensor.....	124

Figure 4.20. Actual and measured frequency values by the frequency sensor.	125
Figure 4.21. Percent error of measured frequency values.....	125
Figure 4.22. Photograph of the LMC assembly and components.	126
Figure 4.23. Measured voltage output from the large mass coil (LMC) design.	128
Figure 4.24. Photograph of the frequency up-converter (FUC) assembly and its components.	129
Figure 4.25. Components of the FUC assembly prepared for testing.	130
Figure 4.26. FUC assembly coupled to the shaker table.	131
Figure 4.27. Simulation and test results plotted on the same set of axis for a single cantilever of the FUC design.	134
Figure 4.28. Close-up view of the simulated and actual results for 2 cycles.	135
Figure 4.29. Close-up view of the simulated and actual results for 1 cycle.....	135
Figure 4.30. Simulation and test results for the variation of the magnitude of the output voltage for different excitation frequencies.....	139
Figure 4.31. Illustration of variation of catch point with increasing frequency.....	141
Figure 4.32. Variation of up-conversion ratio with frequency.....	142
Figure 4.33. Output from two cantilevers with time shift.	143
Figure 4.34. Close-up of the output from two cantilevers with time shift.	144
Figure 4.35. Voltage output from individual cantilevers.	145
Figure 4.36. Output from two cantilevers with small time shift.	146
Figure 4.37. Output from two individual cantilevers with small time shift.	146

Figure 4.38. Summed up voltages from two consecutive cantilevers.....	147
Figure 4.39. Two cantilevers with non-identical natural frequencies.....	147
Figure 4.40. Output from two individual cantilevers with small time shift	148
Figure 4.41. Output from 3 cantilevers with shift in time and natural frequency... ..	149
Figure 4.42. Output from 3 cantilevers with shift in time and natural frequency... ..	150
Figure 4.43. Graphical approach showing the calculation of the release height difference, Δz	155
Figure 4.44. Illustration of the height difference measurement under the probe station.....	158
Figure 4.45. Optimum device configuration for the fabricated batch.....	159
Figure A.1. Layouts of the 1 st mask to fabricate cantilevers from parylene.	178
Figure A.2. Layouts of the 2 nd mask to fabricate the coil turns from titanium-gold (Ti/Au).	179
Figure A.3. Layouts of the 3 rd mask to form the contact pads parylene cantilevers.	180
Figure A.4. Layouts of the 4 th mask to fabricate the metal routes from titanium-gold (Ti/Au).	180
Figure A.5. Layouts of the 5 th mask to fabricate the magnetic actuation areas form nickel (Ni).	181
Figure A.6. Layouts of the 6 th mask for through etch of the wafers from the backside by deep reactive ion etching (DRIE) to release the devices.	182
Figure B.1. Fabrication process outline of the micro generators.....	183

NOMENCLATURE

- a_1 : Height of magnet.
- a_2 : Width of the magnet.
- a_p : Length of the magnet through magnetized direction.
- A_c : Cross-sectional area of the coil.
- A_i : Area of each coil turn.
- A_m : Magnetic contact area between the magnet and the cantilever.
- b : Width of the cantilever.
- b_c : Equivalent damping constant for the cantilever in the frequency up-converter design.
- b_e : Electrical damping constant.
- b_{eq} : Total equivalent damping constant.
- b_m : Equivalent damping constant for the magnet in the frequency up-converter design.
- b_{me} : Mechanical damping constant.
- B : Magnetic field strength of the magnet.
- B_r : Residual magnetic flux density.
- d : Distance from the magnet.
- E : Modulus of elasticity of the cantilever.
- F_e : Electromagnetic force acting on the cantilever.
- F_m : Magnetic attraction force between the magnet and the cantilever.
- g_o : Distance between the cantilever and nearby rigid wall.
- h : Thickness of the cantilever.
- i : Induced current through the circuit.
- I : Area moment of inertia of the cantilever.
- k_c : Equivalent stiffness of the cantilever in the frequency up-converter design.

- k_m : Equivalent stiffness of the diaphragm-magnet assembly in the frequency up-converter design.
 k_{eq} : Equivalent stiffness of the cantilever.
 L : Length of the cantilever.
 L_i : Length of the coil turn.
 L_p : Practical coil length.
 L_w : Length of the coil.
 m : Mass of the cantilever.
 m_c : Mass of the cantilever in the frequency up-converter design.
 m_m : Mass of the magnet in the frequency up-converter design.
 m_{eq} : Equivalent mass of the cantilever.
 n : Total number of coil turns.
 P : Power generated by the micro generator and delivered to a resistive load.
 q : Reciprocal of the frequency ratio.
 r : Frequency ratio.
 R_L : Load resistance.
 t : Time.
 T : Net contact force between the magnet and the cantilever.
 x : Absolute displacement of the cantilever's tip point.
 y : Absolute base displacement of the support.
 Y : Amplitude of input displacement.
 z : Relative displacement of the cantilever tip point with respect to the base.
 \dot{z} : Velocity of the cantilever tip point.
 δ_c : Offset of the cantilever with respect to the base.
 δ_m : Offset of the magnet with respect to the base.
 δ_{mst} : Static deflection of the magnet due to gravity.
 Δz : Displacement of the cantilever tip point corresponding to angular rotation.
 $\Delta\theta$: Angular rotation of the cantilever.
 η : Structural damping coefficient fpr the cantilever.
 μ : Viscosity of air.
 μ_0 : Permeability of free space.

- φ : Phase angle.
 Φ : Magnetic flux density.
 ρ_a : Density of air.
 ρ_b : Density of the cantilever.
 ρ_w : Resistivity of the coil material.
 $\dot{\theta}$: Angular velocity of the cantilever.
 σ : Mechanical stress.
 ζ_{eq} : Overall equivalent damping ratio.
 ζ_{me} : Mechanical damping ratio.
 ζ_e : Electrical damping ratio.
 ω : Excitation frequency.
 ω_d : Damped natural frequency of the cantilever.
 ω_n : Natural frequency of the cantilever.

CHAPTER 1

INTRODUCTION

There has been increasing interest in the Micro Electromechanical Systems (MEMS) technology over the past decade. With the recent improvements in the micro system technology, low-cost and low-power micro scale sensors and actuators can now be more easily manufactured. These systems are employed in many areas, from health monitoring to data transmission systems [1]. They have numerous advantages as being very small, cheap, and undetectable. Also, advances in the digital signal processing (DSP) technology and new architectures have reduced the power consumption of these devices. A wide variety of such pervasive wireless sensors and actuators have been started to be used in our daily life. Typical application areas of these wireless systems are implantable systems for health care and monitoring, automotive industry, for example pressure sensors embedded in tires, structural monitoring and preventive maintenance applications in intelligent buildings for monitoring temperature, light and humidity, and in military applications for powering data transmission devices on soldiers [2, 3]. Considering the small size and wireless nature of these systems, the first question that can be asked is how to supply energy to these systems. Indeed, the energy supply is the main limiting factor in the development and operation of the micro systems. As most of these devices are embedded in different types of systems, they can not be recharged like cell phones or laptop computers. This leads to the fact that they should either operate on their initial energy sources or a means of energy generator that can harvest energy from environmental sources should be developed. As a matter of fact, there are two options, one of which is the use of constant storage supplies like batteries and the other is using already available environmental energy sources like solar, thermal, or

vibration based energy. The latter is currently a promising research area in the literature as it suits better for micro systems.

1.1 Batteries as an Energy Source

After the invention of the battery by Alessandro Volta, it has been extensively used as a portable and conventional energy source from automobiles to music players. However, today's technology has enabled very small and low-power micro devices to be manufactured, and batteries are no more suitable for these kinds of devices. For example, for a low power device operating at an average power consumption of 1mW to have a lifetime of 10 years, it needs a 100 cm³ battery in the best case [4]. The batteries are not improved as fast as other electronic technologies, and in order to illustrate this, the development in laptop computer technology and battery energy densities are plotted on a logarithmic scale and shown in Figure 1.1 [5]. While form factors of the laptop have been improved exponentially, the battery technology almost follows a flat line. In order to overcome this problem, other capacitive type of energy sources such as micro-batteries and micro-fuel cells have been developed, but their disposal and pollution is an important problem. Wireless systems are improved very rapidly and their dependence on capacitive power sources, like in the best case to the micro-batteries and micro-fuel cells, makes them impractical. Conventional micro-batteries and fuel cells limit the lifetime of these systems resulting in inconvenient wireless systems that are unable to operate for long times. Thus, ultimately, new and effective power generation methods must be developed. One promising alternative is the use of environmental energy sources, which will be investigated in detail in the following sections.

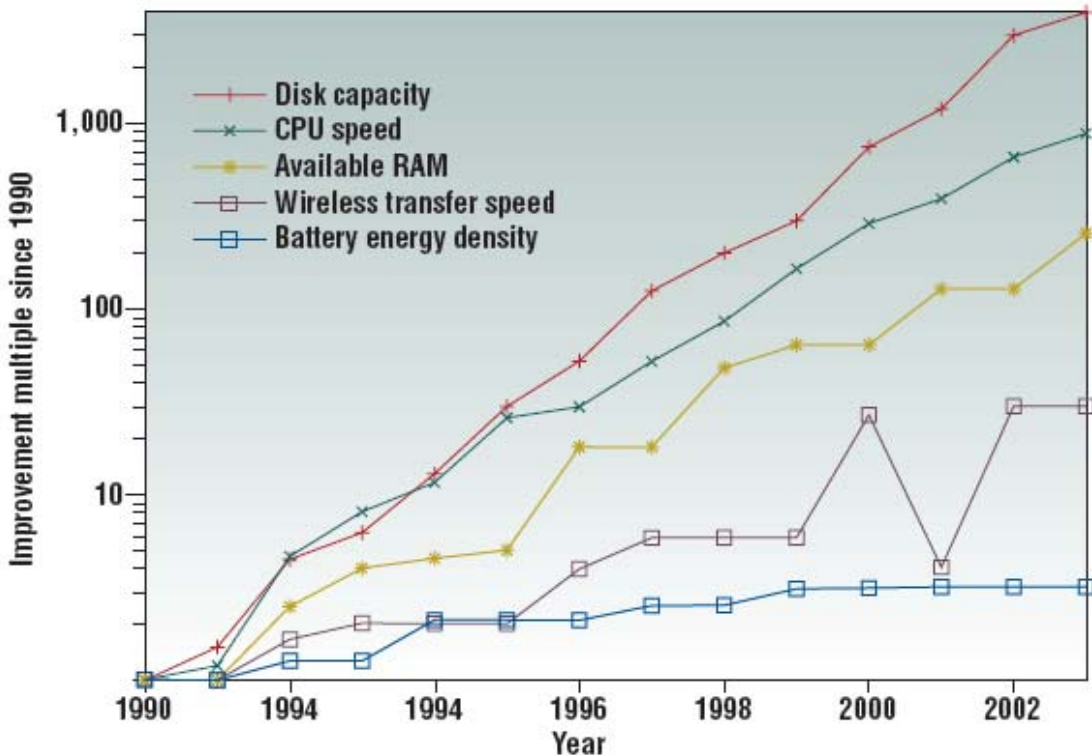


Figure 1.1. Relative improvements in laptop computing technology from 1990-2003 [5].

1.2 Environmental Energy Sources

Considering the application areas, most of the wireless micro systems are embedded, for example to human body or an automobile tire, which makes replacement, recharging and disposal of finite life capacitive energy sources a problem. In order to avoid these drawbacks, energy sources that are designed to power-up wireless micro systems must have a relatively high energy density, be able to be fabricated in micro scale, have a long lifetime, should not need to be disposed or replaced, and be available. Researchers are investigating new energy sources to power up micro systems, which can be listed as solar, vibrations, heat gradients, electromagnetic fields, fuel cells, and radioactive means [6]. In order to give a quick comparison of the above techniques, Table 1.1 shows the comparison of power densities of various types of energy sources [3].

Table 1.1. Comparison of energy scavenging sources [3].

	Power Density ($\mu\text{W}/\text{cm}^2$) 1 Year Lifetime	Power Density ($\mu\text{W}/\text{cm}^2$) 10 Year Lifetime
Solar (Outdoors)	15,000 – direct sun 150 – cloudy day	15,000 – direct sun 150 – cloudy day
Solar (Indoors)	6	6
Vibration	100-200	100-200
Acoustic Noise	0.003 @ 75 dB 0.96 @ 100 dB	0.003 @ 75 dB 0.96 @ 100 dB
Daily Temperature Variation	10	10
Temperature Gradient	15 @ 10°C gradient	15 @ 10°C gradient
Piezoelectric shoe inserts	330	330
Batteries (Lithium) (non-rechargeable)	89	7
Batteries (Lithium) (rechargeable)	13.7	0
Combustion (μ -engine)	403	40.3
Fuel Cells (methanol)	560	56

In Table 1.1, top seven rows denotes energy sources with constant power output, while the bottom four rows indicate sources with a fixed amount of energy. The first and second columns denote the power density in 1 and 10 year lifetime, respectively. In the case of environmental sources, the power density stays the same after 10 years of operation, but for capacitive sources, the power density is just divided into the total number of years of use. Thus, from the given data, it can be seen that when long lifetime operation is considered, scavenging energy from vibrations, piezoelectric shoe inserts and solar power (if available) seem to be the most feasible solutions. Being able to supply continuous power and availability are two important

facts when selecting a suitable energy source. That's why, due to the reasons like low-energy density, replacement and dirt, capacitive type of energy sources can be eliminated in the first case. The solar energy is actually a good alternative with a high energy density, but it is not always available. Finally, piezoelectric shoe inserts are macro scale energy sources and are out of the scope of this study. As a result, the most feasible solution seems to be obtaining energy from environmental energy sources that are especially based on vibrations as its always available and clean, and relatively high energy levels can be obtained.

1.3 Vibration Based Environmental Energy Sources

Researchers have so far designed vibration-based energy harvesters using three type of techniques: electrostatic (capacitive), piezoelectric and electromagnetic (inductive). In several studies [7-10], it has been shown that the energy levels obtained using these techniques are able to power-up various types of micro systems like data transmission and sensor nodes. Thus, it has been practically shown that harvesting energy from environmental vibrations is feasible. Considering factors like availability, energy density, ability to supply continuous power and environmental issues, in this study, it is planned to design and develop an energy harvester that can harvest energy from already available environmental vibrations. In the following subsections, the three type of vibration based energy scavenging techniques are explained in detail.

1.3.1 Electrostatic (Capacitive) Energy Scavengers

Electrostatic energy scavengers generate energy based on a mechanical structure, which changes its capacitance due to external vibrations. The basic equation relating charge to voltage is used in energy generation that is denoted by $q = CV$, where, q, C, and V are the charge, capacitance, and voltage, respectively. Depending on the design, as the capacitance changes the system acts as a voltage or current source and either the voltage or charge is kept constant to achieve these. If the voltage across the capacitor is kept constant, then the charge across the capacitor plates will vary,

and the system will act as a current source. In this case, an extra voltage source is required for keeping the voltage constant. If the charge on the capacitor is kept constant then the voltage will change and the system is going to be a voltage source in which case a separate charge source such as an electret is required to keep the charge constant. In either case, the system converts external vibration energy to electrical energy. Besides conversion type, there are also three types of mechanical designs used to change the capacitance for energy conversion. These are shown in Figure 1.2 and can be listed as,

1. In-plane overlap converter in which the capacitance changes by changing overlap area of the fingers (Figure 1.2.a). This type of scavenger does not need any mechanical stops to avoid collusion of electrodes to each other and it has the highest Q factor compared to the other two types of designs. However, it has stability problems for large deflections and it has the lowest maximum capacitance compared to other two designs.
2. In-plane gap closing converter where the capacitance changes by changing the gap between the fingers (Figure 1.2.b). This design has a larger maximum capacitance compared to the in-plane overlap design, but mechanical stops are necessary to avoid electrodes hit each other.
3. Out-of-plane gap closing converter in which the capacitance changes by changing the gap between two large plates (Figure 1.2.c). This type of design has a good stability the largest maximum capacitance compared to the other two designs. However, it also has the largest mechanical damping, and surface adhesion is also a problem due to the two large areas interacting.

Capacitive type energy scavengers have been investigated extensively in the literature [11-20]. The primary advantage of electrostatic scavengers is that they can readily be implemented in standard micro-machining processes, and they perform better in low-frequency applications. Their main disadvantages are low power output levels as shown in Table 1.2, the need for an extra voltage source or an electret (a material that has permanent electric charge polarization) and the

requirement for a mechanical stop. In Table 1.2, practical maximum values are the maximum energy levels that have been actually obtained so far, and theoretical maximum values are obtained as a result of simulations without practical verifications.

As a result of comparing the advantages and disadvantages, the electrostatic type of energy scavenging is also eliminated and will be kept out of the scope of this study.

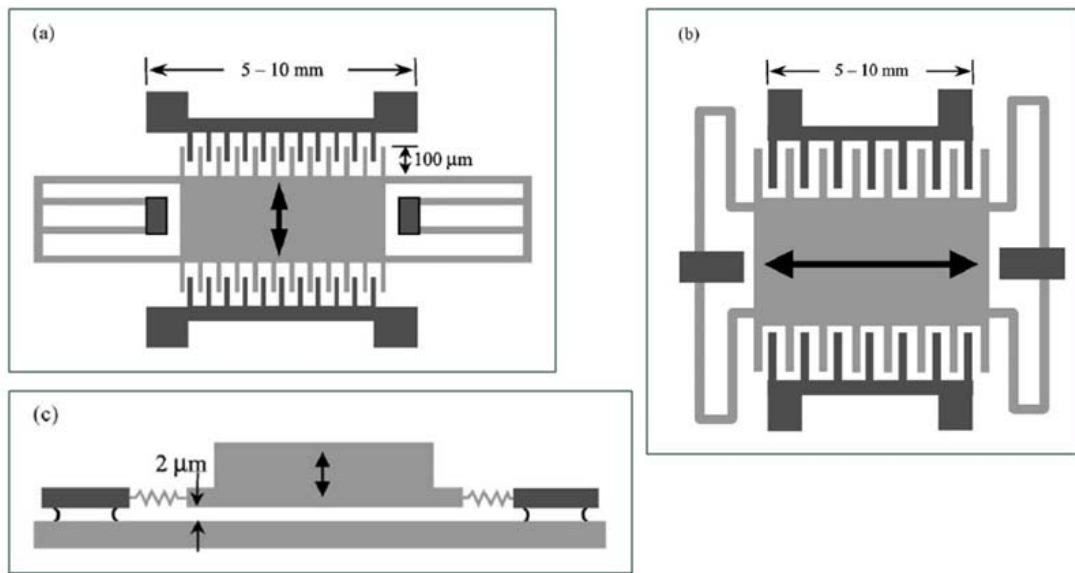


Figure 1.2. Typical types of mechanical structures of an electrostatic energy scavengers, figure courtesy of [12].

Table 1.2. Comparison of energy generation densities [6].

Type	Practical max. (mJ/cm ³)	Theoretical max. (mJ/cm ³)
Piezoelectric	35.4	335
Electrostatic	4	44
Electromagnetic	24.8	400

1.3.2 Piezoelectric Energy Scavengers

The principle of operation of piezoelectric energy scavengers is, as the piezoelectric material is deformed by external vibrations, a voltage is generated across the terminals of the piezoelectric material due to the strain caused by deformation. The generated voltage on the piezoelectric material creates a damping force proportional to the relative velocity of the piezoelectric structure that opposes the motion of the structure. As a result, the mechanical energy is converted to the electrical energy. Figure 1.3 shows the schematic diagram of a typical piezoelectric harvester [21].

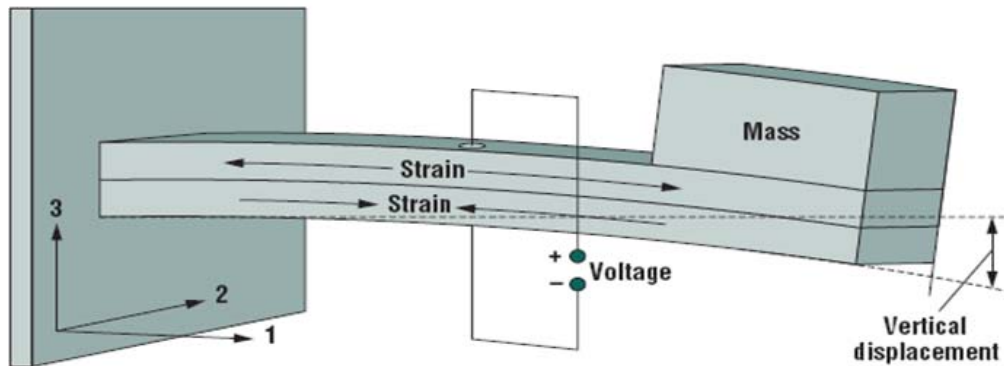


Figure 1.3. Schematic view of a typical piezoelectric harvester [21].

There are usually two types of operations employed in energy scavenging that are named as the “33” and “31” modes of operation. In the “33” mode of operation, force is applied along the axis 3 shown in the figure and the voltage is generated on the faces perpendicular to this direction. In the “31” mode of operation, force is applied along the axis 1 shown in the figure, and again resulting voltage is generated on the faces perpendicular to axis 3.

It is possible to find various studies in the literature on this topic [3, 12, 22-37]. Referring to previous studies, the main advantages of this type of generators are a separate voltage source is not required, a mechanical stop is not necessary, and they

have relatively high energy densities [38]. However, it is hard to manufacture these devices using standard micro fabrication techniques, and their mechanical to electrical conversion efficiency is low.

1.3.3 Electromagnetic (Inductive) Energy Harvesters

Energy generation principle of electromagnetic generators is similar to piezoelectric ones. The schematic representation of the generator is shown in Figure 1.4 [39]. In this case, an electrical energy is generated by the relative motion between a moving coil and a permanent magnet. According to Faraday's Law of Induction, as the coil moves relative to the magnet, the magnetic flux lines are cut by the enclosed area of the coil inducing a current on the coil wire. The induced current on the wire opposes the motion of the coil structure with a force proportional to the relative velocity of the coil with respect to magnet. This actually creates a damping force on the coil structure. As a result, the mechanical energy is converted to electrical energy.

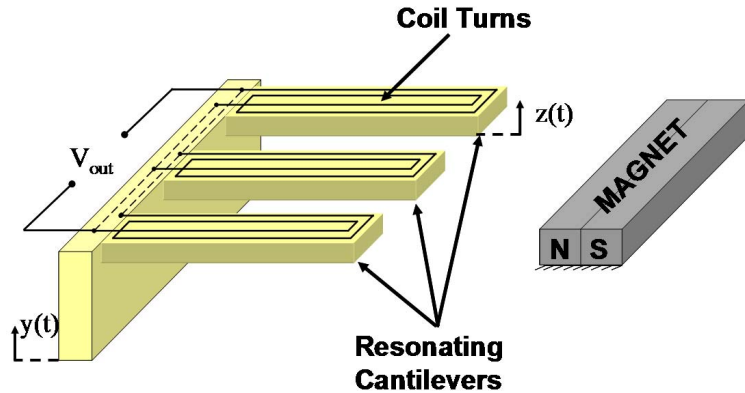


Figure 1.4. Schematic diagram of an electromagnetic energy generator [39].

The main advantages of electromagnetic generators are no separate voltage source and no mechanical stops are required, and they have relatively high power densities with high energy conversion efficiency. The primary disadvantage is that the

generated voltage is relatively low. A detailed review of this type of scavenger is presented in the next section.

Among the three techniques described, the electrostatic type of energy conversion will be out of the scope of this study due to low energy density and dependence on a separate voltage source or an electret. Piezoelectric and electromagnetic energy generation techniques are similar to each other in some aspects. In both cases, a damping force proportional to relative velocity of the moving structure within the casing is generated. This is required to convert mechanical energy to electrical energy. In both techniques no external voltage source and mechanical end stops are required. Finally, energy generation levels of both techniques are almost the same. On the other hand, piezoelectric method has the disadvantage of low conversion efficiency and hard micro machining processes. As a result, considering these facts it is decided to focus on energy generation through electromagnetic induction.

1.4 Review of Electromagnetic (Inductive) Energy Harvesters

Based on the reasons stated earlier, this study plans to focus on energy generation using electromagnetic induction technique. Although significant studies on this topic exist in the literature, most of them are based on simulations in which the mathematical models of the proposed systems are rather simple. Most of the remaining studies are carried out in milli scale. Thus, there are very few micro scale experimental studies accomplished in this area. In addition, most of the studies show that the electromagnetic energy generators are not feasible at low frequencies (10-100 Hz). However, most of the vibrations exist in this frequency range in the nature.

The first significant study in this area is the analysis of a micro electric generator for micro systems carried out by C.B. Williams *et al.* in 1996 from the University of Sheffield [10, 40]. Based on the simulations, they have stated that the proposed generator, having dimensions of 5x5x1mm, could generate power with a magnitude of 1 μ W at 70 Hz input frequency and 30 μ m vibration amplitude and 100 μ W at 330 Hz and 30 μ m vibration amplitude. Also, they are the first researchers, who have stated that the generated power is proportional to the cube of the input frequency,

$P \propto \omega^3$. This comes from the fact that they have stated the power is going to be maximum when the system is excited at the natural frequency of the system, i.e. at $\omega = \omega_n$. Although this last statement is not exactly correct due to the mechanical damping existing in the model, it has been widely used in literature in almost all the studies dealing with this model. This is because if the damping ratio of the system is assumed to be small then such a statement can be made, but still it would have some error. The model they have proposed can be represented by an equivalent accelerometer model as shown in Figure 1.5.

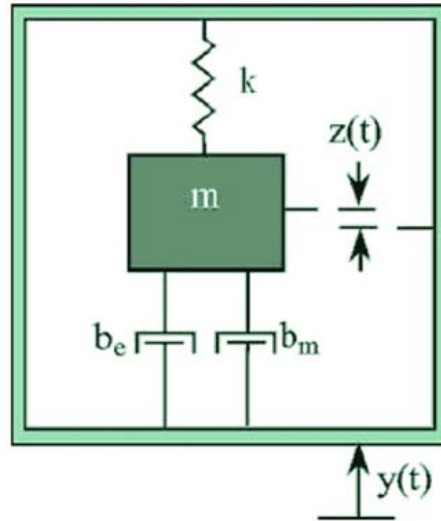


Figure 1.5. Equivalent mass-spring-damper model of the generator [12].

In the model shown above, the mechanical to electrical energy conversion is represented by the electrical damping constant, b_e . This is because the induced current within the generator will try to slow down the motion of the mass with a force proportional to the relative velocity of the mass with respect to the outer casing of the generator. Thus, a generic power equation can be given as,

$$P(t) = \frac{m_{eq} \zeta_e \left(\frac{\omega}{\omega_n} \right)^3 \omega^3 Y^2}{\left(1 - \left(\frac{\omega}{\omega_n} \right)^2 \right)^2 + \left(2(\zeta_e + \zeta_m) \frac{\omega}{\omega_n} \right)^2} \cos^2(\omega t + \phi) \quad (1.1)$$

In (1.1), m_{eq} is the equivalent mass, k_{eq} is the equivalent stiffness, ζ_m is the mechanical damping ratio, ζ_e is the electrical damping ratio, ω is the input excitation frequency, ω_n is the natural frequency of the system, Y is the amplitude of external vibrations, and ϕ is the phase difference between the input excitation and mass displacement.

Firstly, due to the damping terms, it can readily be seen that power is not going to be maximum at $\omega = \omega_n$. Indeed, power is going to have a maximum value at,

$$\omega = \omega_n \sqrt{-2(2\zeta_{eq}^2 - 1) - \sqrt{16\zeta_{eq}^4 - 16\zeta_{eq}^2 + 1}}, \text{ for } \zeta_{eq} \gtrsim 0.25 \quad (1.2)$$

Equation (1.1) is given here to give a concise view of the generated power. The model shown in Figure 1.5 is actually the equivalent lumped, one degree of freedom (DOF) model of a continuous system. One of the aims of this study is to extend this model to a much detailed one so that the dynamics behind power generation can be understood much better.

At the end of 1997, C. Shearwood and R.B. Yates have manufactured and tested the first electromagnetic micro generator in this area [41]. This work was actually a continuation of the work by C.B. Williams *et al.* in 1995. The schematic diagram of the generator is shown in Figure 1.6.

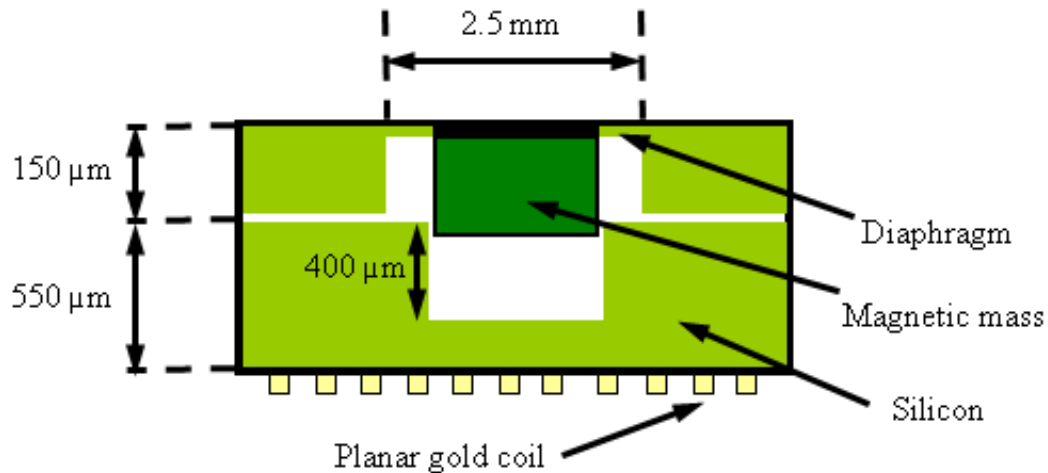


Figure 1.6. Schematic diagram of the first electromagnetic micro generator [41]

The proof magnetic mass (rare earth, SmCo) of 2.4 mg was held by a polyimide diaphragm spring. As the generator is vibrated, the net movement of the magnet within the housing induces current through the planar Au coil of thickness 2.5 μm . It has been reported that the generated power had magnitude 0.3 μW at an excitation frequency of 4.4 kHz, which is actually very high. The amplitude of the input vibrations was 0.5 μm .

M. El-Hami *et al.* have designed and tested an electromagnetic vibration based energy generator in 2000 at the University of Southampton [42]. They have shown that it is possible to generate power more than 0.53 mW within a volume of 240 mm^3 at a vibration frequency of 320 Hz. The amplitude of external vibrations was 25 μm . This design was relatively larger in volume than actual micro power generators. That's why the power output is relatively large. The proposed electromagnetic generator had a C-shape in order to create a uniform magnetic field in the air-gap. In 2003, the same group has constructed two milli scale prototypes and compared their performances [2]. One of the designs had a total volume of 0.84 cm^3 and was based on a moving coil between two magnets. Although this design had useful level of output power, the generated voltage level was low. The other design was 3.15 cm^3 and based around a coil between four moving magnets. The designs were tested by

mounting them on a car engine block. As a result, the second prototype seemed to perform better with an average output power level of $157 \mu\text{W}$. In 2003, to show the feasibility of the generator, it is tested to power-up two different systems [8]. One of the systems was an accelerometer that outputs the results on an LCD. The other was again a sensor, but this time the sensor output signals were transmitted via IR. Both devices were successfully operated. Although, the design is relatively large in volume, it shows that electromagnetic vibration based generators are feasible.

In the work of P.D. Mitcheson *et al.* in 2004, architectures for vibration driven micro power generators has been compared, namely the electromagnetic, piezoelectric and capacitive techniques [43]. Although, the results have not been practically verified, this study is significant as it stresses on the conditions where each technique is useful. The proposed electromagnetic generator model is shown in Figure 1.7, which is similar to the one proposed by C. Shearwood in 1997.

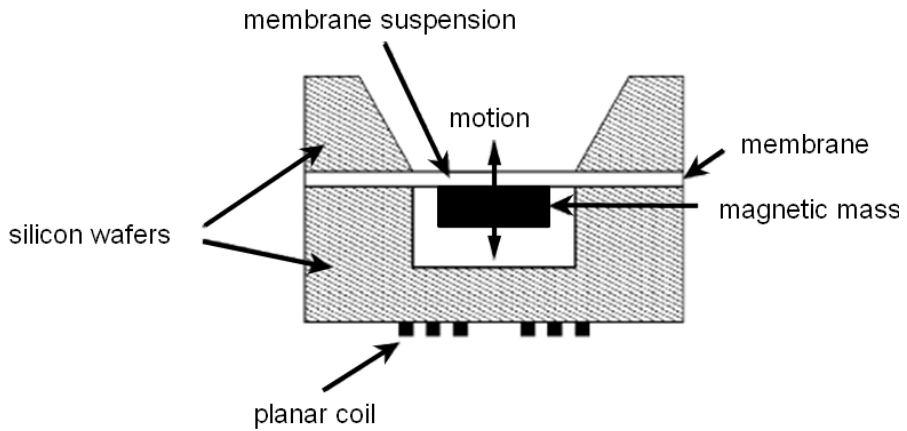


Figure 1.7. Electromagnetic generator proposed P.D. Mitcheson *et al.* [43].

As a result of this study, it is stated that due to the space limitations faced in micro generators, electromagnetic and piezoelectric generators would perform better at high excitation frequencies like a machine powered application where as capacitive type generators are better suited for low frequency excitation such as human powered

applications. The same group of researchers has carried out a study on inertial micro power generators in 2005, which focus on optimization of generator parameters for human walking motion [44]. In this work, by using accelerometers, acceleration levels at certain parts of the human body have been measured during walking. This information is then processed and used as input for simulating the power generation levels. This study is useful especially in terms of generation of power at low level frequency vibrations.

In the literature, it is also possible to find macro scale designs [9, 45-47]. One of such designs is an AA battery sized energy generator [9]. J.M.H. Lee *et al.* designed and tested such an electromagnetic generator that could generate $830 \mu\text{W}$ of power with a peak to peak voltage output of 3 V. The input frequency was 100 Hz with displacement amplitude of $250 \mu\text{m}$. It has also been shown that the generator could power an infrared and an RF transmitter. The same group of researchers has also developed a micro generator with a total volume 1 cm^3 that could output power with a magnitude of about $100 \mu\text{W}$ at $40 \mu\text{A}$ current [47, 48]. In this design, the spring structure was laser micro machined and several spring designs were compared for performance. As a result, due to the design geometry, it has been seen that in the second vibration mode more power could be generated than in the first mode.

R. Amirtharajah *et al.* have proposed a moving coil electromagnetic generator with an average power output of $400 \mu\text{W}$ and peak voltage of 100 mV [49]. Although the estimated power level is reasonably high, the model does not include mechanical losses, which is the main cause that decreases generated power. In this study, the authors mainly focus on regulation of output voltage by using digital signal processing systems so that the generated power can be converted to useful levels.

Dr. S. Roundy of Australian National University has made important contributions to this area. He has mainly focused on energy generation from environmental vibrations using piezoelectric and electrostatic techniques. On the other hand, he had made no significant studies on power generation using the electromagnetic technique. In his Ph.D, thesis, he has mainly focused on energy generation using

piezoelectric and electrostatic techniques [3]. S. Roundy *et al.* have made a comparative study of vibration based techniques [12] in which each technique is described and several important points that should be considered during the design of micro generators are focused.

In the work of M. Mizuno and D.G. Chetwynd, a single glass cantilever on which a 12 turn coil is modeled electromagnetic energy scavenging [13]. It is predicted that 6 nW and 1.4 mV can be generated from input vibrations of 58 kHz and 100 nm. For testing, a glass cantilever sample sized 25 mm x 10 mm x 1 mm with 4 coil turns evaporated on it is used. Measurements show that, a maximum voltage output of 320 μ V could be obtained at a vibration frequency of 700 Hz and 0.64 um displacement amplitude. The corresponding power is calculated to be 0.4 nW for equal coil and load resistances of 128 Ω .

In most of the comparative studies made [1, 23, 25, 42, and 43], it has been stated that electromagnetic generators are suited better for medium scale applications whereas piezoelectric generators for micro scale applications. On the other hand, each method's efficiency depends on its parameters and the design used. Thus, another aim of this thesis study is to show that electromagnetic micro generators can efficiently scavenge energy even at low frequency vibrations.

The final study that is going to be discussed here is the one carried out by H. Kulah and K. Najafi in 2004 [7], and it is also going to form a basis for a part of this thesis study. This study, as others, is based on scavenging energy from environmental vibrations using an electromagnetic generator. Until this work, nobody has ever tried to use a specific mechanical mechanism to increase the generated power. The significance of this study lies in the fact that for the first time a frequency up-conversion technique is used as an energy generation mechanism. The aim of the study is to increase the power output at low-frequencies. This is done by up-converting the input frequency which is on the order of 1-100 Hz to a much higher frequency of 1-10 kHz so that the produced power increases rapidly. The mechanism consists of a large magnet oscillating at the central space of an array of

much smaller sized cantilevers. Small magnets are placed at the tip of the cantilevers. As the large magnet oscillates by input vibrations, it catches the smaller cantilevers, and during the cycle, it releases the cantilevers at some point when the tension in the beams is larger than the magnetic attraction. Thus, the small cantilevers tuned at a much higher resonant frequency are given a displacement initial condition. This mechanism is illustrated in Figure 1.8.

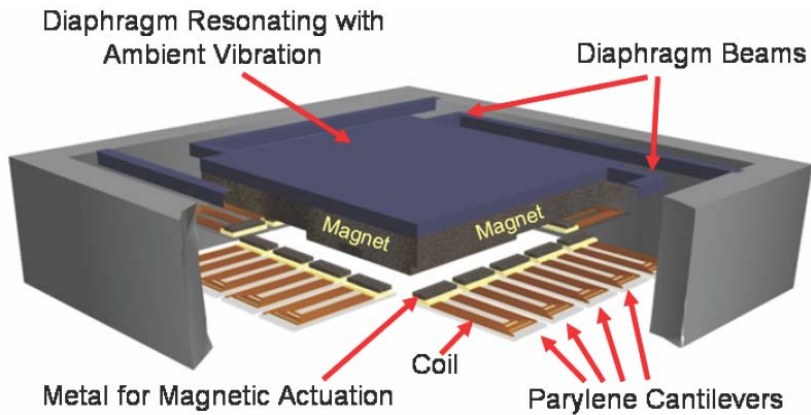


Figure 1.8. Representation of frequency up-conversion mechanism [7].

The main disadvantage of this design is cantilevers oscillation and thus the generated power will die out exponentially by time, but as the external vibrations continue the cycle will go on indefinitely. Simulations show that the generated maximum power is two orders of magnitude larger than the traditional large mass coil case. From a single small cantilever it is expected to generate $2.5 \mu\text{W}$ of power. Also, a milli scale prototype is constructed that produces a power of 4 nW at 1 Hz external vibrations that corresponding to $25\text{-}50 \text{ Hz}$ of up-converted frequency. Another important point in this study is the use of parylene as the beam material instead of silicon. The reason is that parylene is a much elastic material compared to silicon so that it can withstand much larger deflections before mechanic failure [50].

As a result of the review of the previous work, it has been seen that there is still much work that can be done in this area both theoretically and practically. Many of

the models presented in the literature are mathematically incomplete. Thus, there is usually a large difference between theoretical and actual results. Also, the mechanical designs considered in most of the studies are alike, but different designs could have been investigated to improve the efficiency of the micro generators.

Starting by C.B. Williams *et al.* [10], all of the reported generators so far focus on scavenging energy at a single ambient vibration frequency. As a result, they implement devices naturally with small bandwidth (1-100Hz). Thus, if the environmental vibration frequency deviates a little from the designed frequency, which is most of the time the resonance frequency of the device, the generated power decreases rapidly. Even if the environmental frequency is constant, it is really hard to match the resonance frequency of the device to that of the environment due to micro-fabrication accuracy and variation in other physical parameters of the device [4]. In order to solve this problem, several solutions have been proposed in the literature like active/passive tuning techniques [23-25] and widening of the bandwidth [4]. In active/passive tuning techniques, simply the parameters of the generator such as the mass or the stiffness are altered so that the resonance frequency is tuned to match the environmental frequency. In the active tuning technique, this adjustment is done continuously, whereas in the case of passive tuning technique, the tuning actuators turn off after the adjustment [4]. S. Roundy *et al.* [23] mathematically showed with some assumptions that, active tuning techniques are not feasible because the tuning actuators will always require more power than the device can generate. However, passive tuning techniques also require actuators and sensors, which increase the complexity and the cost of the device. Another solution is to widen the bandwidth of the generator. Only Ferrari *et al.* proposed a multi-frequency energy converter [26]; however, this converter covers a limited range (100-300 Hz) with a non-uniform power distribution, and is not compatible with standard fabrication techniques. The study by H. Kulah and K. Najafi also considers a semi-passive adaptive design aiming to increase the efficiency of the generators at low frequencies [7]. That's why a part of this thesis work is going to be based upon this design. In the literature it is also possible to find studies to increase the bandwidth of

micro energy generators. I. Sari *et al.*, showed that by implementing array of cantilevers varying in length, the bandwidth of electromagnetic type energy harvesters could be increased [51, 52]. In another work, the same group has also shown that the same structure could be used as a self-powered frequency sensor [53].

1.5 Objective of the Thesis Study

The main aim of this thesis study is to design, fabricate, and test micro electromechanical systems (MEMS) based energy generators that can efficiently scavenge electrical energy from low frequency environmental vibrations for wireless micro systems. The environmental vibration energy is aimed to be converted to electrical energy by use of electromagnetic induction.

Based on the discussion made in the previous section, the main objectives of this thesis study can be listed as,

1. Design, manufacture, and implement vibration based electromagnetic type energy harvesters in micro scale,
2. Improve the mathematical modeling which is weakly investigated in previous studies and develop detailed models by using continuous vibrations technique,
3. Optimize the parameters of the model so that voltage and power generation is maximized,
4. Improve voltage and power generation at low frequencies, by designing novel generator models,
5. Investigate and design novel active and/or passive adaptive tuning techniques to match the generator's resonant frequency to the fundamental frequency of the external vibrations.

The first item in the above list is going to give experience and insight to this study. The second and third items are going to improve a weakness in the literature and

open a new viewpoint to the researchers working in this area. So far, it has been reported that vibration based generators are not efficient at low frequencies, which is actually what is available in nature. Thus, the fourth item in the above list is aiming to improve this deficiency. Finally, the input excitation frequency to generators will normally be changing by time or at least it will have rich frequency content. That's why the last item is aiming to design novel generators that can adapt varying frequencies and maximize the output power. In order to achieve the above objectives the following methods and steps are planned to be realized.

1. Modeling and design of a single cantilever using equivalent single degree of freedom (DOF) mass, spring, damper model.
2. Development of a suitable optimization algorithm in Matlab[®] in order to obtain optimal parameters of the cantilever for maximum power.
3. Analysis and optimization of performance of an array of cantilevers for varying sizes and volume.
4. Simulation of finalized single cantilever model and array of cantilevers in Matlab[®] Simulink[®].
5. Development of the continuous model of a single cantilever and its comparison with single DOF model.
6. Manufacture of a standard micro generator from parylene and carrying out performance tests.
7. Modeling, design, and optimization of the frequency up-converter proposed in [7].
8. Simulation of the frequency up-converter in Matlab[®] Simulink[®].
9. Fabrication and testing of the frequency up-converter desing.
10. Investigation and modeling of novel passive and active techniques.

11. Design, manufacture and test of feasible novel designs that use passive or active techniques.

1.6 Conclusions

In this chapter, energy harvesting alternatives have been discussed. Among these alternatives, energy scavenging from environmental vibrations is decided to be used in this study. Considering facts like efficiency, ease of fabrication and implementation, the most feasible technique is decided to be electromagnetic induction.

In the first chapter, which is this one, energy harvesting alternatives have been discussed in detail that is followed by the statement of objectives and aims of the study.

In the second chapter, various types of electromagnetic generators have been proposed to accomplish the objectives of the thesis. Detailed mathematical analysis and related simulation results have also been presented in this chapter.

After modeling and simulation, Chapter 3 deals with the detailed micro fabrication procedure of the proposed micro generators.

Chapter 4 presents the test procedure and performance results of the fabricated micro generators. Each micro generator is analyzed separately and their performance is compared with the simulation results presented in Chapter 2. Possible causes of errors and deviations of measurements from simulation results have also been discussed in detail in this chapter.

The study is completed with concluding remarks and recommendations for possible future work.

CHAPTER 2

DESIGN, MODELING, AND SIMULATION OF ELECTROMAGNETIC MICRO ENERGY HARVESTERS

The main focus of this thesis study is to convert environmental vibrations to electrical energy through electromagnetic induction. This can simply be achieved by using Faraday's Law of Induction. For this purpose it is required to have relative motion between a magnet and a coil in such a way that the magnetic flux density passing through the coil is always changing. Depending on the design, either the magnet [10, 40] or the coil [7, 13, 42] can be stationary and the other moving by means of external motion such as environmental vibrations. It is possible to find realizations of both designs in the literature. Within the scope of this thesis study, different types of energy harvester designs are proposed, fabricated, and tested. In this chapter, the conceptual design, mathematical modeling, optimization, and simulation of these designs are presented in the related sections. The proposed designs can be listed as,

- The Array of Cantilevers (AOC) Design,
- The Array of Cantilevers Design with Varying Natural Frequencies (AOC_FS), “The Frequency Sweeper”,
- The Array of Cantilevers Design with Varying Natural Frequencies (AOC_FS) as an Energy Harvesting Frequency Sensor,
- The Large Mass Coil (LMC) Design,
- The Frequency up-Converter (FUC) Design.

2.1 The Array of Cantilevers (AOC) Design

In the first part of this section, the detailed mathematical modeling and analysis of the array of cantilevers design is presented. This is followed by the analysis of effect of certain system parameters on power and voltage output from the proposed generator to have a better understanding of the internal dynamics of the system. Afterwards, mechanical stress equations and modal analysis of the proposed system are presented to determine and better understand the physical limits of the generator. Finally, the section is completed with optimization and simulation results of the generator with sample design parameters.

2.1.1 Mathematical Modeling of the Array of Cantilevers (AOC) Design

Figure 2.1 shows the schematic diagram and the equivalent model of the first design proposed within the scope of this study.

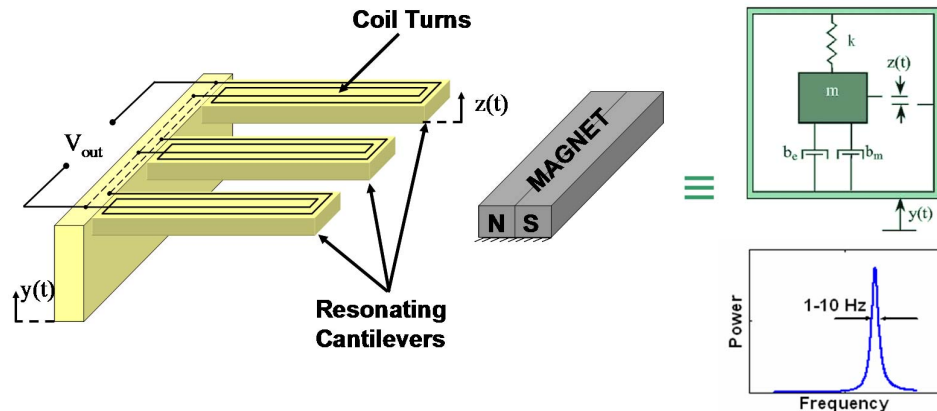


Figure 2.1. Schematic view of the array of cantilevers design (AOC).

In this design, there are resonating identical cantilevers on which planar coils are fabricated. A stationary magnet is placed right in front of the cantilevers. The base is excited by ambient vibrations and as a result, voltage is generated by virtue of the relative motion between the coils and the magnet. The output can be increased by

operating the device at the resonance frequency of the cantilevers and by connecting the coils electrically in series. The main advantages of the model proposed here are, introduction of the array of cantilevers design to superimpose the individual voltage output from each coil and the use of Parylene C as the structural material for the resonating cantilevers. Parylene is a much flexible material compared to silicon and glass so that it allows much larger deflections before mechanical failure [50], which results in increased voltage output. In the literature only Mizuno et al. have investigated a single cantilever design made of glass [13], so the array of cantilevers design itself is a novel architecture that is presented here for the first time.

As the first step of the design procedure, a mathematical model for the generated power and induced voltage at the terminals of the coil turns is constructed in terms of the physical system parameters. Then, the equation of motion of the cantilevers is defined to combine the electrical and mechanical dynamics of the system so that everything can be defined by a single equation. After obtaining necessary equations, the cantilever parameters are optimized using a Pattern Search Algorithm in Matlab to obtain maximum output from the generator. As the final step of the design procedure, the optimized parameters of the cantilevers is checked against mechanical failure using the stress equations developed for the cantilevers.

Figure 2.2 shows the basic electrical model for a single cantilever coil driving an electrical load. In this model, it is assumed that the coil inductance is small compared to the internal resistance of the coil. The power delivered to the resistive load, R_L , can then be obtained from,

$$P = \frac{1}{2} i^2 R_L \quad (2.1)$$

where i is the induced current through the circuit and R_L is the load resistance. The expression for the induced current, i , is given by,

$$i = \frac{\epsilon}{R_L + R_c} \quad (2.2)$$

where ϵ and R_c are the induced voltage at the terminals of the coil turns and coil resistance, respectively.

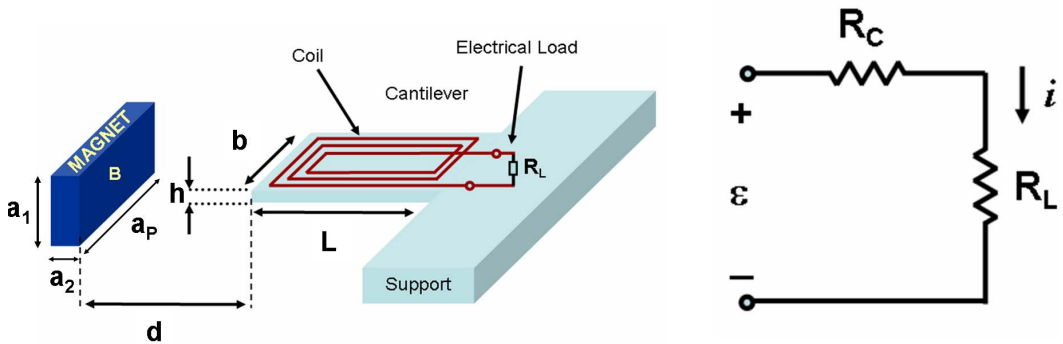


Figure 2.2. Basic electrical model of a coil driving a resistive electrical load.

The resistance of a rectangular cross sectioned coil is defined by,

$$R_c = \rho_w \frac{L_w}{A_c} \quad (2.3)$$

where ρ_w is the resistivity of the coil material ($\Omega \cdot m$), L_w is the length of the coil and A_c is the cross-sectional area of the coil. It is also worthwhile to note here that the coil is totally made up of a uniform conducting material, so throughout the text it can be considered as a conductor.

In order to obtain the induced voltage at the terminals of the coil turns, a suitable electromagnetic model should be constructed. Figure 2.3 shows the illustration of the magnetic field lines with strength B and the orientation of the cantilever. In this model, it is assumed that when the cantilever tip point is displaced by Δz , the cantilever makes a pure rotation by an angle $\Delta\theta$, which is valid as far as the rotation angle is small. In the proposed model, the induced voltage is denoted by ϵ , the length and area of each coil turn is denoted by L_i and A_i , respectively. By using Faraday's Law of Induction, the induced voltage on the coils can be derived as,

$$\varepsilon = -\frac{d\Phi}{dt} = -\frac{d\left(\sum_{i=1}^n (\vec{B} \cdot \vec{A}_i)\right)}{dt} \quad (2.4)$$

where Φ is the magnetic flux density, t is time, B is the magnetic field strength of the magnet, A_i is the area of each coil turn, and n is the total number of coil turns.

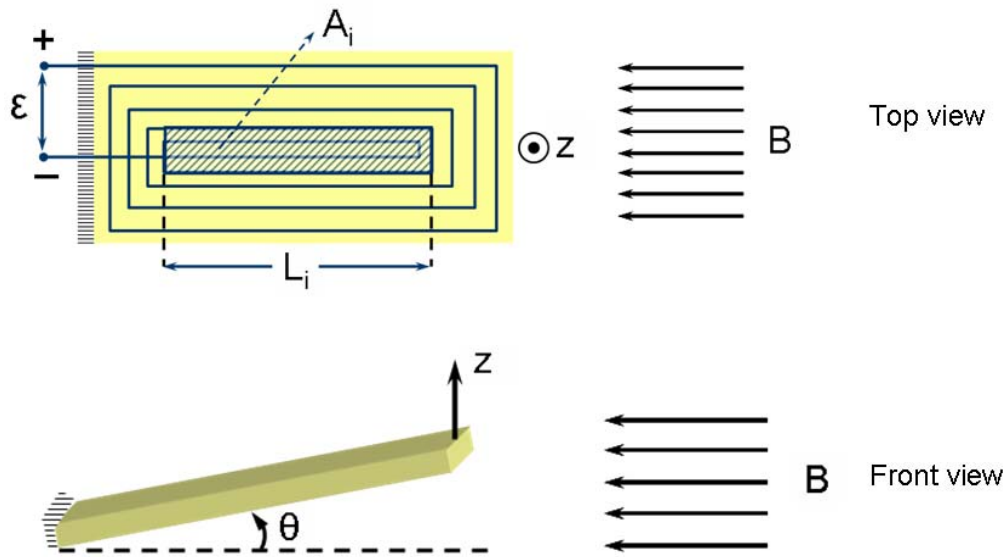


Figure 2.3. Illustration of magnetic field lines and orientation of the cantilever.

Referring to Figure 2.3, (2.4) can be rewritten in open form as,

$$\varepsilon = -\frac{d\left(\sum_{i=1}^n (BA_i \sin(\theta))\right)}{dt} = -B \sum_{i=1}^n A_i \frac{d(\sin(\theta))}{dt} - \sum_{i=1}^n A_i \frac{dB}{dt} \sin(\theta) \quad (2.5)$$

Equation (2.5) can further be expanded to give,

$$\varepsilon = -B \sum_{i=1}^n A_i \dot{\theta} \cos(\theta) - \sum_{i=1}^n A_i \frac{dB}{dz} \frac{dz}{dt} \sin(\theta) \quad (2.6)$$

In (2.6), the first term is related with the change of the area vectors of the coil turns in the direction of motion and the second term is related to the change of the magnetic flux, B with respect to the vertical distance, z . Due to the design geometry, the following relation can be written between the angular velocity, $\dot{\theta}$, of the cantilever and linear tip velocity, \dot{z} , of the cantilever tip point,

$$\dot{z} = L\dot{\theta}\cos\theta \Rightarrow \dot{\theta}\cos\theta = \frac{\dot{z}}{L} \quad (2.7)$$

Substituting the resulting equation in (2.6) and rearranging gives,

$$\varepsilon = -B \left(\sum_{i=1}^n \frac{A_i}{L} \right) \dot{z} - \frac{dB}{dz} \left(\sum_{i=1}^n A_i \right) \sin(\theta) \dot{z} \quad (2.8)$$

Equation (2.8) is a general expression of the induced voltage, which considers both the change of area and magnetic flux lines. For this design the magnetic flux is assumed to be constant along the direction of motion of the cantilevers and thus the second term can be eliminated to give,

$$\varepsilon = -B \left(\sum_{i=1}^n \frac{A_i}{L} \right) \dot{z} = -BL_p \dot{z} \quad (2.9)$$

where L_p is the practical coil length defined by,

$$L_p = \sum_{i=1}^n \frac{A_i}{L} \quad (2.10)$$

Finally the magnetic flux, B , from a rectangular shaped magnet can be expressed by [13],

$$B = \frac{B_r}{\pi} \left(\tan^{-1} \left(\frac{a_1 a_2}{2d\sqrt{a_1^2 + a_2^2 + 4d^2}} \right) - \tan^{-1} \left(\frac{a_1 a_2}{2(d + a_p)\sqrt{a_1^2 + a_2^2 + 4(d + a_p)^2}} \right) \right) \quad (2.11)$$

Here, B_r is the residual magnetic flux density (1.1–1.4 Tesla for NdFeB type magnets), a_p is the length of the magnet through magnetized direction, a_1 is the height of magnet, a_2 is the width of magnet, and d is the distance from the magnet. After obtaining suitable expressions for the practical length, L_p , and the magnetic field, B , the relative velocity term, \dot{z} , is required to be determined. For this purpose a suitable mechanical model for the cantilevers should be constructed. This can be achieved by constructing an equivalent 2nd order mechanical model like the one shown in Figure 2.4.

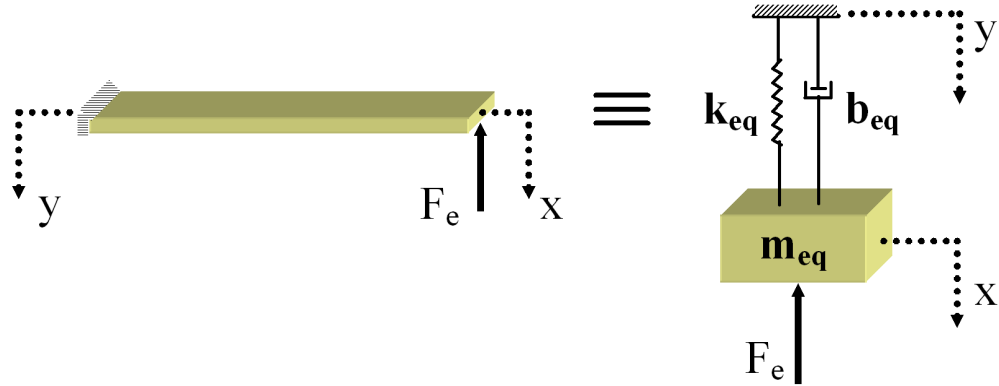


Figure 2.4. Equivalent 2nd order mechanical model.

Using Newton's 2nd Law of motion, the differential equations of motion of the equivalent mechanical system shown in Figure 2.4 can be obtained as,

$$m_{eq} \ddot{x} + b_{me} (\dot{x} - \dot{y}) + k_{eq} (x - y) = -F_e \quad (2.12)$$

In this equation, m_{eq} , k_{eq} , and b_{me} are the equivalent mass, equivalent stiffness, and mechanical damping constant, respectively. F_e is the electromagnetic force acting on the cantilever. x is the absolute displacement of the cantilever's tip point and y is the absolute base displacement of the support. Let the relative displacement of the mass with respect to the displacement of the support be defined as,

$$z = x - y \quad (2.13)$$

so that (2.12) becomes,

$$m_{eq}(\ddot{z} + \ddot{y}) + b_{me}\dot{z} + k_{eq}z + F_e = 0 \quad (2.14)$$

$$m_{eq}\ddot{z} + b_{me}\dot{z} + k_{eq}z + F_e = -m_{eq}\ddot{y} \quad (2.15)$$

Equation (2.15) is the dynamic equation of motion of the lumped system model. Note that ‘x’ and accordingly ‘z’ are measured from the static equilibrium position of the equivalent mass so that the effect of gravity is taken care by the static deflection of the spring. In this equation, the electromagnetic force induced over the cantilever or on the corresponding equivalent lumped mass, F_e , can be obtained using Faraday’s and Ohm’s Laws. The following equation can be used to define the electromagnetic force on the coils.

$$F_e = \vec{i} \times \vec{B} L_p \quad (2.16)$$

By substituting equations (2.2) and (2.9) in the final equation, an expression for F_e in terms of systems parameters can be obtained.

$$F_e = \frac{(BL_p)^2}{R_L + R_c} \dot{z} \quad (2.17)$$

The electromagnetic force induced on the coils always opposes the motion of the cantilever. This is due to the fact that, the induced current through the coils is always in a direction that creates a magnetic flux in a direction to compensate the net change of magnetic flux through the coils at that instant. When the final equation is substituted in the motion equation the following is obtained.

$$m_{eq}\ddot{z} + \left(b_{me} + \frac{(BL_p)^2}{R_L + R_c} \right) \dot{z} + k_{eq}z = -m_{eq}\ddot{y} \quad (2.18)$$

Referring to (2.17), the induced electromagnetic force on the coils is proportional to the velocity of the cantilever. This means that, this force actually creates a viscous damping effect over the dynamic motion of the cantilevers. Thus, it can be considered as an electrical damping that is defined as,

$$b_e = \frac{(BL_p)^2}{R_L + R_c} \quad (2.19)$$

The mechanical and electrical damping terms can be represented by an equivalent damping, b_{eq} , defined simply as,

$$b_{eq} = b_{me} + b_e \quad (2.20)$$

Substituting the final equation, together with (2.19) in (2.18), gives a more compact motion equation as,

$$m_{eq}\ddot{z} + b_{eq}\dot{z} + k_{eq}z = -m_{eq}\ddot{y} \quad (2.21)$$

The mechanical damping is generated from air flow force, air squeeze force, support loss, and internal friction, which is investigated in detail by Hosaka [54] and can be expressed by,

$$b_{me} = \frac{(3\pi\mu b + (3/4)\pi b^2 \sqrt{2\rho_a \mu \omega})m_{eq}}{\rho_b b^2 h} + \frac{\mu b^2 m_{eq}}{\rho_b g_0^3 h} + \frac{\eta}{\omega} k_{eq} + \frac{(0.23h^3)}{L^3} 2m_{eq}\omega_n \quad (2.22)$$

where μ is the viscosity of air (1.81×10^{-5} Pa · s), ρ_a is the density of air (1.3 kg/m 3), ρ_b is the density of the cantilever, g_0 is the distance between the cantilever and nearby rigid wall, η is the structural damping coefficient determined by the material properties (5×10^{-6} [54]), ω is the displacement frequency of the tip point of the cantilever, and ω_n is the natural frequency of the cantilever. In (2.22), the first two terms are related with air squeeze and air flow damping and are dominant over the other two.

Using the second order mathematical model given in (2.21), the natural frequency of the first bending mode can be defined as,

$$\omega_n = \sqrt{\frac{k_{eq}}{m_{eq}}} = 3.57 \sqrt{\frac{EI}{mL^3}} \quad (2.23)$$

where E, I, m, and L are modulus of elasticity, area moment of inertia, mass and length of the cantilever, respectively. The equivalent mass and stiffness terms are two important design parameters defined by [55],

$$k_{eq} = \frac{3EI}{L^3} \quad (2.24)$$

$$m_{eq} = \frac{33}{140} m \quad (2.25)$$

For a rectangular cross sectioned beam, the area moment of inertia is defined as,

$$I = \frac{1}{12} bh^3 \quad (2.26)$$

Where, b and h are the width and thickness of the beam, respectively.

Finally, in order to express the power and voltage outputs from the generator, an expression for \dot{z} should be found. The steady-state sinusoidal response of the proposed energy harvester is important considering long term operation. Thus, its transient response can be ignored. As a result, a steady-state sinusoidal solution for \dot{z} can be obtained by firstly taking the Laplace of (2.21) and substituting $s = j\omega$. The relative displacement of the mass, z, in Laplace domain is given by,

$$Z(s) = -\frac{m_{eq}s^2}{m_{eq}s^2 + b_{eq}s + k_{eq}} Y(s) \quad (2.27)$$

Let the input displacement be sinusoidal and given by,

$$y(t) = Y \sin(\omega t) \quad (2.28)$$

where Y is the magnitude of the input signal and ω is its frequency. Then the magnitude of the relative displacement can be obtained by substituting $s = j\omega$ in (2.27). The time varying portion is also going to be sinusoidal with the same frequency of the input signal, but with some phase difference. As a result, the steady-state sinusoidal value of, $z(t)$, is going to be,

$$z(t) = \left| \frac{m_{eq}\omega^2 Y}{-m_{eq}\omega^2 + j\omega b_{eq} + k_{eq}} \right| \sin(\omega t + \phi) \quad (2.29)$$

where ϕ is the phase angle defined by,

$$\phi = -\tan^{-1} \left(\frac{2\zeta_{eq} \frac{\omega}{\omega_n}}{1 - \left(\frac{\omega}{\omega_n} \right)^2} \right) \quad (2.30)$$

In the last equation, ζ_{eq} is the overall damping ratio described by,

$$\zeta_{eq} = \zeta_{me} + \zeta_e = \frac{b_{me}}{2m_{eq}\omega_n} + \frac{b_e}{2m_{eq}\omega_n} = \frac{b_{eq}}{2m_{eq}\omega_n} \quad (2.31)$$

where ζ_{me} and ζ_e are mechanical and electrical damping ratios, respectively.

After some manipulations and making necessary substitutions, the relative velocity term given in (2.29) can be also be expressed as,

$$z(t) = \frac{\left(\frac{\omega}{\omega_n} \right)^2 Y}{\sqrt{\left(1 - \left(\frac{\omega}{\omega_n} \right)^2 \right)^2 + \left(2\zeta_{eq} \frac{\omega}{\omega_n} \right)^2}} \sin(\omega t + \phi) \quad (2.32)$$

Finally, the relative velocity of the tip point, $\dot{z}(t)$, can be obtained by taking the time derivative of (2.32).

$$\dot{z}(t) = \frac{\left(\frac{\omega}{\omega_n}\right)^2 \omega Y}{\sqrt{\left(1 - \left(\frac{\omega}{\omega_n}\right)^2\right)^2 + \left(2\zeta_{eq} \frac{\omega}{\omega_n}\right)^2}} \cos(\omega t + \varphi) \quad (2.33)$$

When (2.27) is substituted back in (2.9), the induced voltage can be expressed in terms of the system parameters as,

$$e = -BL_p \frac{\left(\frac{\omega}{\omega_n}\right)^2 \omega Y}{\sqrt{\left(1 - \left(\frac{\omega}{\omega_n}\right)^2\right)^2 + \left(2\zeta_{eq} \frac{\omega}{\omega_n}\right)^2}} \cos(\omega t + \varphi) \quad (2.34)$$

The power term is obtained by substituting equations (2.2) and (2.34) in (2.1) as,

$$P(t) = \frac{1}{2} b_e \left(\frac{R_L}{R_L + R_c} \right) \frac{\left(\frac{\omega}{\omega_n}\right)^4 \omega^2 Y^2}{\left(1 - \left(\frac{\omega}{\omega_n}\right)^2\right)^2 + \left(2\zeta_{eq} \frac{\omega}{\omega_n}\right)^2} \cos^2(\omega t + \varphi) \quad (2.35)$$

By making the $b_e = 2m_{eq}\zeta_e\omega_n$ substitution, the power term can also be defined as,

$$P(t) = \left(\frac{R_L}{R_L + R_c} \right) \frac{m_{eq}\zeta_e \left(\frac{\omega}{\omega_n}\right)^3 \omega^3 Y^2}{\left(1 - \left(\frac{\omega}{\omega_n}\right)^2\right)^2 + \left(2\zeta_{eq} \frac{\omega}{\omega_n}\right)^2} \cos^2(\omega t + \varphi) \quad (2.36)$$

2.1.2 Effect of System Parameters on Power Output

After deriving the equations that describe the dynamic motion of the cantilevers and defining the output power and voltage from the proposed generator, effect of certain system parameters like the excitation frequency, ω , and damping on output power will be analyzed. For this purpose the power term given by (2.35) is represented in a more compact form by defining and making the following substitution,

$$\Lambda = \frac{1}{2} b_e \left(\frac{R_L}{R_L + R_c} \right) Y^2 \quad (2.37)$$

After some arrangements, the power equation can also be represented by,

$$|P(t)| = \frac{\Lambda \left(\frac{\omega}{\omega_n} \right)^6 \omega_n^2}{\left(1 - \left(\frac{\omega}{\omega_n} \right)^2 \right)^2 + \left(2\zeta_{eq} \frac{\omega}{\omega_n} \right)^2} \quad (2.38)$$

It should be noted that while obtaining (2.38) and through out this analysis, it is assumed that the natural frequency, ω_n and the term, Λ , defined by (2.37) are constant so that the only variable is the excitation frequency, ω , itself. This is also useful to define the power term in a *non-dimensional* form as,

$$|\bar{P}(t)| = \frac{|P(t)|}{\Lambda \omega_n^2} = \frac{\left(\frac{\omega}{\omega_n} \right)^6}{\left(1 - \left(\frac{\omega}{\omega_n} \right)^2 \right)^2 + \left(2\zeta_{eq} \frac{\omega}{\omega_n} \right)^2} \quad (2.39)$$

As a result, the magnitude of non-dimensional power can be plotted with respect to the frequency ratio, $r = \frac{\omega}{\omega_n}$, as shown in Figure 2.5 for values of the frequency ratio $0 \leq r \leq 5$ and the damping ratio $0.1 \leq \zeta_{eq} \leq 0.5$. It should be noted that while

obtaining this plot, the frequency ratio, r , is varied by varying the excitation frequency, ω , since the natural frequency, ω_n , is assumed to be constant.

From Figure 2.5 it can be seen that the generated power increases indefinitely by the square of the excitation frequency for values of the damping ratio $\zeta_{eq} \gtrsim 0.25$. If the damping ratio is $\zeta_{eq} \lesssim 0.25$ then the power first makes a local maximum at $\omega \approx \omega_n$ and then makes a local minimum and afterwards it increases indefinitely by the square of the excitation frequency.

The generated power makes a local maximum at the following frequency ratios, for $\zeta_{eq} \gtrsim 0.25$,

$$r_{max} = \frac{\omega}{\omega_n} = \sqrt{-2(2\zeta_{eq}^2 - 1) - \sqrt{16\zeta_{eq}^4 - 16\zeta_{eq}^2 + 1}}, \text{ for } \zeta_{eq} \gtrsim 0.25 \quad (2.40)$$

The generated power makes a local minimum at the following frequency ratios, for $\zeta_{eq} \lesssim 0.25$,

$$r_{min} = \frac{\omega}{\omega_n} = \sqrt{-2(2\zeta_{eq}^2 - 1) + \sqrt{16\zeta_{eq}^4 - 16\zeta_{eq}^2 + 1}}, \text{ for } \zeta_{eq} \lesssim 0.25 \quad (2.41)$$

Thus, for effective power generation, if the excitation frequency, ω , is the only design parameter and the natural frequency, ω_n , is constant, then either the generator should be tuned to operate at r_{max} defined by (2.40) or the excitation frequency, ω , should be kept as high as possible by taking into account the local minimums.

The above analysis is useful if the natural frequency, ω_n , is constant. If this term is not constant, then this analysis should be made from another point of view. For this purpose the power term given by (2.36) is represented in another form as,

$$|P(t)| = \frac{\Lambda\omega^2}{\left(\left(\frac{\omega_n}{\omega}\right)^2 - 1\right)^2 + \left(2\zeta_{eq}\frac{\omega_n}{\omega}\right)^2} \quad (2.42)$$

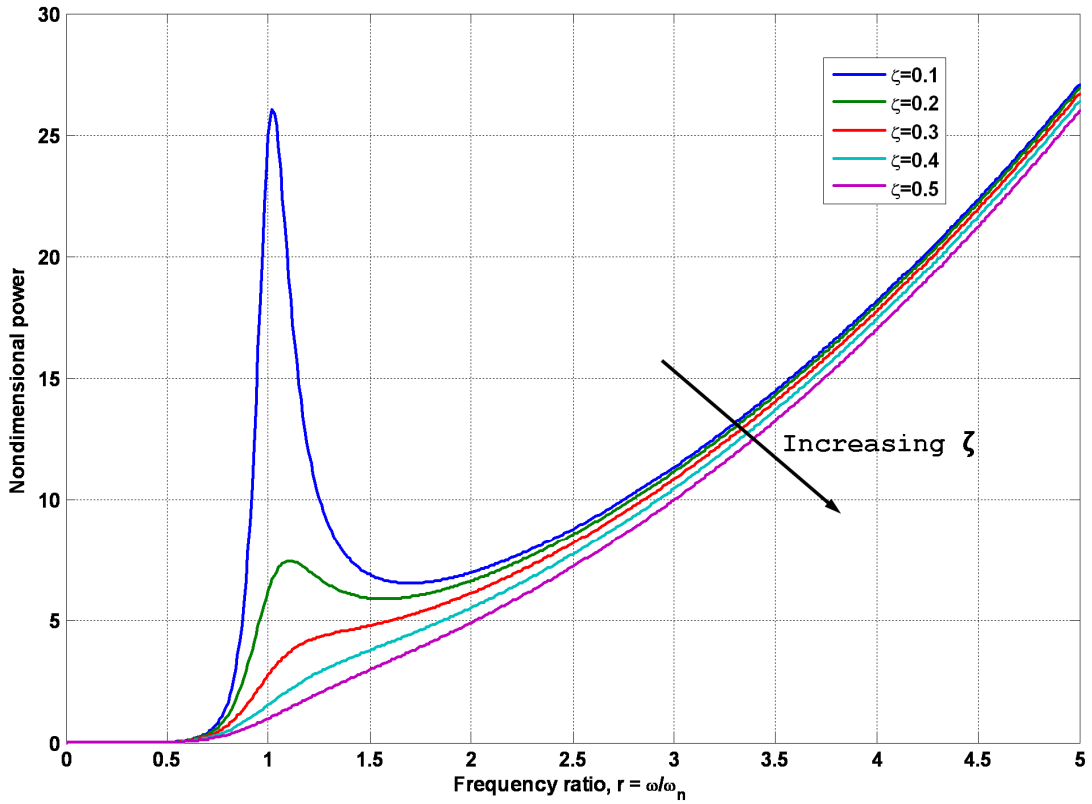


Figure 2.5. Non-dimensional power with respect to frequency ratio, r .

It should be noted that while obtaining (2.42) it is assumed that this time, the excitation frequency, ω , and the term, Λ , defined by (2.37) are constant so that the only variable is the natural frequency, ω_n , itself. This is useful to define the power term in a *non-dimensional* form as before,

$$|\bar{P}(t)| = \frac{|P(t)|}{\Lambda \omega^2} = \frac{1}{\left(\left(\frac{\omega_n}{\omega} \right)^2 - 1 \right)^2 + \left(2\zeta_{eq} \frac{\omega_n}{\omega} \right)^2} \quad (2.43)$$

The magnitude of non-dimensional power can be plotted with respect to the frequency ratio, $q = \frac{\omega_n}{\omega}$, as shown in Figure 2.6 for values of the frequency ratio $0 \leq q \leq 5$ and the damping ratio $0.1 \leq \zeta_{eq} \leq 0.5$. While obtaining this plot, the

frequency ratio, q , is incremented by varying the natural frequency, ω_n , since the excitation frequency, ω , is assumed to be constant.

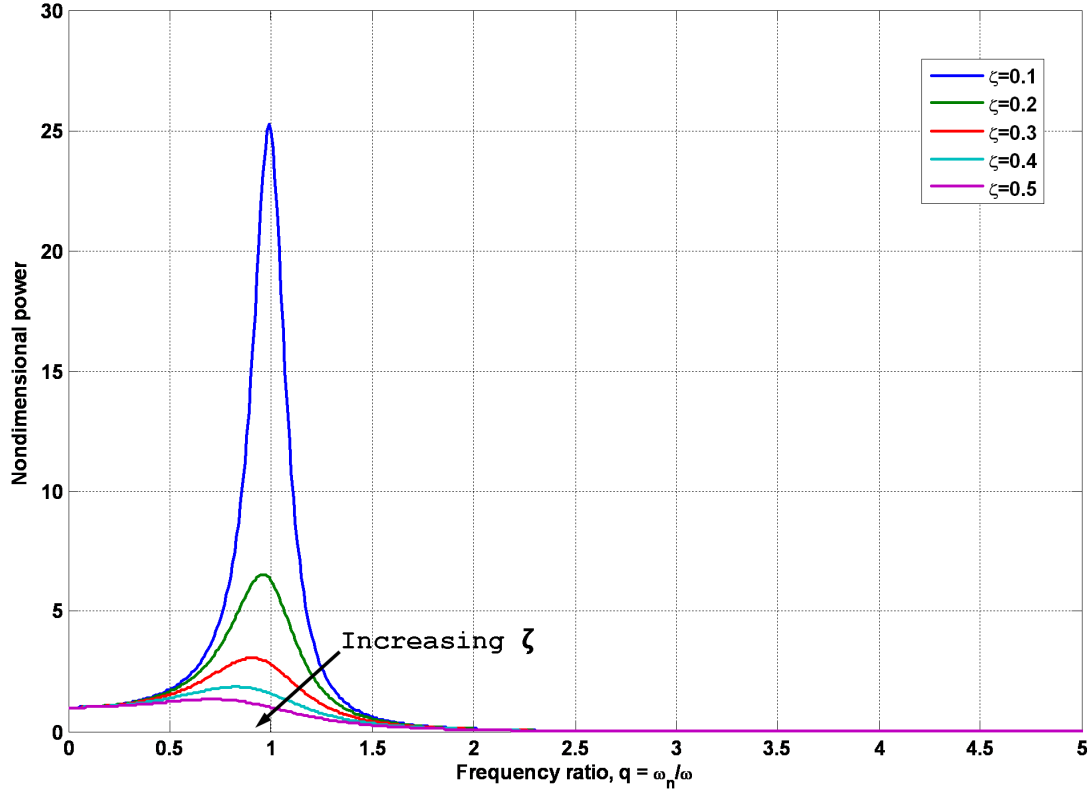


Figure 2.6. Non-dimensional power with respect to frequency ratio, q .

The power term does not make any local minimums, contrary to the previous case, when the natural frequency is considered as a variable. It only makes a maximum at $\omega_n \equiv \omega$ and it approaches unity and zero at low and high frequency ratios, respectively. The power term defined by (2.43) makes a maximum at the following frequency ratios,

$$q_{\max} = \frac{\omega_n}{\omega} = \sqrt{1 - 2\zeta_{\text{eq}}^2} \quad (2.44)$$

As a result, it can be deduced that if the natural frequency, ω_n , is the only design parameter and the excitation frequency cannot be altered then the generator should be designed to operate at q_{\max} defined by (2.44) for maximum power generation.

Figure 2.7 shows the 3-dimensional plot of power magnitude, in order to visualize the effects of excitation and natural frequencies on output power at the same time. This plot is obtained by using the following equation that is derived from (2.38),

$$\frac{|P(t)|}{\Lambda} = \frac{\left(\frac{\omega}{\omega_n}\right)^4 \omega^2}{\left(1 - \left(\frac{\omega}{\omega_n}\right)^2\right)^2 + \left(2\zeta_{eq} \frac{\omega}{\omega_n}\right)^2} \quad (2.45)$$

The ' ω^2 ' term in the numerator of (2.45) avoids this expression to be expressed as a function of the frequency ratios. For this reason, this plot is obtained by using sample numerical values of ω and ω_n . Figure 2.8 shows the 3-dimensional power plot for upper limit of ω less than ω_n . This helps the plot to appear asymmetrically and outlines some important aspects of the plot. Figure 2.9 shows the cutlets of Figure 2.8 for sample ω_n values. In the same manner, Figure 2.10 is the 3-dimensional power plot for upper limit of ω higher than ω_n and Figure 2.11 shows the cutlets of Figure 2.10 for sample ω values. All of these plots are obtained for a damping ratio of $\zeta_{eq} = 0.2$ for easier visualization of the local maximums and minimums of the power plots.

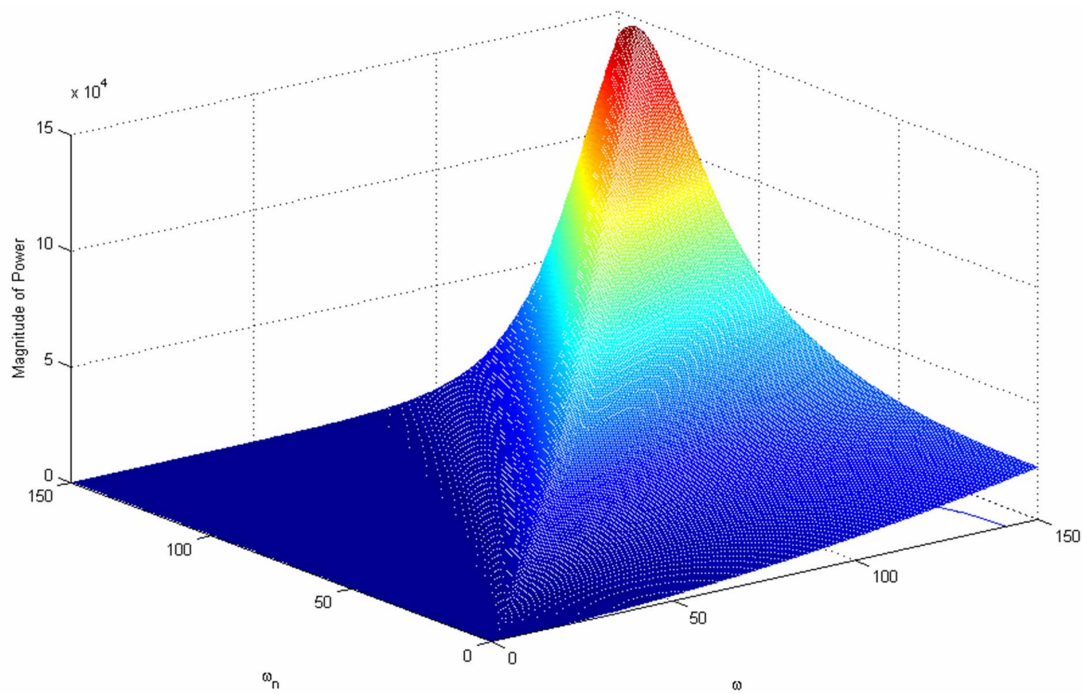


Figure 2.7. 3-dimensional plot of power magnitude, $\zeta_{\text{eq}} = 0.2$.

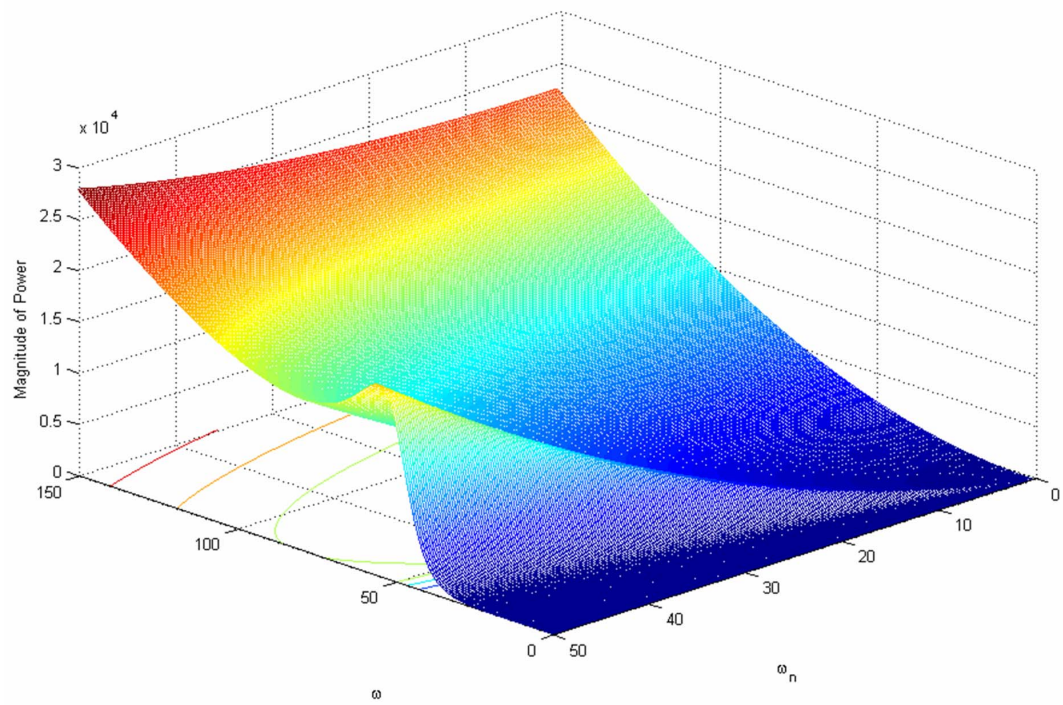


Figure 2.8. 3-dimensional plot of power for upper limit of $\omega < \omega_n$, $\zeta_{\text{eq}} = 0.2$.

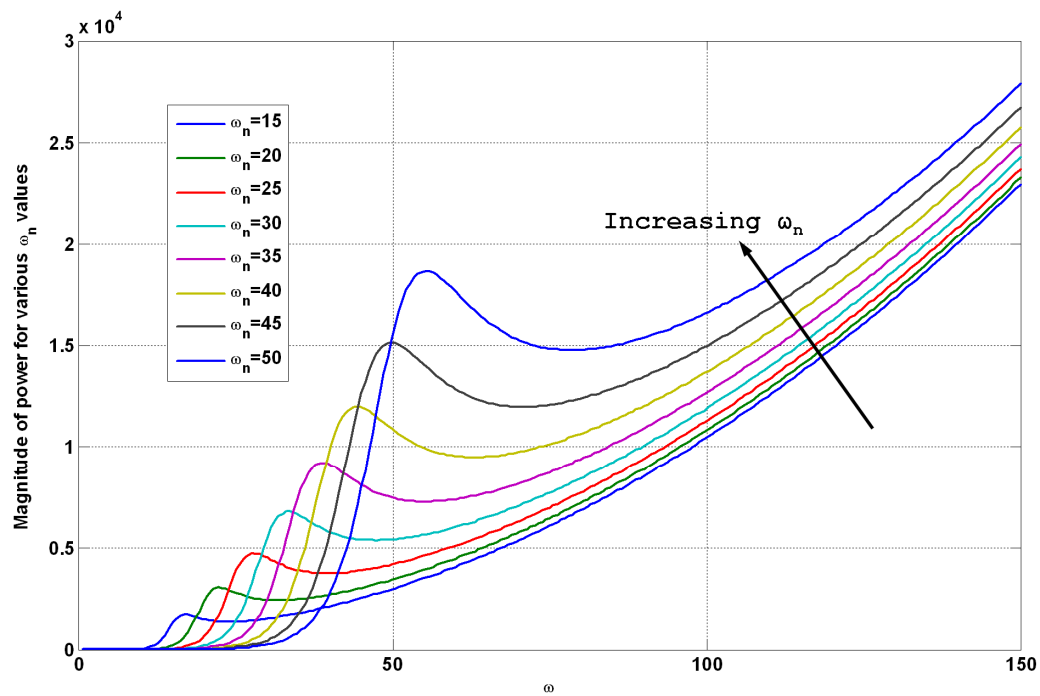


Figure 2.9. Cutlets of power magnitude for sample ω_n values, $\zeta_{\text{eq}} = 0.2$.

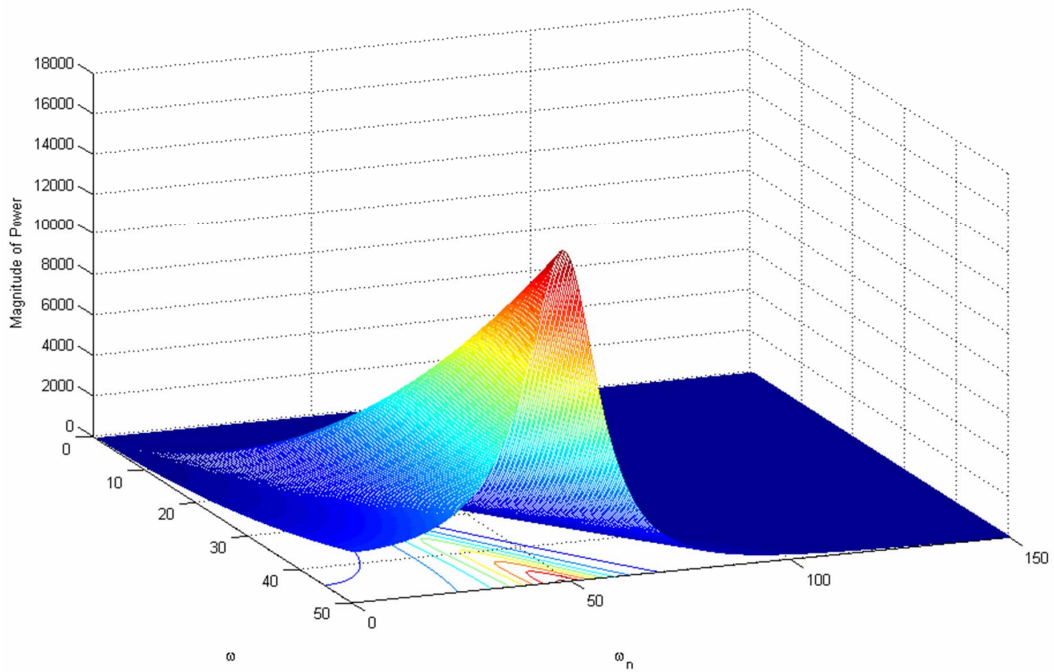


Figure 2.10. 3-dimensional plot of power for upper limit of $\omega > \omega_n$, $\zeta_{\text{eq}} = 0.2$.

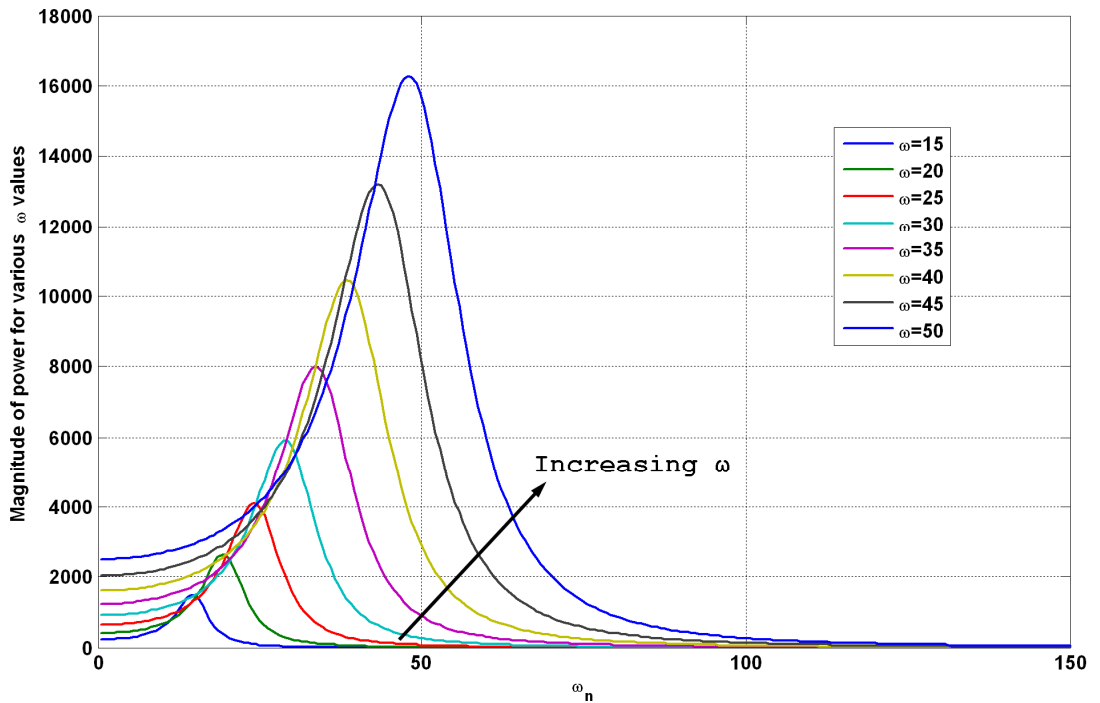


Figure 2.11. Cutlets of power magnitude for sample ω values, $\zeta_{\text{eq}} = 0.2$.

Another parameter influencing the power output is the damping term, which is composed of two components, the electrical and mechanical damping ratios as depicted by (2.31). For this purpose, Figure 2.12 shows the variation of log magnitude of power with respect to electrical and damping ratios, ζ_e and ζ_m , respectively. While obtaining the power points, at each (ζ_e, ζ_m) pair, the frequency ratio giving maximum power is used. As a result, each power point on the plot is actually a local maxima of the in the P vs (ω, ω_n) plane.

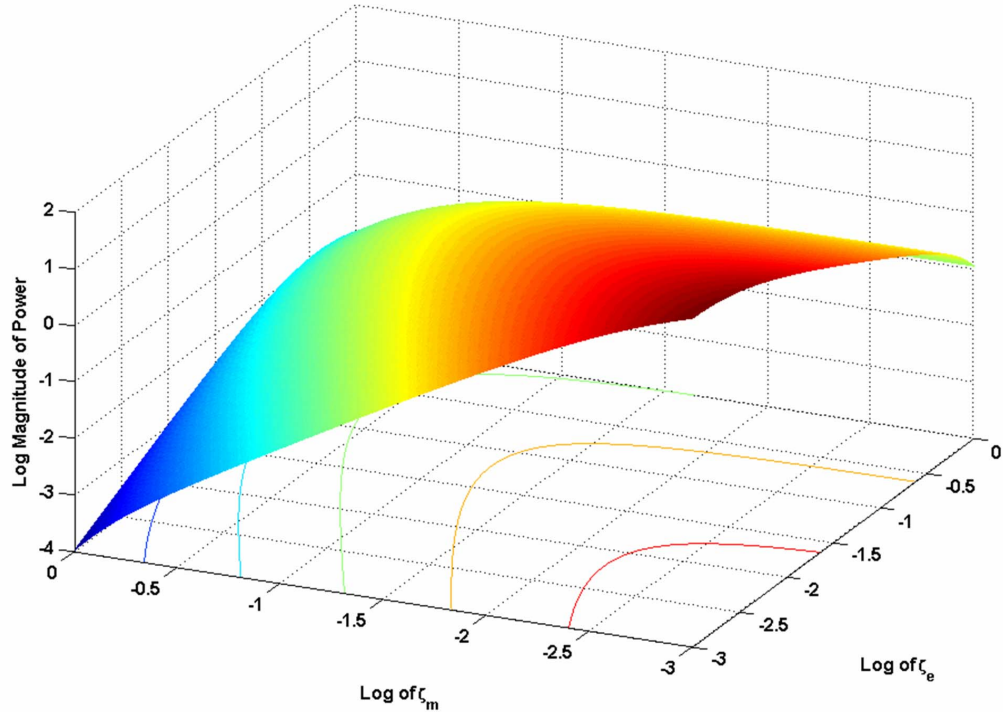


Figure 2.12. Variation of power with respect to electrical and mechanical damping ratios.

From the plot given above it can be deduced that, the maximum power is obtained when $\zeta_e \approx \zeta_m$ and when they are as small as possible. Also, the magnitude of power decreases rapidly, when ζ_m is high and ζ_e is small at the same time. When ζ_e is large, the power magnitude of power is not severely affected from high ζ_m . This means that for efficient power generation, these two parameters should be kept as close as possible or at least the electrical damping should be much higher than the mechanical damping ratio. This is also clear from the physical interpretation of the output power; as some of it is transferred to mechanical energy in the form mechanical losses and the rest is transferred to electrical energy as induced voltage. The coupling factors for the input and output domains are the mechanical and electrical damping terms and they determine how much of the output power is going to be converted to mechanical and electrical energy.

2.1.3 Analysis of Mechanical Stress Induced on the Cantilevers

The stress developed in the cantilevers is an important design parameter that should be considered during the design of the micro generator. Only the tensile stress will be considered since the cantilevers only go through bending motion. Tensile stress due to shear will also be neglected since it is usually much smaller than the tensile stress due to pure bending. The dynamic motion equation of an equivalent second order model for a cantilever is previously defined by (2.21) as,

$$m_{eq}\ddot{z} + b_{eq}\dot{z} + k_{eq}z = -m_{eq}\ddot{y} \quad (2.45)$$

Only inertial forces act on the structure as illustrated in Figure 2.13 and the net force over the structure is lumped at the tip point, which is given by,

$$\sum F = m_{eq}(\ddot{z} + \ddot{y}) = -(b_{eq}\dot{z} + k_{eq}z) \quad (2.46)$$

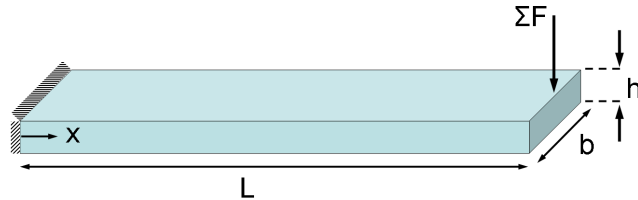


Figure 2.13. Force acting on the structure.

The net force and resulting moment diagrams are shown in Figure 2.14.

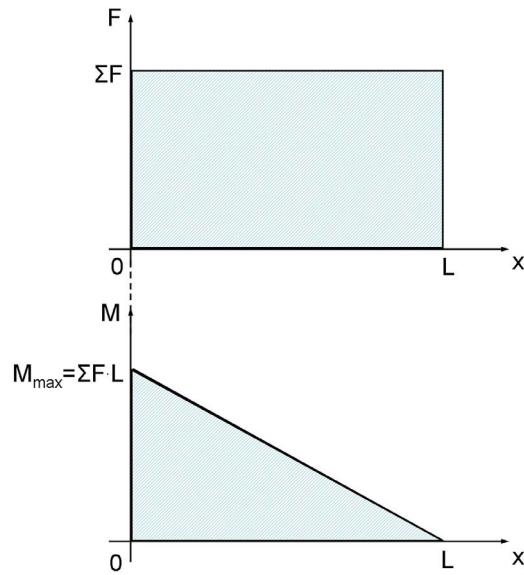


Figure 2.14. Illustration of moment on the structure.

From Figure 2.14, the maximum moment, M_{\max} , occurs at the support point that is the fixed end and is expressed by the following equation,

$$M_{\max} = \sum F \cdot L \quad (2.47)$$

Thus, the maximum stress will also occur at the support and on the top or bottom surface of the cantilever that is parallel to the applied force vector. The resulting stress is given by,

$$\sigma_{\max} = \frac{M_{\max} c}{I} \quad (2.48)$$

In the last two equations, M_{\max} is the moment at the support point as illustrated in Figure 2.14 and L is the distance between the tip point of the structure to the support that is the length of the cantilever in this case. Also, c is the distance between the neutral axis that is the centroid of the cross section, to the surface of the cantilever. In this case it is given by,

$$c = \frac{h}{2} \quad (2.49)$$

Finally, I is the area moment of inertia of the beam as defined before. Substituting (2.46), (2.47) and (2.49) in (2.48) gives,

$$\sigma_{MAX} = \frac{(b_{eq}\dot{z} + k_{eq}z)L\left(\frac{h}{2}\right)}{I} = \frac{(b_{eq}\dot{z} + k_{eq}z)Lh}{2I} \quad (2.50)$$

Equation (2.50) expresses the tensile stress for the dynamic case. If the static case is desired then the velocity term in this equation should be omitted to have,

$$\sigma_{MAX} = \frac{k_{eq}Lh}{2I} z \quad (2.51)$$

Note that, $k_{eq} = \frac{3EI}{L^3}$ and $I = \frac{1}{12}bh^3$ where defined previously for the cantilever and when these terms are substituted in the final equation, the maximum stress for the static case becomes,

$$\sigma_{MAX} = \frac{3Eh}{2L^2} z \quad (2.52)$$

In this case for safe operation,

$$\sigma_{MAX} \leq \sigma_{ALLOWABLE} \quad (2.53)$$

This means that, from the above equation it can be deduced that the thickness and displacement should be kept small while the length of the cantilever should be kept as large as possible to avoid mechanical failure.

2.1.4 Optimization and Simulation of the Array of Cantilevers (AOC) Design

After obtaining the mechanical and electrical models, cantilever dimensions and performance parameters are optimized using a Pattern Search Algorithm in Matlab®. Before deciding on this algorithm, various optimization routines such as direct slope

search methods have been tried in Matlab[®], but due to local minimums, reliable results could not be obtained. This is because direct slope search methods converge to the local minimums that are usually closest to the given initial conditions. Therefore, “Genetic Algorithm” and “Pattern Search” algorithms have also been tried and Pattern Search algorithm is found to be more suitable for the type of optimization problem in this study. This algorithm, mainly finds the global maximum of the defined objective function, for example, the induced voltage on the coils in this case. Linear and nonlinear constraints can be defined together with upper and lower bounds of the design parameters. The main advantage of this algorithm is that local minimums are avoided, which is hard to achieve by direct line search algorithms. Besides, all the design parameters are considered and optimized at once to give the optimum solution. Referring to the mathematical model of the system given in the previous section, the objective function of the system is chosen as the induced voltage defined by (2.34). The parameters to be optimized are determined to be the cantilever dimensions (length and width), coil area (length, width) and coil width. Afterwards, linear and nonlinear constraint functions are constructed for the necessary system parameters such as the maximum allowable deflection of the cantilevers and the tolerance on physical system parameters. Then, upper and lower bounds for the optimization parameters are determined by considering that the generators are going to be fabricated in micro scale and excited by environmental vibrations. The lower and upper frequency bounds for the optimization are set by taking into account power output levels and practical operation frequency levels, respectively. The constructed mathematical model is then optimized according to this procedure. The resulting optimized parameters of the micro generator are obtained and listed in Table 2.1.

Table 2.1. Optimized parameters of the generator.

Operation medium	Vacuum	Air
Input vibration frequency	3.4 kHz	3.4 kHz
Input displacement	1 μm	1 μm
Magnet type	NdFeB (1.18 T)	NdFeB (1.18 T)
Magnet size	6 x 6 x 6 mm ³	6 x 6 x 6 mm ³
Device dimensions	9.5 x 8 x 6 mm ³	9.5 x 8 x 6 mm ³
Cantilever dimensions	890 x 670 x 12 μm^3	890 x 670 x 12 μm^3
Cantilever structural material	Parylene C	Parylene C
Natural frequency of the cantilevers	3.4 kHz	3.4 kHz
Bandwidth of the cantilevers	34 Hz	140 Hz
Total number of cantilevers	20	20
Damping ratio of the cantilevers	0.005	0.020
Distance from cantilevers to magnet	500 μm	500 μm
Magnetic flux density	0.24 Tesla	0.24 Tesla
Coil metal width	10 μm	10 μm
Coil thickness	0.1 μm	0.1 μm
Coil resistance (single cantilever)	680 Ohm	680 Ohm
Load resistance (single cantilever)	250 Ohm	250 Ohm
Number of coil turns	16	16
Total coil length (single cantilever)	29.4 mm	29.4 mm
Practical coil length (single cantilever)	5.8 mm	5.8 mm
Overall peak power output from 20 cantilevers	24 nW (1.2 nW/cantilever)	1.5 nW (75 pW/cantilever)
Overall peak voltage output from 20 cantilevers	57.6 mV (2.88 mV/cantilever)	14.4 mV (0.72 mV/cantilever)

From the given data, it can be seen that a maximum output voltage of 14.4 mV (0.72 mV per cantilever) can be obtained from 20 consecutive cantilevers when the generator is operated in air. The generator is excited at the resonance frequency of the cantilevers of 3.4 kHz with an input displacement of 1 μm that corresponds to an acceleration of 46.5 g. If the generator is operated in vacuum then the output voltage increases by four times to 57.6 mV (2.88 mV per cantilever). The generated power for a load resistance of 250 Ohm is determined as 24 nW and 1.5 nW for vacuum and air operations, respectively.

Figure 2.15 shows the frequency response plots of the designed generator to a constant displacement input of 1 μm for various damping ratios. From the plot, it can be observed that a maximum voltage output just less than 15 mV can be obtained from the overall device at a resonance frequency of 3.4 kHz and for a damping ratio of $\zeta = 0.02$. The increasing trend of the voltage plot after resonance is due to the free ‘ ω ’ term in the numerator of (2.34).

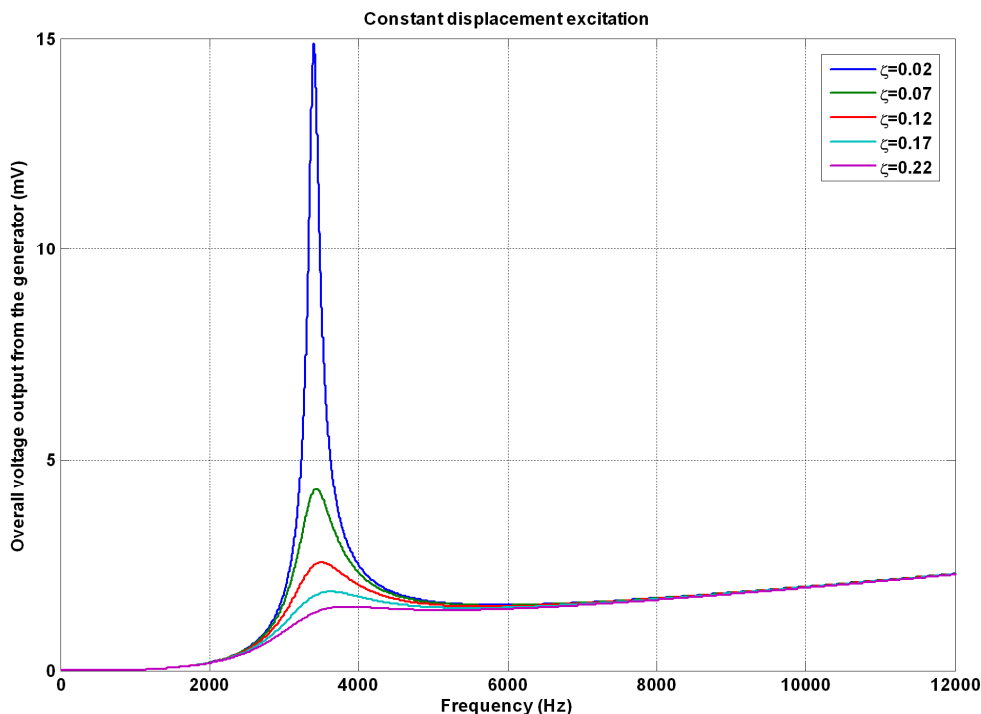


Figure 2.15. Voltage output from the generator for various values of damping.

2.2 The Array of Cantilevers Design with Varying Natural Frequencies (AOC_FS), “The Frequency Sweeper”

In the previous section, the proposed micro generator is capable of generating voltage at the designed natural frequency of the cantilevers. This type of single frequency generators have been widely investigated in the literature [2, 7, 13, 39, 48, 56-61]. These generators have low bandwidth due to their nature and so they are only efficient around the resonance frequency of the cantilevers or the moving proof mass. However, once the device is fabricated and installed for use, it is a matter of chance for the frequency of ambient vibrations to match the optimum operating frequency that is the resonance frequency of the device. In the literature it is possible to find a few studies that attempt to actively or passively tune the natural frequency generators to the frequency of the environment [62-65]. However, most of these studies remain in theory without any applications.

In this section, the proposed design of the previous section is brought one step further to implement a micro generator that is effective in a predetermined and wider frequency range. Figure 2.16 shows the proposed generator at the bottom together with the standard design at the top. The proposed design, namely the “frequency sweeper”, employs a series of cantilevers with varying lengths and resonance frequencies to increase the bandwidth of the overall structure. By adjusting the length increments sufficiently small, cantilevers will have an overlapping frequency spectrum with the peak voltages at close but different frequencies. This will result in widening of the overall bandwidth of the device, as well as an increase in the overall generated voltage. One possible disadvantage of this approach is that the maximum power will be smaller than the case of using identical cantilevers. However, this can be eliminated by increasing the cantilever number at each incremental frequency without increasing the overall chip area significantly. Another possible limitation can be the adjustment of length increments. Depending on the cantilever material, fabrication may limit the minimum increment size, and hence optimization of the cantilever lengths and uniform band coverage may become a problem. This issue is resolved by choosing Parylene C as the cantilever structural material. Parylene has a

much lower modulus of elasticity compared to silicon [50]. This allows much larger deflections before mechanical failure and increased voltage generation. Also, using parylene permits adjustment of cantilever parameters (e.g. stiffness and natural frequency) over a wide range, providing flexibility to the designer in the design phase.

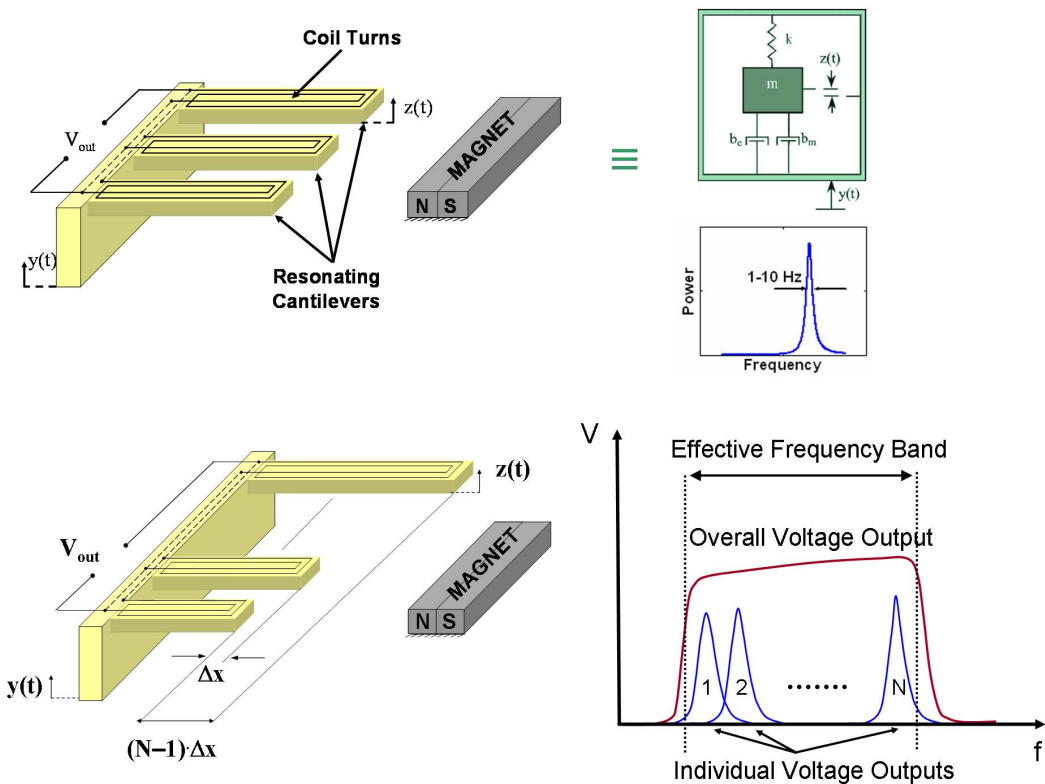


Figure 2.16. Schematic view of the array of cantilevers design with varying natural frequencies (AOC_FS).

The natural frequency of each cantilever can be controlled by adjusting the cantilever lengths as shown in Figure 2.17. Although, there is a quadratic relation between the natural frequency and the cantilever length in the form of $\omega_n \propto \frac{1}{L^2}$, this relation can be considered as linear for a narrow range of cantilever length as shown in the figure.

This makes it possible to linearly increment the cantilever lengths to have equally spaced natural frequencies, which would allow the design and optimization to be carried out much easily.

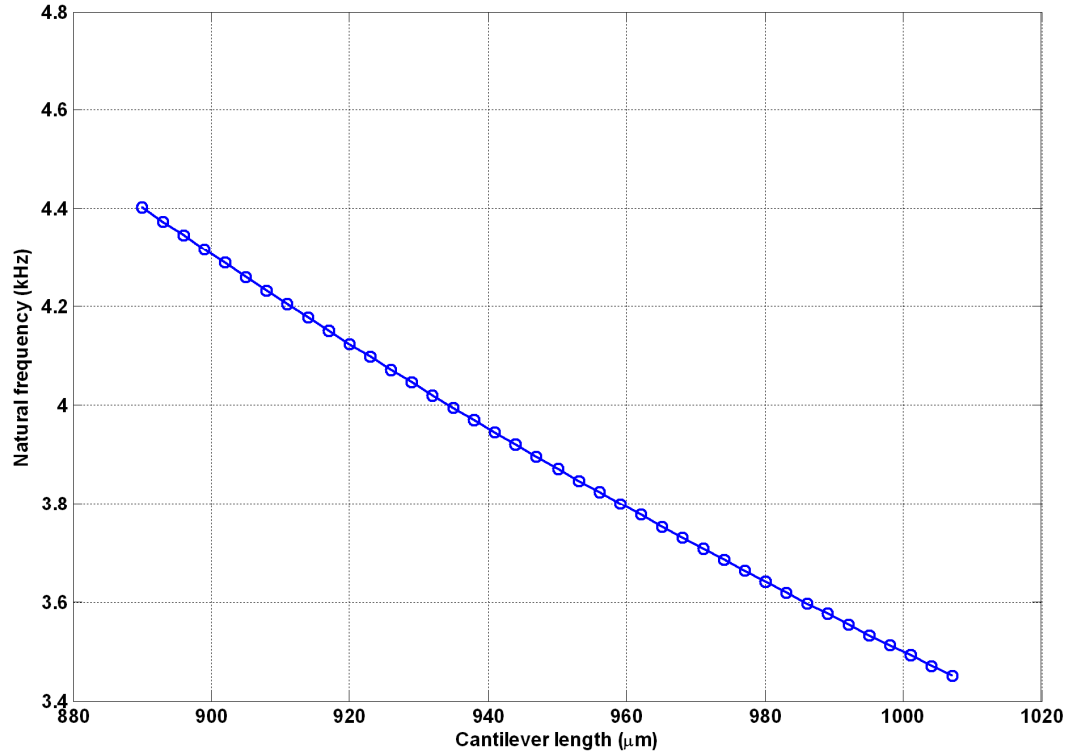


Figure 2.17. Variation of natural frequency with cantilever length.

For wideband operation, it is very critical to optimize the length increments together with other parameters of the generator to achieve a continuous and uniform spectrum. In order to illustrate this, Figure 2.18 shows the estimated power output of the system when 40 cantilevers are used within an input excitation range of 3.3-4.8 kHz for three different cases. In each case, the upper plot is the superimposed overall voltage output whereas the bottom plot is the individual voltage output from each cantilever. If for example the length increments were chosen as $25 \mu\text{m}$ then the bandwidth would increase, but the voltage output would be discontinuous as shown in Figure 2.18.a. On the other hand, if they were chosen too small, for example as 1

μm , then the overall power output will increase, but the total bandwidth would be smaller as shown in Figure 2.18.b. Finally, Figure 2.18.c shows the case of optimized length increment of 3 μm . In this case, both a wide bandwidth and a smooth overall voltage output can be obtained. Thus, optimization of the length increments is necessary in order to have a continuous and steady voltage output from the device. Table 2.2 shows the optimized dimensions and expected performance parameters for a constant vibration acceleration of 45g, which corresponds to a displacement input of 0.91 to 0.55 μm in a frequency range of 3.5 to 4.5 kHz, respectively. For the proposed design, optimum length increments are determined as 3 μm when a total number of 40 cantilevers are used.

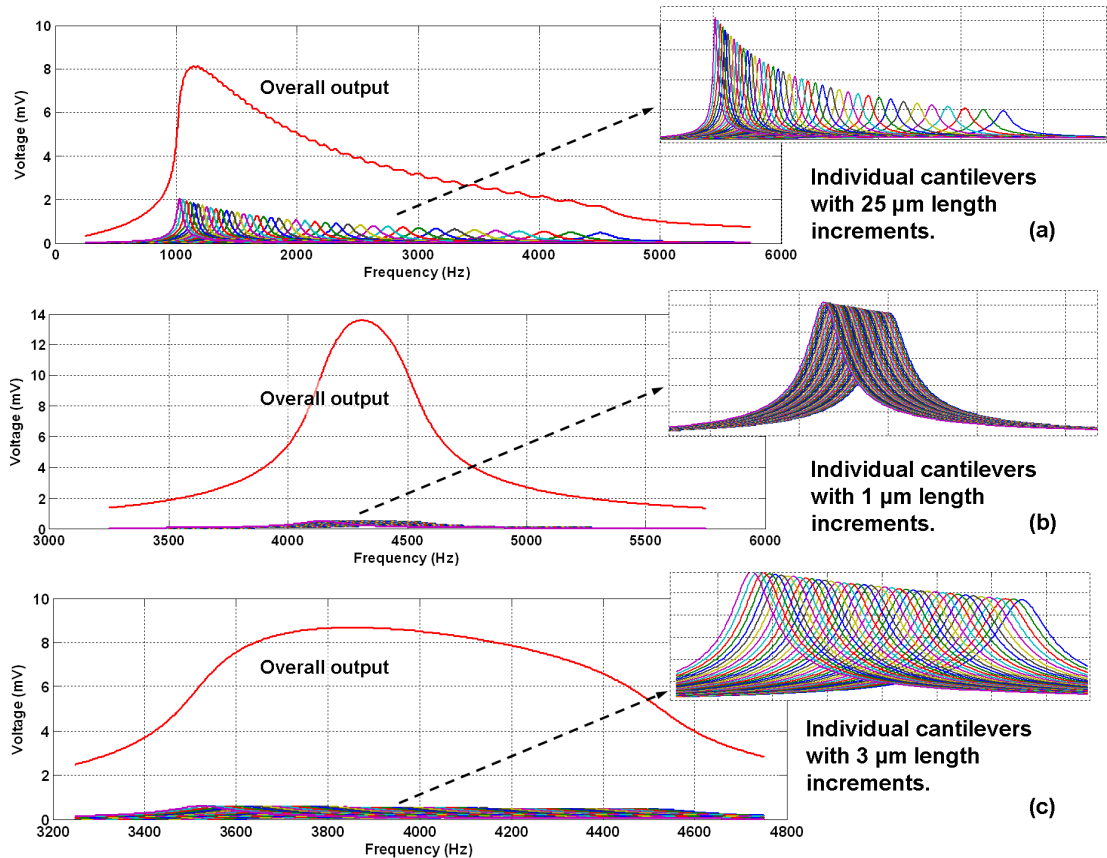


Figure 2.18. Overall and individual outputs from the proposed design for various cantilever length increments.

From Figure 2.18 and Table 2.2, it can be seen that a maximum steady output of 9 mV can be obtained from the proposed design with an overall bandwidth of 1 kHz.

Table 2.2. Optimized parameters of the generator.

Vibration amplitude (constant acceleration)	45 g
Natural freq. of cantilevers	3.5-4.5 kHz
Number of cantilevers	40
Cantilever material	Parylene C
Cantilever dimensions	(890-1007) x 670 x 15 μm^3
Cantilever length increments	3 μm
Device dimensions	14 x 12.5 x 8 mm ³
Magnet type	NdFeB (1.18 T)
Magnet dimensions	8 x 8 x 8 mm ³
Distance between cantilevers to magnet	500 μm
Magnetic flux density	0.4 Tesla
Damping ratio	0.02
Number of coil turns	10
Coil length	19.6-21.9 mm
Practical coil length (single cantilever)	2.9-3.0 mm
Coil metal width	20 μm
Coil thickness	0.1 μm
Coil resistance (single cantilever)	110 Ω
Overall bandwidth of the cantilevers	1 kHz
Estimated maximum power (from all 40 cantilevers)	2.7 nW
Estimated maximum voltage (from all 40 cantilevers)	9 mV

Compared to the estimated bandwidth of 140 Hz for the array of cantilevers design, an improvement of in the order of about 7 times would be made if such a design is implemented. It can be seen from the frequency response curve of the proposed design that the generator is effective in a relatively wider bandwidth. With suitable design architecture, this feature can also be used to detect the frequency of the environment if it can be implemented as part of a frequency sensor. This architecture is explained in detail in the next section.

2.3 The Array of Cantilevers Design with Varying Natural Frequencies (AOC_FS) as an Energy Harvesting Frequency Sensor

Frequency measurements are used in many different applications including condition monitoring of rotating machinery, predictive maintenance, machine diagnostics, and seismometry [66-68]. Each of these applications requires sensors operating at different frequency ranges with different resolutions. Besides the range and resolution, power supply requirements can be a critical parameter for some cases. In certain circumstances, frequency measurements need to be taken periodically in embedded environments where it is not easy to reach and replace the battery or the sensor itself. Once the sensor is installed, it should be able to operate without a need for battery replacement. This can be achieved by powering the sensor using the already available environmental vibration energy. For the cases where the generated energy is not enough to power up the sensor, it can still be used for battery life time improvement. In this section, a new sensor capable of detecting the frequency of environmental vibrations in a frequency band determined by the design parameters is presented. The proposed system is also capable of generating power by electromagnetic induction, which can be used to increase the life-time of the battery powering the readout circuitry [51 and 52], which is actually the system proposed in the previous section. By combining these properties, it is aimed to take the first steps in developing a self sufficient frequency sensing system [53]. Figure 2.19 shows the proposed system which has mainly two parts, the sensing structure and the readout circuitry. The sensing structure outputs a sinusoidal voltage at the same frequency

with environmental vibrations. This voltage is then processed digitally by the readout circuitry to generate the final output.

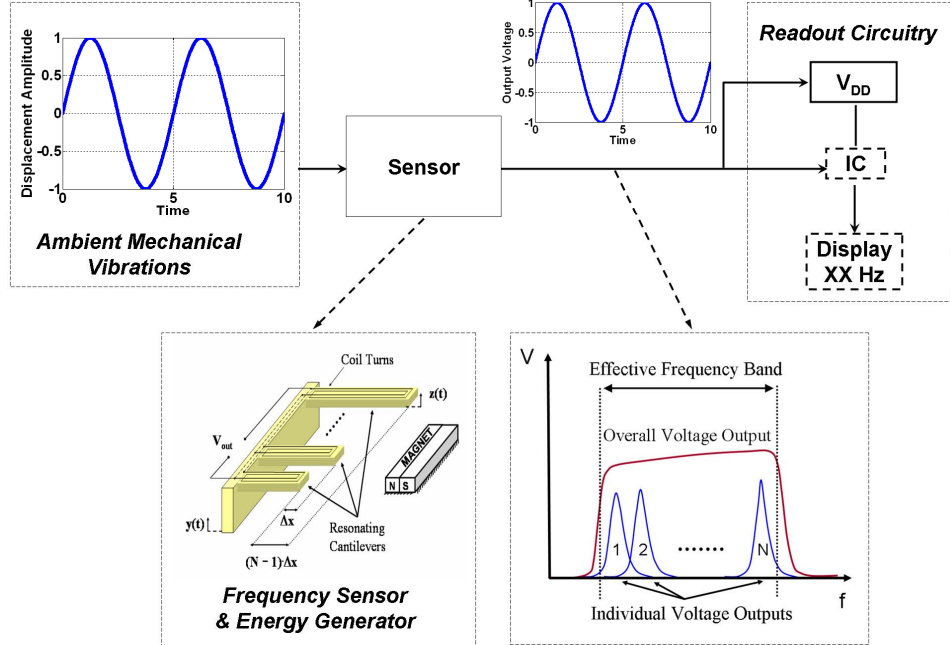


Figure 2.19. Block diagram of the proposed frequency detector.

The sensing structure is composed of serially connected cantilevers that generate voltage at the same frequency with the ambient vibration. Besides sensing the ambient frequency, this structure operates as an energy harvester as well, which is explained in detail in the previous section. Although the power generated by the detector is not enough to power up the readout circuitry yet, it can be used to improve the life-time of the battery. Also the power level can be increased by increasing the number of cantilevers at each resonance frequency, without increasing the overall sensor area significantly.

The sinusoidal output voltage from the sensing structure is then transferred to the readout circuitry, which should ideally be a low-power custom integrated circuit employing an amplifier and an electronic frequency counter. In this work, a basic

discrete component, programmable circuit is implemented for the proof of concept. Figure 2.20 shows this circuit consisting of an amplifier and a Programmable Integrated Controller (PIC). The amplifier amplifies and converts the input signal to a square wave. Afterwards, the resulting square wave is amplified and processed by the code running on the PIC. The code counts the pulses per second and converts this information to frequency, which in turn is displayed at each successive cycle. The use of PIC gives the flexibility to run any desired code without changing the circuitry. For example if it is desired to determine the whole ambient vibration frequency spectrum instead of the dominant frequency input, then simply a Fast Fourier Transform (FFT) algorithm can be embedded in the PIC.

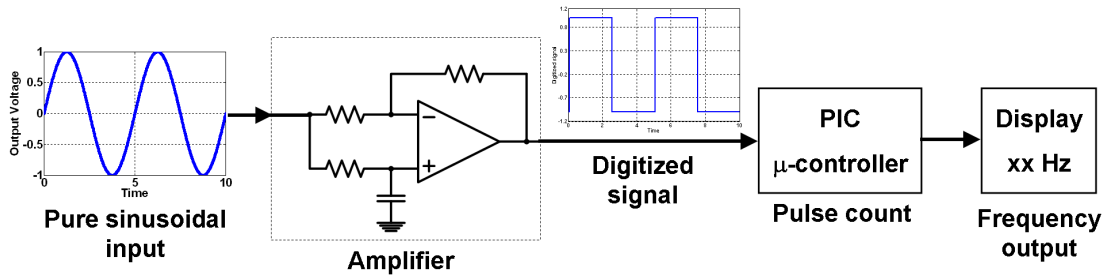


Figure 2.20. Block diagram of the read out circuitry.

2.4 The Large Mass Coil (LMC) Design

Another type of design that is investigated within the scope of this thesis study is called the Large Mass Coil Design. It has been widely investigated in the literature and will be considered within this study for comparison purposes only. Figure 2.21 shows a generic view of a traditional large mass coil design while Figure 2.22 is its equivalent single DOF model. Governing differential equations of motion of the system is the same as the array of cantilevers, so they will not be repeated here. The main difference between the large mass coil and array of cantilevers is that in the case of the large mass coil design, a moving magnet-diaphragm assembly and a

relatively stationary coil structure is realized. The magnet is attached to a diaphragm and is capable of moving with respect to the coil turns by ambient vibrations.

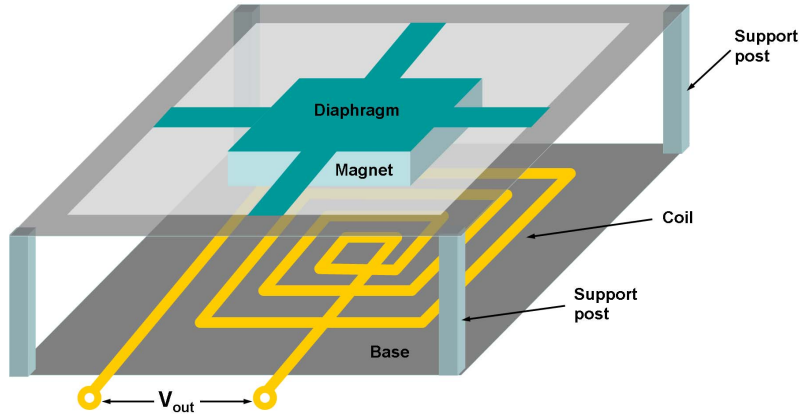


Figure 2.21. Schematic view of the large mass coil (LMC) design.

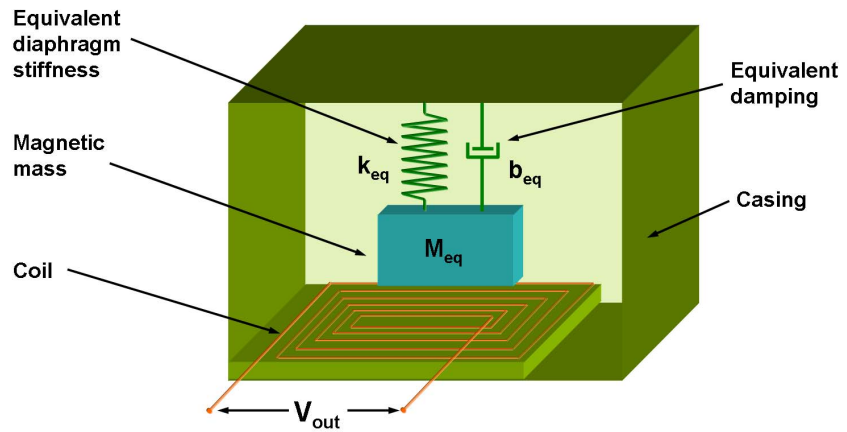


Figure 2.22. Equivalent model representation of the large mass coil (LMC) design.

The equivalent mass and stiffness terms for the LMC design are different than the ones derived for the cantilevers, which were defined in Section 2.1. For this reason, these parameters will be derived in this section for the LMC design. Figure 2.23

shows the diaphragm that is composed of four identical beams fixed at one end, which carry the lumped magnetic mass, M , located at the center.

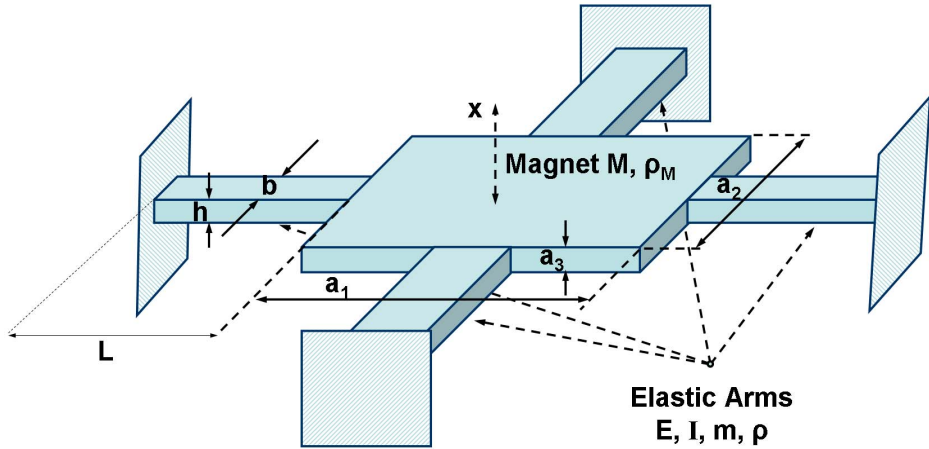


Figure 2.23. Representation of the elastic arms and the mass for the diaphragm.

During the transverse motion, each beam will deflect such that the slope at the tip point of each beam will be zero due to the rigid body attached at the end point. Thus, the diaphragm can be viewed as two fixed-fixed beams (arms) of length “ $2L$ ” carrying a lumped mass at the center. Thus, there exist two fixed-fixed elastic elements (arms) with length “ $2L$ ”. For a fixed-fixed beam with length “ $2L$ ” and loaded by a concentrated force at the center, the stiffness equation can be written as,

$$(k_{eq})_{\text{arm}}^{\text{single}} = \frac{192EI}{(2L)^3} = \frac{24EI}{L^3} \quad (2.54)$$

where, E , I and L are the modulus elasticity, area moment of inertia and length of each arm. Then, for two arms connected in parallel, the stiffness equation can be defined as,

$$k_{eq} = 2(k_{eq})_{\text{arm}}^{\text{single}} = \frac{48EI}{L^3} \quad (2.55)$$

The equivalent mass lumped at the midpoint for a fixed-fixed beam with mass “2m” can be determined to be,

$$m_{eq} = \frac{13}{35}(2m) = 0.37(2m) = 0.74m \quad (2.56)$$

Since there are two arms and a lumped magnetic mass, M, the total equivalent mass becomes,

$$m_{eq} = 1.48 m + M \quad (2.57)$$

As a result, for the diaphragm, the natural frequency of the first bending mode is,

$$\omega_n = \sqrt{\frac{k_{eq}}{m_{eq}}} = \sqrt{\frac{48EI}{(1.48m + M)L^3}} \quad (2.58)$$

Table 2.3 presents the important design parameters and simulation results for this design. According to the simulation results, a maximum voltage output of 0.4 mV can be obtained at the natural frequency of the diaphragm of 113 Hz.

Table 2.3. Optimized parameters of the generator.

Input vibration frequency	113 Hz
Input acceleration	45 g
Magnet type	NdFeB (1.18 T)
Magnet size	3.8 x 3.8 x 1.5 mm ³
Device dimensions	8.5 x 7 x 2.5 mm ³
Diaphragm structural material	Parylene C
Length of each diaphragm arm	1000 μm
Width of each diaphragm arm	555 μm
Thickness of each diaphragm arm	15 μm
Total number of diaphragm arms	16
Magnet area on the diaphragm	3.95 x 3.95 mm ²
Natural freq. of diaphragm	113 Hz
Magnetic flux density	0.19 Tesla
Coil width	160 μm
Coil thickness	0.1 μm
Coil resistance	235 Ω
Number of coil turns	13
Total coil length	168.5 mm
Practical coil length	29.7 mm
Collected energy in 1 s	42 pJ
Peak output power	85 pW
Peak output voltage	0.4 mV

2.5 The Frequency up-Converter (FUC) Design

The maximum generated power for the traditional techniques is proportional to the cube of the external vibration frequency [39], and drops dramatically at low frequencies (1-100Hz). However, it is at these low frequencies where most ambient vibration exists. Most of the reported devices operate effectively at frequencies of several kHz and they are not effective at lower frequencies. The proposed design solves this problem by converting the low frequency environmental vibrations to a higher vibration frequency. Figure 2.24 shows the proposed system which is composed of two mechanical structures; the upper diaphragm and the array of cantilevers located below the diaphragm.

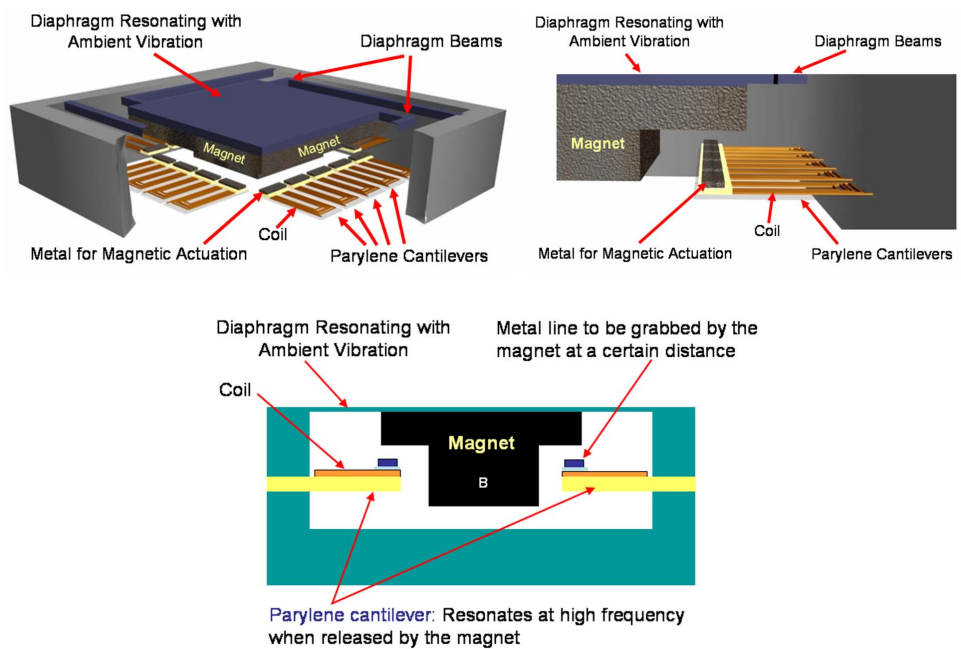


Figure 2.24. Schematic view of the frequency up-converter (FUC) design.

The diaphragm is made of parylene and holds a NdFeB magnet for both mechanical frequency up-conversion and power generation. This diaphragm resonates by environmental vibrations in the order of 100 Hz. The array of cantilevers have a

higher resonance frequency (2-3 kHz), and supports a coil for power generation, and a nickel electroplated tip that could be attracted to the magnet. As the diaphragm resonates in response to external vibration, it gets closer to the cantilever array located beneath. The distance between them is adjusted such that the magnet catches the cantilevers at a certain point of its movement, pulls them up and then releases at another point. The released cantilevers start resonating at their damped natural frequency, and hence mechanical frequency conversion is realized. The motion is exponentially decaying out, and before it totally decays out the cycle restarts. The mathematical modeling of the FUC is different than the design presented before in this chapter. This is simply because of the mechanical interaction between two different bodies; the cantilevers and the diaphragm and also the cantilevers are now excited mainly by the given initial conditions. Thus, before going into simulation work, the dynamic model of the system should be constructed. For this purpose the equivalent mechanical model of the system is shown in Figure 2.25.

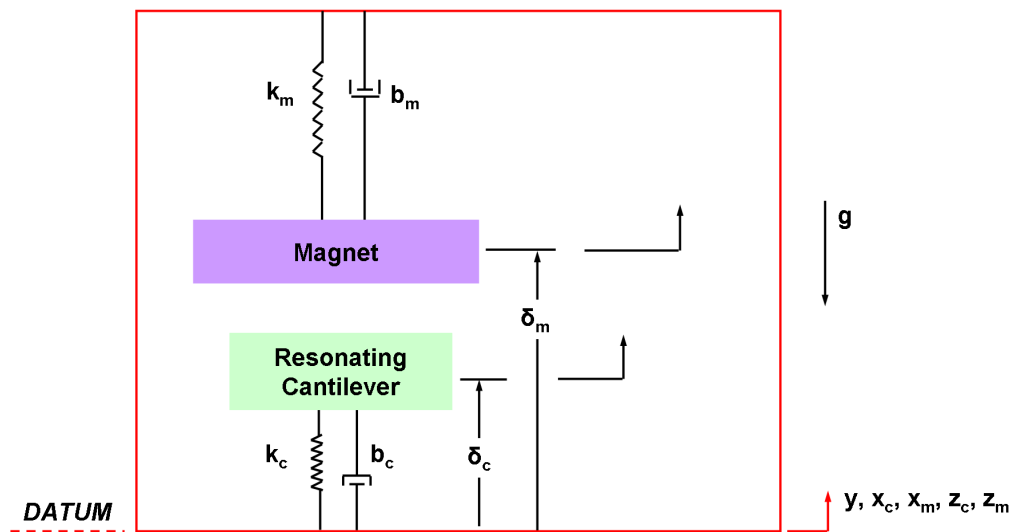


Figure 2.25. Equivalent mechanical model of the system.

The mechanical structure shown in the figure above is excited by environmental vibrations, the displacement of which is described by 'y' and as a result the magnet is

displaced by ' x_m '. This motion causes the magnet to catch and release the cantilever continuously giving the cantilever an initial condition. This results in the cantilever to oscillate with its damped natural frequency. The environmental vibration frequency is well below the natural frequency of the cantilever so it does not affect the motion of the cantilever as a separate input. Thus, the dynamic behavior of the magnet can be represented by the following equation.

$$m_m \ddot{z}_m + b_m \dot{z}_m + k_m z_m = -m_m \ddot{y} \quad (2.59)$$

In the model given above $z_m = x_m - y_m$ is the displacement of the magnetic mass with respect to the base. The magnetic interaction between the magnet and cantilever is assumed to be small and it is not shown in the equations. Besides ' z_m ' is measured from the static equilibrium position so that the effect of gravity is taken care of by the static deflection of the spring. The resulting steady-state behavior of the magnet can then be represented by the following equation.

$$z_m(t) = \left| \frac{m_m \omega^2 Y}{-m_m \omega^2 + j\omega b_m + k_m} \right| \sin(\omega t + \phi) \quad (2.60)$$

The phase angle is given by,

$$\phi = -\tan^{-1} \left(\frac{\omega b_m}{k_m - m_m \omega^2} \right) = -\tan^{-1} \left(\frac{2\zeta_m \frac{\omega}{\omega_n}}{1 - \left(\frac{\omega}{\omega_n} \right)^2} \right) \quad (2.62)$$

In the last three equations, z_m , is the relative displacement of the magnet with respect to the base, m_m is the mass of the magnet, k_m is the equivalent stiffness of the diaphragm, b_m is the equivalent damping constant for the magnet-diaphragm and ζ_m is the damping ratio of the magnet-diaphragm.

The dynamic behavior of the cantilever can be represented by the following equation.

$$m_c \ddot{z}_c + b_c \dot{z}_c + k_c z_c = 0 \quad (2.63)$$

While constructing the above equation, it is assumed that the environmental vibration frequency is much smaller than the natural frequency of the cantilever, so that it does not affect the relative motion of the cantilever with respect to the base. In the final equation, z_c , is the relative displacement of the cantilever with respect to the base, m_c is the equivalent mass, k_c is the equivalent stiffness, b_c is the equivalent damping constant and ζ_c is the damping ratio of the cantilever.

The relative displacement of the cantilever tip point with respect to the base, z_c , can be obtained by solving the above equation with the initial conditions $z_c(0) = z_o$, $\dot{z}_c(0) = 0$. As a result using Laplace transformation the relative displacement of the tip point is given by,

$$z_c(t) = z_o \frac{e^{-\zeta_{eq}\omega_n t}}{\sqrt{1 - \zeta_{eq}^2}} \left(\zeta_{eq} \sin(\omega_d t) + \sqrt{1 - \zeta_{eq}^2} \cos(\omega_d t) \right) \quad (2.64)$$

The relative velocity of the cantilever's tip point is obtained simply by taking the time derivative of the above equation, which results in,

$$\dot{z}_c(t) = -z_o \omega_n \frac{e^{-\zeta_{eq}\omega_n t}}{\sqrt{1 - \zeta_{eq}^2}} \sin(\omega_d t) \quad (2.65)$$

As a result when only the initial conditions are considered the output voltage generated by a single cantilever becomes,

$$\varepsilon = -BL_p \dot{z}_c \quad (2.66)$$

which can be expanded as,

$$\varepsilon = BL_p z_o \omega_n \frac{e^{-\zeta_{eq}\omega_n t}}{\sqrt{1 - \zeta_{eq}^2}} \sin(\omega_d t) \quad (2.67)$$

In a similar manner, the power term can be derived as,

$$P = \frac{1}{2} b_e \left(\frac{R_L}{R_L + R_c} \right) \dot{z}_c^2 \quad (2.68)$$

and

$$P = \frac{1}{2} b_e \left(\frac{R_L}{R_L + R_c} \right) \left[z_o \omega_n \frac{e^{-\zeta_{eq}\omega_n t}}{\sqrt{1 - \zeta_{eq}^2}} \sin(\omega_d t) \right]^2 \quad (2.69)$$

In the equations given above ω_d is the damped natural frequency of the cantilevers defined by,

$$\omega_d = \omega_n \sqrt{1 - \zeta_{eq}^2} \quad (2.70)$$

From (2.67) and (2.69) it can immediately be seen that the voltage and power obtained from the generator will be decaying out signals.

Before going into simulation of the system, the equations given above must be modified so that both the cantilever and the magnet positions are measured from the same reference position. The offsets of the magnet, δ_m , and cantilever, δ_c , from the base position are as shown in Figure 2.25. If the casing's base is taken as the datum and $z_m = x_m - y_m$, then the dynamic motion equation for the magnet can be written as,

$$m_m \ddot{z}_m + b_m \dot{z}_m + k_m (z_m - \delta_m - \delta_{mst}) = -m_m \ddot{y} - m_m g \quad (2.71)$$

In the last equation δ_m is the offset of the magnet from the base to the static equilibrium position and δ_{mst} is the static deflection of the magnet due to gravity. The static deflection and gravity terms will cancel out each other to give,

$$m_m \ddot{z}_m + b_m \dot{z}_m + k_m (z_m - \delta_m) = -m_m \ddot{y} \quad (2.72)$$

Similarly for the cantilever the following equation can be written,

$$m_c \ddot{z}_c + b_c \dot{z}_c + k_c (z_c - \delta_c) = -m_c \ddot{y} \quad (2.73)$$

The simulation of the system actually consists of two modes; the first mode is the separate motion of the magnet and cantilever in which the last two equations are used. The second mode is the combined motion of the magnet and cantilever where the magnet and cantilever moves together as a single body due magnetic interaction. The governing equation for the second mode can be defined as follows,

$$(m_m + m_c) \ddot{z} + (b_m + b_c) \dot{z} + k_m (z - \delta_m) + k_c (z - \delta_c) = -(m_m + m_c) \ddot{y} \quad (2.74)$$

The condition of transition between these two modes can be defined with reference to the contact force between the magnet and the cantilever. The contact force must be compressive (positive) or if it is incompressive (negative) it should be analytically larger than the magnetic attraction force for the bodies to remain intact, else they will move independently. This condition can be represented by the following inequality and referring to Figure 2.26 for the directions,

$$\begin{aligned} \text{Combined operation } T &> -F_m \\ \text{Separate operation } T &< -F_m \end{aligned} \quad (2.75)$$

T is the contact force between the bodies and it is compressive if $T > 0$. The minus sign in the above inequality is due to this fact. F_m is the magnetic attraction force between the bodies during contact and it is defined by,

$$F_m = \frac{B^2 A_m}{2\mu_0} \quad (2.76)$$

In the final equation, B is the magnetic flux density defined previously, A_m is the magnetic contact area, and μ_0 is the permeability of free space given by $\mu_0 = 4\pi \cdot 10^{-7} \text{ T} \cdot \text{m/A} = 4\pi \cdot 10^{-7} \text{ N/A}^2$.

The contact force, T , can be expressed by either of the following two equations, which are derived with reference to Figure 2.26.

$$\begin{aligned} m_m \ddot{z} + b_m \dot{z} + k_m (z - \delta_m) &= -m_m \ddot{y} + T \\ \Rightarrow T &= m_m (\ddot{z} + \ddot{y}) + b_m \dot{z} + k_m (z - \delta_m) \end{aligned} \quad (2.77)$$

$$\begin{aligned} m_c \ddot{z} + b_c \dot{z} + k_c (z - \delta_c) &= -m_c \ddot{y} - T \\ \Rightarrow T &= -(m_c (\ddot{z} + \ddot{y}) + b_c \dot{z} + k_c (z - \delta_c)) \end{aligned} \quad (2.78)$$

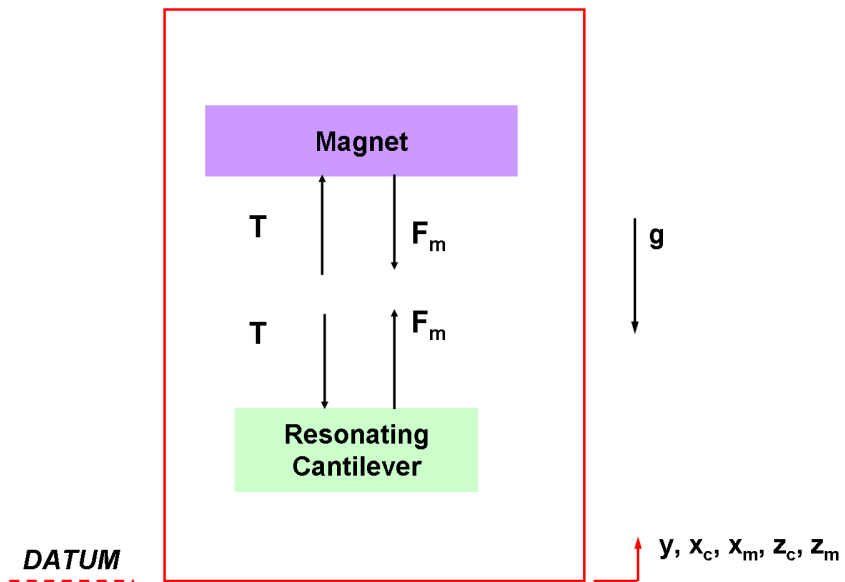


Figure 2.26. Representation of the contact force.

Although in Figure 2.26 the magnetic force F_m is shown, it is not reflected to dynamic equations (2.77) and (2.78) since it is a gluing force between the two bodies. The contact force can then be calculated from either (2.77) or (2.78). The catch and release points are determined from either of these equations together with the conditions defined by (2.75). The release point can simply be determined by comparing the spring force with the magnetic attraction force, which is already covered in (2.77) and (2.78) with a more complete form. Using the model described

by (2.72)-(2.74) and contact force defined by (2.78), the system is optimized and simulated in Matlab® Simulink® environment. Table 2.4 shows the optimized parameters and simulation results for the FUC design. Figure 2.27 shows the Matlab® Simulink® model used to simulate the FUC design.

Table 2.4. Optimized parameters of the generator.

Input vibration frequency	50-200 Hz
Input acceleration	40 g
Magnet type	NdFeB (1.18 T)
Magnet dimensions	3.8 x 3.8 x 1.5 mm ³
Device dimensions	8.5 x 7 x 2.5 mm ³
Total number of cantilevers	20
Natural frequency of the cantilevers	2 kHz
Cantilever size	1000 x 430 x 15 μm ³
Material for magnetic actuation	Nickel
Magnetic actuation area	430 x 225 x 9 μm ³
Nickel thickness	9 μm
Cantilever structural material	Parylene C
Diaphragm structural material	Parylene C
Length of each diaphragm arm	1000 μm
Width of each diaphragm arm	555 μm
Thickness of each diaphragm arm	15 μm
Total number of diaphragm arms	16
Magnet area on the diaphragm	3.95 x 3.95 mm ²
Natural frequency of the diaphragm	113 Hz
Release height of the cantilevers	200 μm

Table 2.4. (cont'd).

Effective frequency of the device	50-200 Hz
Damping ratio of the cantilevers	0.02
Magnetic flux density	0.19 Tesla
Distance between cantilevers to magnet	500 μ m
Coil width	20 μ m
Coil thickness	0.1 μ m
Total coil length (single cantilever)	13.1 mm
Coil resistance	160 Ω
Practical coil length (single cantilever)	1.4 mm
Number of coil turns	6
Overall collected energy in 1 s from 20 cantilevers	610 pJ (30.5 pJ/cantilever)
Overall peak power output from 20 cantilevers	6.6 nW (0.33 nW/cantilever)
Overall peak voltage output from 20 cantilevers	13.5 mV (0.67 mV/cantilever)

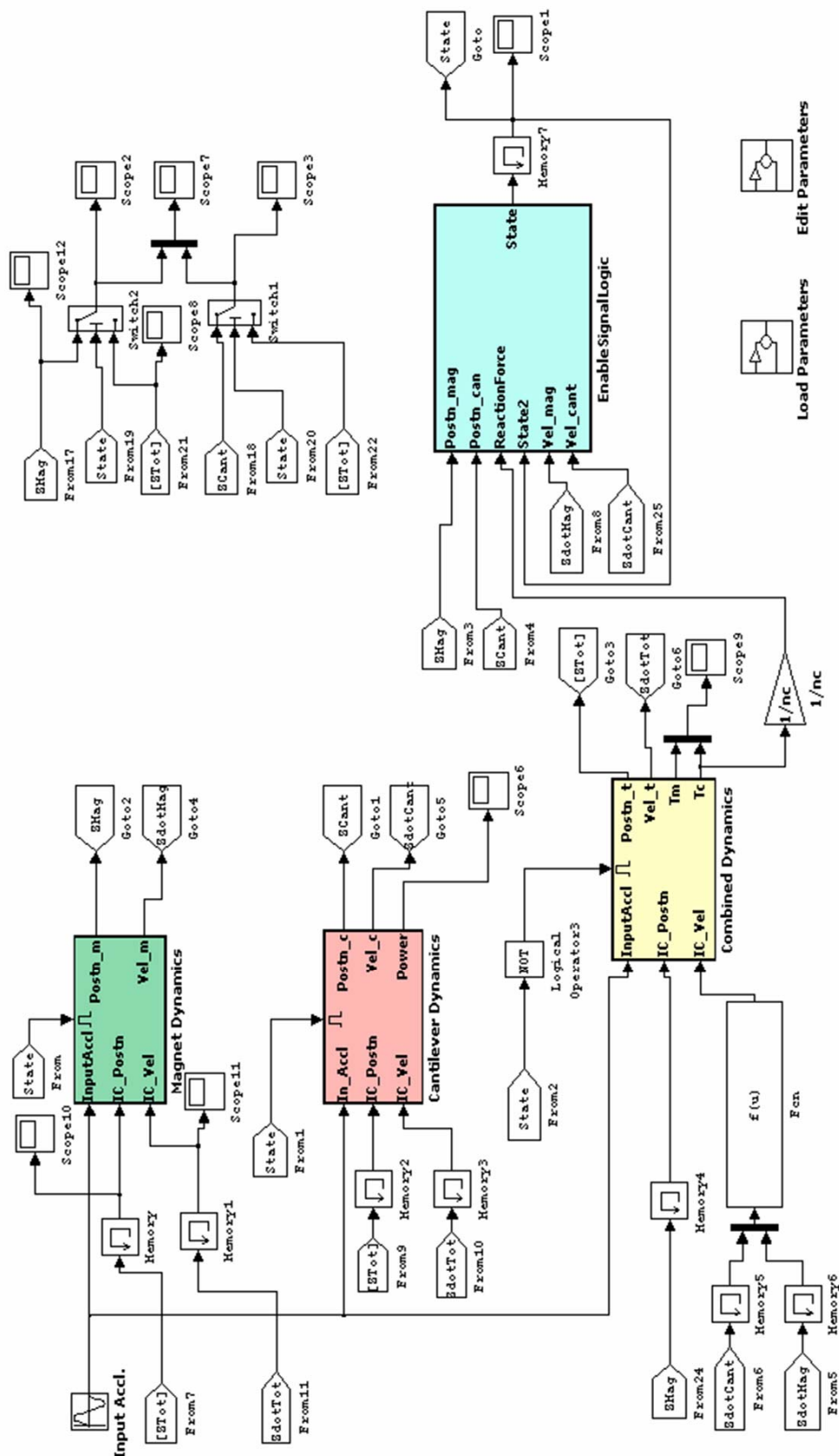


Figure 2.27. Matlab® Simulink® model used to simulate the frequency up-converter (FUC) design.

In this model there are three different dynamics; the motion of the cantilevers, the magnet-diaphragm assembly and the combined motion of the cantilevers and the magnet, which are embedded within the pink, green and yellow subsystems, respectively, as shown in the Simulink model below. Each dynamic model is defined with the corresponding mathematical dynamic differential motion equations and solved separately in the Simulink model. At each sample time interval, the separate or combined motion condition defined by (2.75) is checked using the logic model embedded in the light blue subsystem, which is shown in detail in Figure 2.28.

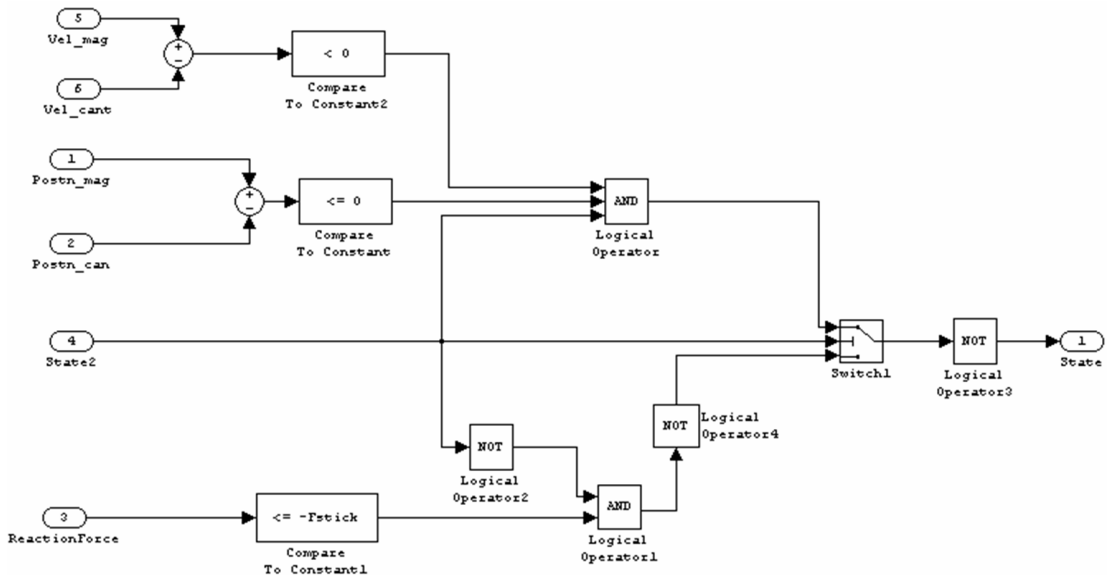


Figure 2.28. Simulink® subsystem used to determine the final state of the model.

This logic subsystem shown in the last figure is composed of boolean operators that check for the current states such as the position and velocity of the cantilevers, the reaction force between the cantilevers and magnet and current state of the model (combined or separate motion). After considering all these parameters, the state of the model is updated to combined or separate motion. The states of the cantilever and the magnet such as the displacement and the velocity are also transferred to the next mode for continuity of the simulation. For transition from separate to the

combined motion, the common velocity is estimated assuming that the collision is fully elastic. However, this is not the case in the actual operation, but it is quite hard to model such a nonlinear impact phenomena.

Figure 2.29 shows the simulated relative displacements of the cantilevers and the magnet for a vibration frequency of 95 Hz. As estimated and shown in Table 2.4, the cantilevers are released at a distance 200 μm above from their initial equilibrium position. There are two different dynamic modes of operation; separate motion of the cantilevers and magnet and their combined motion as a single body. The lower frequency green line, indicated in the light blue area in the graph is the combined motion of the cantilevers and magnet where they act as a single combined body. When the cantilevers are released, the magnet and cantilevers move as two independent bodies as shown in the light orange area in the graph. In this area, the higher frequency green line represents the displacement of the cantilevers and the lower frequency blue line shows the displacement of the magnet.

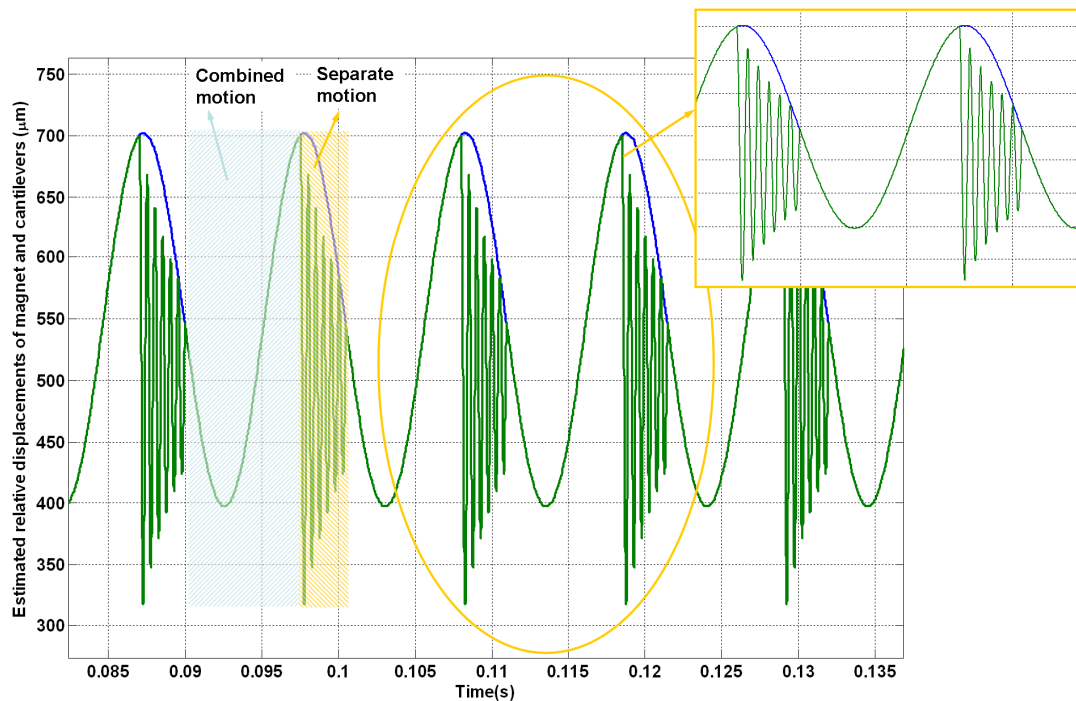


Figure 2.29. Relative displacements of the cantilevers and the magnet.

Figure 2.30 shows the voltage output from a single cantilever of the FUC. A maximum voltage output of 0.67 mV is estimated to be obtained from a single cantilever of the FUC design. This corresponds to an overall voltage output of 13.5 mV from all 20 cantilevers. In the previous section, it is estimated that from a same sized traditional large mass coil design 0.4 mV can be obtained under the same operation conditions. This indicates that, by the FUC design the maximum voltage output can be increased by about 33 times of a same sized traditional micro energy generator. Besides frequency up-conversion, another important feature of the FUC design is that it can operate at any frequency as far as the cantilevers are caught and released. This makes the generator to operate regardless of matching of the resonance frequency of the diaphragm and the environmental excitation frequency. When AOC or LMC designs are considered, they have a limited bandwidth and the output would degrade rapidly as the excitation frequency deviated from resonance.

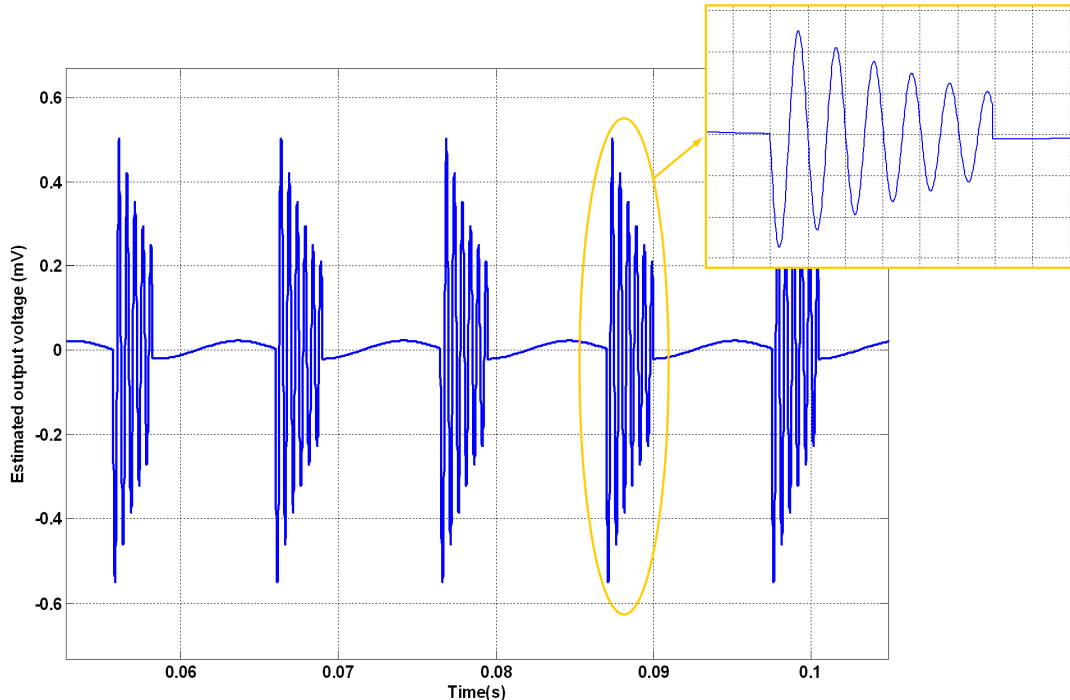


Figure 2.30 Simulated voltage output from a single cantilever of the frequency up-converter (FUC) design.

2.6 Conclusions

In this chapter, the micro generator designs proposed within the scope of this study have been presented. A detailed mathematical analysis and optimized parameters of each generator model with governing motion equations have been given. These equations and parameters are then used to simulate each design under the corresponding heading. The simulations results and parametric analysis are used to have an idea of the behavior of each proposed model. These results are also used to design the micro fabrication steps of the models. As a result, in the next chapter, the fabrication of the micro generators will be discussed based upon the simulation results and parameters obtained in this chapter.

CHAPTER 3

FABRICATION OF THE MICRO GENERATORS

In this chapter, the micro fabrication steps of the proposed generator designs are explained. Before fabrication of the micro generators, the layout drawings that are used to manufacture the glass masks utilized during the micro fabrication of the designs, are drawn and compiled by Cadence® Virtuoso® software. Although all of the proposed micro generators have different layout drawings, their design allows them to have the same fabrication sequence. For this reason in this chapter, firstly the properties of each proposed generator is explained in Sections from 3.1 to 3.5 and then the detailed fabrication steps are investigated under a single heading for all of the designs in Section 3.6.

3.1 Properties of the Array of Cantilevers (AOC) Design

Figure 3.1 shows the schematic drawing of the array of cantilevers (AOC) design. The areas shown in pink color are silicon forming the base whereas the green area is the empty space for the magnet. The blue lines are the metal routings used to form the coils. The cantilevers are right below this metal layer. The device and cantilever dimensions are 9.5 x 8 mm and 890 x 690 μm , respectively as shown in the figure. There are a total number of 20 cantilevers and 16 coil turns on each cantilever that are formed by the first metal layer. The coils are formed by 10 μm width and 0.1 μm thick metal layers. The second metal layer is used for electrical routing to connect each coil electrically in series. The two metal layers are insulated and separated from each other by a thin layer parylene film. In order to measure and carry out the output voltages, the two larger electrical contact pads that are located on the lower-left hand side of the device are used. Also, test contact pads are formed to measure outputs from a number of cantilevers for benchmarking as shown in the figure.

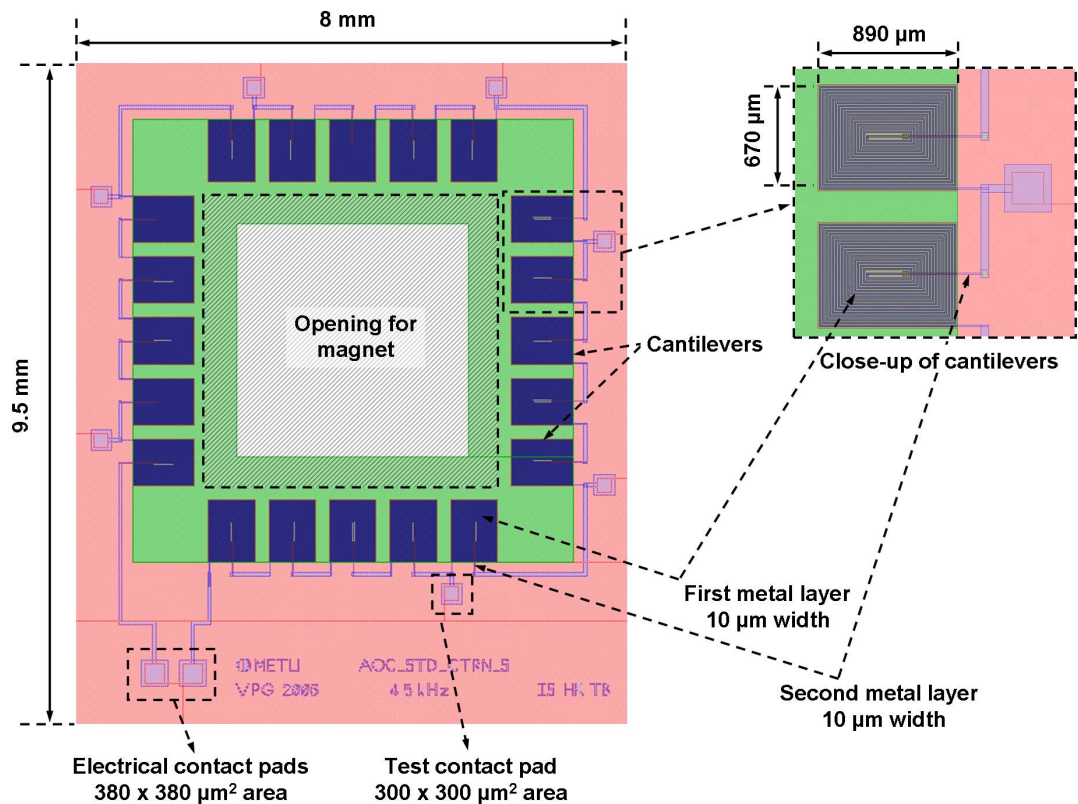


Figure 3.1. Schematic drawing of the AOC design.

3.2 Properties of the Array of Cantilevers Design with Varying Natural Frequencies (AOC_FS)

Figure 3.2 shows the schematic drawing of the array of cantilevers design with varying natural frequencies (AOC_FS). This design is quite similar to the array of cantilevers (AOC) design in terms of its schematics, but it has a different functionality as explained in the previous chapter. The array of cantilevers design with varying natural frequencies (AOC_FS) is indeed a modification of the array of cantilevers design (AOC). In the case of the array of cantilevers design with varying natural frequencies (AOC_FS), the cantilever numbers are increased to 40 and the

cantilevers' length are incremented by 3 μm from 890 to 1007 μm . The metal layers are the same as the ones explained in the previous section. The device is sized 14 x 12.5 mm in this case and there are 10 coil turns on each cantilever. The coils are 20 μm width and 0.1 μm thick.

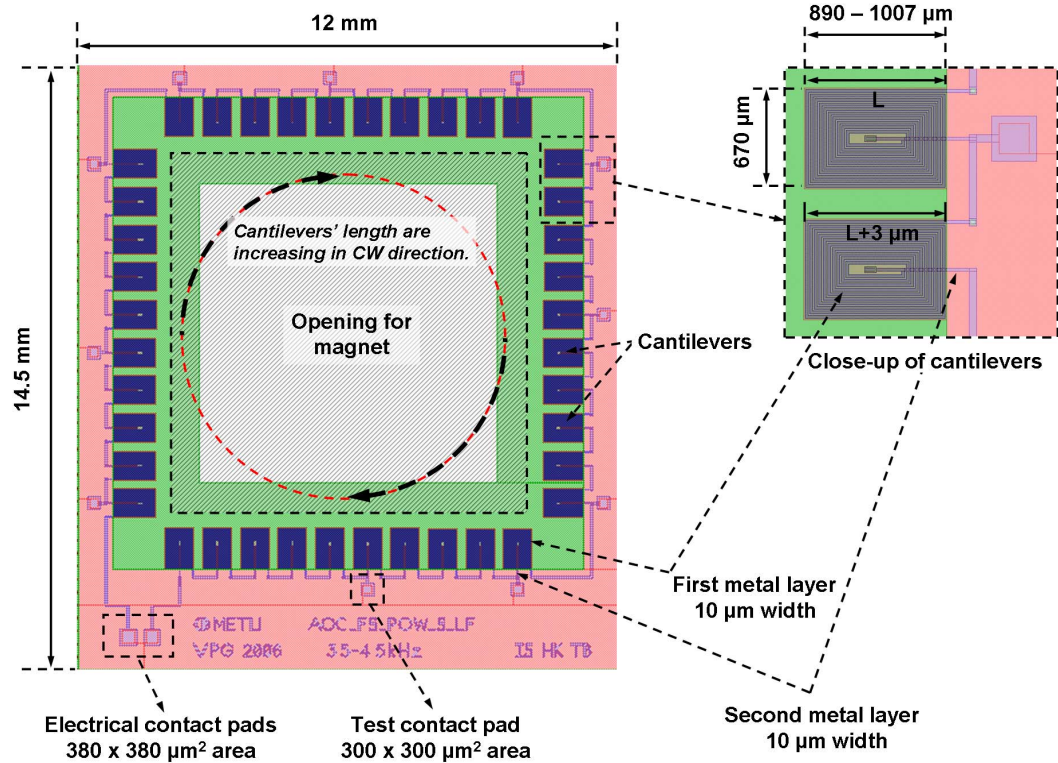


Figure 3.2. Schematic drawing of the AOC_FS design.

3.3 Properties of the Large Mass Coil (LMC) Design

Figure 3.3 shows the schematic drawing of the large mass coil (LMC) design. On the left hand side the base and the on the right hand side the diaphragm is shown. The base is basically composed of a total number of 13 coil turns that are formed by a 160 μm wide and 0.1 μm thick metal layer. Again, the main electrical contact pads are used to measure the output from the generator. The diaphragm is made from a 15 μm thick parylene layer and the magnet is placed right in between the marked

notches on the diaphragm. In order provide a controlled elasticity for the diaphragm, a total number of 16 arms connect the central region to the sidewalls. Each arm is 1 mm long, 0.555 mm wide, and 15 μm thick.

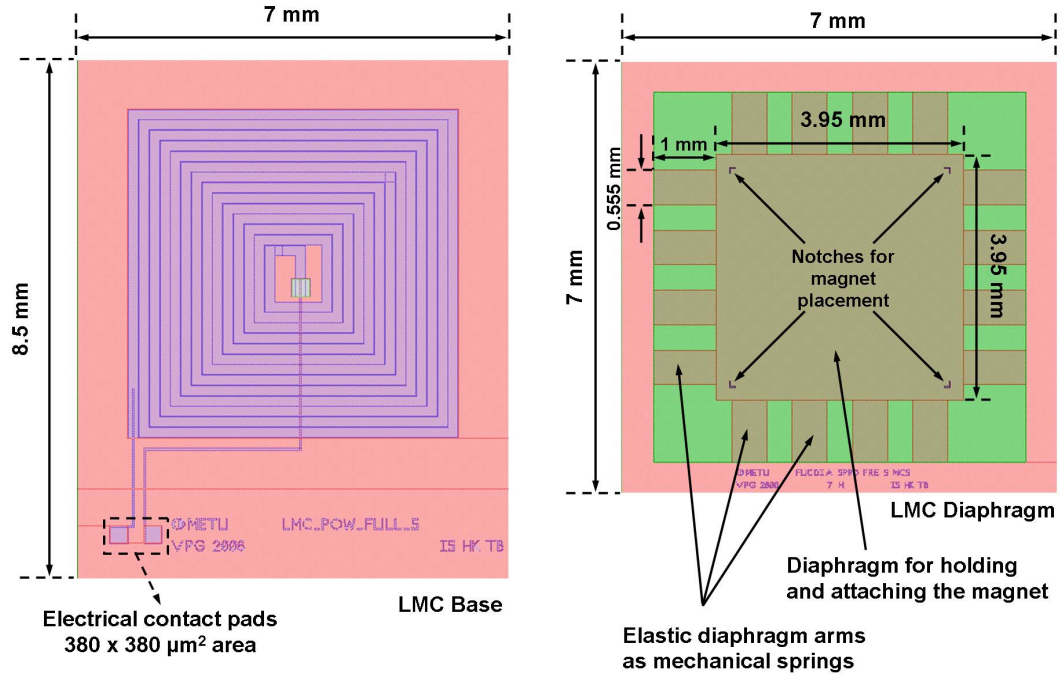


Figure 3.3. Schematic drawing of the LMC design.

3.4 Properties of the Frequency up-Converter (FUC) Design

Figure 3.4 shows the schematic drawing of the frequency up-converter (FUC) design. On the left hand side the base and on the right hand side the diaphragm is shown. The physical architecture of the base and the diaphragm are similar to the base of the array of cantilevers (AOC) design and the diaphragm of large mass coil (LMC) design, respectively. The base is formed of 20 parylene cantilevers with dimensions $1000 \times 430 \times 15 \mu\text{m}^3$. Each cantilever holds 6 coil turns formed by 20 μm wide and 0.1 μm thick metal layers. At the tip of each cantilever, a $430 \times 225 \times 9 \mu\text{m}^3$ nickel layer is formed for magnetic interaction to catch and release the cantilevers. Other critical dimensions for the design are given on the layout drawing below. The

diaphragm layer is very similar to that of the LMC design with some small variation in dimensions.

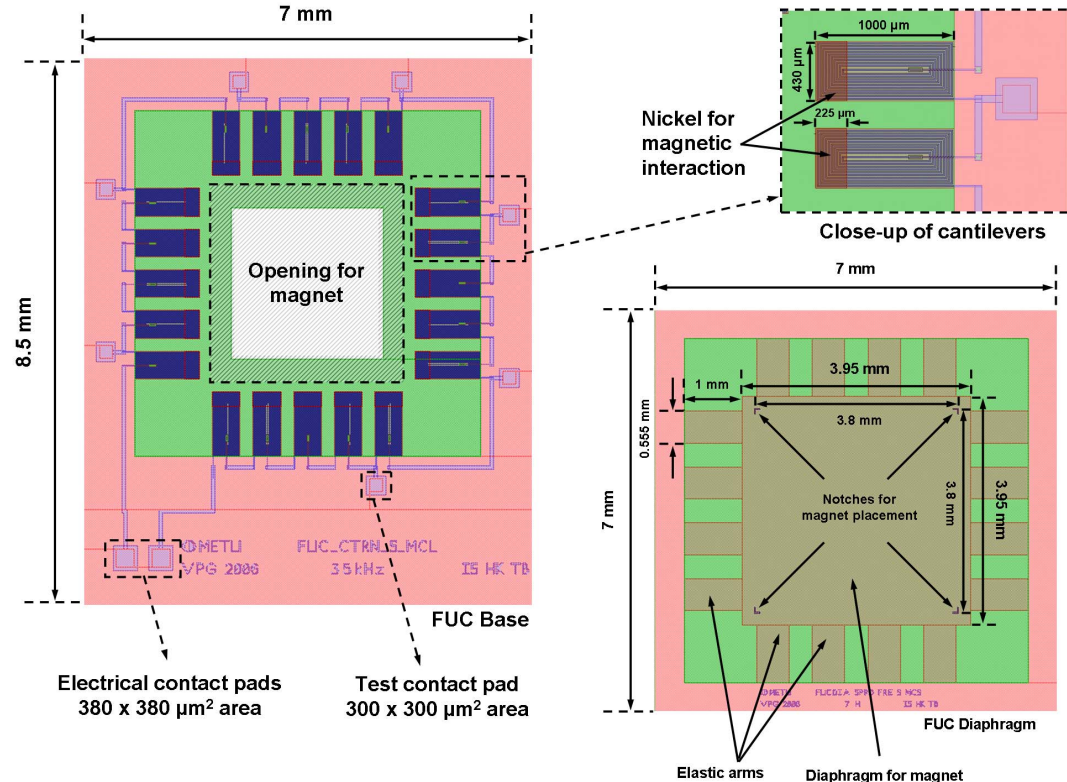


Figure 3.4. Schematic drawing of the FUC design.

3.5 Schematic Drawing of the Whole Wafer

Figure 3.5 shows the schematic drawing and the setup of all the devices over a 4" wafer. There are a total number of 90 devices in this layout in which a multiple number of each design is present so that a batch of devices is available for testing after the fabrication on each set of wafers.

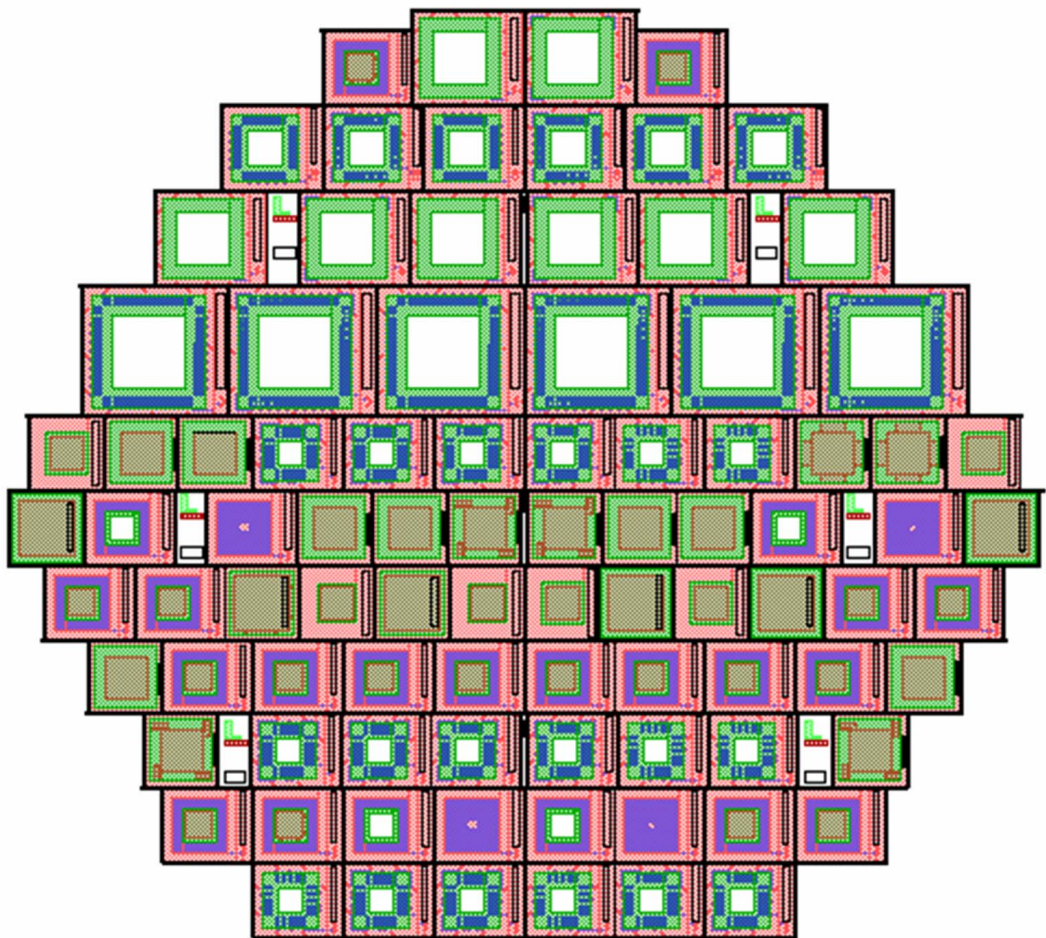


Figure 3.5. Schematic drawing of the whole wafer over a 4" silicon wafer.

3.6 Fabrication Steps of the Micro Generators

In this section, the fabrication steps of the designed micro generators are explained. As explained and shown in section 3.5, the layouts for all of the designs are drawn and placed on the same 4" sized layout. The fabrication steps of each unique model are designed to be the same so that when the wafer is released, all of the proposed designs will be available for use at the end of the fabrication. This makes the fabrication procedure practical and each unique design is determined by the corresponding patterns on the layouts and masks.

The FUC and LMC designs are both fabricated as two separate chips to be combined at the end of the process. One of the chips forms the base and the other forms the diaphragm. The formation steps of FUC base are very similar to the base of the AOC and AOC_FS designs. The most complicated design in terms of fabrication is the FUC, so in order to generalize the explanations, the fabrication steps of this design are focused on.

In order to realize the micro fabrication steps of the generators, a total number of 6 masks are designed and fabricated. The first and second sets of masks are purchased from ML&C GmbH and the other sets are fabricated directly at METU-MET facilities. These masks are vital in photolithography to fabricate the devices. The details of photolithography and micro fabrication have been extensively investigated in literature and can be found in sources like [69 and 70]. Each mask is made of quartz and has very thin 2 dimensional chromium (Cr) patterns of the layer that is intended to be fabricated. In this study, they are indeed fabricated from each layer of the layout given in Figure 3.5. This layout is actually composed of by 6 different layouts forming each layer of the devices and they are shown one on top of the other in the figure. These layers are shown separately in Appendix A. The masks are drawn in such a way that there is no need for dicing after the devices are released. This is achieved by forming tunnels of 200 μm wide between each device. After release, each device is attached to each other by a very thin parylene layer of 15 μm ,

which can easily be torn off by applying a very light force with the tip of a razor blade to completely separate the devices from each other.

In order to have a better understanding of the relative locations of the mask patterns with respect to each other, Figure 3.6 illustrates the used layers in the order of fabrication process flow and for a part of the FUC base to demonstrate how each physical layer is formed.

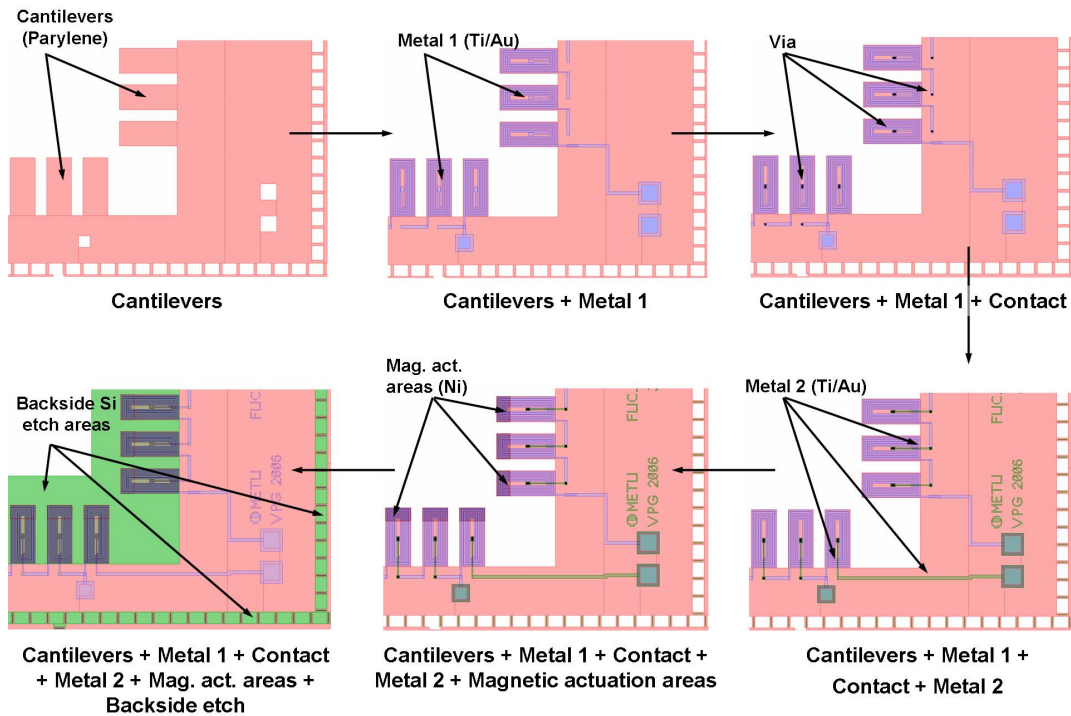


Figure 3.6. Relative positions of the masks with respect to each other.

Table 3.1 summarizes the corresponding masks and their function. All masks are fabricated with an accuracy of $2 \mu\text{m}$ so that features greater than $2 \mu\text{m}$ are able to be fabricated within the tolerances by photolithography. For this process, the minimum feature size is $10 \mu\text{m}$, which is well above the fabrication tolerance of the masks. The dark and clear field property indicated in Table 3.1 specifies whether the patterns (clear field) or open fields (dark field) are drawn on the masks. Also, the

corresponding layout drawing of each mask pattern is given in Appendix A as stated in the corresponding column of the table given below.

Table 3.1. List of the masks used in micro fabrication of the micro generators.

Mask #	Mask name	Layout in Figure	Field type	Patterned or etched material	Description
1	Cantilever	A.1	Clear	Parylene	Form the cantilevers and the diaphragms.
2	Coil turn	A.2	Clear	Ti/Au	Form the coil turns.
3	Metal routes	A.3	Clear	Ti/Au	Form the metal routes.
4	Contact	A.4	Dark	Parylene	Etch parylene to form the vias.
5	Magnetic actuation	A.5	Dark	Ni	Form magnetic actuation area for the FUC design.
6	Backside etch	A.6	Dark	Silicon (Si)	Etch Si wafer from backside to release the devices.

All of the micro fabrication steps of the micro generators are carried out at Middle East Technical University, Micro Electronic Technologies (METU-MET) facilities. 4" Si wafers are used for the fabrication process. Figure 3.7 shows the fabrication process flow of the micro generators, more specifically the frequency up-converter (FUC) design since it is the most general and complicated one among the designs. First, a thermal oxide layer of thickness 2000 Å is grown on the silicon substrate. This layer provides isolation between metal contact pads and the silicon substrate.

Next, a 1 μm -thick parylene is deposited by chemical vapor deposition (CVD) and patterned by reactive ion etching (RIE) at the contact pads and cantilever areas (3.7.a). Then, coil turns are formed by sputtering and patterning the first metal layer (3.7.b). As the next step, a second 1 μm -thick parylene layer is formed on the metal and patterned at the contact areas between two metal layers to provide electrical isolation between the first and second metal layers and vias are opened at the necessary positions on parylene by RIE to provide contact between the first and second metal layers (3.7.c). The second metal layer is then sputtered and patterned to complete the metal routes (3.7.d). The main thicknesses of the cantilevers are defined by the deposition of the third layer of 13 μm thick parylene and patterning (3.7.e). Afterwards, a 9 μm nickel is deposited by electroplating and patterned by lift off to form the magnetic actuation areas specifically for the FUC design (3.7.f). Then, a final layer of 1 μm thick parylene is deposited and patterned to act as a protection layer for the magnetic areas (3.7.g). Finally, Si through etched from the backside by deep reactive ion etching (DRIE) (3.7.h). The exposed oxide layer on the back is wet etched in a buffered hydro-fluoric acid (BHF) solution to release the devices (3.7.i). The devices are then cleaned in acetone and isopropyl alcohol (IPA). Then the magnet is glued to the diaphragm (3.7.j) and the two chips are combined together to form a single device (3.7.k). The distance between the magnet and the cantilevers are defined by using a spacer.

The fabrication steps explained above are the same for all the designs. The devices are differentiated by the patterns on each mask. The array of cantilevers (AOC) and the array of cantilevers with varying natural frequencies (AOC_FS) designs can directly be tested after release since they are mainly composed of a single base only. The large mass coil (LMC) and the frequency up-converter (FUC) designs are released as two chips to be combined later on. The first chip is the base holding the coils and the second chip is the diaphragm where a magnet with a suitable size is glued as explained above.

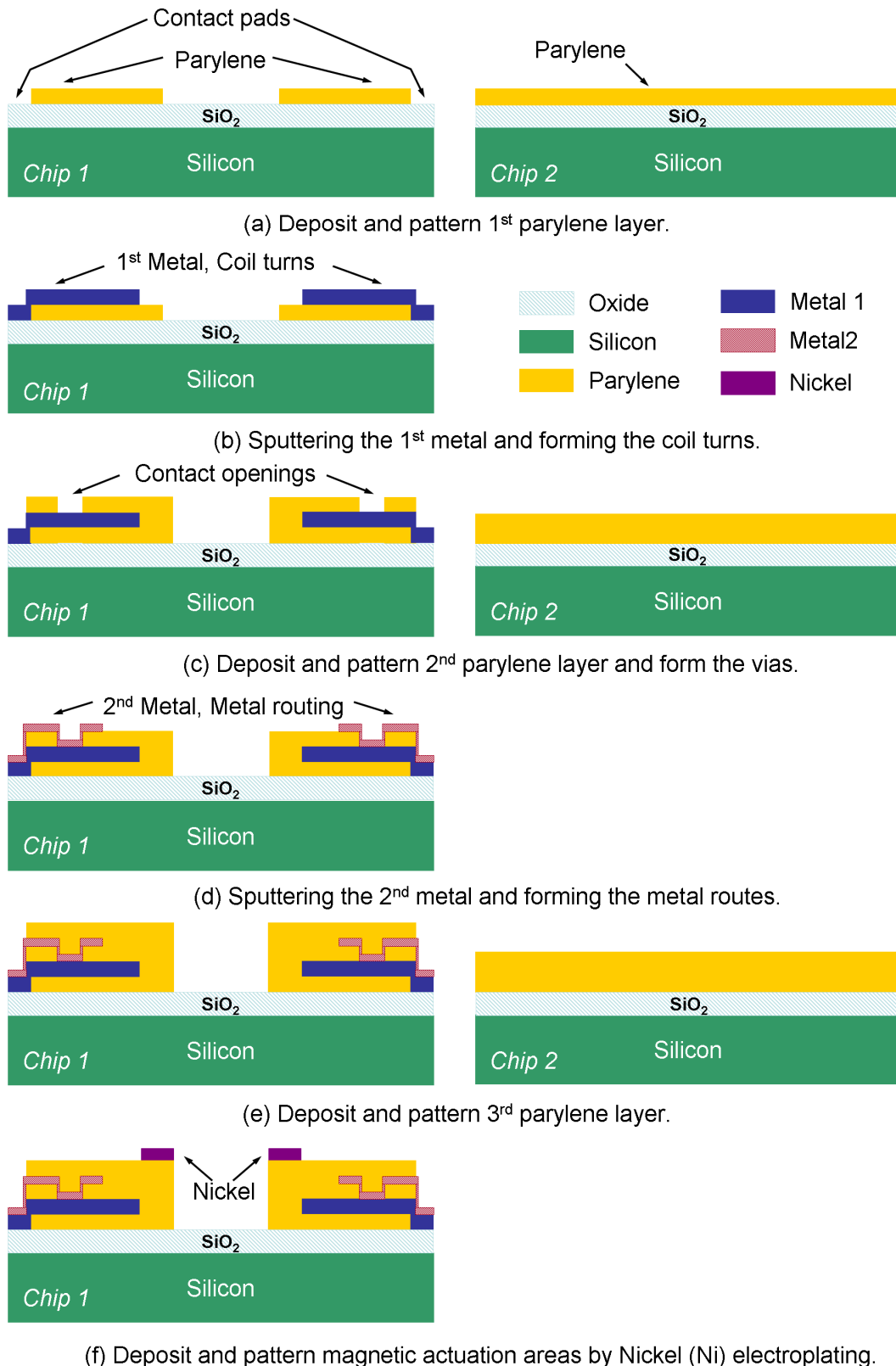
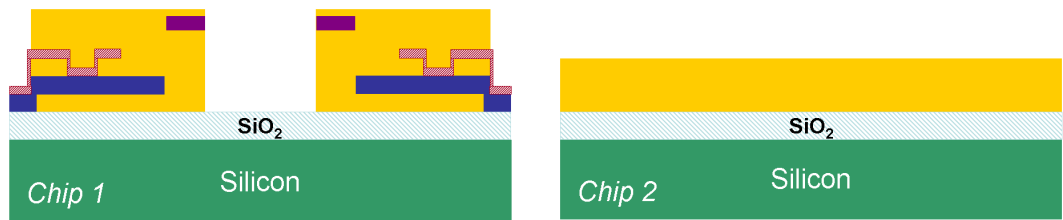
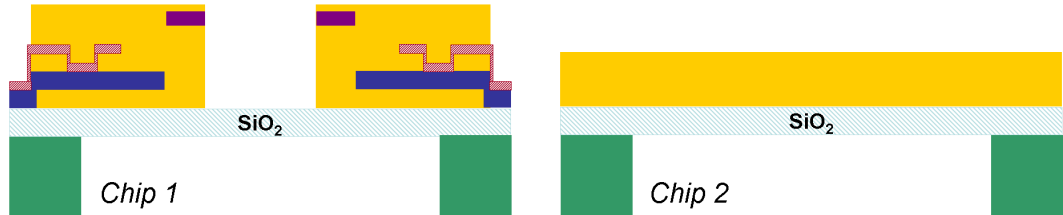


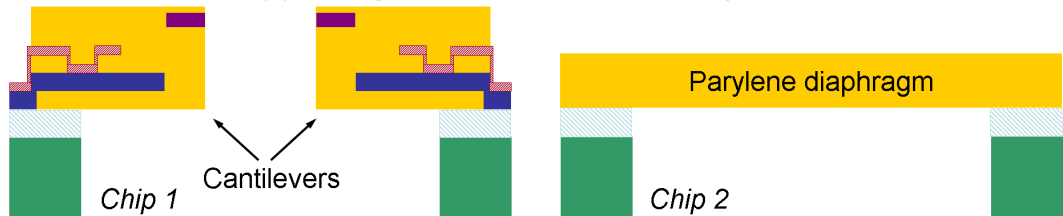
Figure 3.7. Micro fabrication steps of the FUC design.



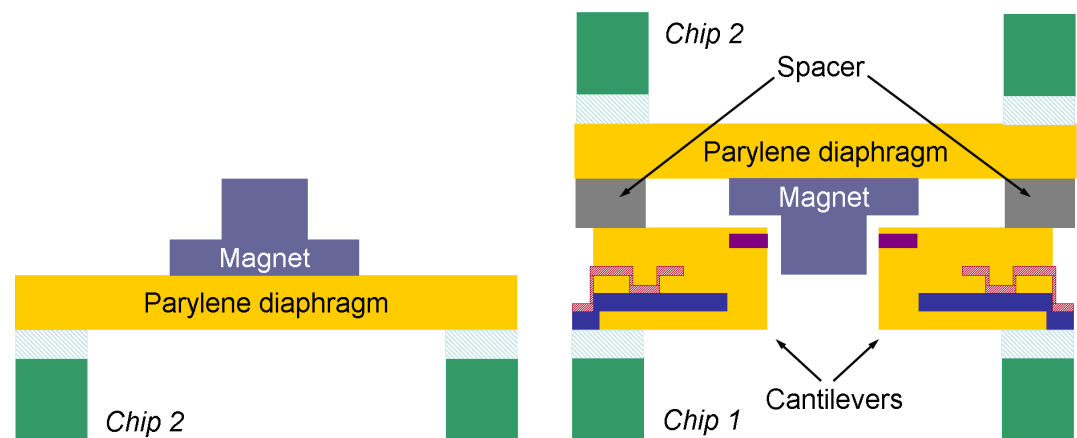
(g) Deposit and pattern the final parylene layer.



(h) Through etch of Si from backside by DRIE.



(i) SiO₂ etch and release of the devices.



(j) Assemble the diaphragm and the magnet.

(k) Combine the two chips.

Figure 3.7. (cont'd).

After giving a brief outline of the fabrication process, the detailed process recipe of each step is explained in the following paragraphs. Tables 3.2 through 3.8 describe the “process recipe” of each step. The “process recipe” is a custom made

consecutive and interrelated steps of process parameters used to fabricate the devices. They are mainly developed based upon micro fabrication theory and previous know-how and by trial and error. Thus, it is a rather tedious and time taking job as the designs are unique and this process is carried out for the first time. Once they are determined and optimized, the forthcoming fabrication run would be much faster and better. The generalized process flow of the micro generators are graphically shown in Appendix B.

The first step in the fabrication process, after growing 2000 Å thick oxide on Si (SiO_2), is parylene deposition and patterning. Parylene C is a recently developed biocompatible and hydrophobic material and at the moment it is used extensively in the MEMS market due to its mechanical and chemical properties. It can be found in the form dimer in the market and can be deposited by chemical vapor deposition (CVD) technique. It is fully compatible with micro fabrication procedures and conformal deposition at room temperature and good step coverage properties makes it a popular material. It can be dry etched very easily by regular O_2 plasma or RIE based O_2 plasma. For this study, it is specifically chosen because it is much more elastic compared to silicon ($E_{\text{parylene}} = 2.75 \text{ GPa}$, $E_{\text{silicon}} = 155 \text{ GPa}$). This allows much larger deflections before mechanic failure and thus leads to increased voltage generation. In addition the deposition and patterning steps are much easier compared to silicon so that improved control over cantilever dimensions can be obtained.

Table 3.2 shows the detailed process recipe of the first step that is the parylene deposition and patterning. This step starts with the deposition of 1 μm thick Parylene C on blank SiO_2 wafer. The backside of the wafer is protected by a weakly adhesive tape to prevent the back surface being coated and after deposition, it can easily be removed. Parylene is coated by CVD and the parylene coater, model PDS 2010, from Specialty Coating Systems (SCS), is specifically used for this purpose. Figure 3.8 shows the photograph of this tool.

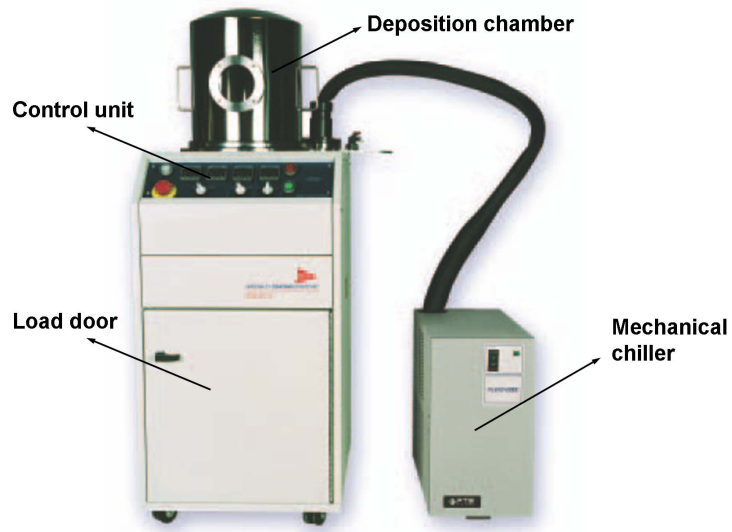


Figure 3.8. Photo and main components of the parylene deposition system, SCS PDS 2010, courtesy of SCS Inc.

The tool is composed mainly a loading door, deposition chamber, main control unit and a mechanical chiller. Parylene is loaded to the coater in the form of so called “dimer”. Approximately 2 g of dimer is necessary for each 1 μm thickness of parylene to be coated. This value also depends on the total surface area of the substrates loaded in the machine for coating. Then wafers are loaded into the deposition chamber and after necessary adjustment of process parameters, the machine is operated by the main control unit. The mechanical chiller is connected to a cold trap tube that is kept at -75°C to catch the foreign particles before reaching the vacuum pump. The deposition process is realized under vacuum and at room temperature. In this step the process parameters are set as SP:15 and PLA1:10 that corresponds to the desired pressure and lower pressure threshold of the deposition process, respectively. The lower the desired value, the better will be the deposited parylene in terms of quality. The disadvantage will be that the process will take longer and it may not be possible to carry on the process at the set pressure if it is too low. Another important point is that in order to improve the adhesion of parylene to

certain type of substrates, for this case SiO_2 , a solution called A174 Silane should be used.

Table 3.2. Process steps of the 1st parylene layer.

Cantilever Mask	A1	Parylene Deposition (1 μm)	SP:15, PLA1:10, use A174-Silane (Protect backside by tape.)
	A2	Lithography	
	A2.1	Dehydration	Dehydrate 10 mins. in oven @120°C. Cool down in desiccator for 5 mins.
	A2.2	PR Spin	SPR 220-3 @2500rpm, t=30 s (3.5 μm aimed)
	A2.3	Softbake	Softbake t=90s over contact hotplate @T=115°C
	A2.4	Expose	Expose 7 sec. (Vacuum contact)
	A2.5	Rehydration	Rehydrate 30 mins. prior to develop with 1 pipette full of water in closed box
	A2.6	Develop	MF24A, 40-50 sec.
	A3	Parylene Etch by RIE	~5 mins. (~0.33-0.43 $\mu\text{m}/\text{min}$), O ₂ Plasma, 100 sccm, 100 mTorr, 100 Watt
	A4	PR Strip	Acetone + IPA + DI Water

After parylene deposition, the wafers are spin coated by SPR 220-3 type photoresist (PR) at a spin speed of 2500 rpm to obtain a thickness of 3.5 μm . The wafers are then softbaked over hotplate at a temperature of 115°C for 90 s. Then, the wafers are exposed by the “cantilever mask” shown in Figure A.1 for 7 s at a constant power intensity of 8.8 mW/cm². For this purpose an EVG 620 model mask alignment tool is used. The exposed substrates are then developed in MF24A type developer for about 40-50 s to remove the exposed PR. The final step of the parylene patterning is, parylene etch by O₂ plasma in Surface Technology Systems (STS) RIE tool. The

process settings are 100 sccm O₂ flow, 100 mTorr process pressure and 100 W power. The etch rate is about 0.33-0.43 μm/min and 1 μm parylene is etched for 5 mins. to be on the safe side. This step is completed by the removal of the PR and cleaning of the wafers in acetone, IPA and deionized (DI) water.

The second step in the fabrication process is the deposition and patterning of the first metal layer to form the coil turns. Table 3.3 shows the detailed process parameters of this step. Firstly, the wafers are fully dried in oven at a temperature of 120°C for about 10 mins., to evaporate any moisture and particles right before metal deposition. Then titanium (Ti) and gold (Au) is sputtered with a thickness of 200 Å and 2000 Å, respectively. For this purpose an 8" sputtering tool from Bestec is used. Ti is actually required to assist the adhesion of Au to the substrate since it has poor adhesion characteristics. After sputtering, the wafers are spin coated with PR, exposed and developed with the same process flow of the first step. The only difference is that, in this step "Coil Turn (Metal 1) Mask" shown in Figure A.2 is used to expose the PR. Then, the wafers are kept in O₂ plasma for about 1-2 mins. to remove any exposed, but undeveloped, remaining PR especially between 10 μm wide coil lines. After this step, the wafers are hardbaked in oven at 120°C, for about 10 mins. to harden the patterned PR in order to improve its strength in the solutions that are used in the following step. The masked metal layers are patterned by wet etching. Firstly, Au layer which is on the top is etched with a commercial Au etchant from Transene. This is a very strong solution and Au is etched very rapidly. It takes about 25-32 s for 2000 Å thick Au to be etched. Then, Ti is etched in a custom made highly diluted Ti etchant, which is prepared by firstly mixing 80 ml DI water (H₂O) +10 ml hydrofluoric acid (HF) + 10 ml hydrogen peroxide (H₂O₂). Then 25 ml of this solution is further diluted with 1575 ml of DI H₂O and this final solution is used to etch Ti. It takes about 80 s to etch 200 Å thick Ti. Finally, this step is finished with the removal of the PR and cleaning of the wafers in acetone, IPA and DI water.

Table 3.3. Deposition and patterning of the 1st metal layer.

Coil Turn (Metal 1) Mask	B1	Dehydration	Right before sputter, dehydrate 10 mins. in oven @120°C, cool down in desiccator for 5 mins.
	B2	Ti sputter (200 Å)	Endpoint thickness=75A, MFC1=2 sccm
	B3	Au Sputter (2000 Å)	Timer 2=180s (will be used), MFC1=6.2 sccm
	B4	Lithography	
	B4.1	Dehydration	Dehydrate 10 mins. in oven @120°C, Cool down in desiccator for 5 mins.
	B4.2	PR Spin	SPR 220-3 @2500rpm, t=30 s (3.5 µm aimed)
	B4.3	Softbake	Softbake t=90s over contact hotplate @T=115°C
	B4.4	Expose	Expose 7 sec. (Vacuum contact)
	B4.5	Rehydration	Rehydrate 30 mins. prior to develop with 1 pipette full of water in closed box
	B4.6	Develop	MF24A, 40-50 sec.
	B4.7	O ₂ Plasma	O ₂ Plasma @ 0.2-0.3 Torr for 1-2 mins. (Remove exposed, but undeveloped PR specially between 10 µm lines)
	B4.8	Hardbake	Hardbake (for Metal etch) @120°C for 10 mins., Cool down in desiccator 5 mins.
	B5	Au Wet Etch	Au etchant 25-32 s.
	B6	Ti Wet Etch	Ti etchant, prepare 100 ml (80% H ₂ O+10% HF+10% H ₂ O ₂), 25 ml Ti etchant + 1575 ml DI H ₂ O, ~80 sec.
	B7	PR Strip	Try Acetone + IPA, else use SVC

After forming the coil turns, a 2nd metal layer is necessary to complete the metal routes, but in order to prevent short circuit between overlapping metal layers, an insulation layer between this patterned metal layer and upcoming 2nd metal layer is necessary. For this purpose, parylene is used as an electrical insulator since it is already used a structural material in the process and has very good electrical

insulation properties with volume resistivity of 8.8×10^{16} Ohm-cm at 23°C and 50% relative humidity [50]. As a result, in this step, a 1 μm parylene layer is deposited and patterned to form this electrical insulation layer. The process steps are exactly the same as the first process step (Step A) and will be not be repeated here again. Table 3.4 shows the details of this process step for convenience.

Table 3.4. Process steps of the 2nd parylene layer.

Cantilever Mask	C1	Parylene Deposition (1 μm)	SP:15, PLA1:10, use A174-Silane (Protect backside by tape.)
	C2	Lithography	
	C2.1	Dehydration	Dehydrate 10 mins. in oven @120°C. Cool down in desiccator for 5 mins.
	C2.2	PR Spin	SPR 220-3 @2500rpm, t=30 s (3.5 μm aimed)
	C2.3	Softbake	Softbake t=90s over contact hotplate @T=115°C
	C2.4	Expose	Expose 7 sec. (Vacuum contact)
	C2.5	Rehydration	Rehydrate 30 mins. prior to develop with 1 pipette full of water in closed box
	C2.6	Develop	MF24A, 40-50 sec.
	C3	Parylene Etch by RIE	~5 mins. (~0.33-0.43 $\mu\text{m}/\text{min}$), O ₂ Plasma, 100 sccm, 100 mTorr, 100 Watt
	C4	PR Strip	Acetone + IPA + DI Water

Before going on to processing of the 2nd metal layer, vias should be opened on the final layer of patterned parylene. In this intermediate step no deposition is made as it is only going to be photolithography with a different mask and etching of the 2nd parylene layer with the “Contact Mask” shown in Figure A.3. The process details of this step are given in Table 3.5, which are actually very similar to the process steps

from C2 to C4. It is also, worthwhile to note that Steps C and D can be combined to shorten the process time as there is no deposition process in Step D. This can be done simply by consecutive exposures of the PR spun in Step C2.2 with the “Cantilever Mask” and “Contact Mask”. As both of these masks overlap, there will not be any structural change on the processed parylene layer. One minor disadvantage will be that the alignment marks Step D, which also give information on the accuracy of the photolithography, would not be visible due to consecutive exposures. After a few trials, these two steps are actually combined with the optimized process parameters.

Table 3.5. Process steps of contact opening on 2nd parylene layer.

Contact Mask	D2	Lithography	
	D2.1	Dehydration	Dehydrate 10 mins. in oven @120°C. Cool down in desiccator for 5 mins.
	D2.2	PR Spin	SPR 220-3 @2500rpm, t=30 s (3.5 μm aimed)
	D2.3	Softbake	Softbake t=90s over contact hotplate @T=115°C
	D2.4	Expose	Expose 7 sec. (Vacuum contact)
	D2.5	Rehydration	Rehydrate 30 mins. prior to develop with 1 pipette full of water in closed box
	D2.6	Develop	MF24A, 40-50 sec.
	D3	Parylene Etch by RIE	~5 mins. (~0.33-0.43 μm/min), O ₂ Plasma, 100 sccm, 100 mTorr, 100 Watt
	D4	PR Strip	Acetone + IPA + DI Water

The next step is the deposition and patterning of Ti/Au just like in the 2nd step (Step B). In this case it is aimed to complete the metal routing by patterning this 2nd metal and getting contact to the first metal through the vias opened on the parylene that is

deposited and patterned in the previous step. All the process parameters except for the mask used during exposure are the same as in Step B. In this case, the mask pattern shown in Figure A.4 is used and Table 3.6 gives the detailed process flow for this step.

After having constructed the metal lines, a 3rd layer of parylene is deposited to define the cantilever thickness in the following fabrication step. For this purpose it is aimed to deposit and pattern a 13 µm thick parylene layer. In order to obtain this thickness, 26 g of Parylene C dimer is used with the deposition settings of SP: 25 and PLA1: 10. The SP (setpoint) value is increased in this case since the amount of parylene coated is quite larger than the previous parylene deposition steps. Also in this step, A174 Silane is used to improve the adhesion of parylene to the coated surface. The lithography of this step is a bit different than the previous parylene lithography steps of Steps A and C due to the parylene thickness. In this case, the mask pattern shown in Figure A.1 is used and Table 3.6 gives the detailed process flow for this step. In this case, the main difference from previous parylene depositions is the use of thick resist of AZ9260. It is spin coated 18 µm to let it last until the end of parylene etch. After coating the overflow at the edge of the wafer is removed by edge bead removal (EBR). Before exposure, wafers are rehydrated for 60 mins. to allow enough time for the free water molecules to penetrate into the thick resist film. The wafers are then exposed for 55 s and developed AZ826 MIF developer for about 15 min. Finally, parylene etch is carried out in RIE O₂ plasma in two consecutive 30 min. cycles (with a total etch time of 60 min.) to prevent parylene being cracked due to generated heat during etching. The wafers are then cleaned in acetone, IPA and DI water.

Table 3.6. Deposition and patterning of the 2nd metal layer.

Metal Routing (Metal 2) Mask	E1	Dehydration	Right before sputter, dehydrate 10 mins. in oven @120°C, cool down in desiccator for 5 mins.
	E2	Ti sputter (200 Å)	Endpoint thickness=75A, MFC1=2 sccm
	E3	Au Sputter (2000 Å)	Timer 2=180s (will be used), MFC1=6.2 sccm
	E4	Lithography	
	E4.1	Dehydration	Dehydrate 10 mins. in oven @120°C, Cool down in desiccator for 5 mins.
	E4.2	PR Spin	SPR 220-3 @2500rpm, t=30 s (3.5 µm aimed)
	E4.3	Softbake	Softbake t=90s over contact hotplate @T=115°C
	E4.4	Expose	Expose 7 sec. (Vacuum contact)
	E4.5	Rehydration	Rehydrate 30 mins. prior to develop with 1 pipette full of water in closed box
	E4.6	Develop	MF24A, 40-50 sec.
	E4.7	O ₂ Plasma	O ₂ Plasma @ 0.2-0.3 Torr for 1-2 mins. (Remove exposed, but undeveloped PR specially between 10 µm lines)
	E4.8	Hardbake	Hardbake (for Metal etch) @120°C for 10 mins., Cool down in desiccator 5 mins.
	E5	Au Wet Etch	Au etchant 25-32 s.
	E6	Ti Wet Etch	Ti etchant, prepare 100 ml (80% H ₂ O+10% HF+10% H ₂ O ₂), 25 ml Ti etchant + 1575 ml DI H ₂ O, ~80 sec.
	E7	PR Strip	Try Acetone + IPA, else use SVC

Table 3.7. Process steps of the 3rd parylene layer.

Cantilever Mask	F1	Parylene Deposition (13 μm)	SP:15, PLA1:10, use A174-Silane (Protect backside by tape.)
	F2	Lithography	
	F2.1	Dehydration	Dehydrate 10 mins. in oven @120°C. Cool down in desiccator for 5 mins.
	F2.2	PR Spin	AZ9260 @900 rpm, , t=30 s (18 μm aimed) + EBR with the same settings.
	F2.3	Relaxation	Keep in desiccator in horizontal position for t=10 min.
	F2.4	Softbake	Softbake t=18 min. over contact hotplate @T=100°C
	F2.5	Expose	Expose 55 sec. (Vacuum contact)
	F2.6	Rehydration	Rehydrate 60 mins. prior to develop with 5 pipette full of water in closed box.
	F2.7	Develop	AZ826 MIF, 15 min.
	F3	Parylene Etch by RIE	30 + 30 mins. (~22 $\mu\text{m}/\text{min}$), O ₂ Plasma, 100 sccm, 100 mTorr, 100 Watt
	F4	PR Strip	Acetone + IPA + DI Water

As the next step in the fabrication, the nickel (Ni) deposition and patterning is carried out. Ni is used form the magnetic areas for the FUC design due to its ferromagnetic properties. It is deposited by electroplating since a 9 μm thickness is required, which is quite hard to achieve with sputtering. Ni is patterned by forming PR molds that are patterned prior to electroplating and their removal after deposition. In order to form the PR molds the mask shown in Figure A.5 is used. Table 3.8 gives the details of the Ni deposition and patterning steps. As the first step, a seed layer of 200 Å/2000 Å Ti/Au layer is deposited as a seed layer for Ni electroplating. Then by photolithography, 18 μm thick PR molds are formed to define the empty patterns for depositing Ni on. Then, Ni is electroplated with the process settings of step G5 to

have an electroplated Ni pattern with a thickness of 9 μm . After cleaning the wafers, the PR mold is removed and Ti/Au layer is etched by using the already deposited Ni pattern as a mask.

Table 3.8. Process steps of Ni electroplating.

Nickel Mask	G1	Dehydration	Right before sputter, dehydrate 10 min. in oven @120°C Cool down in desiccator for 5 min.
	G2	Ti sputter (200 Å)	Endpoint thickness=75A, MFC1=2 sccm
	G3	Au Sputter (2000 Å)	Timer 2=180s (will be used), MFC1=6.2 sccm
	G4	Lithography	
	G4.1	Dehydration	Dehydrate 10 mins. in oven @120°C Cool down in desiccator for 5 mins.
	G4.2	PR Spin	AZ 9260 @900 rpm, t=30 s spin, (~18 μm aimed) + EBR with same settings
	G4.3	Air Dry	Dry in desiccator for 15 min. in horizontal position
	G4.4	Softbake	Softbake t=20 min. @100°C
	G4.5	Rehydration (relaxation)	Rehydrate 60 mins prior to develop with 5 pipette full of water in closed box (Humidity should be at least 50%)
	G4.6	Expose	Expose 55 s in vacuum contact
	G4.7	Develop	AZ 826 MIF, 15 min.
	G4.8	Hardbake	No
	G5	Ni Electroplating (9 μm)	T=50°C, $I_d=8.1 \text{ A/dm}^2$, $A=0.0033 \text{ dm}^2$ (FUC Series Ni mask), duty=0.04, $T_{on}=0.1 \text{ ms}$, $T_{off}=2.4 \text{ ms}$, $I_{avg}=0.012 \text{ A}$
	G6	Au Wet Etch	Au etchant 25-32 s.
	G7	Ti Wet Etch	Ti etchant, prepare 100 ml (80% H ₂ O+10% HF+10% H ₂ O ₂), 25 ml Ti etchant + 1575 ml DI H ₂ O, ~80 sec.
	G8	PR Strip	Acetone + IPA +DI Water.

After Ni electroplating a 1 μm parylene is deposited and patterned at the cantilever areas as a protection layer for Ni. For this purpose firstly, 1 μm parylene is deposited as in Step A and its lithography is carried out by the thick resist AZ 9260 as in Step F. After etching the parylene layer by RIE O₂, the wafers are cleaned. Table 3.9 shows the details of this step.

Table 3.9. Process steps of the 4th parylene layer.

Cantilever Mask			
Cantilever Mask	H1	Parylene Deposition (1 μm)	SP:25, PLA1:10, use A174-Silane (Protect backside by tape.)
	H2	Lithography	
	H2.1	Dehydration	Dehydrate 10 mins. in oven @120°C. Cool down in desiccator for 5 mins.
	H2.2	PR Spin	AZ9260 @900 rpm, , t=30 s (18 μm aimed) + EBR with the same settings.
	H2.3	Relaxation	Keep in desiccator in horizontal position for t=10 min.
	H2.4	Softbake	Softbake t=18 min. over contact hotplate @T=100°C
	H2.5	Expose	Expose 55 sec. (Vacuum contact)
	H2.6	Rehydration	Rehydrate 60 mins. prior to develop with 5 pipette full of water in closed box.
	H2.7	Develop	AZ826 MIF, 15 min.
	H3	Parylene Etch by RIE	30 + 30 mins. (~22 $\mu\text{m}/\text{min}$), O ₂ Plasma, 100 sccm, 100 mTorr, 100 Watt
	H4	PR Strip	Acetone + IPA + DI Water

After patterning the final parylene layer, the wafers are etched from the backside by DRIE to release the devices. Table 3.10 shows the process flow details of this step. The backsides of the wafers are masked by 18 μm thick AZ9260 with similar

lithography steps to those of Steps F, G and H. The main difference is that the wafers are aligned to the mask shown in Figure A.6 by backside alignment, and at the end of lithography, the edge beads are reconstructed manually to prevent etching of the outer circumferences of the wafers. Afterwards, the wafers are attached to handle wafers by thermal (cool) grease (CGR 7016 from AI Technology Inc.), as a thermal interference material to improve the thermal conduction between the two wafers. Then backside SiO₂ is removed in RIE under 100 mTorr pressure, 300 W of power, chiller temperature set to 20°C and gas flows set as 12 sccm for CF₄ and 38 sccm for CHF₃. Right after this procedure, exposed Si is etched from the backside up to the front side SiO₂. This etching step is carried out in STS DRIE tool and it takes about 100 min. to finish the through etch of a single wafer. Afterwards, the front side SiO₂ is etched in 5:1 BHF solution of 500 ml NH₄F (ammonium fluoride) + 100 ml HF (hydrofluoric) acid. Finally, the process is completed with the release of the devices by keeping them in acetone for one day. The fabrication process steps from A to J are given in a continuous manner in Appendix C for convenience.

Figures 3.9 through 3.12 show the photos of the fabricated devices. The photos show the designs just before the release steps. The release step is the DRIE process detailed in Step J above.

Table 3.10. Process steps backside through etch of Si.

DRIE Mask	J1	Backside lithography	
	J1.1	Dehydration	Dehydrate 10 min. in oven @120°C, Cool down in desiccator for 5 min.
	J1.2	PR Spin	AZ 9260 @900 rpm, t=30 s spin, (~20 µm aimed)
	J1.3	Relaxation	Dry in desiccator for 15 min. in horizontal position
	J1.4	Softbake	Softbake 20 min. @100°C
	J1.5	Rehydration	Rehydrate 60 mins prior to develop with 5 pipette full of water in closed box.
	J1.6	Expose	Expose 65 s in vacuum contact
	J1.7	Develop	AZ 826 MIF, 15 min.
	J1.8	Reconstruct EB at the backside	Reconstruct edge bead at the back with AZ9260 @750 rpm (spin PR to the edge only), wait 5 mins., softbake @100°C, t=5 mins., cool down in desiccator
	J2	Attachment of handle wafer	Attach handle wafer to the process wafer by thermal gress over hot plate @115°C
	J3	Backside SiO ₂ etch by RIE	Use the DRIE mask, 100 mTorr, 300 W, Chiller Temp.=20°C, CF ₄ =12 sccm, CHF ₃ =38 sccm, t=~6 mins.
	J4	Backside Si etch by DRIE	About 100 mins.
	J5	Frontside SiO ₂ etch by RIE	Use the DRIE mask, 100 mTorr, 300 W, Chiller Temp.=20°C, CF ₄ =12 sccm, CHF ₃ =38 sccm, t=~6 mins.
	J6	Frontside SiO ₂ wet etch	Buffered HF (BHF), 5:1 (500 ml NH ₄ F + 100 ml HF), ~10 mins.
	J7	Release	Keep the wafer in acetone about one day.

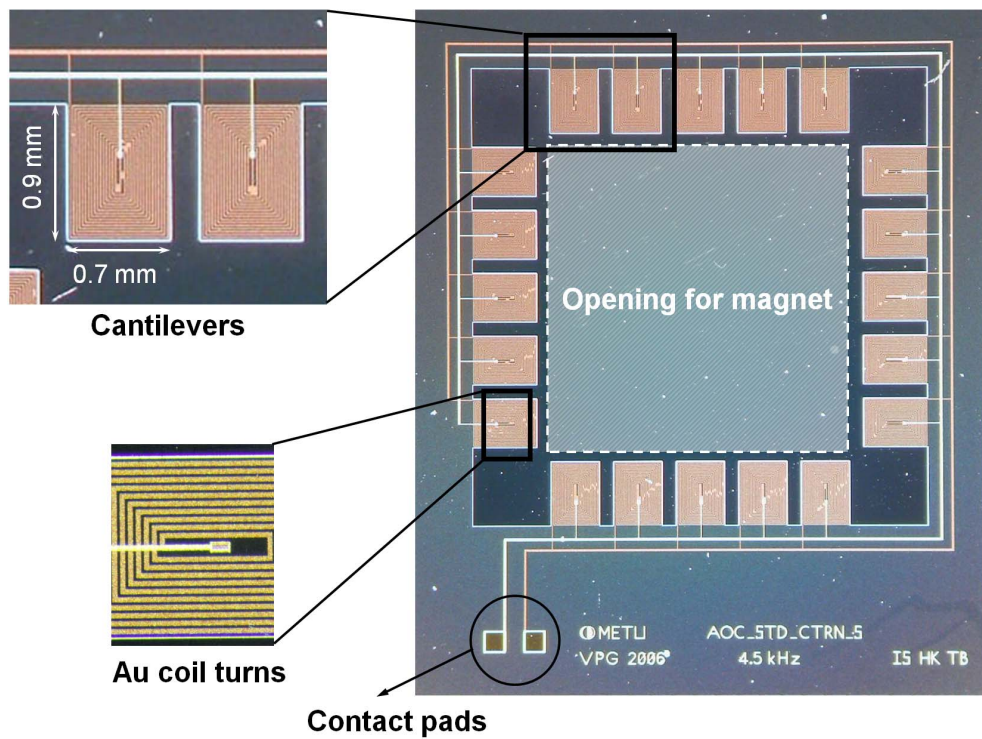


Figure 3.9. Photo of the AOC design just before release.

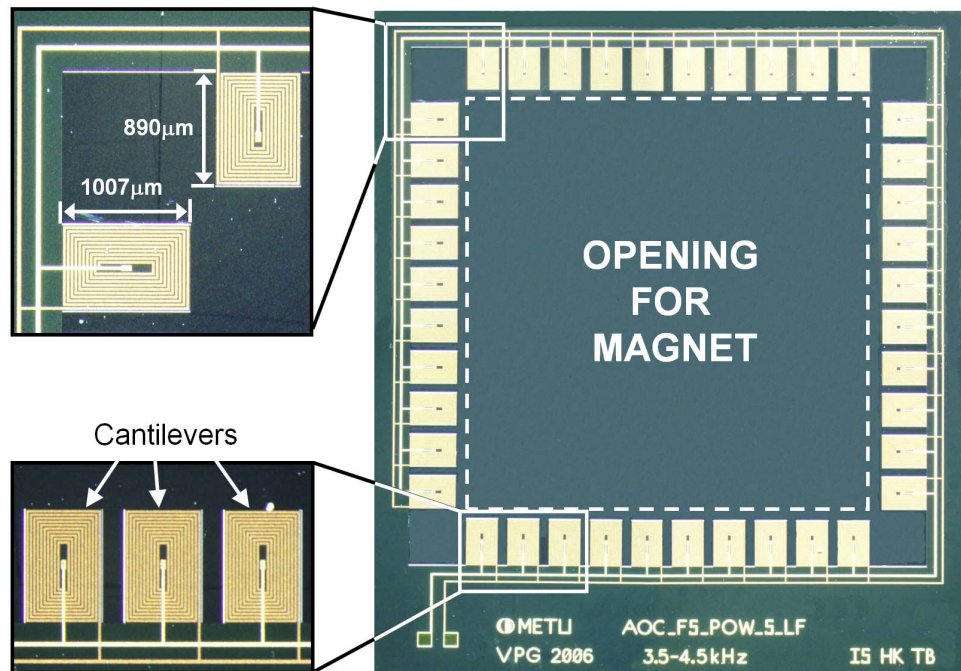


Figure 3.10. Photo of the AOC_FS design just before release.

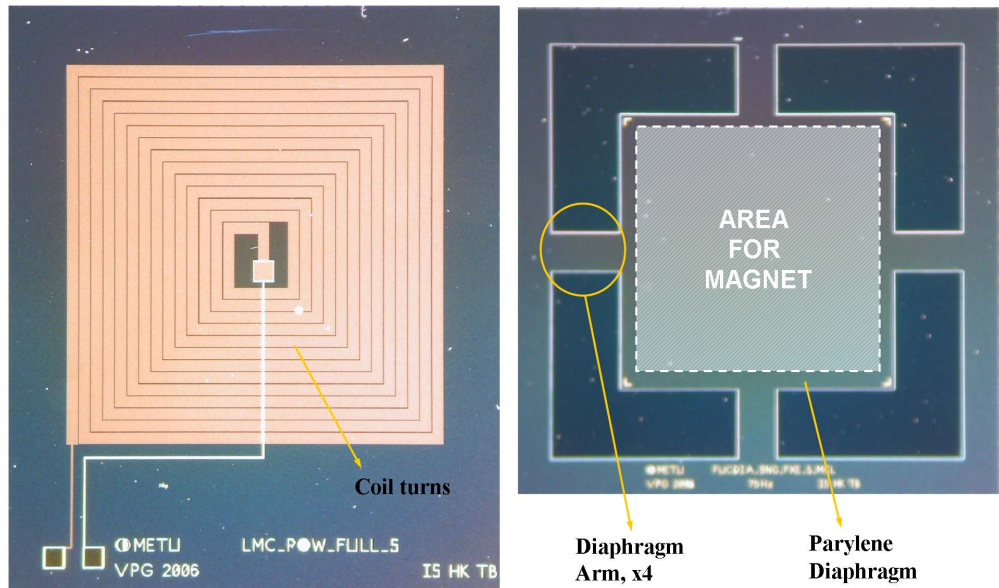


Figure 3.11. Photo of the LMC design base (left) and diaphragm (right).

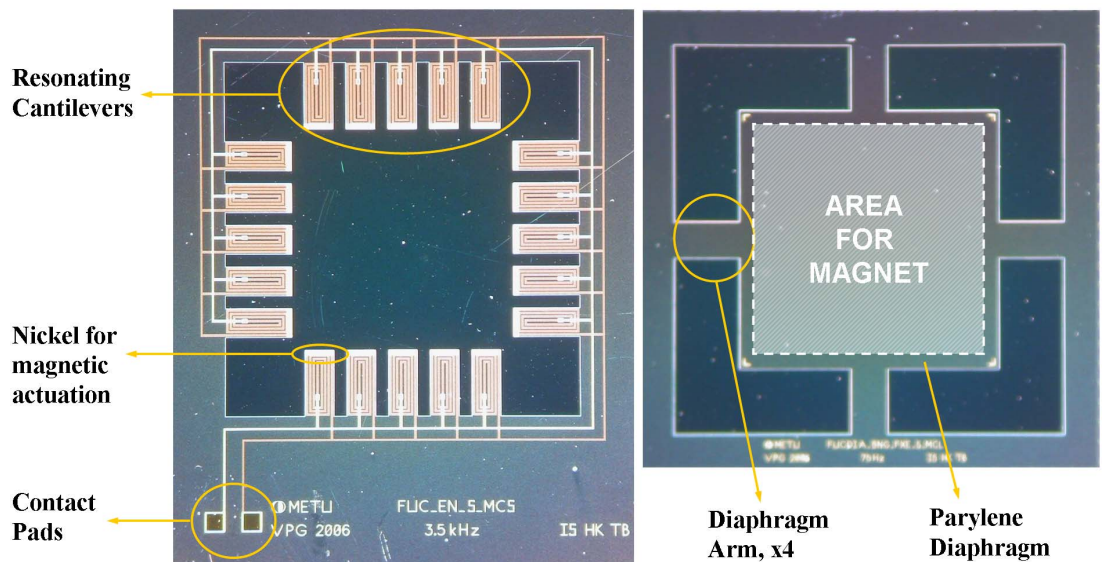


Figure 3.12. Photo of the FUC design base (left) and diaphragm (right).

3.7 Conclusions

In this chapter the microfabrication steps of the proposed generators has been presented in detail. The properties of each design in term of fabrication are explained. This is followed by the description of generalized fabrication steps with all process parameters. Although different designs have been proposed, their fabrication steps are designed such that all of them can be fabricated on the same wafer using the same fabrication steps. This lets all of the devices to be available for testing right after release. The chapter is finalized with the photos of the devices just before the release step. After fabrication, the devices are tested for performance, which is the topic of the next chapter.

CHAPTER 4

TEST OF THE MICRO GENERATORS

In this chapter, the test results of the designed and fabricated micro generators are presented. The chapter starts with the description of the test setup and continues with the presentation of individual test results of the proposed designs. The test results are then compared with the estimated results obtained by simulations and deviations are explained with mathematical and/or extra tests where applicable.

4.1 Test Setup

The fabricated micro generators are tested using a vibration shaker system purchased from Brüel&Kjaer. Figure 4.1 shows the schematic diagram (upper) and corresponding photos (lower) of the shaker system that is composed of a shaker table, a control unit, an amplifier, an accelerometer and software interface. Desired control input values, such as acceleration, velocity and displacement levels, operation frequency range, and other settings are all entered to the system through a user interface running on a computer. The software then downloads these operation parameters to the main control unit that runs the shaker table at the desired modes and levels of operation. The command signals from the controller are amplified before being transmitted to the shaker table by an amplifier unit. In order to run the shaker table in a closed loop manner, operation acceleration and frequency levels are measured continuously by an accelerometer and fed back to the controller unit. Important properties of the shaker system are shown in Table 4.1. Tests can be carried out in a frequency range of 10 Hz to 20 kHz and up to a bare table acceleration of 75 g with a maximum force rating of 45 N.

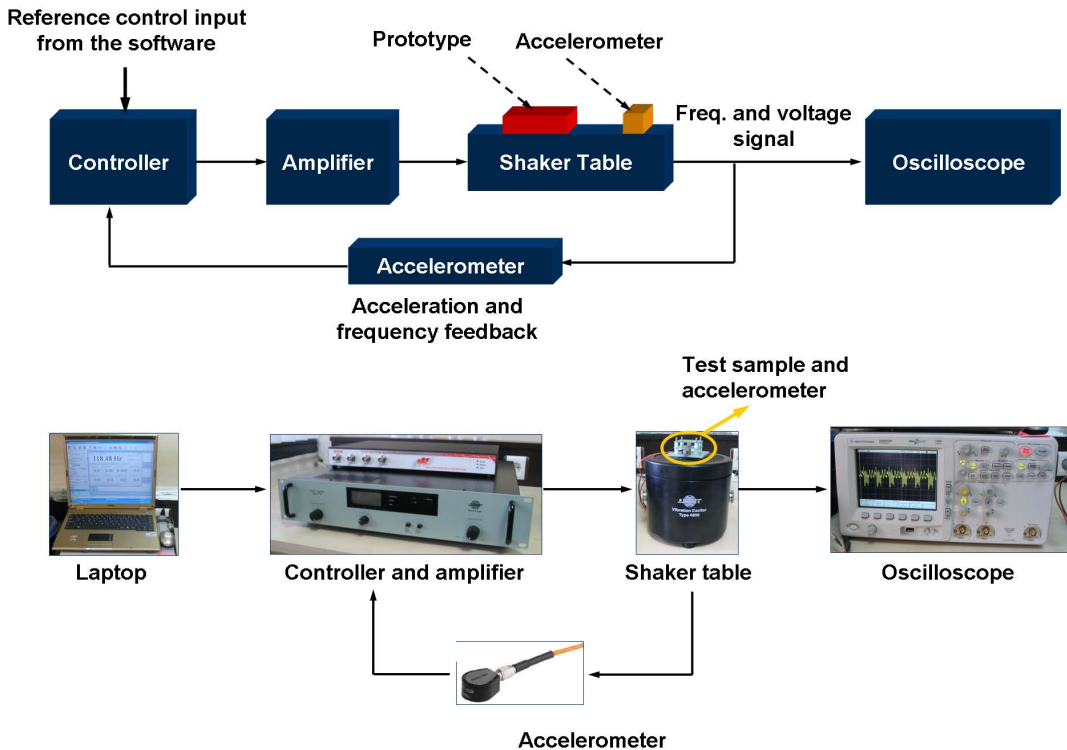


Figure 4.1. Block diagram of the test setup and photos of the components.

Table 4.1. Important properties of the shaker system.

Shaker table brand and model	Brüel & Kjaer, 4809, Vibration exciter
Controller model	VR-8500-1, VibrationVIEW
Amplifier model	2718, Power amplifier
Accelerometer	4517-002, Miniature accelerometer
Control software	VR-610, SineVIEW
Shaker table dimensions and weight	149 mm diameter, 143 mm height and 8.3 kg
Frequency range	10 Hz to 20 kHz
Acceleration	75 g max. (Bare table)
Force rating	45 N
Control methods	All programmable sinusoidal acceleration, velocity and displacement sweep modes of operation.

4.2 The Tests of the Array of Cantilever (AOC) Design

The array of cantilever (AOC) design has identical resonance cantilevers designed to operate effectively mainly at the resonance frequency of the cantilevers. Before testing, the fabricated array of cantilever (AOC) chip is attached to a printed circuit board (PCB) by epoxy. The printed circuit board (PCB) has a custom layout for each design and is used mainly to have the contacts on the devices wire bonded to larger areas for practical use. The PCB is then fixed to the shaker table by using a coupling base, which enables it to be tightened directly to the shaker table by screws. Figure 4.2 shows the test sample attached to the PCB with the close-up view of the prototype (lower-right) and the cantilevers (upper-right).

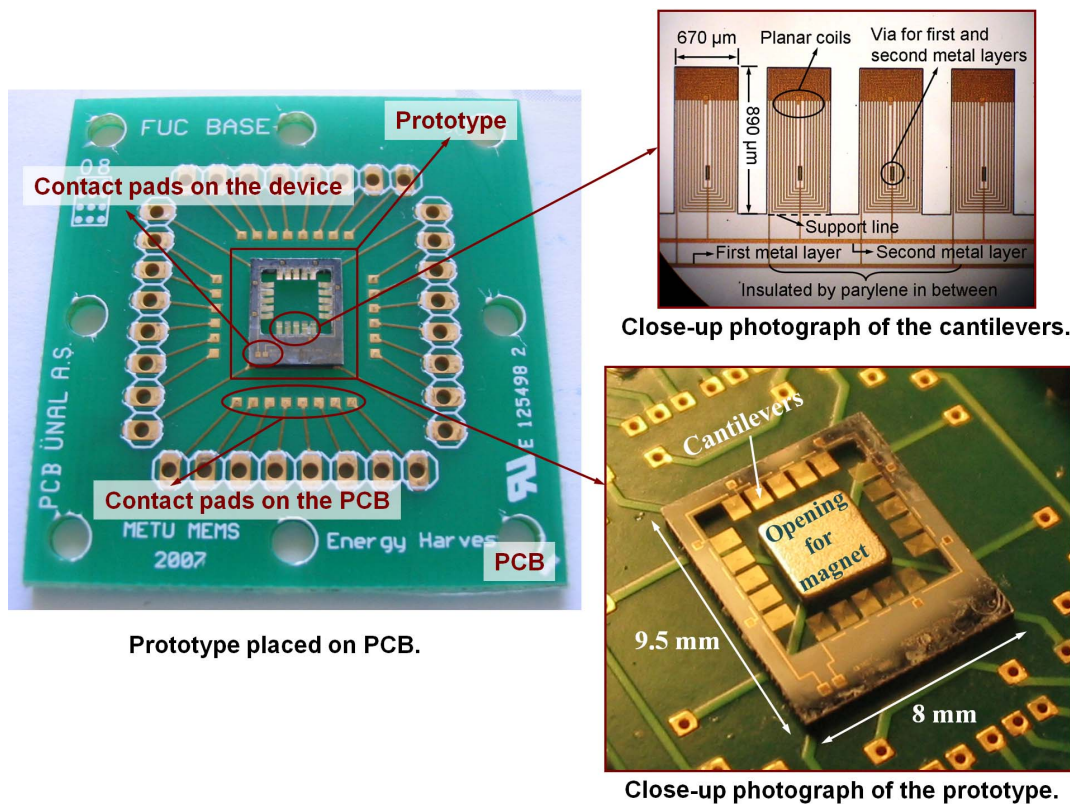


Figure 4.2. Photograph of the AOC design attached to the PCB (left) with close-up view of the prototype (lower-right) and the cantilevers (upper-right).

A rare earth type, neodymium-iron-boron (NdFeB) magnet with dimensions 6 x 6 x 6 mm³ is attached to a holding base in the same manner using an epoxy. This type of magnet is used as it has a higher magnetic flux density compared to other type of commercially available ones. The used magnets are N42 grade having a residual magnetic flux density of about 1.2 Tesla. Spacers are used to adjust the spacing between the magnet assembly and the printed circuit board (PCB) base holding the sample. Figure 4.3 shows the photographs of the printed circuit board (PCB) base, magnet assembly, spacers and nuts.

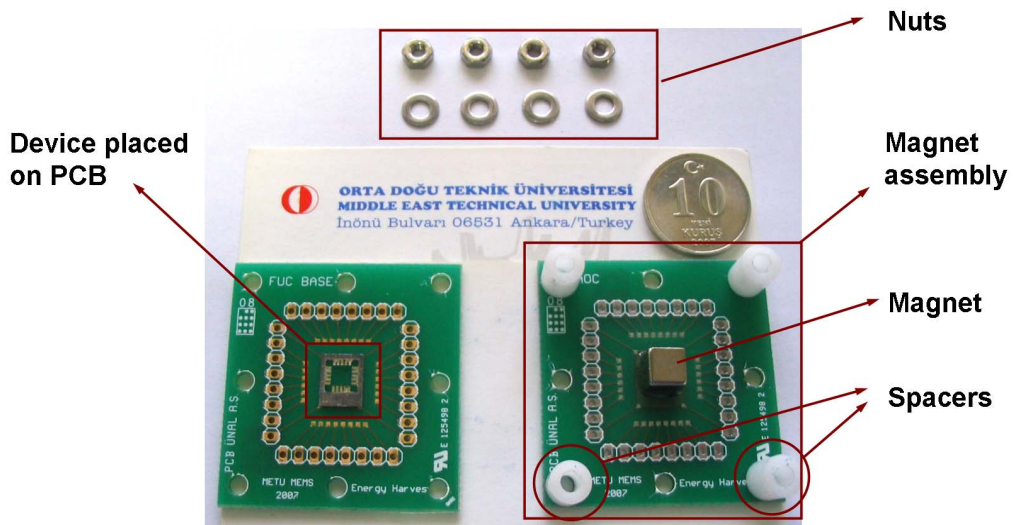


Figure 4.3. Photographs of the PCB base, magnet assembly, spacers and nuts.

Figure 4.4 shows the assembling steps of the sample to the coupling base and the magnet assembly. First of all the sample attached to the printed circuit board (PCB) is placed on the coupling base through four M3 screws (a and b). Then the spacers are passed through these screws and magnet assembly is placed on the resulting structure (c). The screws are tightened by corresponding nuts to make the assembly rigid.

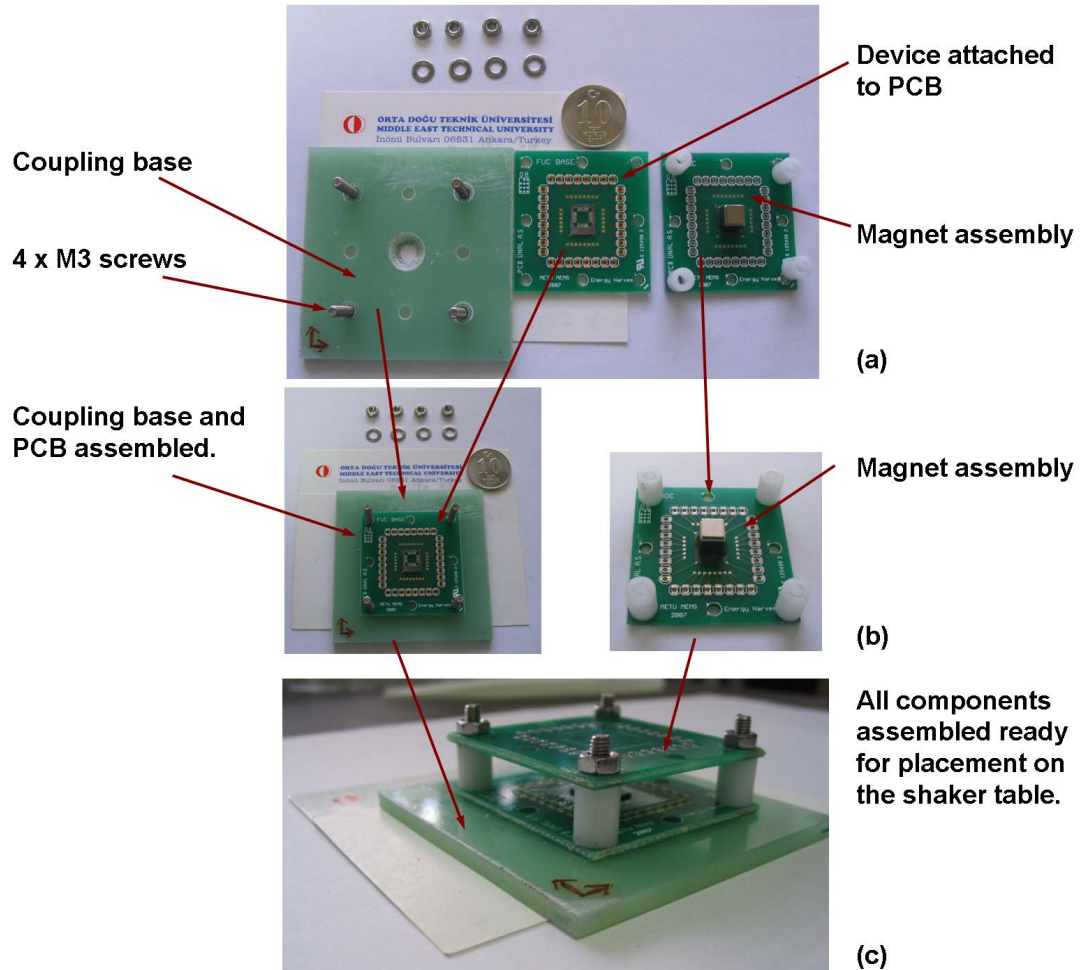


Figure 4.4. Assembling procedure of the components of the test sample.

Finally, the test sample is mounted on the shaker table using a M5 hole at the center of the shaker table. Figure 4.5 shows the photograph of the mounted test sample to the shaker table. The prototype is ready to be tested after this point.



Figure 4.5. Assembled sample mounted on the shaker table.

The test of the array of cantilever (AOC) design is carried out by sweeping the frequency from 3 to 6 kHz at a constant acceleration of 45 g. Table 4.2 shows the test results for a single cantilever of the array of cantilever (AOC) together with the simulation results obtained in Chapter 2. A maximum peak voltage output of 0.67 mV is generated at a vibration frequency of 3.4 kHz and an acceleration of 45 g that corresponds to an input displacement of 0.97 μm from a **single cantilever** of the prototype. The estimated peak voltage output from a single cantilever is 0.72 mV. It follows from (2.34) that the maximum voltage output at resonance can be approximated by the following equation,

$$|e_{\max @ \omega \approx \omega_n}| \approx \frac{BL_p \omega_n Y}{2\zeta_{eq}} \quad (4.1)$$

From Table 4.2 it can be seen that the estimated and measured values for the natural frequency, input displacement, and equivalent damping ratio are close. Thus, the main source of error is due to the estimation of the magnetic flux density, which is a nonlinear quantity and hard to estimate exactly. The practical coil length is a virtual quantity that cannot be measured, but it is assumed that it is estimated correctly.

Table 4.2. Simulation and test results for a single cantilever of the AOC design.

	Simulation	Test
Operation medium	Air	Air
Input vibration frequency	3.4 kHz	3.45 kHz
Input displacement	1 μm	0.97 μm
Magnet type	NdFeB (1.18 T)	NdFeB (1.18 T)
Magnet size	6 x 6 x 6 mm ³	6 x 6 x 6 mm ³
Device dimensions	9.5 x 8 x 6 mm ³	9.5 x 8 x 6 mm ³
Cantilever dimensions	890 x 670 x 12 μm^3	890 x 670 x 12 μm^3
Cantilever structural material	Parylene C	Parylene C
Natural frequency of the cantilevers	3.4 kHz	3.45 kHz
Bandwidth of cantilevers	140 Hz	140 Hz
Total number of cantilevers	20	20
Damping ratio of the cantilevers	0.020	0.022
Distance between cantilevers to magnet	500 μm	500 μm
Magnetic flux density	0.24 Tesla	Not measured.
Coil metal width	10 μm	10 μm
Coil thickness	0.1 μm	0.1 μm
Coil resistance (single cantilever)	680 Ohm	750 Ohm
Number of coil turns	16	16
Total coil length (single cantilever)	29.4 mm	Not measured.
Practical coil length (single cantilever)	5.8 mm	Not measurable.
Peak power output from a single cantilever	75 pW/cantilever	56 pW/cantilever
Peak voltage output from a single cantilever	0.72 mV/cantilever	0.67 mV/cantilever

After testing a single cantilever, 4 consecutive cantilevers are tested for performance. Figure 4.6 shows the overall voltage output from **4 consecutive cantilevers** of the generator with respect to excitation frequency.

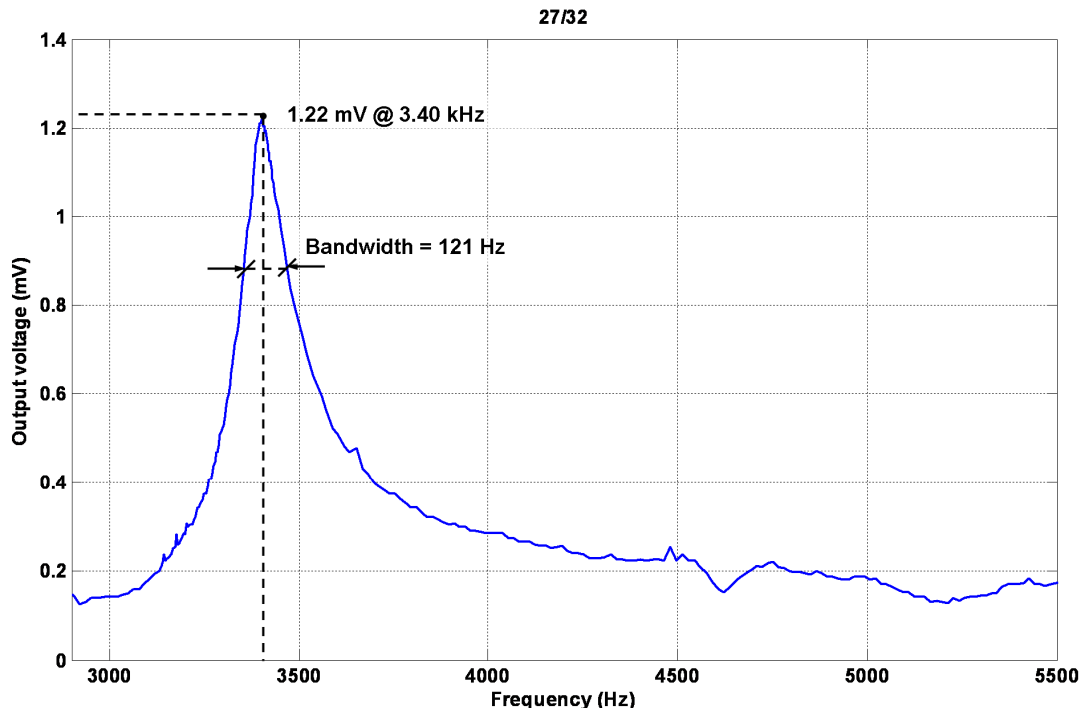


Figure 4.6. Measured voltage output from 4 consecutive arms of the generator.

A maximum peak voltage output of 1.22 mV is generated at a vibration frequency of 3.4 kHz from these 4 arms. The bandwidth of the generator is 121 Hz with a damping ratio of 0.022. The decreasing trend of the output voltage after resonance is due to the free ‘ ω ’ term in the denominator of the *steady state* voltage equation that is derived for constant acceleration by the help of (2.34).

$$\varepsilon_{ss} = -BL_p \frac{A}{\omega} \quad (4.2)$$

Although the estimated and measured voltages from a single cantilever match, the overall voltage output from 4 consecutive cantilevers is **not 4 times** the output from a single cantilever. This is due to the variation between the natural frequencies of the cantilevers that results in phase shift between the outputs of each cantilever degrading the overall output. Figure 4.7 shows the phase angle between the displacement input and voltage output of the generator with respect to frequency for various values of damping. From the given plot, it can be seen that, especially for low values of damping, the phase angle changes rapidly around resonance.

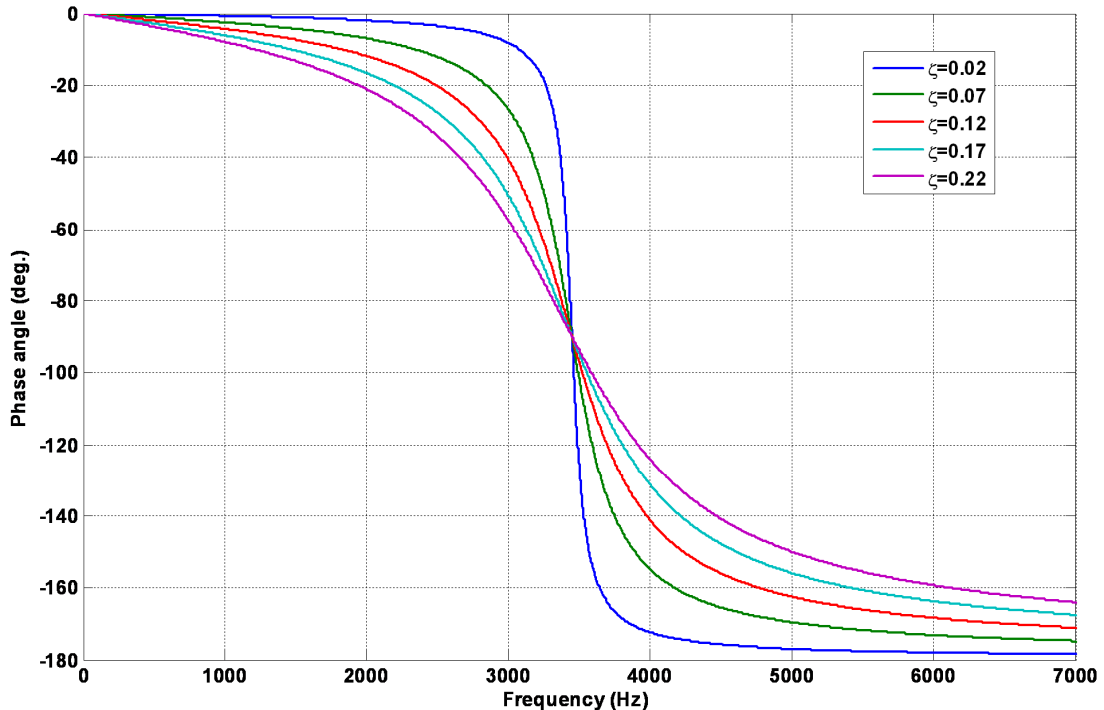


Figure 4.7. Phase angle plots for various values of damping.

In the actual case, the damping ratio is, $\zeta=0.02$ and Figure 4.8 shows the close-up view of the phase angle for this value of the damping ratio. Form the given plot, it can be seen that, for example a difference of 100 Hz in the natural frequency of two cantilevers would cause a phase angle difference of 75° . Considering that the outputs

are sinusoidal, at a phase angle difference of 180° , the outputs would completely cancel out each other. Thus, a phase angle difference of 75° is actually quite high.

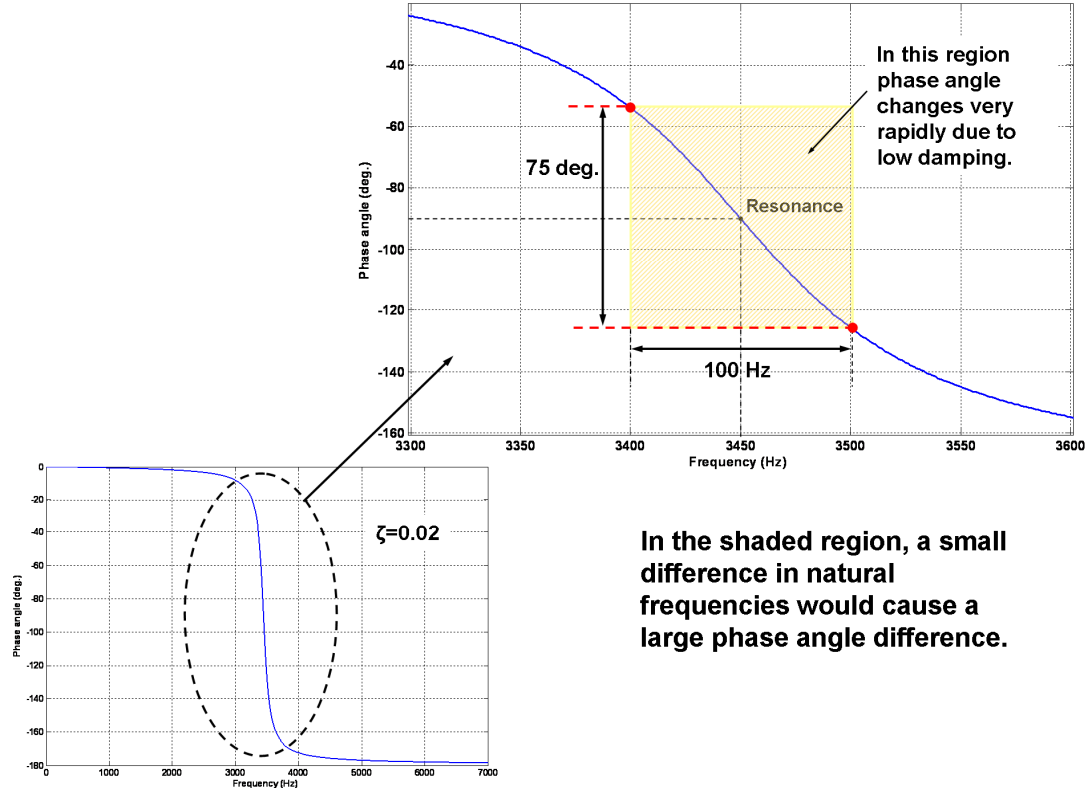


Figure 4.8. Close-up view of phase angle for $\zeta=0.02$.

In order to investigate and show the amount of phase angle difference in the measured results, the sinusoidal overall voltage output from a single cantilever and 5 consecutive cantilevers are shown in Figure 4.9. Both outputs are recorded exactly at the same time interval. Figure 4.10 is the close-up view of Figure 4.9 for further analysis. From Figure 4.10, it can be seen that, there is indeed a time difference of $20 \mu\text{s}$ between the occurrence of each signal corresponding to a phase angle difference of 24° , which is calculated from,

$$\Delta\varphi = \omega_n \Delta t \quad (4.3)$$

where $\Delta\phi$ is the phase angle difference between the outputs and Δt is the time difference.

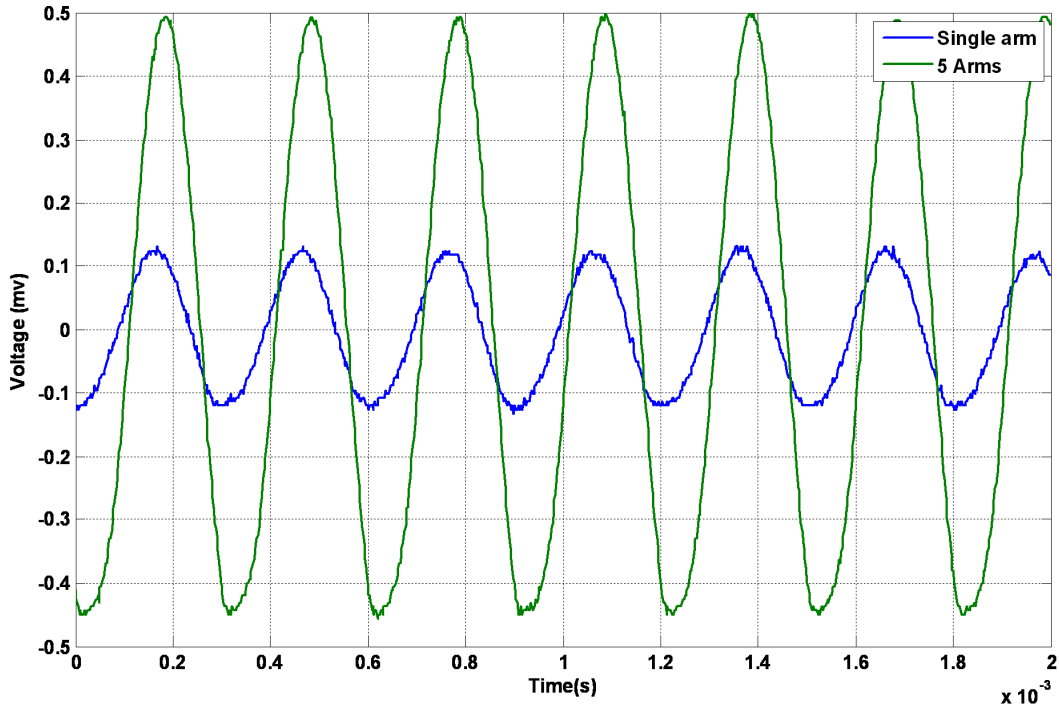


Figure 4.9. Voltage output of a single cantilever and 5 consecutive cantilevers.

From Figure 4.10 it can also be calculated that there is a difference of 17 Hz between the natural frequencies of the signals. This difference together with the phase difference of 24° is compatible with the phase angle plot given in Figure 4.8.

Figure 4.11 and 4.12 show another example of phase angle difference. Again Figure 4.12 is the close-up view of Figure 4.11. In this case, the phase angle difference is more, having a value of 46° . There is also a natural frequency difference of 25 Hz between the signals. As a result, even a deviation of 0.75 % from the nominal value of the natural frequency of 3.33 kHz makes a quite much phase angle difference of 46° .

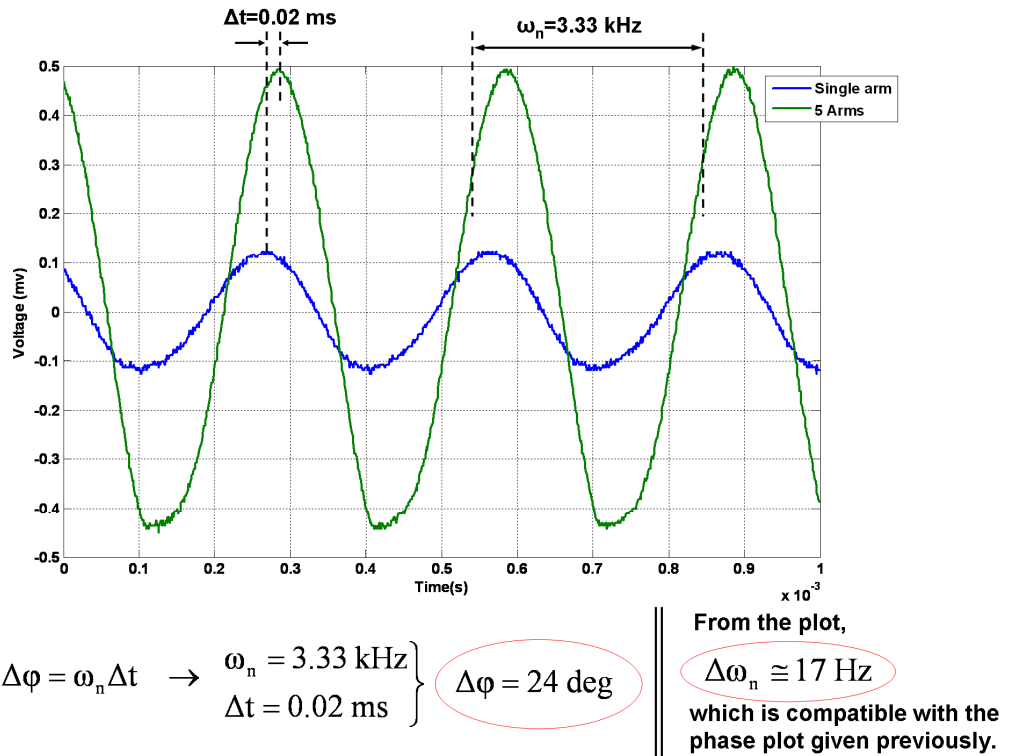


Figure 4.10. Zoomed in view of Figure 4.9 for further analysis.

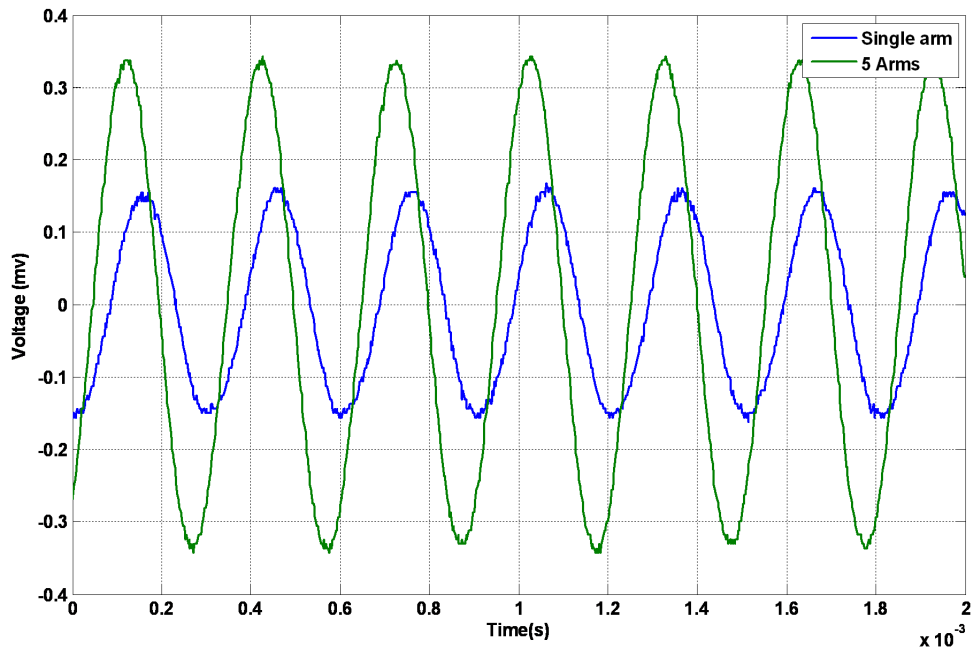


Figure 4.11. Voltage output of a single cantilever and 5 consecutive cantilevers.

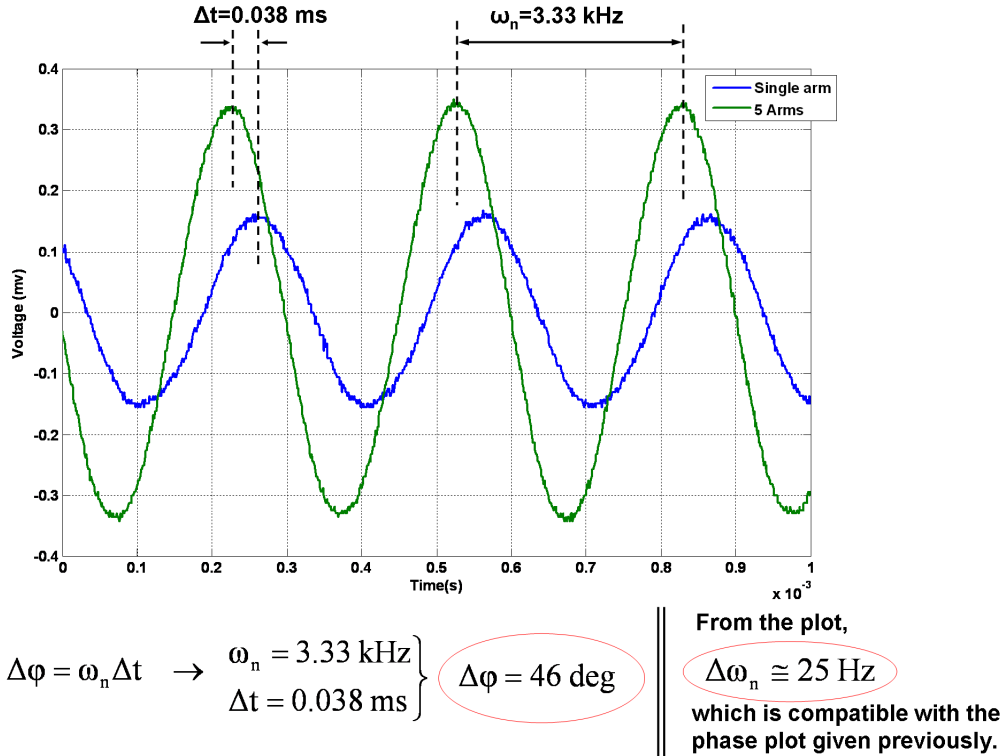


Figure 4.12. Zoomed in view of Figure 4.11 for further analysis.

The main cause of the difference in the natural frequencies of the cantilevers is due to thermal (cool) grease (CGR 7016 from AI Technology Inc.) residues remaining at the final step of the fabrication procedure. This substance is used to attach the process wafer to a handle wafer to improve thermal conduction during the DRIE step. However, it is quite hard to clean it afterwards, which results in residues remaining on the cantilevers. These remains change the effective mass and thus the natural frequency of the cantilevers and cause the overall output from the generator to degrade. Figure 4.13 shows the thermal grease residues remaining on the wafer after the release of the devices. Even after a detailed cleaning of the wafers in acetone, IPA, and methyl-ethyl-ketone (MEK), which are all known solvents for thermal grease, residues can still be observed. Piranha cleaning is also an alternative, but this solution would also etch the Ni deposited in the previous steps. No further

cleaning is possible due to thin cantilever layers that may be damaged very easily in any further clean-up process.

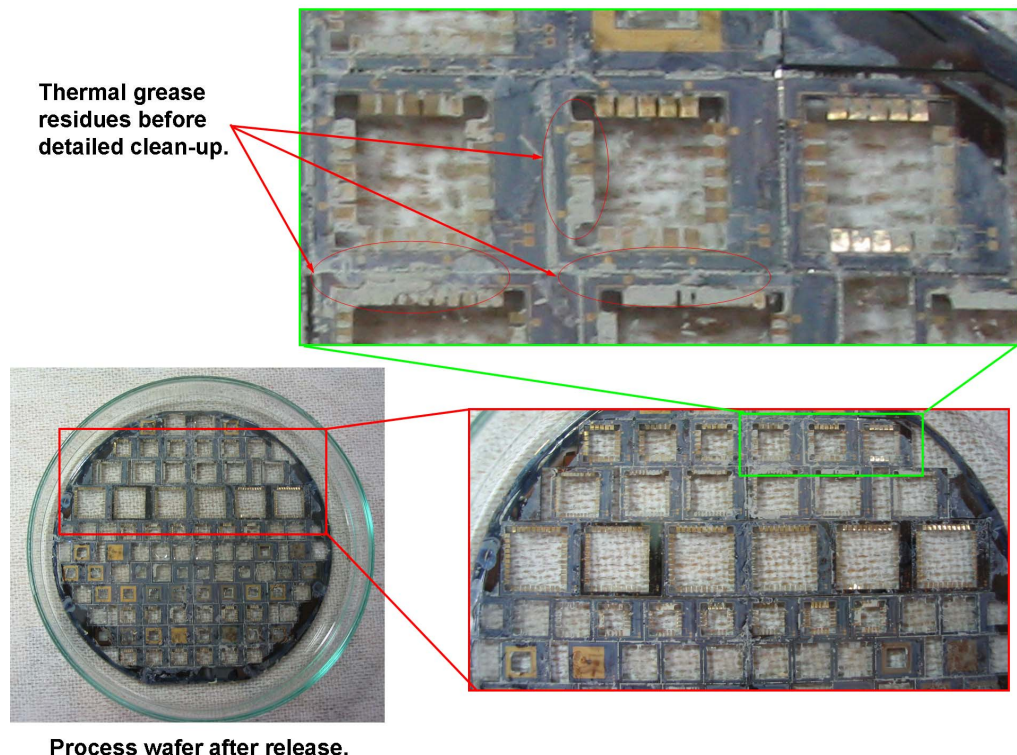


Figure 4.13. Thermal grease residues remaining on the cantilevers after release.

Table 4.3 shows the amount of necessary deviation between the mass of two cantilevers that would create corresponding natural frequency difference given in Figures 4.10 and 4.12. It has been calculated that a single cantilever has an equivalent lumped mass of about $2.174 \mu\text{g}$. For a difference of 25 Hz between the natural frequencies, a mass deviation of $0.0326 \mu\text{g}$ (32.6 pg) is necessary. The mass density of thermal grease is 1.6 g/cm^3 and the above deviation can be created by a residue of size about $50 \times 50 \times 5 \mu\text{m}^3$ that can easily be done when the cantilever and residues' dimensions are compared.

Table 4.3. Necessary variation required in equivalent mass term to cause the corresponding change in natural frequency.

Reference Figure #	$\Delta\omega_n$ (Hz)	$(\omega_{n1}/\omega_{n2})^2$	$\Delta m_{eq}(\text{cant.})$ $(m_{eq}(\text{cant.})=2.174 \mu\text{g})$	Cantilever dimensions	Corresponding residue dimensions
4.10	17	1.010	21.7 pg (0.0217 μg)	890 x 670 x 12 μm^3	50 x 50 x 5 μm^3
4.12	25	1.015	32.6 pg (0.0326 μg)	890 x 670 x 12 μm^3	64 x 64 x 5 μm^3

In conclusion, the test of the array of cantilevers (AOC) design has been carried out and the test results are compared with the estimated simulation results. Although single cantilever results match, there seems to be a deviation between the simulation and test results of multiple cantilevers, which is mainly due to the phase angle difference between the cantilevers that degrades the overall output. This is mainly caused by the thermal grease residues remaining that can not be fully cleaned on the cantilevers. These remains change the effective mass and thus the natural frequency of the cantilevers causing the overall output to degrade. Actually in the literature, problems caused by thermal grease residues after the through etch of Si wafers by DRIE is a known problem. There is not an effective alternative solution to this problem, but it might be beneficial to replace it with an equivalent substance that can be cleaned more easily such as Cool Pad CP 7506 from AI Technology, Inc. or Crystal Bond 555 HMP from SPI Supplies and Structure Probe, Inc.

4.3 The Tests of the Array of Cantilevers Design with Varying Natural Frequencies (AOC_FS), “The Frequency Sweeper”

The next design that the performance tests are carried out is the array of cantilevers design with varying natural frequencies (AOC_FS) as in the order of appearance in the text. As explained in detail in Chapter 2, the main difference of this design from the array of cantilevers (AOC) design is that it has cantilevers with varying length from 890 to 1007 μm to create a variation in the natural frequency of the cantilevers

to increase the bandwidth of the generators. Figure 4.14 shows the fabricated prototype of the array of cantilevers design with varying natural frequencies (AOC_FS) right after release.

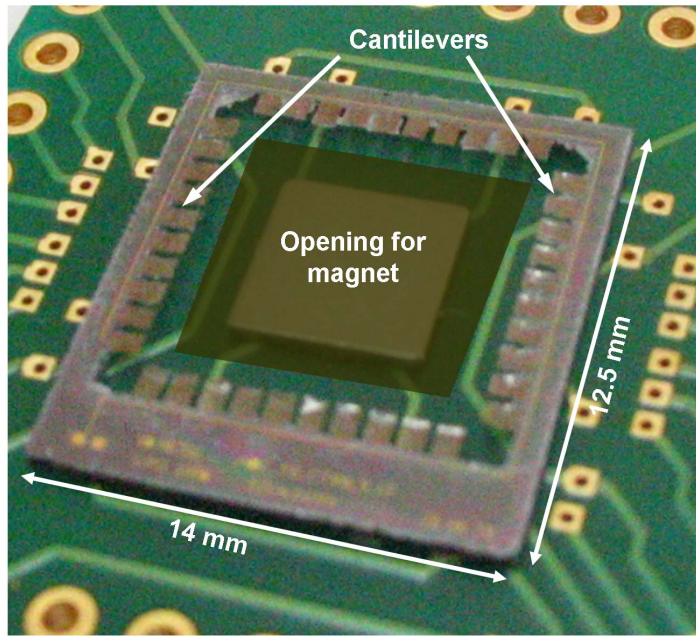


Figure 4.14. Photograph of the AOC_FS design after release.

The test setup and the way the test sample attachment to the shaker table is the same as the array of cantilevers (AOC) design, so these steps will not be repeated here. The only difference is that, in this case a $8 \times 8 \times 8 \text{ mm}^3$ sized magnet is used since the area of the array of cantilevers design with varying natural frequencies (AOC_FS) design is larger than the array of cantilevers (AOC) design. Table 4.4 lists the simulation and test results for the proposed AOC_FS design. The tests are carried out by sweeping the frequency from 2.5 to 6 kHz, at a constant acceleration of 45 g and for various combination of number of cantilevers, i.e. for 20, 35 and 40 cantilevers. Thus, the result obtained from each set is different. Individual results are investigated in the following paragraphs with supporting plots obtained from tests.

Table 4.4. Simulation and test results for the AOC_FS design.

	Simulation	Test
Vibration amplitude (const. acceleration)	45 g	45 g
Natural freq. of cantilevers	3.5-4.5 kHz	3.5-4.5 kHz
Number of cantilevers	40	20, 35 and 40
Cantilever material	Parylene C	Parylene C
Cantilever dimensions	(890-1007) x 670 x 15 μm^3	(890-1007) x 670 x 15 μm^3
Cantilever length increments	3 μm	3 μm
Device dimensions	14 x 12.5 x 8 mm ³	14 x 12.5 x 8 mm ³
Magnet type	NdFeB (1.18 T)	NdFeB (1.18 T)
Magnet dimensions	8 x 8 x 8 mm ³	8 x 8 x 8 mm ³
Distance between cantilevers to magnet	500 μm	500 μm
Magnetic flux density	0.4 Tesla	Not measured.
Damping ratio	0.02	0.022
Number of coil turns	10	10
Coil length	19.6-21.9 mm	Not measured.
Practical coil length (single cantilever)	2.9-3.0 mm	Not measurable.
Coil metal width	20 μm	20 μm
Coil thickness	0.1 μm	0.1 μm
Coil resistance (single cantilever)	110 Ω	200 Ω
Overall bandwidth of cantilevers	1 kHz	0.5 to 1 kHz in various tests (see related plots below)
Estimated maximum power (from all 40 cantilevers)	2.7 nW	0.2 to 1.7 nW in various tests
Estimated maximum voltage (from all 40 cantilevers)	9 mV	3 to 9 mV in various tests (see related plots below)

From the data of given in the table above, it can be seen that a maximum voltage output of 3 to 9 mV can be obtained from the overall device corresponding to an overall voltage output of 0.2 to 1.7 nW, respectively. Figure 4.15 shows peak voltage output plot of the AOC_FS design for 20 cantilevers together with the output from a single cantilever.

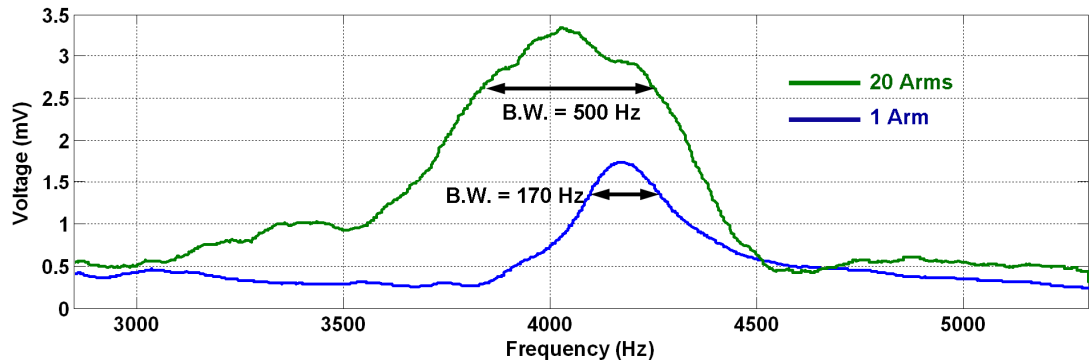


Figure 4.15. Voltage output from 20 cantilevers and comparison of bandwidth with a single cantilever.

The overall bandwidth of 20 cantilevers is 500 Hz, which is compatible with the estimations and a 3 fold improvement has been made in the bandwidth of the generator compared to a single cantilever. The overall voltage output is not 20 times the output from a single cantilever since only the cantilevers around corresponding resonance are active at each frequency interval. Figure 4.16 shows the test result from another AOC_FS test sample. In this case, all 40 cantilevers are used for testing. The overall peak voltage output from the prototype is about 9 mV as estimated, but the bandwidth of the generator is around 500 Hz, half of what is actually estimated by simulations. The deviation is most probably due to deviation in the designed natural frequencies as explained in the previous section.

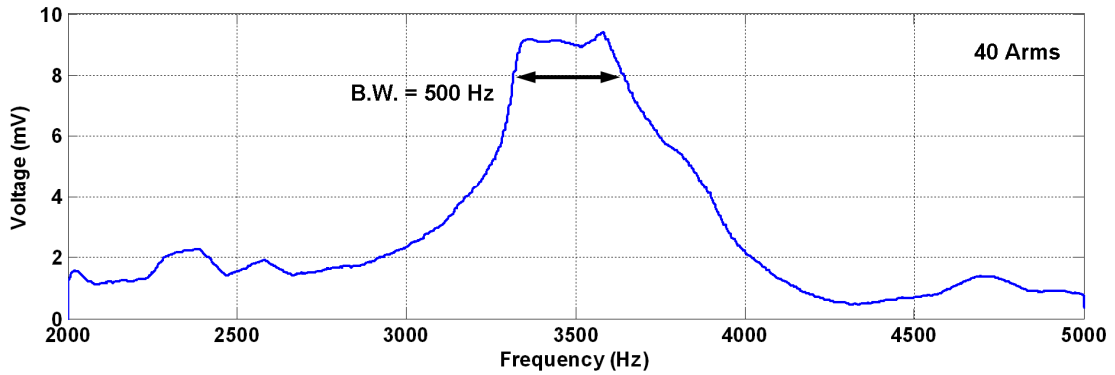


Figure 4.16. Overall voltage output from all 40 cantilevers of the AOC_FS.

Figure 4.17 is the test result from another prototype in which 35 arms of the device are used. In this case, the overall measured peak voltage output from the device is 5 mV whereas the bandwidth is 800 Hz. These values are close to what is estimated by simulations considering the number of cantilevers used.

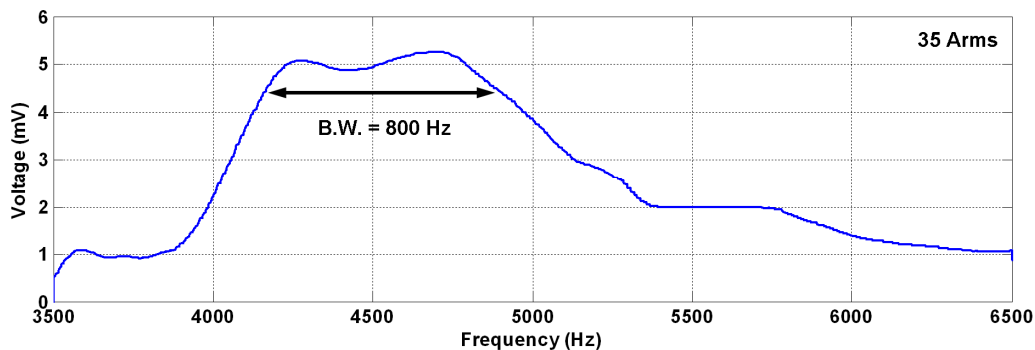


Figure 4.17. Measured voltage output from 35 cantilevers of the AOC_FS.

The final plot that is going to be investigated here is shown in Figure 4.18. In this case, all 40 arms are used and an overall bandwidth of 1 kHz is obtained. The overall voltage output is low compared to estimated results due to phase angle difference between the cantilevers. The main cause of this difference is due to

thermal grease residues remaining after fabrication, which is investigated in detail in the previous section.

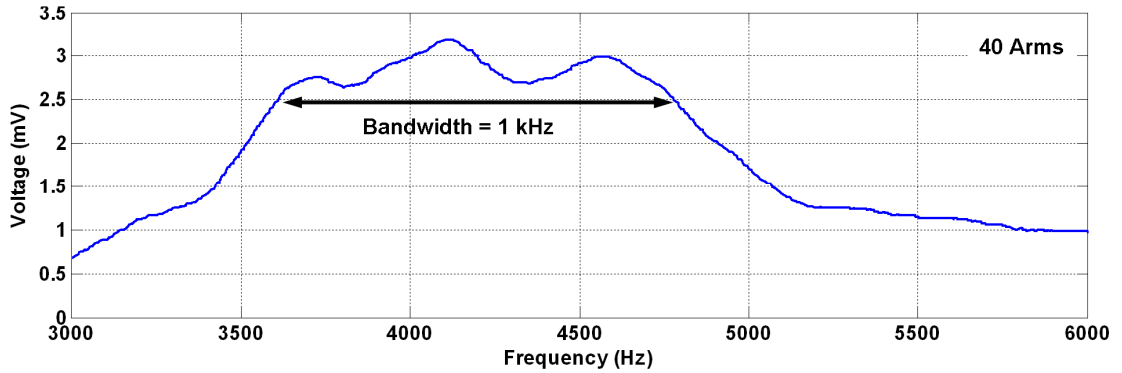


Figure 4.18. Measured voltage output from 40 cantilevers of the AOC_FS.

4.4 The Tests of the Array of Cantilevers Design with Varying Natural Frequencies (AOC_FS) as an Energy Harvesting Frequency Sensor

In Chapter 2, it has been conceptually shown that the AOC_FS design can also be used as an energy harvesting frequency detector. Within the scope of this thesis study, initial tests of such a structure have also been made to show the validity of the proposed structure. For detailed explanation of the design and its operation principle of this device, Section 2.3 may be referred. Figure 4.21 shows the block diagram of the frequency sensor that is already given in Section 2.3 and repeated here for convenience. In this work, a basic discrete component, programmable circuit is implemented for the proof of the concept. This circuit consists of an amplifier and a Programmable Integrated Controller (PIC). The amplifier amplifies and converts the input signal from the AOC_FS design to a square wave. Afterwards, the resulting square wave is amplified and processed by the code running on the PIC. The code counts the pulses per second and converts this information to frequency, which in turn is displayed at each successive cycle. The use of PIC gives the flexibility to run any desired code without changing the circuitry. For example if it is desired to

determine the whole ambient vibration frequency spectrum instead of the dominant frequency input, then simply a Fast Fourier Transform (FFT) algorithm can be embedded in the PIC.

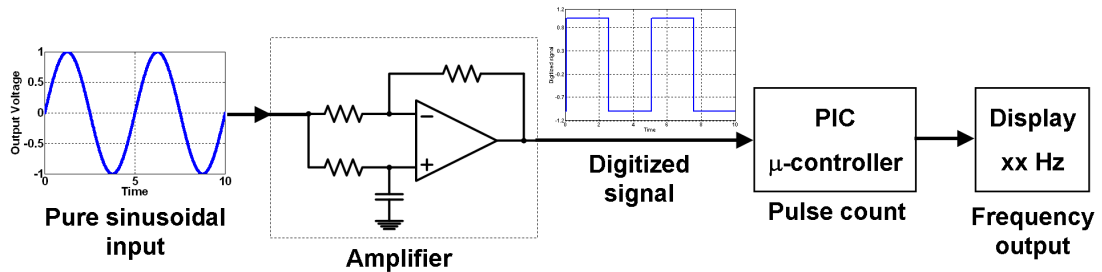


Figure 4.19. Block diagram of the proposed frequency sensor.

Figure 4.20 shows the measured and actual frequency values. The frequency measurements are taken in a range of 2.5-5.5 kHz. In order to visualize the difference between the measured and actual values of the frequency, the percentage error at each data point is shown in Figure 4.21. From the given plot it can be seen that the percent error is less than 0.02 % within the designed operation band of 3.5-4.5 kHz, which corresponds to an accuracy of ± 1 Hz. Outside this band, the measurements start deviating from the actual values. This is because, the output voltage starts decreasing outside the designed frequency band and thus it can not be handled properly by the readout circuitry. Effective frequency detection is still possible just outside the designed band, but this is not really useful since the element can not act as an energy harvester in these regions any more.

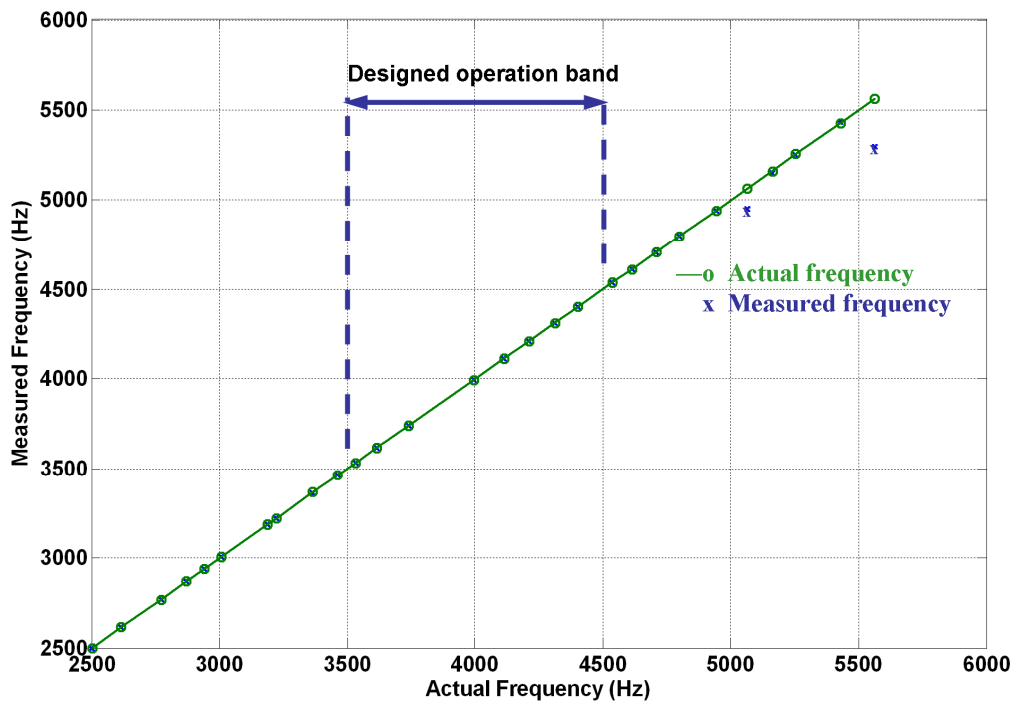


Figure 4.20. Actual and measured frequency values by the frequency sensor.

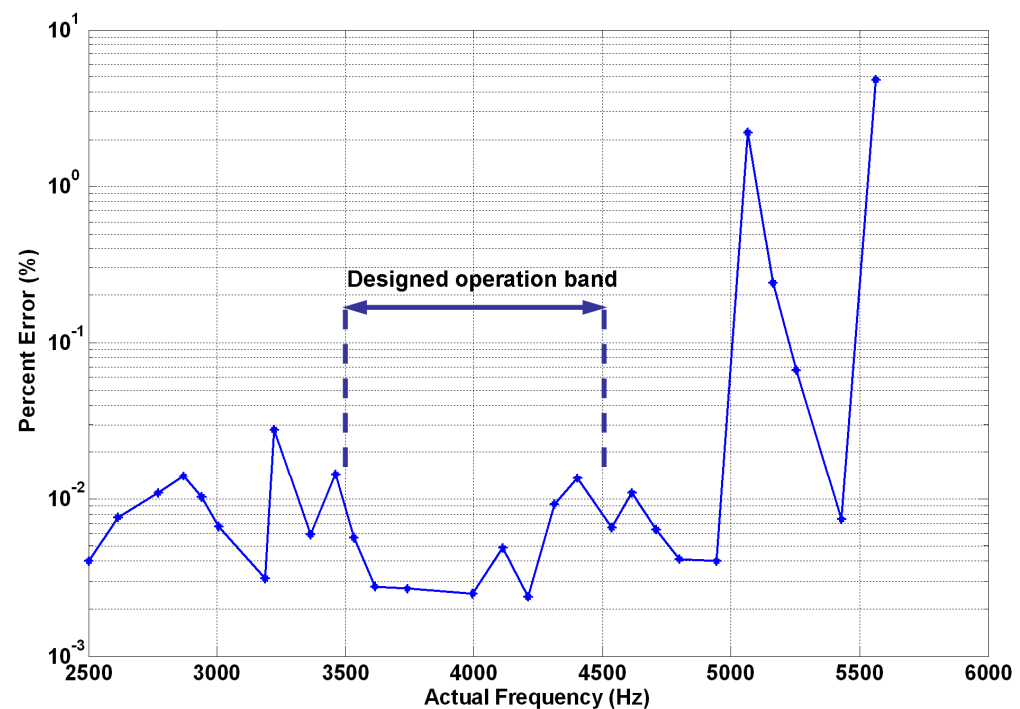


Figure 4.21. Percent error of measured frequency values.

4.5 The Tests of the Large Mass Coil (LMC) Design

The large mass coil (LMC) design has already been widely investigated in the literature. The aim of designing and testing this design is to use it as a benchmark model for the frequency up-converter (FUC) design. Figure 4.22 shows the photograph of the LMC design assembly prepared for testing. It is composed of mainly three parts, a stationary base that has the coil fabricated upon, a diaphragm-magnet assembly capable of vibrating with environmental vibrations and finally a spacer to adjust the distance between the magnet and the coils.

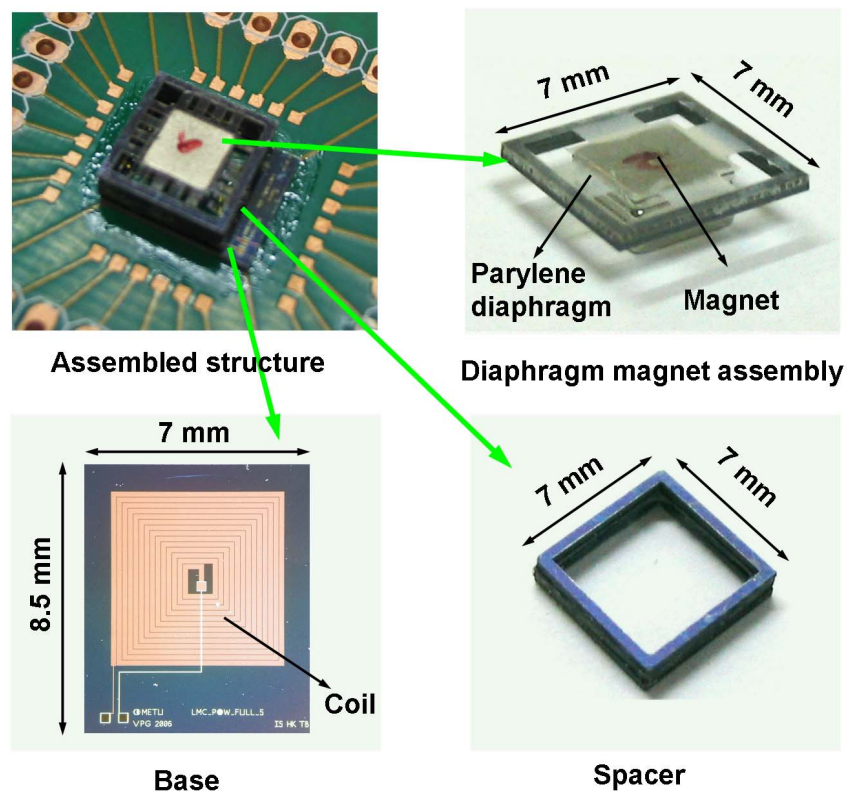


Figure 4.22. Photograph of the LMC assembly and components.

Table 4.5 lists the simulation and test results for the proposed LMC design.

Table 4.5. Simulation and test results for the LMC design.

	Simulation	Test
Input vibration frequency	113 Hz	113 Hz
Input acceleration	45 g	45 g
Magnet type	NdFeB (1.18 T)	NdFeB (1.18 T)
Magnet size	3.8 x 3.8 x 1.5 mm ³	3.8 x 3.8 x 1.5 mm ³
Device dimensions	8.5 x 7 x 2.5 mm ³	8.5 x 7 x 2.5 mm ³
Diaphragm structural material	Parylene C	Parylene C
Length of each diaphragm arm	1000 µm	1000 µm
Width of each diaphragm arm	555 µm	555 µm
Thickness of each diaphragm arm	15 µm	15 µm
Total number of diaphragm arms	16	16
Magnet area on the diaphragm	3.95 x 3.95 mm ²	3.95 x 3.95 mm ²
Natural frequency of the diaphragm	113 Hz	113 Hz
Magnetic flux density	0.19 Tesla	Not measured.
Coil metal width	160 µm	160 µm
Coil thickness	0.1 µm	0.1 µm
Coil resistance	235 Ω	257 Ω
Number of coil turns	13	13
Total coil length	168.5 mm	Not measured.
Practical coil length	29.7 mm	Not measurable.
Collected energy in 1 s	42 pJ	23 pJ
Peak output power	85 pW	40 pW
Peak output voltage	0.4 mV	0.3 mV

The tests are carried out by sweeping the frequency from 75 to 200 Hz, at a constant acceleration of 45 g that corresponds to an input vibration displacement of 0.88 mm at 113 Hz. The sweep frequencies and vibration levels are set the same as those of the frequency up-converter design for comparison purposes. Figure 4.23 shows the sinusoidal voltage output from the generator at a vibration frequency of 113 Hz.

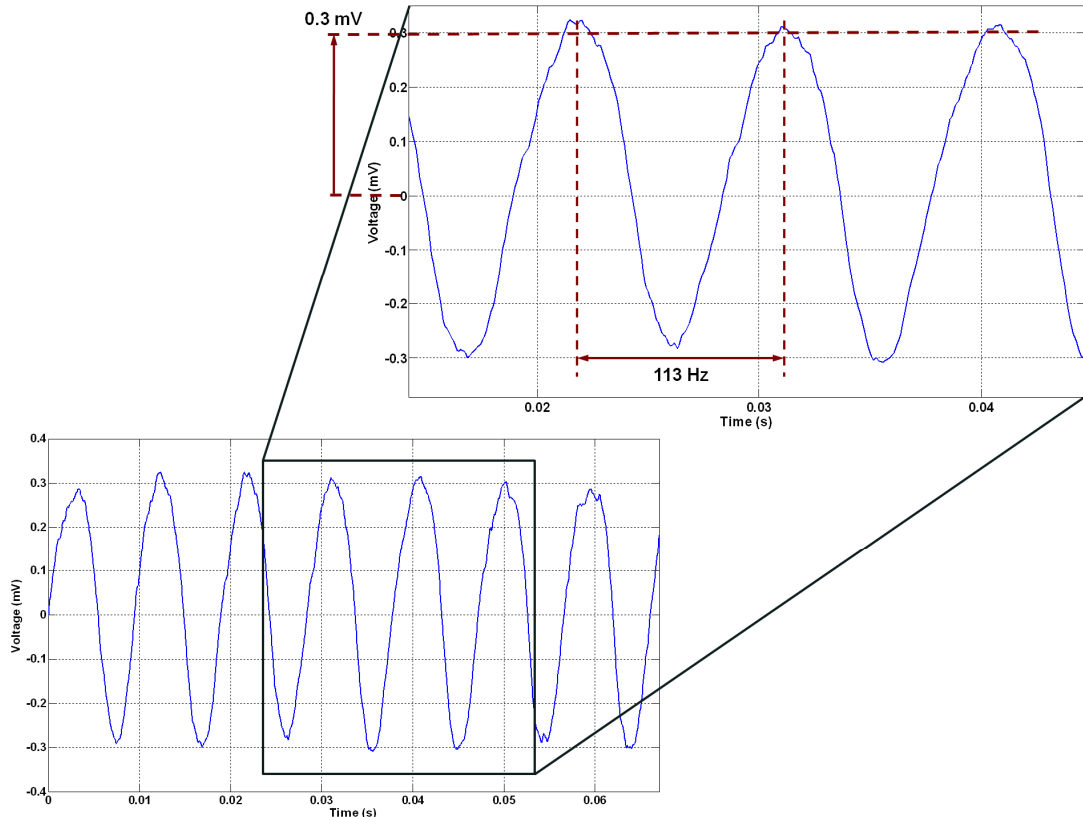


Figure 4.23. Measured voltage output from the large mass coil (LMC) design.

A maximum peak voltage output of 0.3 mV is obtained at 113 Hz from the proposed large mass coil (LMC) design. The deviation between the estimated and actual test outputs are due to the error in estimation of the magnetic flux density, which is quite hard to estimate. The performance of the large mass coil (LMC) design will be compared with the frequency up-converter (FUC) design in the next section, after giving the test results for the frequency up-converter (FUC) design.

4.6 The Tests of the Frequency up-Converter (FUC) Design

One of the main objectives of this thesis study is to improve the efficiency of vibration based micro generators at low frequencies since the output degrades rapidly with the cube of the frequency, at low excitation frequencies. The frequency up-converter (FUC) design is a solution to this problem. The operation mechanism and simulations of the proposed frequency up-converter (FUC) design is already given in detail in Chapter 2. In this section, the test results of the frequency up-converter (FUC) design is presented. Its performance is also compared with the large mass coil (LMC) design that is proposed in this study and a traditional large mass coil (LMC) design from literature. Figure 4.24 shows the photograph of the frequency up-converter (FUC) design assembly prepared for testing.

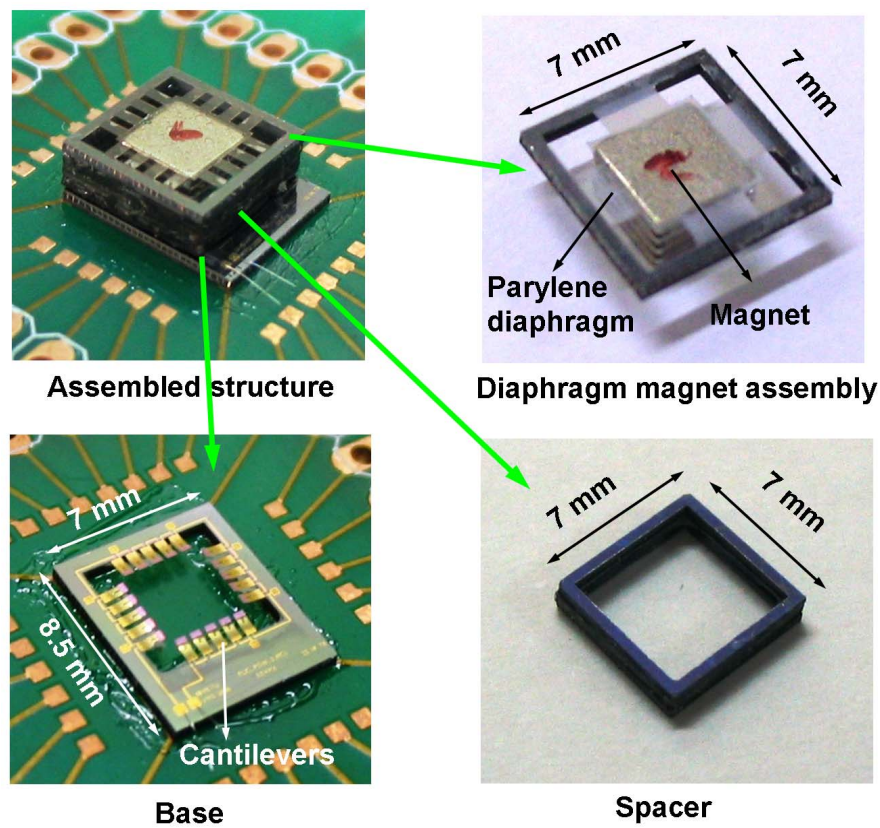


Figure 4.24. Photograph of the frequency up-converter (FUC) assembly and its components.

The frequency up-converter (FUC) assembly, shown on the upper left hand side is composed four major components that are the PCB, the FUC base, diaphragm and spacer. The base is glued permanently to the PCB using an epoxy. The epoxy is applied as a two part glue that hardens very rapidly when mixed. It can be applied as a thin film so that minimum roughness can be achieved after its application to the surface. Then, the magnet is attached to the diaphragm manually using the same epoxy under the microscope for best alignment. The distance between the FUC base and diaphragm magnet assembly is adjusted using Si spacers of 0.5 mm thick each. They can be put and glued on top of each other to increase the distance when necessary. Figure 4.25 shows the components of the frequency up-converter (FUC) assembly prepared for testing.

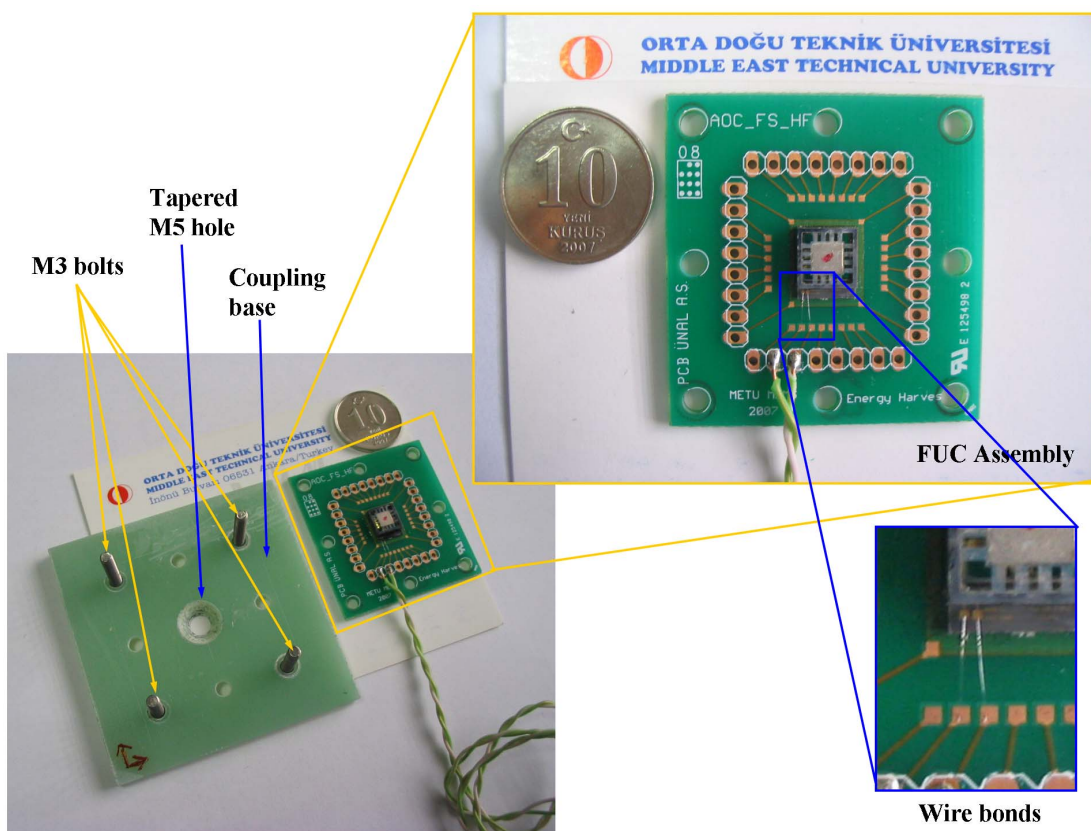


Figure 4.25. Components of the FUC assembly prepared for testing.

On the lower left hand side of the figure given above, the frequency up-converter (FUC) assembly just before being attached to the coupling base is shown. The tapered M5 hole on the coupling base is used to attach the whole assembly to the shaker table. The two thin wire bonds that carries out the output signals from the device to the PCB can also be seen in the lower right hand side of the figure.

Figure 4.26 is the photograph of the FUC assembly coupled to the shaker table. In order to provide space for the accelerometer shown in the lower right hand corner, four 9 mm long spacers with internal radius of 3.05 mm are used. The M3 bolts pass through these spacers and are fixed by corresponding nuts.

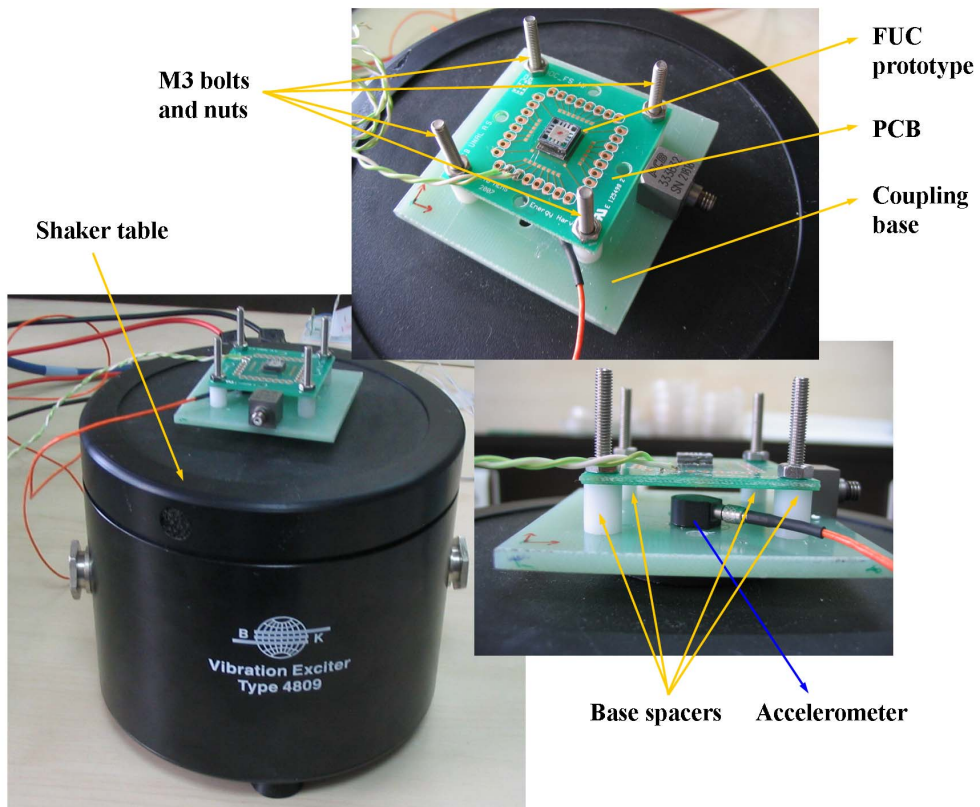


Figure 4.26. FUC assembly coupled to the shaker table.

Table 4.6 lists the simulation and test results for the proposed FUC design. The tests are carried out by sweeping the frequency from 50 to 200 Hz, at a constant acceleration of 40 g that corresponds to an input vibration displacement of 0.78 mm at 113 Hz. These settings are kept the same as the LMC design test settings as much as possible for comparison purposes. From the table it can be seen that a maximum peak voltage output of 0.57 mV is obtained from a single cantilever of the FUC design, at an excitation frequency of 95 Hz and an acceleration of 40 g.

Table 4.6. Simulation and test results for the FUC design.

	Simulation	Test
Input vibration frequency	50-200 Hz	50-200 Hz
Input acceleration	40 g	40 g
Magnet type	NdFeB (1.18 T)	NdFeB (1.18 T)
Magnet dimensions	3.8 x 3.8 x 1.5 mm ³	3.8 x 3.8 x 1.5 mm ³
Device dimensions	8.5 x 7 x 2.5 mm ³	8.5 x 7 x 2.5 mm ³
Total number of cantilevers	20	20
Natural frequency of the cantilevers	2 kHz	2 kHz
Cantilever size	1000 x 430 x 15 µm ³	1000 x 430 x 15 µm ³
Magnetic actuation area	430 x 225 x 9 µm ³	430 x 225 x 9 µm ³
Material for magnetic actuation	Nickel	Nickel
Cantilever structural material	Parylene C	Parylene C
Diaphragm structural material	Parylene C	Parylene C
Length of each diaphragm arm	1000 µm	1000 µm
Width of each diaphragm arm	555 µm	555 µm
Thickness of each diaphragm arm	15 µm	15 µm
Total number of diaphragm arms	16	16

Table 4.6. (cont'd).

Magnet area on the diaphragm	3.95 x 3.95 mm ²	3.95 x 3.95 mm ²
Natural frequency of the diaphragm	113 Hz	113 Hz
Release height of the cantilevers	200 μm	200 μm
Effective frequency of the device	50-200 Hz	50-200 Hz
Damping ratio of the cantilevers	0.02	0.02
Magnetic flux density	0.19 Tesla	Not measured.
Distance between cantilevers to magnet	500 μm	500 μm
Coil metal width	20 μm	20 μm
Coil thickness	0.1 μm	0.1 μm
Total coil length (single cantilever)	13.1 mm	Not measured.
Coil resistance	160 Ω	150 Ω
Practical coil length (single cant.)	1.4 mm	Not measurable.
Number of coil turns	6	6
Collected energy in 1 s (single cantilever)	30.5 pJ	20 pJ
Peak power output (single cantilever)	0.33 nW	0.25 nW
Peak voltage output (single cantilever)	0.67 mV	0.57 mV

It follows from (2.67) that the peak voltage output from the generator in this case is determined by,

$$|\varepsilon| = \frac{BL_p Z_o \omega_n}{\sqrt{1 - \zeta_{eq}^2}} \quad (4.4)$$

The parameters except for the magnetic flux density are assumed to be calculated or modified correctly. The only source of error in the estimation of the voltage output is arises from the magnetic flux density.

Figure 4.27 shows the estimated and measured output voltage from a single cantilever plotted on the same set of axis. In the figure, the catch and release points of the cantilevers and peak voltage output is indicated. A total number of 5 cycles are shown in the figure. Each cycle lasts about 10 ms that is composed of the combined motion and the individual motion of the cantilevers and the magnet. Voltage generation is realized right after the release phase of the cantilevers where they oscillate with their damped natural frequencies.

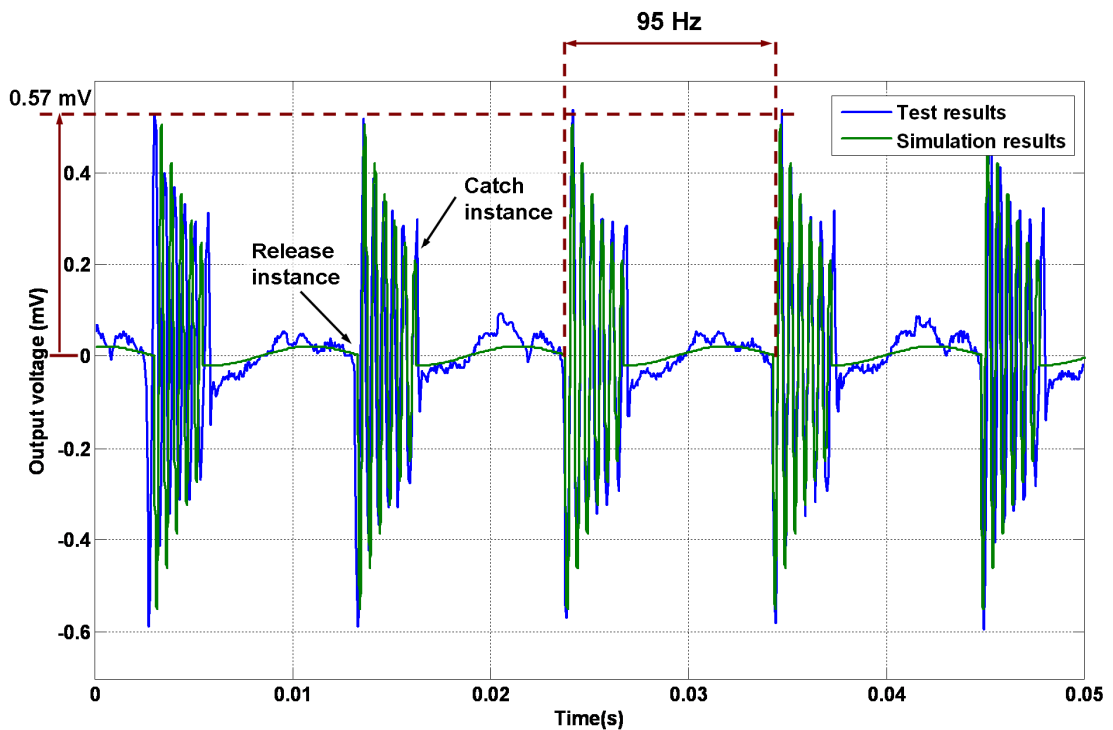


Figure 4.27. Simulation and test results plotted on the same set of axis for a single cantilever of the FUC design.

Figure 4.28 and 4.29 show the close-up views of Figure 4.27. From these figures, the catch and release points and maximum generated voltage are clearly seen. It can be deduced that the simulated and actual voltage waveforms are quite close to each other for a single cantilever of the device.

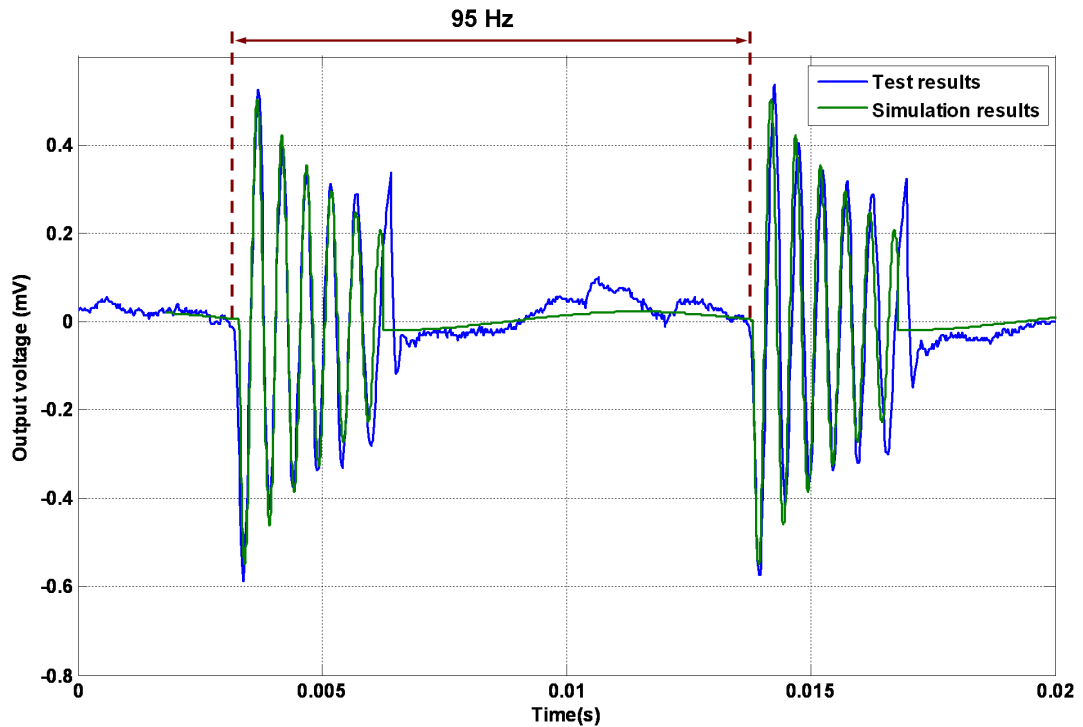


Figure 4.28. Close-up view of the simulated and actual results for 2 cycles.

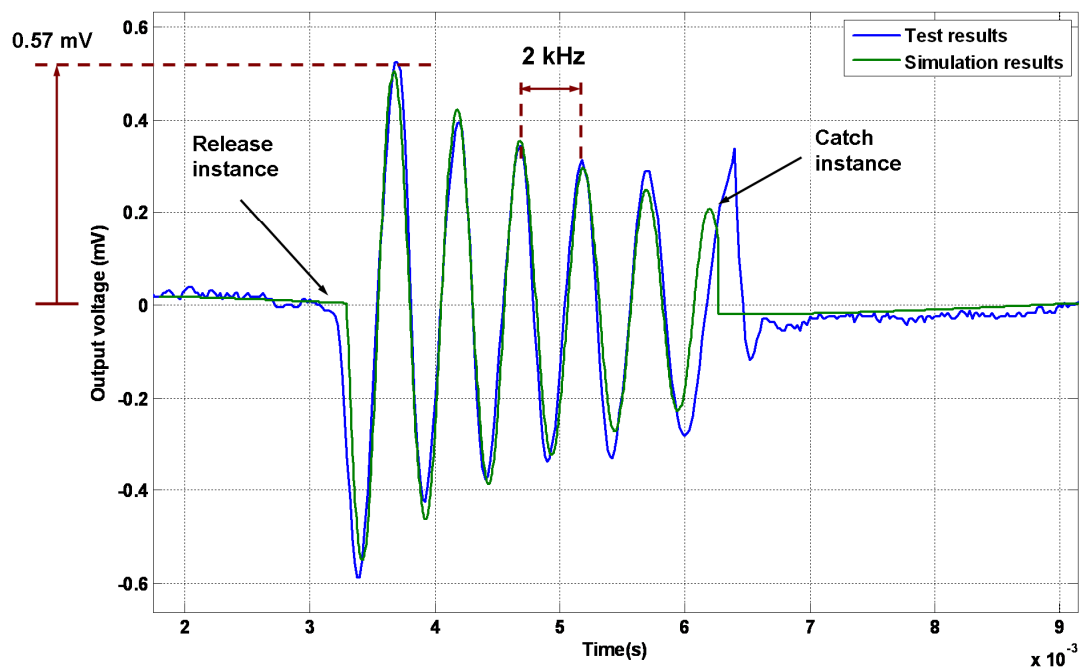


Figure 4.29. Close-up view of the simulated and actual results for 1 cycle.

Before going any further, as the next step, the performance of the large mass coil (LMC) and the frequency up-converter (FUC) designs will be compared. For this purpose Table 4.7 lists important performance parameters of the large mass coil (LMC) and frequency up-converter (FUC) designs. From the given data, it can be seen that even a single cantilever of the frequency up-converter (FUC) design is capable of generating almost twice the voltage and four times the power of the traditional large mass coil (LMC) design. However, considering that the large mass coil (LMC) and frequency up-converter (FUC) designs has sinusoidal and decaying out wave forms, respectively, it would be more meaningful to compare the total energy generated in a certain cycle of for example 1 s. In this case, the LMC design can collect 23 pJ whereas the single cantilever of FUC design can 20 pJ. Considering that there are a total number of 20 cantilevers used in the FUC design, the proposed frequency up-conversion mechanism performs 17 times better than the LMC design. Besides it should also be noted that, the LMC design is effective only at the resonance frequency of the device, but the FUC design will have almost the same output performance in any frequency as far as the cantilevers are caught and released within the physical limits of the generator.

In order to compare the performance of the frequency up-converter (FUC) design with a traditional generator from the literature, Table 4.8 shows important performance parameters of a large mass coil (LMC) design proposed by Williams et al. [71] and the frequency up-converter. The first row is the original parameters of the design presented in the work of Williams et al. whereas in the second row, the scaled down version of this design is shown, simply obtained by recalculating the performance of the device at 113 Hz. Referring to the table, a single cantilever of the proposed frequency up-converter (FUC) design has a better performance compared to the scaled down large mass coil (LMC) design proposed by Williams et al. in terms of both power and voltage levels. The energy level of the design by Williams is much higher than that a single cantilever of the frequency up-converter (FUC). However, when the overall performance of 20 cantilevers is considered, the proposed design would still perform much better than the traditional generator.

Table 4.7. Comparison of the performances of the large mass coil (LMC) and the frequency up-converter (FUC) designs.

	LMC	FUC (single cantilever)
Input vibration frequency	50-200 Hz	50-200 Hz
Input acceleration	45 g	40 g
Magnet dimensions	3.8 x 3.8 x 1.5 mm ³	3.8 x 3.8 x 1.5 mm ³
Device dimensions	8.5 x 7 x 2.5 mm ³	8.5 x 7 x 2.5 mm ³
Natural frequency of the cantilevers	N.A.	2 kHz
Cantilever size	N.A.	1000 x 430 x 15 μm ³
Magnet area on the diaphragm	3.95 x 3.95 mm ²	3.95 x 3.95 mm ²
Natural frequency of the diaphragm	113 Hz	113 Hz
Release height of cantilevers	N.A.	200 μm
Effective frequency of the device	113 Hz	50-200 Hz
Distance between coil to magnet	500 μm	500 μm
Coil metal width	160 μm	20 μm
Coil thickness	0.1 μm	0.1 μm
Total coil length	168.5 mm	13.1 mm
Coil resistance	257 Ω	150 Ω
Practical coil length	29.7 mm	1.4 mm
Number of coil turns	13	6
Collected energy in 1 s	23 pJ	20 pJ
Peak power output	0.04 nW	0.25 nW
Peak voltage output	0.3 mV	0.57 mV

Another point is that, the power and energy levels by Williams might seem high due to the coil resistance, which is 31Ω only and quite low. In the optimum case, the output power is maximized when the load and coil resistances are roughly equal to each other. Then, the output power is inversely proportional to the coil resistance, $P \propto 1/R_c$, but if it is kept too small then load impedance matching will be a problem.

Table 4.8. Comparison of performances of the LMC design by Williams et al. and the FUC designs.

	LMC (Williams et al.)	LMC scaled (Williams et al.)	FUC (single cantilever)
Input vibration frequency	4 kHz	113 Hz	113 Hz
Magnet dimensions	1 x 1 x 0.3 mm ³	1 x 1 x 0.3 mm ³	3.8 x 3.8 x 1.5 mm ³
Magnet area on the diaphragm	2.5 mm in diameter	2.5 mm in diameter	3.95 x 3.95 mm ²
Device dimensions	6.5 x 6.5 x 0.7 mm ³	6.5 x 6.5 x 0.7 mm ³	8.5 x 7 x 2.5 mm ³
Coil resistance	31 Ω	31 Ω	150 Ω
Coil thickness	2.5 μm	2.5 μm	0.1 μm
Coil metal width	20 μm	20 μm	20 μm
Number of coil turns	13	13	6
Collected energy in 1 s	0.15 μJ	116 pJ	20 pJ
Peak power output	0.3 μW	0.23 nW	0.25 nW
Peak voltage output	8.7 mV	0.24 mV	0.57 mV

The significance of the design by Williams is, it is the first type of vibration based electromagnetic micro energy generator proposed in the literature and has been used

as a benchmark model in most of the studies. That's why it is used as a comparison model here.

As mentioned above, the FUC design can operate around the natural frequency of its diaphragm as long as the input displacement amplitude is enough to achieve the catch and release of the cantilevers. In order prove this, Figure 4.30 shows the magnitude of peak output voltage at sample frequency points.

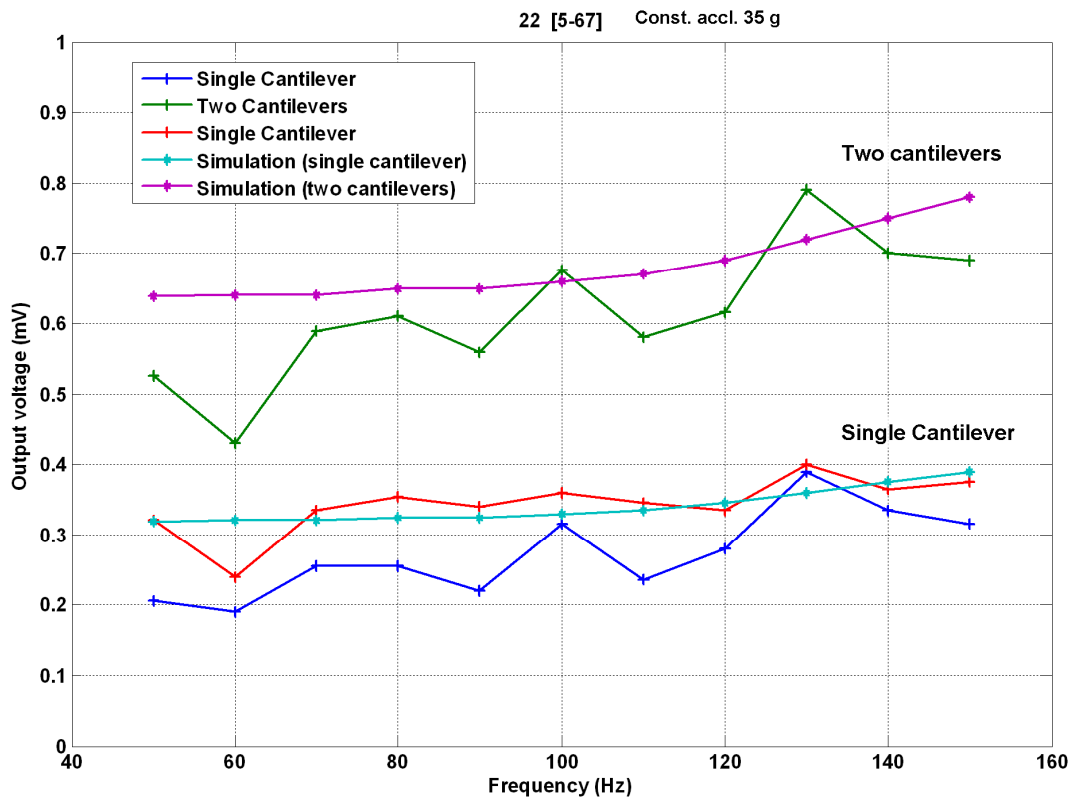


Figure 4.30. Simulation and test results for the variation of the magnitude of the output voltage for different excitation frequencies.

The figure shown above is obtained by sweeping the frequency slowly from 50 Hz to 150 Hz, at a constant test acceleration of 35 g and recording the peak amplitudes at certain frequencies. In the plot, the data from two different single cantilevers and

sum of two cantilevers, as well as the corresponding simulation results are shown for comparison. From the given figure it can be seen that there is a slightly increasing trend of output voltage with excitation frequency. This is because as the frequency increases the initial release velocity of the cantilevers and thus the release heights also increase slightly, resulting in an increase in the output voltage. This can also be verified by the simulation results shown in the figure. This test shows that continuous and constant voltage generation in a frequency range is possible with the proposed FUC design unlike traditional generators.

The excitation frequency has another effect on the generated voltage under certain circumstances. If the input excitation displacement or acceleration is just enough to catch and release the cantilevers, which means that the absolute maximum displacement of the diaphragm is close to the absolute release height of the cantilevers, then as the frequency increases, the frequency up-conversion ratio decreases. This is illustrated in Figure 4.31 that shows the absolute maximum displacement of the magnet and the cantilevers. In this figure, it can be seen that under the stated conditions above, as the frequency increases, the catch point moves to the left decreasing the number of oscillations of the cantilevers before catch.

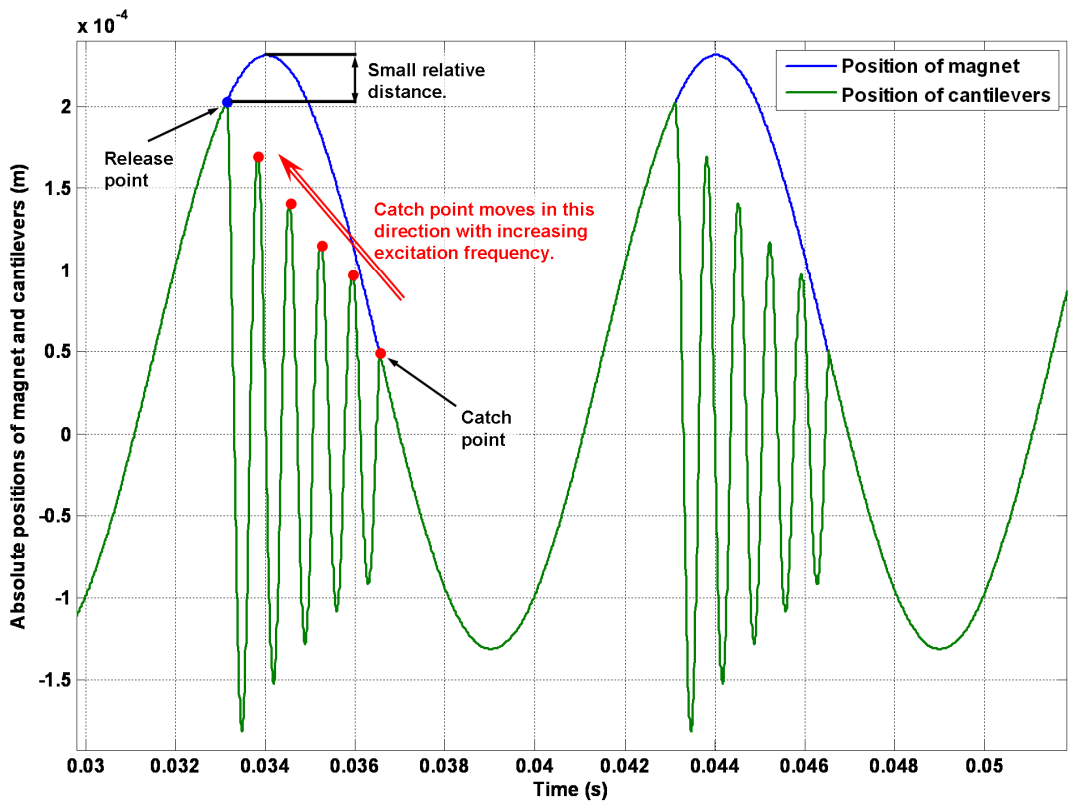


Figure 4.31. Illustration of variation of catch point with increasing frequency.

The above discussion can be made clearer with the help of the test results shown in Figure 4.32. These results are obtained by slowly sweeping the frequency from 50 to 110 Hz at a constant acceleration of 25 g. It can be clearly seen that as the excitation frequency increases, the number of decay outs also decreases meaning that the cantilevers are caught earlier.

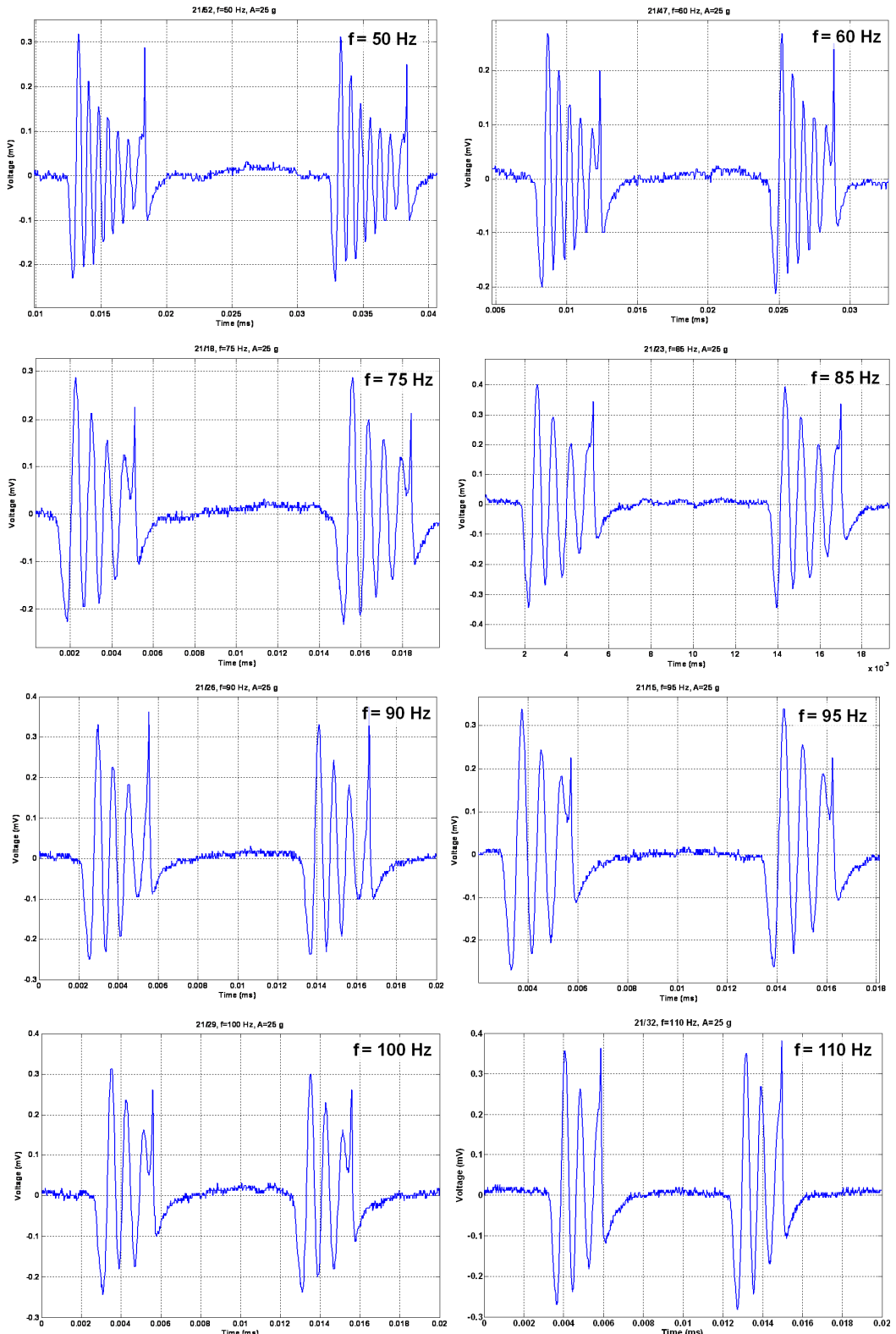


Figure 4.32. Variation of up-conversion ratio with frequency.

In this section, the test results of a single cantilever have been given so far. After this point, the main characteristics of multiple cantilevers will be covered. First of all, during the tests it has been observed that, the voltage output from multiple cantilevers is not integer multiples of a single cantilever's output. This is mainly due to difference in the release heights (leading to time shift or phase angle difference) and the natural frequency between the outputs of individual cantilevers. In order to show these effects on output, first of all the performance of two cantilevers will be investigated. Figure 4.33 shows the output from two consecutive cantilevers. One of the plots belongs to a single cantilever whereas the other one is the sum of the two. The plot is obtained at 100 Hz, 45 g.

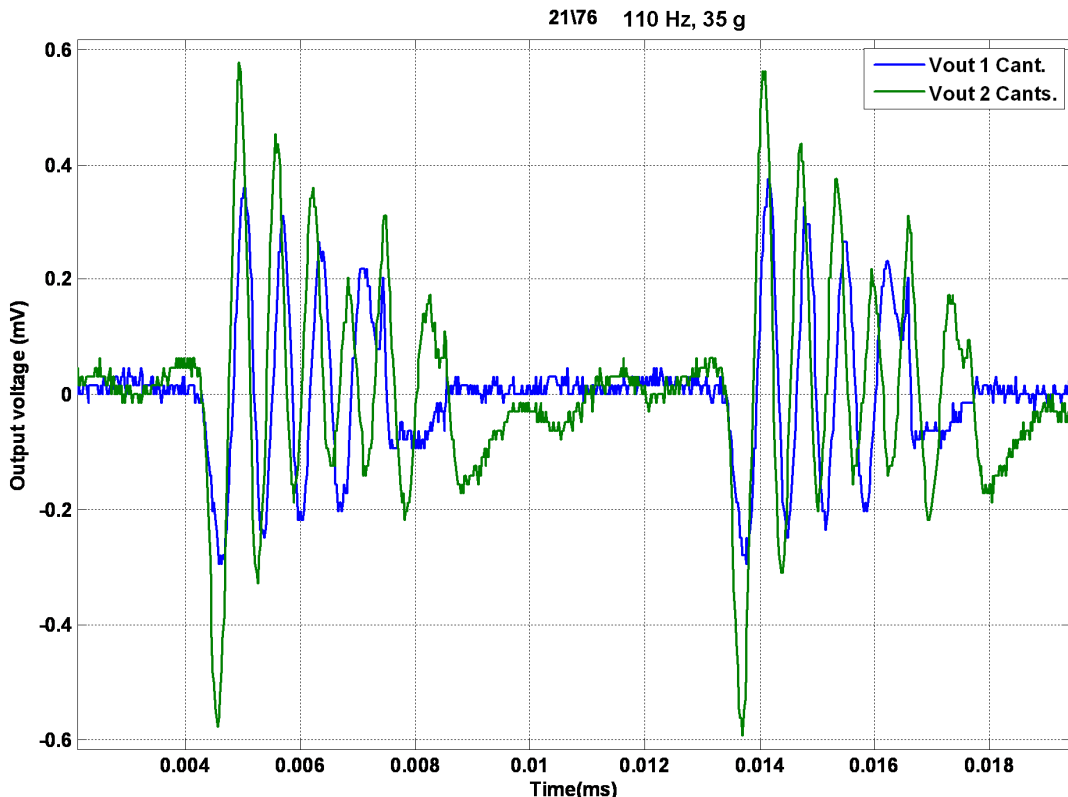


Figure 4.33. Output from two cantilevers with time shift.

The output from the two cantilevers is not two times the output from a single cantilever, which is due to the time shift between the cantilevers. This can be observed more clearly in the close-up view of the above plot given in Figure 4.34.

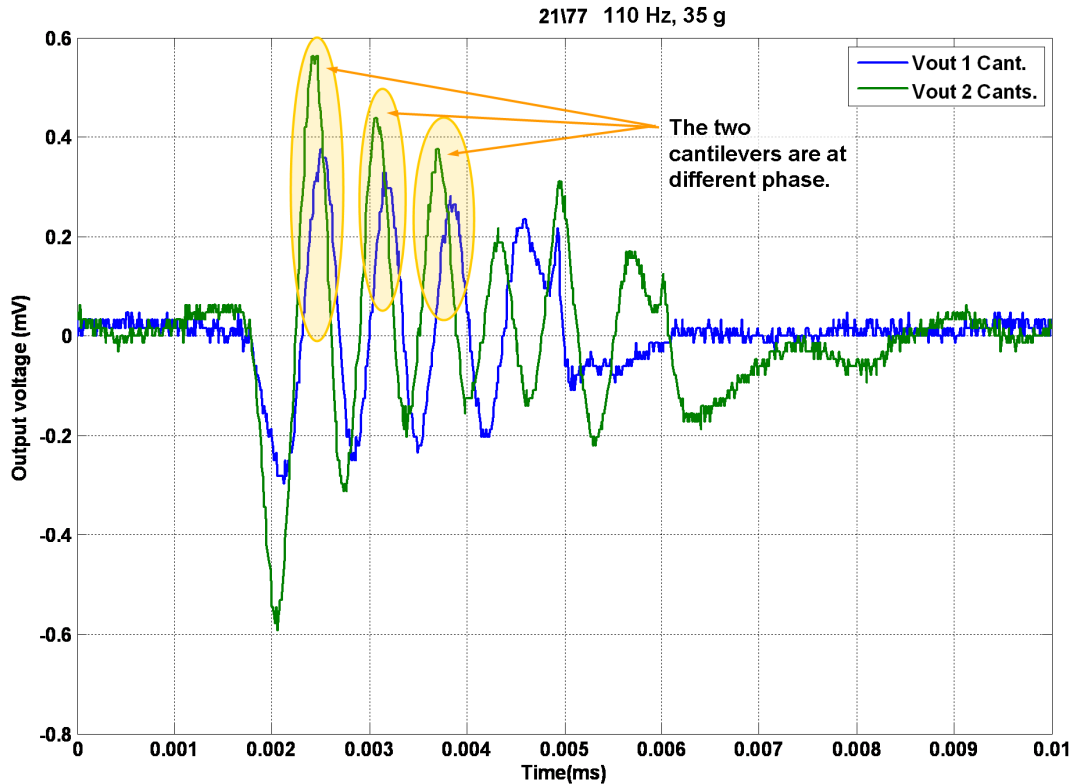


Figure 4.34. Close-up of the output from two cantilevers with time shift.

Note that, in the above figures, one of the plots belongs to the sum of the two cantilevers. In order to see the individual cantilevers separately, the output of the single cantilever is subtracted from the double cantilever as plotted in Figure 4.35. In this figure, the red plot shown at the bottom of the upper two plots is obtained in the described manner and represents the output from the second cantilever. The close-up view of the plot is shown on the lower side.

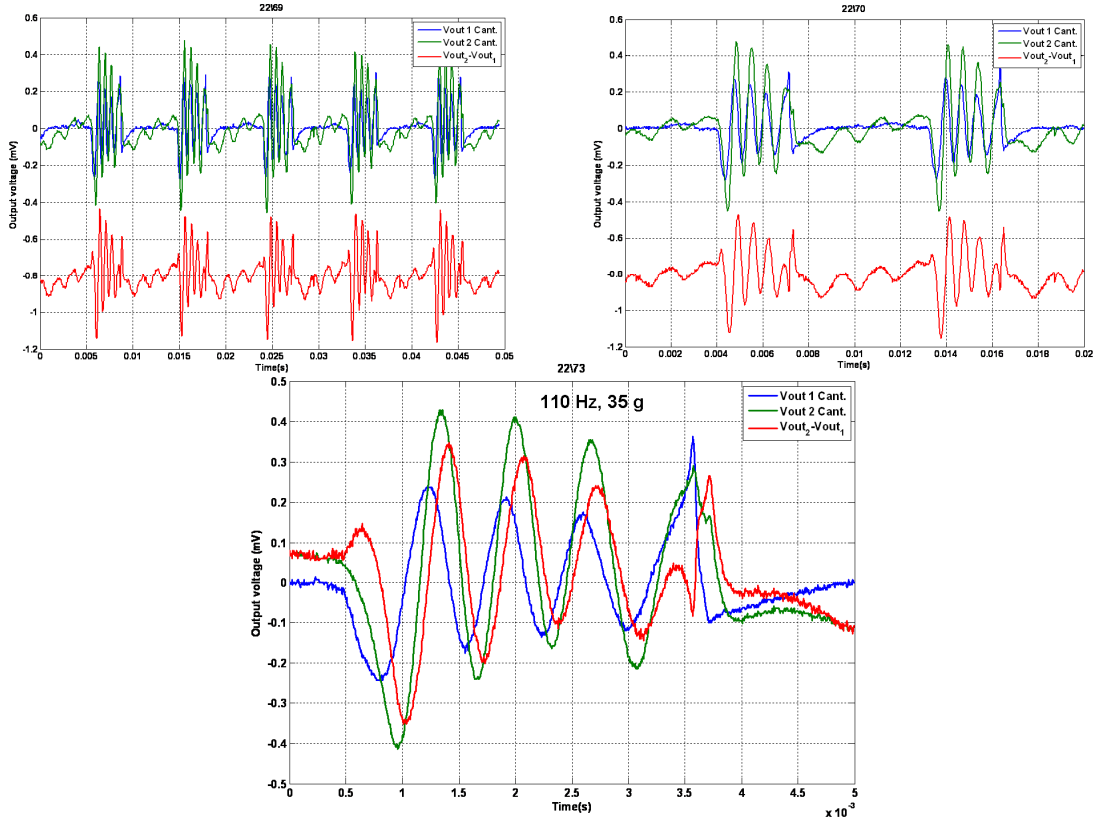


Figure 4.35. Voltage output from individual cantilevers.

There are also cases where there is no or small time shift for the case of two consecutive cantilevers. Figure 4.36 shows such an example, which is again the output from two cantilevers, but in this case the time shift is quite small compared to the previous case and as a result the overall output is very close to two times of a single cantilever. Figure 4.37 and 4.38 shows two individual cantilevers and their summation, respectively. In this case also, it can be observed that the time difference is quite small. Figure 4.39 shows two cantilevers with small time shift, but non-identical natural frequencies. It can be observed that, although the cantilevers are released at the same time, they separate from each by time, which is possibly due to a small difference in their natural frequencies. The last example in this case is shown in Figure 4.40 in which two consecutive cantilevers with small time and natural frequency shift are observed.

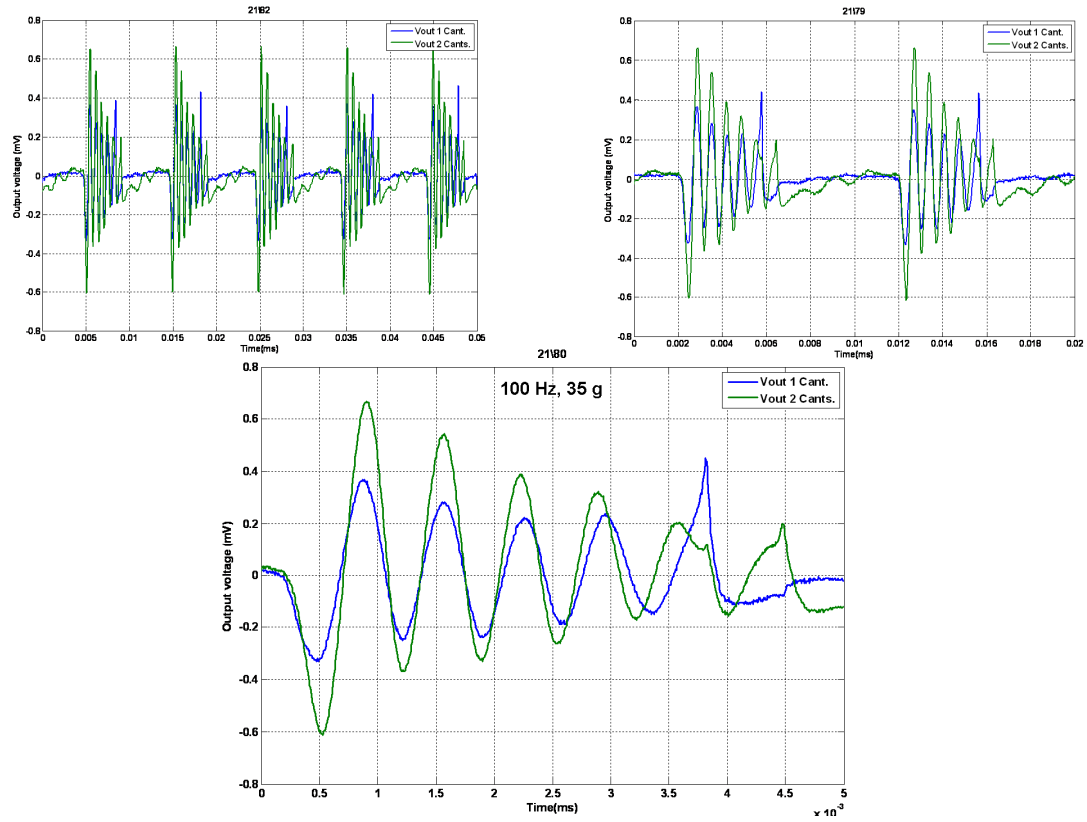


Figure 4.36. Output from two cantilevers with small time shift.

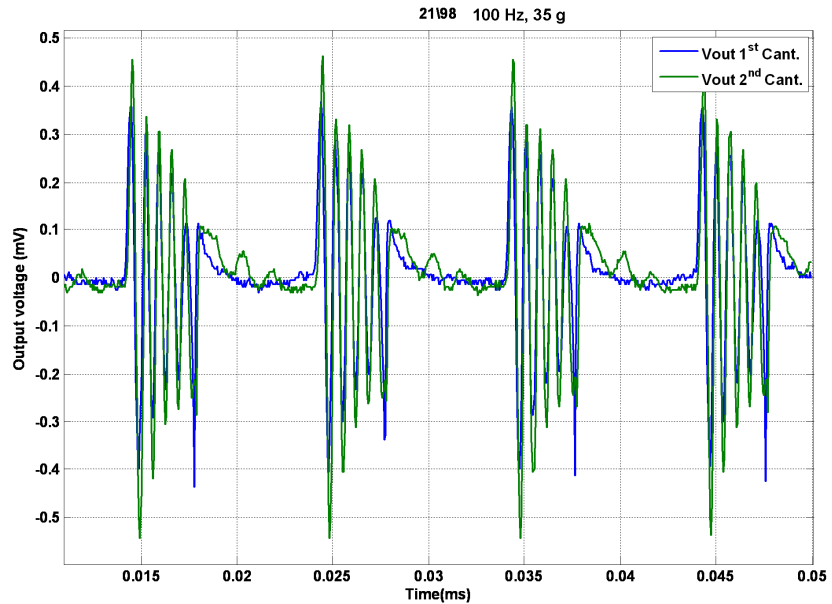


Figure 4.37. Output from two individual cantilevers with small time shift.

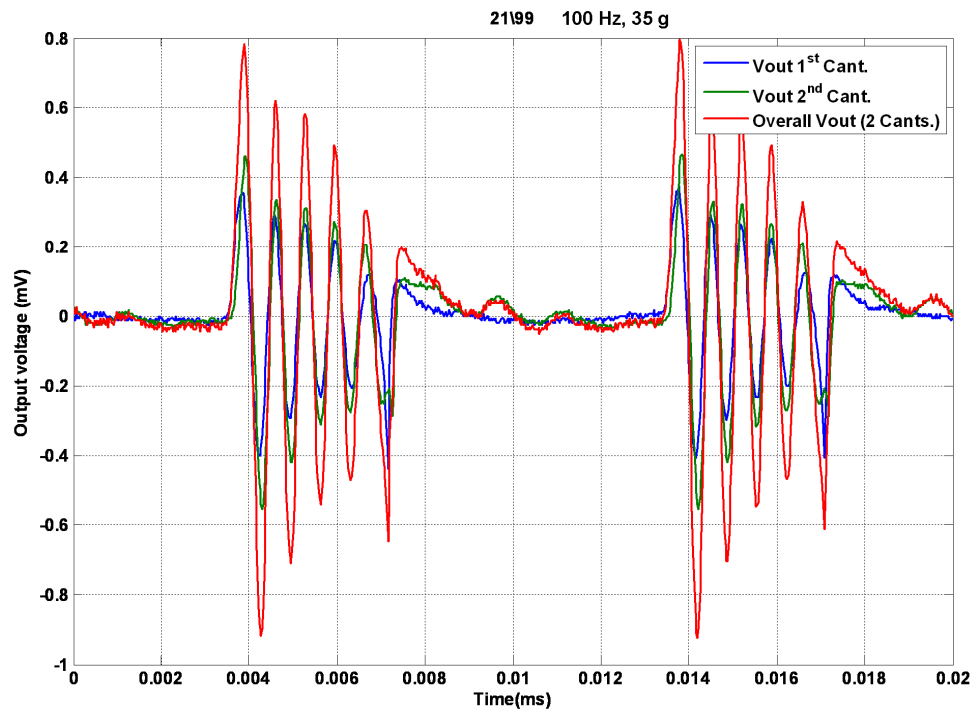


Figure 4.38. Summed up voltages from two consecutive cantilevers.

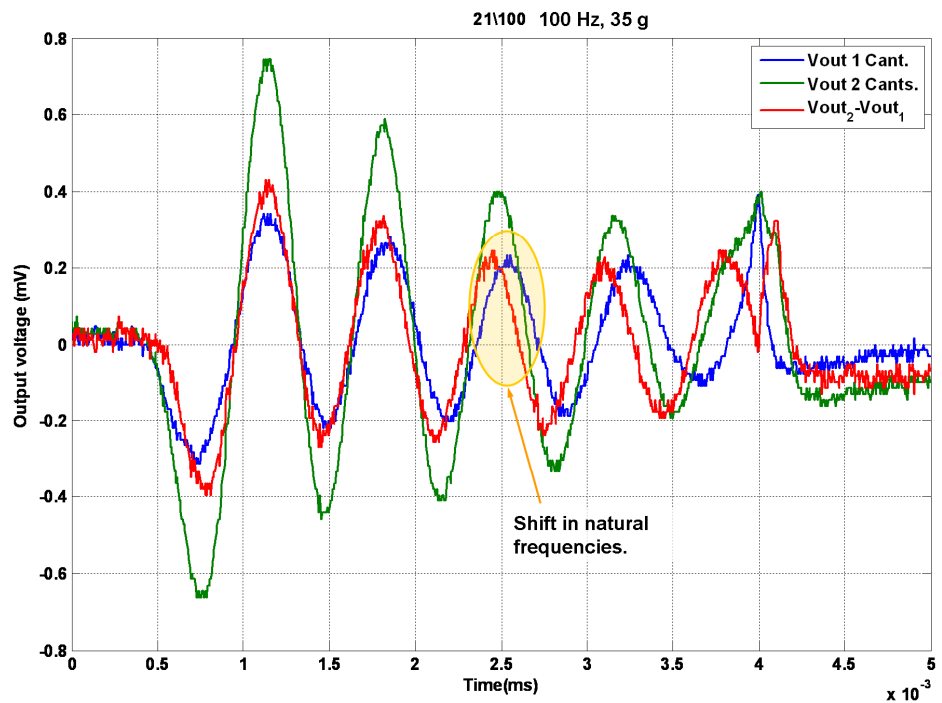


Figure 4.39. Two cantilevers with non-identical natural frequencies.

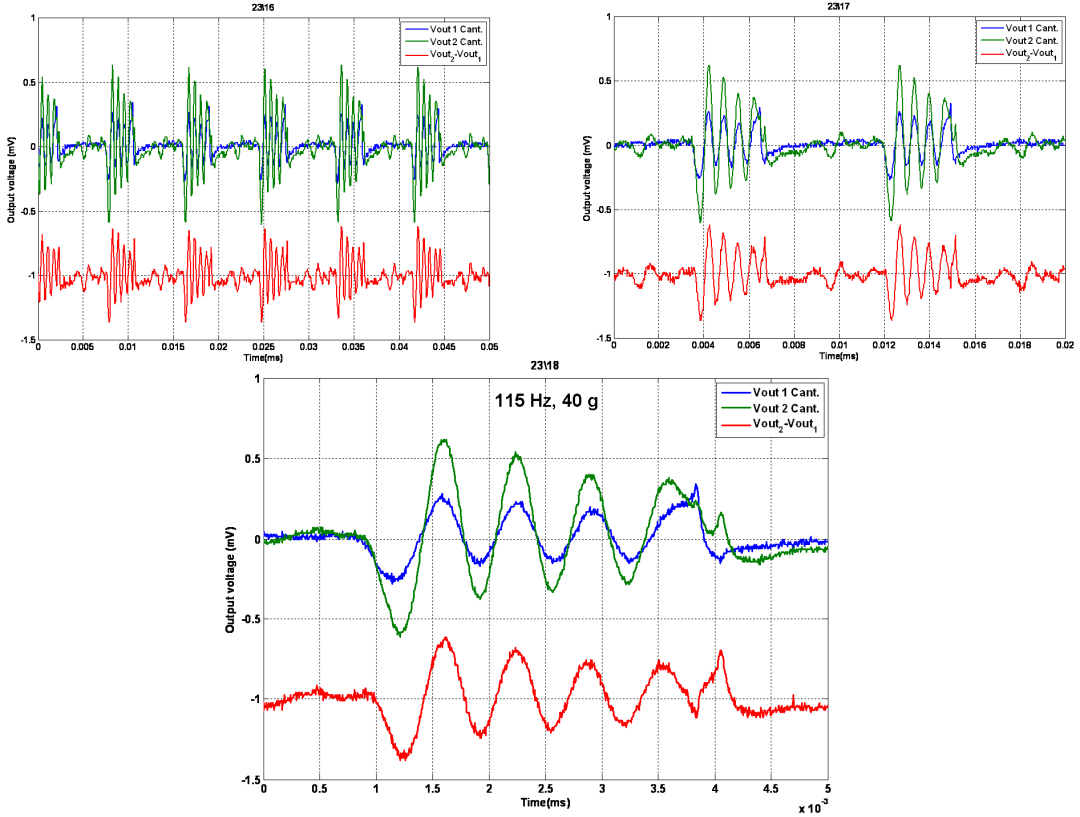


Figure 4.40. Output from two individual cantilevers with small time shift.

In order to expand the examples, tests with three cantilevers have also been carried out. Figure 4.41 shows the output from three consecutive cantilevers with time shift. For comparison purposes the output from a single cantilever has also been shown. The plots on the upper left and right hand side of the figure are the outputs from a single and three cantilevers, respectively and they are shown individually for visual clarity. On the bottom left and right, the outputs from a single and three cantilevers are shown at the same time for comparison purposes. It can be clearly seen that the output from three cantilevers is greatly distorted due to the difference in the natural frequency of the cantilevers. Figure 4.42 shows the output from another set of arms, but with smaller shift in time and frequency. On the upper hand side, the outputs are shown together and on the lower hand side a close-up view is given. Also, in the plot shown in the lower hand side, the output from two cantilevers are also given that is

obtained by subtracting the signal from three cantilevers from the output of a single cantilever. It can be seen that the overall output from the cantilevers are much more uniform compared to the previous case.

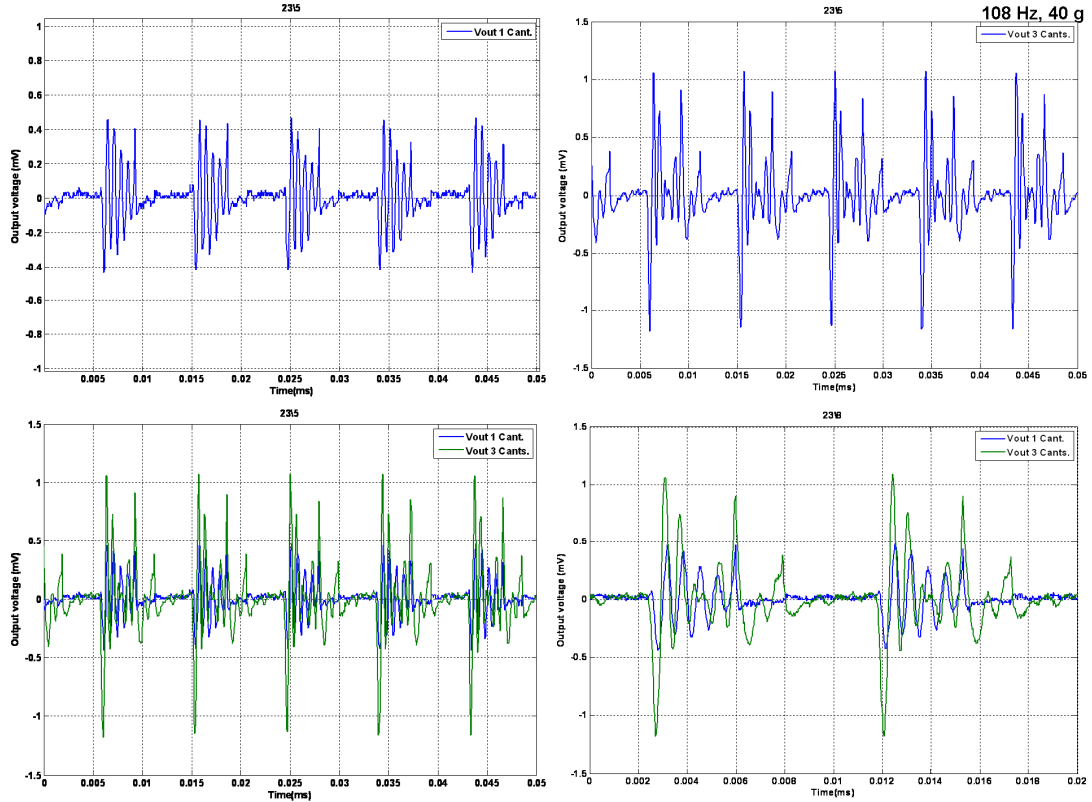


Figure 4.41. Output from 3 cantilevers with shift in time and natural frequency.

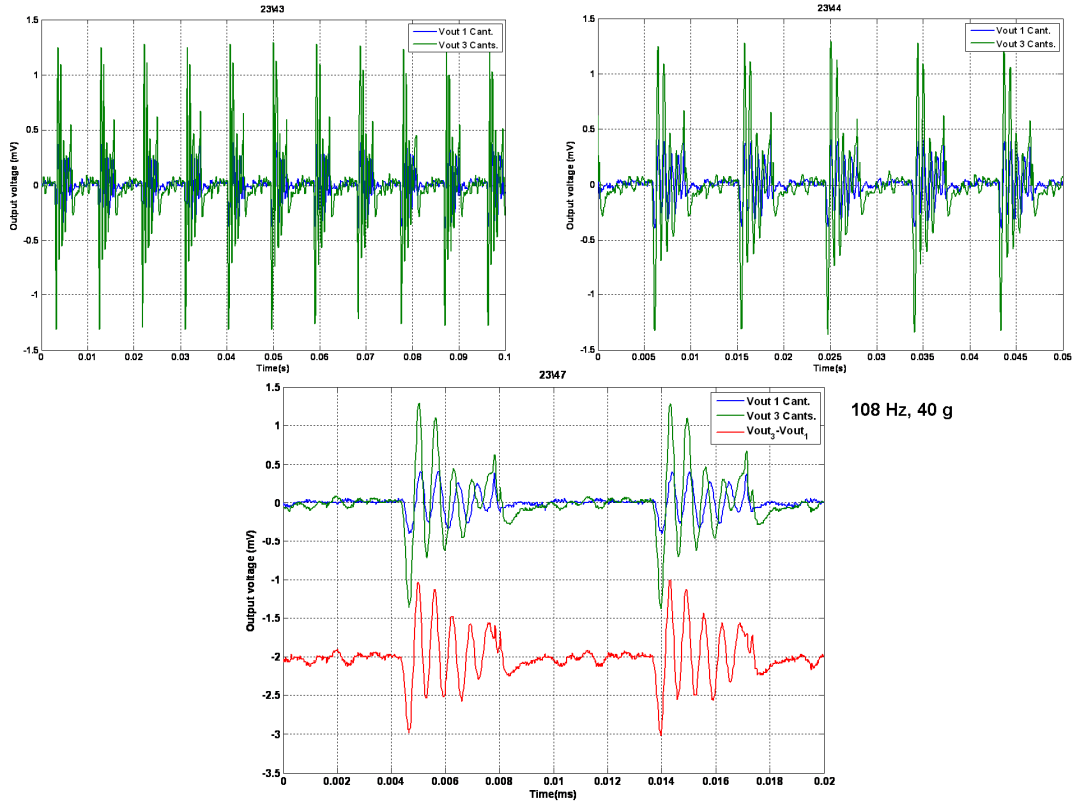


Figure 4.42. Output from 3 cantilevers with shift in time and natural frequency.

The analysis made so far show that although the simulation and test results match for a single cantilever, the output from multiple cantilevers in some cases are distorted due to the time shift and difference in natural frequency of the cantilevers, which are investigated under separate headings in the following two sections.

4.6.1 Analysis of Difference in the Natural Frequency of the Cantilevers

In this section, the causes of difference in natural frequency of the cantilevers are investigated. First of all, corresponding variation required in physical system parameters are tabulated and supported by sample plots. Then, the reason of such variation is explained upon these results.

The natural frequency of a cantilever is approximately, but effectively defined by,

$$\omega_n = \sqrt{\frac{k_{eq}}{m_{eq}}} \quad (4.5)$$

where the stiffness and mass terms are defined in terms of systems parameters as,

$$k_{eq} = \frac{3EI}{L^3} = \frac{Ebh^3}{4L^3} \quad \text{and} \quad m_{eq} = \underbrace{\frac{33}{140} m_b}_{\substack{\text{equivalent mass} \\ \text{of cantilever}}} + \underbrace{m_{Ni}}_{\substack{\text{mass of nickel}}} \quad (4.6)$$

It can be straightly stated that a variation in natural frequency can only be caused by a variation in the parameters making it up defined by the last two equations above. Table 4.9 shows numerical examples from the tests to show the possible amount variation and corresponding qualitative effect on output. On the first column of the table, the figure that the data is actually taken from is given for reference. From the given the data, it can be seen that a deviation more than 5 % in natural frequencies, which corresponds to a difference of 77 Hz, makes the output unpleasant. The square of frequency ratios are given since the equivalent mass and stiffness terms are proportional to the square of the natural frequency and this value directly shows the necessary deviation in these two terms to cause a corresponding variation in the natural frequency.

Table 4.9. Numerical test examples of shift in natural frequency.

Figure #	ω_{n1} (Hz)	ω_{n2} (Hz)	$\Delta\omega_n$ (Hz)	ω_{n1}/ω_{n2}	$(\omega_{n1}/\omega_{n2})^2$	Effect on output
4.38	1515	1471	44	1.03	1.06	⊖
4.34	1562	1515	47	1.03	1.06	⊖
4.35	1515	1429	86	1.06	1.12	⊖
4.36	1515	1438	77	1.05	1.10	⊖
4.39	1538	1429	109	1.08	1.16	⊖

In order to make a deeper analysis, Table 4.10 shows the amount of variation required in the system parameters of the equivalent stiffness of the cantilevers to reflect the corresponding amount of change in the natural frequencies stated above. The nominal values of the parameters are also given to state the absolute variation required in each parameter. The symbols used in the table are ΔL , Δh and Δb for the variation in length, thickness and width of the cantilevers, respectively. The amounts of variations for all of the parameters of the stiffness are within the tolerance of the micro fabrication steps, meaning that the variation in the natural frequencies can not be caused by these parameters. Besides, if a dimension of one of the cantilevers is deviated then one would be able to see about the same amount of deviation in the consecutive cantilever as they are quite close to each other.

As the next parameter, the equivalent mass term is investigated for which the results are tabulated in Table 4.11. The mass of the cantilever can be analyzed in two parts, one of which is the mass of the parylene and the other is the mass of the nickel deposited at the tip. The stated amounts of variations are both within the micro fabrication limits and thus the variation between consecutive cantilevers cannot be caused by these parameters.

Table 4.10. Necessary variation required in equivalent stiffness term to cause the corresponding change in natural frequency.

Figure #	$\Delta\omega_n$ (Hz)	$(\omega_{n1}/\omega_{n2})^2$	Δk_{eq} ($k_{eq} = 1$ N/m)	ΔL ($L = 1000$ μm)	Δh ($h=15$ μm)	Δb ($b = 430$ μm)
4.38	44	1.06	0.06 N/m	20 μm	0.29 μm	25.8 μm
4.34	47	1.06	0.06 N/m	20 μm	0.29 μm	25.8 μm
4.35	86	1.12	0.12 N/m	38 μm	0.58 μm	51.6 μm
4.36	77	1.10	0.10 N/m	32 μm	0.48 μm	43.0 μm
4.39	109	1.16	0.16 N/m	51 μm	0.76 μm	68.8 μm

Table 4.11. Necessary variation required in equivalent mass term to cause the corresponding change in natural frequency.

Figure #	$\Delta\omega_n$ (Hz)	$(\omega_{n1}/\omega_{n2})^2$	Δm_{eq} (cant.) (m_{eq} (cant.)= 2.09 μg)		Δm_{Ni} ($m_{Ni} = 8.6$ μg)
4.38	44	1.06	0.13 μg	+	0.52 μg
4.34	47	1.06	0.13 μg	+	0.52 μg
4.35	86	1.12	0.25 μg	+	1.03 μg
4.36	77	1.10	0.21 μg	+	0.86 μg
4.39	109	1.16	0.33 μg	+	1.37 μg

As a result, the only possible cause of the variation in the natural frequency is due to the thermal grease residues remaining after the release of the devices, which creates a random variation in the mass of the cantilevers and thus their natural frequencies. The remains are verified by optical inspection as already shown previously in Figure

4.13. Also, in Table 4.3 of Section 4.2, it has been verified that the size of these remains are large enough to create stated differences in the natural frequencies.

4.6.2 Analysis of Shift in Time in the Actuation of the Cantilevers

In Section 4.6, it has been shown that the overall output voltage from the device is attenuated and distorted from being a sinusoid. This is mainly caused by the difference in the release heights of the cantilevers that result in time shift or phase angle difference in the generated voltage of individual cantilevers. The time shift and phase angle difference are related to each other with the damped natural frequency of the cantilevers and is determined by the following equation.

$$\Delta t = \frac{\Delta\phi}{\omega_d} \quad (4.7)$$

where Δt , $\Delta\phi$ and ω_d are the time and phase angle difference and damped natural frequency of the cantilevers, respectively. The phase angle difference is a quantity that is much easier to interpret, for example a given quantity of Δt might not be as meaningful as stating the $\Delta\phi$. For example, stating that $\Delta\phi = 180^\circ$ between two cantilevers directly implies that the overall output from these two cantilevers are zero, since the positive and negative intervals of these two decaying out sinusoidal signals directly overlap then. Table 4.12 also tabulates sample values of time and frequency shift and corresponding release height difference, Δz , for a nominal release height of $z = 200 \mu\text{m}$, a damped natural frequency of $\omega_d = 1500 \text{ Hz}$ and an excitation frequency of $f = 100 \text{ Hz}$.

Table 4.12. Sample values relating time and phase shift to release height difference for a damped natural frequency of $\omega_d=1.5 \text{ kHz}$ and $f=100 \text{ Hz}$.

$\Delta t (\Delta\Phi)$	0.17 ms (90°)	0.33 ms (180°)	0.67 ms (360°)
$\Delta z (z=200 \mu\text{m})$	14 μm	25 μm	56 μm

From the tabulated values above, it can be seen that a release height difference of only 25 μm would create a phase angle difference of 180°.

Figure 4.43 shows the graphical calculation of the release height difference, Δz for sample set of values. The figure shows the absolute positions of magnet and two cantilevers about the release point. The release height difference is graphically determined from the intersection of the positions of the cantilevers with the position of the magnet. Individual release heights are determined from the graph then they are subtracted analytically from each other to obtain their difference. It is also possible to find analytical approaches, but the graphical method presented here is more practical.

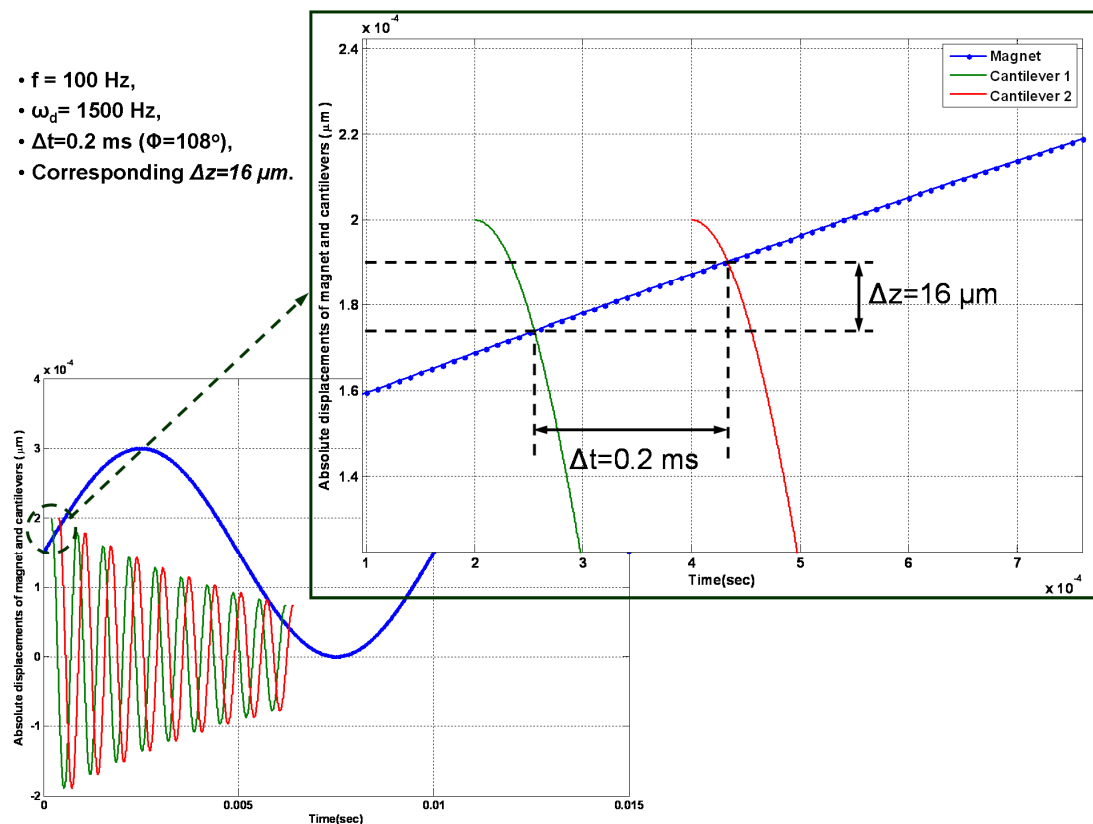


Figure 4.43. Graphical approach showing the calculation of the release height difference, Δz .

In order to give some realistic values, Table 4.13 shows some typical experimental values of time difference Δt (and phase difference $\Delta\phi$) and corresponding release height difference Δz .

Table 4.13. Experimental values showing time shift, Δt and corresponding release height difference, Δz .

Figure #	ω_d (Hz)	Δt (ms)	Φ (deg.)	Δz (z=200 μm)	Effect on output
4.38	1515	0.1	54°	8 μm	⊖
4.34	1562	0.1	56°	9 μm	⊖
4.35	1515	0.2	109°	17 μm	⊖
4.36	1515	0.03	16°	3 μm	⊕
4.39	1538	0.05	28°	5 μm	⊕

From Table 4.13 it can be seen that there is an inaccuracy of 3 μm to 17 μm in the attachment of magnet to diaphragm and/or spacers that result in a time shift of 0.03 ms (16°) to 0.2 ms (109°), respectively. Test results show that a time shift more than 0.1 ms attenuates the overall output of the cantilevers. These results are graphically given previously in Section 4.6 and corresponding figure numbers are listed in the first column of Table 4.13.

There can be two possible reasons affecting the release height of the cantilevers. One of them is the variation in the stiffness of the cantilevers, which is inversely proportional with the release height of the cantilevers, $z \propto \frac{1}{k_{eq}}$, and the other can be due to the varying distance between each cantilever and the magnet which is caused by manual attachment of the components by epoxy.

Table 4.14 shows the necessary variation in the parameters of the cantilevers to create a difference in the stiffness of the cantilevers and time shift.

Table 4.14. Necessary variation required in the equivalent stiffness term to cause corresponding time shift.

Figure #	Δt (ms)	Δz ($z = 200$ μm)	$(z + \Delta z)/z$	Δk_{eq} ($k_{\text{eq}} = 1 \text{ N/m}$)	ΔL ($L = 1000$ μm)	Δh ($h = 15$ μm)	Effect on output
4.38	0.1	8 μm	1.04	0.04 N/m	13 μm	0.20 μm	\otimes
4.34	0.1	9 μm	1.05	0.05 N/m	15 μm	0.22 μm	\ominus
4.35	0.2	17 μm	1.09	0.09 N/m	28 μm	0.41 μm	\otimes
4.36	0.03	3 μm	1.02	0.02 N/m	5 μm	0.08 μm	\odot
4.39	0.05	5 μm	1.03	0.03 N/m	8 μm	0.12 μm	\odot

The parameter variations calculated from experimental data and given in the table above are all within the tolerance of the micro fabrication steps. Thus, they can not be a reason of the release height difference. Another possible reason of the release height difference is the different relative distances from each cantilever to the magnet that is caused due to manual attachment of the components by epoxy. During the manual application of the epoxy by hand, the topology of it can be made smooth up to a certain extend that would create tilt on the mating surfaces that are attached. In order show whether such a tilt exists, the vertical height of each side of the magnet assembly is measured under the probe station that is illustrated in Figure 4.44. The height of each corner is measured with respect to the smooth PCB surface. Then the height difference between consecutive cantilevers is calculated from similar triangles, using the following equation,

$$\Delta z_{ij} = \Delta h_{ij} \frac{\Delta d}{\Delta r} = \Delta h_{ij} \frac{500}{7000} \quad (4.8)$$

where Δh_{ij} is the difference in the heights of the corners with respect to the PCB base i.e. $\Delta h_{ij} = h_{kl} - h_{ij}$ and Δz_{ij} is the corresponding height difference between the height of each cantilever with respect to the diaphragm. In the final expression, i, j, k, and l represent the corner numbers and in (4.8) the terms Δd and Δr correspond to the horizontal distance between each cantilever and corner in μm , respectively. The measurements have been made from various devices and typical results are then tabulated and shown in Table 4.15.

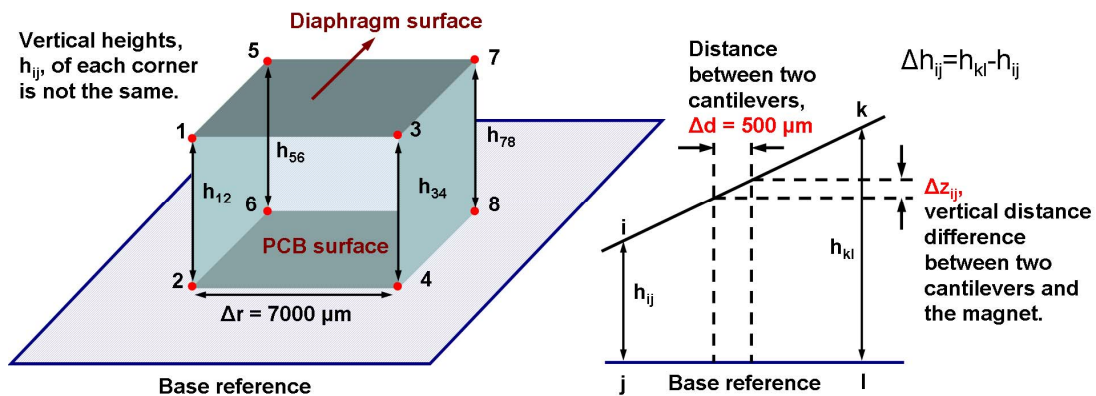


Figure 4.44. Illustration of the height difference measurement under the probe station.

Table 4.15. Results of height difference measurements under the probe station.

	h_{12}	h_{34}	h_{56}	h_{78}	$\Delta z_{ij}(\text{max.})$
Test 1	3360 μm	3690 μm	3500 μm	3530 μm	11 μm
Test 2	3810 μm	3490 μm	3380 μm	3490 μm	31 μm

In the final table given above, the maximum height variation, Δz_{ij} (max.), in each data set is shown. The measurements show that the vertical height difference between the cantilevers and the magnet are compatible with the ones derived from

the time difference values tabulated in Table 4.14. This proves that indeed, the time differences between the cantilevers are due to the manual attachment of the device components such as the spacers, magnet, and diaphragm.

Finally, Figure 4.45 shows the optimum device configuration for the FUC design to have the best performance out of it. This configuration is determined according to the test results that have been carried out so far. In the optimum configuration of the device a total number of 3 cantilevers magnets and 3 spacers are used. According to this configuration there is an initial gap of about 200 μm between the bottom surface of the magnet and the tip of the cantilevers. Also, it has been observed that if the magnet-diaphragm assembly is misaligned by 200-350 μm then better results can be obtained. However, then due to this misalignment, only 10 cantilevers would be operating instead of 20.

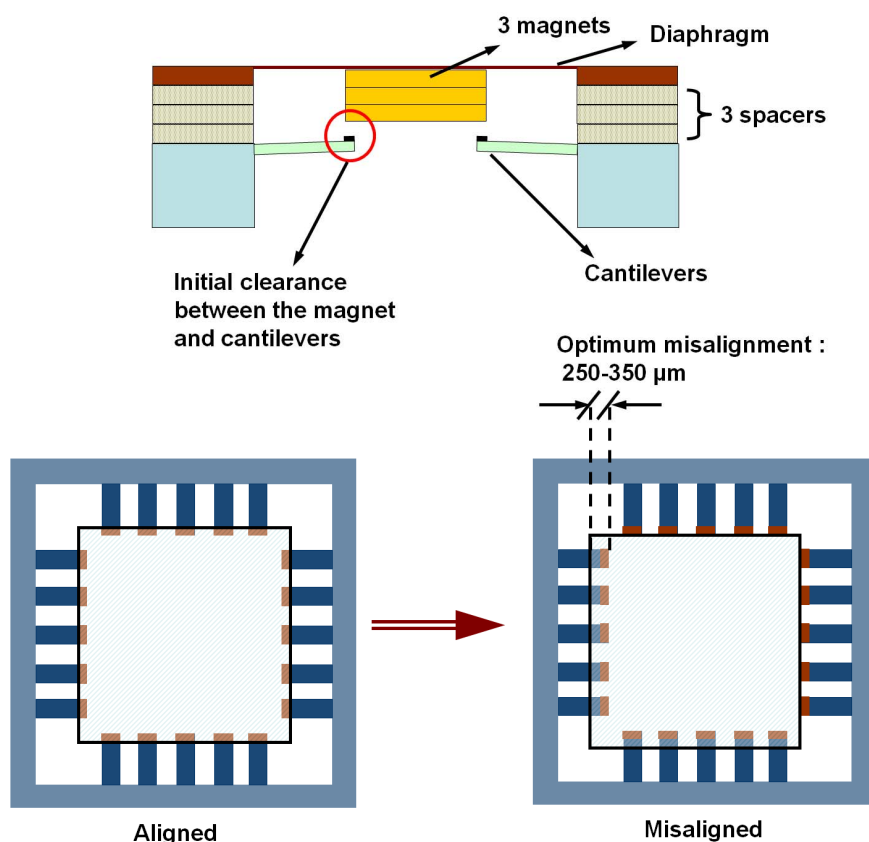


Figure 4.45. Optimum device configuration for the fabricated batch.

4.7 Conclusions

In this chapter, the test of the designs proposed in this thesis study has been presented. All the conceptual designs have shown to be working as expected; the array of cantilevers (AOC) and large mass coil (LMC) designs are effective around a single frequency and it is possible to increase the bandwidth by the array of cantilevers design with varying natural frequencies (AOC_FS). A frequency detecting sensor has also been proposed and tested developed on the basis of the array of cantilevers design with varying natural frequencies (AOC_FS). The most important design of the study is the frequency up-converter (FUC) design since it is quite a tedious job to mechanically operate such a design in micro scale. It has been shown with the test results that this design is indeed operational in micro scale and much more effective than traditional micro generators.

The reasons of possible causes of deviations between the estimated and measured results have also been investigated in detail. The tests are carried out using a shaker table, which is specially purchased for the test of the fabricated devices. In general the deviations between the estimated and measured voltage outputs arise from the thermal grease residues remaining after the release of the devices. These remains change the natural frequency of the cantilevers used in the designs and cause the overall voltage output to degrade. In the case of the frequency up-converter (FUC) design there is also the problem of manual coupling of the base and the diaphragm-magnet assemblies that causes inaccuracies in the release height of the cantilevers.

The study is concluded at this point with discussions and future recommendations that are presented in the next chapter.

CHAPTER 5

CONCLUSIONS AND FUTURE WORK

In this thesis study, electromagnetic type micro energy harvesters have been designed, fabricated and tested for performance. Mainly four types of designs have been proposed and three of these designs are investigated for the first time in the literature. The names, short definitions and important properties of these designs can be listed as follows:

1. The first design considered is the array of cantilevers (AOC) design that is composed of identical parylene cantilevers on which coils are fabricated. This generator is proposed for the first time in the literature and the main aim of it is voltage and power generation around a single excitation frequency that is close to the resonance frequency of the cantilevers. In the proposed design, the coils are connected electrically in series so that the induced voltage can be summed-up to increase the overall voltage levels. Tests show that a maximum voltage of 0.67 mV at 3.4 kHz with a power level of 56 pW can be obtained from a single cantilever of the proposed design in a bandwidth of 140 Hz. Voltage and power levels can be increased by simply increasing the number of coil turns and the cantilevers.
2. The second proposed design is the array of cantilevers design with varying natural frequencies (AOC_FS), which is based on the array of cantilevers design (AOC). In this case the cantilever lengths are varied such that the overall bandwidth of the proposed generator is 1 kHz. This is done to make the generator effective in a wider frequency range unlike traditional single frequency designs. The tests show that, indeed by implementing such a system, the bandwidth can be increased to 1 kHz with maximum continuous

voltage and power output of levels of 9 mV and 1.7 nW, respectively, from all of the cantilevers.

Based upon this design, an energy harvesting MEMS frequency sensor has also been proposed and tested. This structure has the ability to harvest energy using the scheme explained above and it can also detect and output the frequency of the environment using a microcontroller. The harvested energy is used to support the power supply of the microcontroller. Such a design has many benefits over battery powered sensors. It is a self sufficient system and there will be no need to change the batteries, and it can be operated in harsh and complex structures where it is hard to reach and replace the sensor.

3. The large mass coil (LMC) design is the third design that is proposed and tested within the scope of this study. Although this generator has its own original mechanical design, conceptually it has been extensively investigated in literature widely. This generator is composed of two; a diaphragm-magnet assembly oscillating with environmental vibrations and a stationary coil base for voltage generation. Tests show that 0.3 mV can be generated at a vibration frequency of 113 Hz with a power output level of 40 pW. The main aim of this design is to be a benchmark model for the next proposed design which is the frequency up-converter (FUC).
4. The frequency up-converter (FUC) design is the final generator that is proposed within the scope of this study. It is the first time in literature that this design is proposed and shown to work in micro scale. It is composed of two components; the base that constitutes an array of cantilevers with ferromagnetic tips and a diaphragm-magnet assembly at the top. The operation of this structure is already explained in detail in the previous sections, so it will not be repeated here. The aim of implementing such a design is to up-convert mechanical input frequency to a higher frequency where more voltage and power would be generated. The proposed generator is fabricated in micro scale and tested for performance. Tests results show

that the frequency up-conversion is realized in micro scale and a maximum voltage and power level of 0.57 mV and 0.25 nW can be obtained, respectively, from a single cantilever of the device at an excitation frequency of 113 Hz. This shows that even a single cantilever of the proposed design is much more effective than the traditional large mass coil (LMC) design and proves the effectiveness of the generator.

Table 5.1 summarizes important performance parameters of the micro generators considered in this study.

Table 5.1. Important performance parameters of the micro generators.

Name of the design	Excitation frequency and amplitude	Voltage output (*)	Energy collected in 1 s (*)	Power output (*)
Array of cantilevers design	3.45 kHz, 0.97 μm	0.67 mV	Not measured.	56 pW
Array of cantilevers design with varying natural frequencies	3.5–4.5 kHz, 45 g	3 to 9 mV in various tests.	Not measured.	0.2 to 1.7 nW in various tests.
Large mass coil design	113 Hz, 45 g	0.3 mV	23 pJ	40 pW
Frequency up-converter design	113 Hz, 40 g	0.57 mV	20 pJ	0.25 nW

(*) From a single cantilever except for the large mass coil design.

After summarizing the performance of the designs, the achievements of this thesis study can be listed as,

1. The design, optimization, fabrication and implementation of micro electromagnetic type energy harvesters are presented. It has been proved that the proposed generators operate as designed and they are capable of generating voltage and power in micro scale by environmental vibrations.

Also, a new micro fabrication procedure is developed and implemented to fabricate the designed generators.

2. The use of parylene as a structural material for the cantilevers and the diaphragms is introduced, which enables increased deflections before mechanical failure compared to silicon.
3. The array of cantilevers concept is introduced that enables increased voltage generation without increasing the device volume by simply multiplying the number of cantilevers or increasing the number of coil turns.
4. The bandwidth of the traditional micro generators is increased so that they are effective in a much wider frequency range.
5. A new type of self sufficient and standalone sensor concept is introduced that can operate without need to replace the batteries. The sensor itself is actually an energy harvester in this case.
6. The frequency up-conversion concept is implemented and realized in micro scale for the first time in the literature. It has been shown that the efficiency of the micro energy harvesters can be increased by implementing such a design that is capable of converting low frequency vibrations to a higher level.

This thesis work covers all the major objectives that are planned to be undertaken that were stated at the proposal of the study. However, there are still some points that can be improved or advised to be done as a future work. Some of these points can be listed as:

1. During the modeling and designing stage of the micro generators, second order equivalent models are used for simulation and optimization purposes. However some of the parameters are quite nonlinear and complex to estimate using equivalent models such as the damping ratio and the magnetic flux density. These parameters cause deviations between the estimated and test

results. One possible solution can be to use finite element models and integrate them into simulation steps, which would also increase the solution time for the simulations and complexity of the models used.

2. Thermal (cool) grease (CGR 7016 from AI Technology Inc.) is used at the final step of the fabrication and it is quite hard to clean it after its application. Although various solvents like acetone, isopropyl alcohol (IPA) and methyl-ethyl-ketone (MEK) have been tried, still traces of it are left on the devices that changed the characteristics of the cantilevers. In the future, it would be beneficial to replace it with an equivalent substance that can be cleaned more easily such as Cool Pad (CP 7506 from AI Technology Inc.) or Crystal Bond (555 HMP from SPI Supplies and Structure Probe Inc.). These two substances have never been tried, but they might be good alternatives to start with in the future as a replacement material for thermal grease. If none of these work, then one possible solution would be to change the through etch recipe of the Si wafer in the final fabrication step from dry etching by DRIE to anisotropic wet etching.
3. The frequency up-converter (FUC) design requires a ferromagnetic material to be deposited at the tip point of the cantilevers for magnetic interaction of the cantilevers with the magnet. For this purpose nickel (Ni) is deposited by electroplating. However, deposited nickel (Ni) area is very small compared to the overall area of the wafer. This results in the maximum instantaneous current passing through the wafer during Ni deposition to be uncontrollable by the current controller and results in non-uniform deposition of nickel (Ni). One solution could be to electroplate Ni in dummy areas to reduce the ratio of deposited areas, which would require a new mask. Another solution to this problem could be to use sputtering instead of electroplating. By this way alternative materials such as mu-metal or permalloy with very high relative permeability could also be used so that the magnetic force between the magnet and the magnetic actuation are would be increased. However,

sputtering a ferromagnetic material requires the sputtering tool at METU-MET facilities to be modified, which would be quite costly.

4. One final improvement about the fabrication of the micro generators would be to use diluted AZ 400K developer (in dilutions of 1:4 or 1:3) from MicroChemicals Inc. instead of the AZ 826 MIF developer from the same company that is used to develop the thick photoresist AZ 9260. This is a quite bulky and thick photoresist and is used extensively during the fabrication procedure. However, due to its properties, development of it is quite hard with the AZ 826 MIF developer. It has been later discovered that AZ 400 K can better suit for this application.
5. The manual assembly of the components of the frequency up-converter (FUC) design, such as the combination of the magnet to the diaphragm and the attachment of the spacers to the base and the magnet-diaphragm subassembly reduces the accuracy of the relative positions of these components with respect to each other. This results in cantilevers to be released at different times and overall output to degrade considerably. Either a more accurate assembly mechanism should be developed or the cantilevers on each side should be fabricated as a single body to avoid the aforementioned problem.
6. Some of the physical parameters of the designs were not able to be measured due to the lack of necessary measuring devices. Thus, it would be good to use measuring equipments like laser inferometer to measure the displacement and track the motion of the devices under operation and a gaussmeter to measure the magnetic flux density. These parameters can then be used to better understand the physics of the devices and also back calculate the amount of voltage and power generated by the generators to reduce the amount of deviation between the simulation and test results.
7. During the tests of the frequency up-converter (FUC), it has been discovered that misalignment of the magnet-diaphragm assembly with respect to the

cantilevers results in better catch and release, but this reduces the total number of active cantilevers. Instead, either increasing the magnet area or cantilever length would be a better solution. Also increasing the length of diaphragm arms would result in better linear approximation for the motion of the diaphragm-magnet assembly.

8. Another improvement for the frequency up-converter (FUC) design can be to modify the coil locations on the cantilevers. It has been sometimes observed that coils are broken due to physical impact with the magnet. The effect of this impact can be reduced by fabricating the coil turns as close to the neutral axis of the cantilevers as possible. This would reduce the stress on the coils due to bending. However, doing so would also make it hard to have the contact from the first metal layer to the second metal layer due to increased via depth.
9. It would always be a good practice to find ways of increasing the output voltage levels from the generators. From the mathematical analysis and tests done so far, this can be achieved in three different ways:
 - a. The first and most straightforward one would be to simply increase the number of coil turns by decreasing the coil width. However, increasing coil turns would also require the fabrication accuracy to be increased due to decreased coil width or increase the device size due to increased coil area. Also there is the problem of increased impedance, which may create a problem in matching the coil and load impedances, but this can be overcome by simply depositing thicker coil turns for example by electroplating to reduce the coil impedance.
 - b. As a second alternative coil layers can be added on top of each other as an apartment within the same cantilever. This would also be an effective solution, but it would certainly increase the fabrication time of the devices.

- c. The final alternative would be to increase the coil area by using cantilevers with larger surface areas. However, this would result in device dimensions to increase.
10. As a final future improvement, the proposed designs can be conceptually brought one step further if a signal condition circuitry is added to the overall architecture so that the output from the generators can be converted from AC to DC signals usable by a device. After initial design and testing of the electrical circuitry, it can then be fabricated by preferably CMOS allowing the devices to be fabricated right on top of the CMOS chip (Post-CMOS) to make a compact single device. As a final product, the resulting design can be integrated to for example a sensor to make a fully functional system e.g. a pressure sensor embedded in a car tire that is powered only with the proposed generators.

This thesis study is concluded here with the achievement of the objectives stated before. There are still some points that can be investigated as a future study, which are listed above. It is believed that, the results presented in this thesis study can be used to design and fabricate much effective micro energy generators in the future.

REFERENCES

1. R. Amirtharajah, J. Collier, J. Siebert, B. Zhou, and A. Chandrakasan, “DSPs for energy harvesting sensors: Applications and architectures,” IEEE Pervasive Computing, vol. 4, pp. 72-79, Jul-Sep 2005.
2. P. Glynne-Jones, M.J. Tudor, S.P. Beeby, and N.M. White, “An electromagnetic, vibration-powered generator for intelligent sensor systems,” Sensors and Actuators a-Physical, vol. 110, pp. 344-349, Feb 1 2004.
3. S. Roundy, “Energy Scavenging for Wireless Sensor Nodes with a Focus on Vibration to Electricity Conversion,” Ph. D. Thesis in Mechanical Engineering, University of California, Berkeley, 2003.
4. A.D. Joseph, A. Kansal, M.B. Srivastava, J. Randall, T. Buren, G. Troster, T.J. Johnson, W.W. Clark, L. Mateu, and F. Moll, “Energy Harvesting Projects,” Pervasive Computing, IEEE, vol. 4, issue 1, pp.69-71, 2005.
5. J.A. Paradiso and T. Starner, “Energy Scavenging for Mobile and Wireless Electronics,” IEEE Pervasive Computing, vol. 4, issue 1, pp. 18-27, 2005.
6. Wireless sensors-buyer beware, April 2001. Available from <http://www.sensorsmag.com/articles/0401/18/index.htm>.
7. H. Kulah and K. Najafi, “An electromagnetic micro power generator for low-frequency environmental vibrations,” Micro Electro Mechanical Systems, 2004. 17th IEEE International Conference on MEMS, pp. 237-240.
8. E. P. James, M. J. Tudor, S. P. Beeby, N. R. Harris, P. Glynne-Jones, J. N. Ross, and N. M. White, “An investigation of self-powered systems for

- condition monitoring applications," Sensors and Actuators a-Physical, vol. 110, pp. 171-176, Feb 1 2004.
9. J.M.H. Lee, S.C.L. Yuen, W.J. Li, and P.H.W. Leong, "Development of an AA size energy transducer with micro resonators," Circuits and Systems, 2003. ISCAS '03. Proceedings of the 2003 International Symposium on Volume 4, 25-28 May 2003, pp.876-879.
 10. C.B. Williams and R.B. Yates, "Analysis of a micro-electric generator for microsystems," Physica A 52 (1/3), pp. 8–11, 1996.
 11. F. Peano and T. Tambosso, "Design and Optimization of a MEMS Electret-Based Capacitive Energy Scavenger," Journal of Microelectromechanical Systems, vol. 14, No. 3, pp. 429-435, 2005.
 12. S. Roundy, P. K. Wright, and J. Rabaey, "A study of low level vibrations as a power source for wireless sensor nodes," Computer Communications, vol. 26, pp. 1131-1144, Jul 1 2003.
 13. M. Mizuno and D.G. Chetwynd, "Investigation of a resonance microgenerator," J. Micromech. Microeng. vol. 13, pp.209-216, 2003.
 14. S. Roundy, P.K. Wright, and K.S.J. Pister, "Micro-Electrostatic Vibration-to-Electricity Converters," ASME IMECE, New Orleans, Louisiana, 2002.
 15. A. Nounou and H.F. Ragaie, "A lateral comb-drive structure for energy scavenging," Electrical, Electronic and Computer Engineering, ICEEC '04 International Conference, pp. 553 – 556, 2004.
 16. P. D. Mitcheson, P. Miao, B. H. Stark, E. M. Yeatman, A. S. Holmes, and T. C. Green, "MEMS electrostatic micropower generator for low frequency operation," Sensors and Actuators a-Physical, vol. 115, pp. 523-529, Sep 21 2004.
 17. T. Sterken, P. Fiorini, K. Baed, R. Puers, and G. Borghs, "An Electret-Based Electrostatic μ -Generator," 12th International Conference on Solid State Sensors, Actuators and Microsystems, Boston, pp. 1291-1294, 2003.

18. S. Meninger, J. O. Mur-Miranda, R. Amirtharajah, A. P. Chandrakasan, and J. H. Lang, “Vibration-to-electric energy conversion,” IEEE Transactions on Very Large Scale Integration (VLSI) Systems, vol. 9, pp. 64-76, Feb 2001.
19. B. C. Yen and J. H. Lang, “A variable-capacitance vibration-to-electric energy harvester,” IEEE Transactions on Circuits and Systems I-Regular Papers, vol. 53, pp. 288-295, Feb 2006.
20. W. Ma, L. Rufer, Y. Zohar, and M. Wong, “Design and Implementation of an Integrated Floating-Gate Electrostatic Power Micro-Generator,” The 13th International Conference on Solid-State Sensors, Actuators and Microsystems, Transducers’05, Seoul, Korea, June 5-9, 2005, pp. 299-302.
21. S. Roundy, E. S. Leland, J. Baker, E. Carleton, E. Reilly, E. Lai, B. Otis, J. M. Rabaey, P. K. Wright, and V. Sundararajan, “Improving power output for vibration-based energy scavengers,” IEEE Pervasive Computing, vol. 4, pp. 28-36, Jan-Mar 2005.
22. P. Glynne-Jones, S. P. Beeby, and N. M. White, “Towards a piezoelectric vibration-powered microgenerator,” Iee Proceedings-Science Measurement and Technology, vol. 148, pp. 68-72, Mar 2001.
23. G. Poulin, E. Sarraute, and F. Costa, “Generation of electrical energy for portable devices Comparative study of an electromagnetic and a piezoelectric system,” Sensors and Actuators a-Physical, vol. 116, pp. 461-471, Oct 29 2004.
24. T. Sterken, K. Baert, C. Van Hoof, R. Puers, G. Borghs, and P. Fiorini, “Comparative modeling for vibration scavengers,” Sensors, Proceedings of IEEE, vol. 3, pp.1249-1252, 2004.
25. N.S. Shenck and J.A. Paradiso, “Energy Scavenging with Shoe-Mounted Piezoelectrics,” IEEE Micro, vol.21, issue 3, pp. 30-42, 2001.
26. S. Roundy, B.P. Otis, Y. Chee, J.M. Rabaey, and P. Wright, “A 1.9 GHz Transmit Beacon using Environmentally Scavenged Energy,” ISPLED 2003, August 25-27, 2003, Seoul, Korea.

27. A. Lal, R. Duggirala, and H. Li, "Pervasive power: A radioisotope-powered piezoelectric generator," IEEE Pervasive Computing, vol. 4, pp. 53-61, Jan-Mar 2005.
28. Y. B. Jeon, R. Sood, J. H. Jeong, and S. G. Kim, "MEMS power generator with transverse mode thin film PZT," Sensors and Actuators A-Physical, vol. 122, pp. 16-22, Jul 29 2005.
29. J. Kang, H. Kim, J. Kim, and T. Kim, "Optimal Design of Piezoelectric Cantilever for a Micro Power Generator with Microbubble," 2nd Annual International IEEE-EMBS Special Topic Conference on Microtechnologies in Medicine & Biology, May 2-4, 2002, Madison, Wisconsin, USA, pp. 424-427.
30. D. Guyomar, A. Badel, E. Lefevre, and C. Richard, "Toward energy harvesting using active materials and conversion improvement by nonlinear processing," IEEE Transactions on Ultrasonics Ferroelectrics and Frequency Control, vol. 52, pp. 584-595, Apr 2005.
31. C.G. Xu, T.S. Fiez, and K. Mayaram, "Nonlinear finite element analysis of a thin piezoelectric laminate for micro power generation," Journal of Microelectromechanical Systems, vol. 12, pp. 649-655, Oct 2003.
32. J. Han, A. Jouanne, T. Le, K. Mayaram, and T.S. Fiez, "Novel Power Conditioning Circuits for Piezoelectric Micro Power Generators", Applied Power Electronics Conference and Exposition, 2004, APEC '04, pp.1541-1546.
33. G.A. Lesieutre, G.K. Ottman, and H.F. Hofmann, "Damping as a result of piezoelectric energy harvesting," Journal of Sound and Vibration, vol. 269, pp. 991-1001, Jan 22 2004.
34. M. Renaud, T. Sterken, P. Fiorini, R. Puers, K. Baert, and C. Hoof, "Scavenging Energy from Human Body: Design of a Piezoelectric Transducers," The 13th International Conference on Solid-State Sensors, Actuators and Microsystems, Transducers'05, Seoul, Korea, June 5-9, 2005, pp. 784-787.

35. E.S. Leland, E.M. Lai, and P.K. Wright, "A Self-Powered Wireless Sensor for Indoor Environmental Monitoring," Symposium, University of Texas, Austin, 20-22 October, 2004.
36. E.S. Leland, and P.K. Wright, "Resonance tuning of piezoelectric vibration energy scavenging generators using compressive axial preload," Smart Materials & Structures, vol. 15, pp. 1413-1420, Oct 2006.
37. M. Ferrari, V. Ferrari, M. Guizzetti, D. Marioli, and A. Taroni, "Piezoelectric multifrequency energy converter for power harvesting in autonomous microsystems," Sensors and Actuators A-Physical, vol. 142, pp. 329-335, Mar 10 2008.
38. S. Roundy, "Energy scavenging for wireless sensor nodes with a focus on vibration-to-electricity conversion," Ph. D. thesis presentation, University of California, Berkeley, 2003.
39. I. Sari, T. Balkan and H. Kulah, "Design and optimization of an electromagnetic micro energy scavenger with parylene cantilevers," PowerMEMS 2007, Freiburg, Germany, November 28-29, 2007, pp. 81-84.
40. C.B. Williams, R.C. Woods, and R.B. Yates, "Feasibility study of a vibration powered micro-electric generator," Compact Power Sources (Digest No. 96/107), IEE Colloquium on, 8 May 1996, pp. 7/1 - 7/3.
41. C. Shearwood and R.B. Yates, "Development of an electromagnetic micro-generator," Electronics Letters, 23rd October 1997, vol. 33, no. 22, pp. 1883-1884.
42. M. El-hami, R. Glynne-Jones, N. M. White, M. Hill, S. Beeby, E. James, A. D. Brown, and J. N. Ross, "Design and fabrication of a new vibration-based electromechanical power generator," Sensors and Actuators a-Physical, vol. 92, pp. 335-342, Aug 1 2001.

43. P. D. Mitcheson, T. C. Green, E. M. Yeatman, and A. S. Holmes, "Architectures for vibration-driven micropower generators," *Journal of Microelectromechanical Systems*, vol. 13, pp. 429-440, Jun 2004.
44. T. von Buren, P. D. Mitcheson, T. C. Green, E. M. Yeatman, A. S. Holmes, and G. Troster, "Optimization of inertial micropower generators for human walking motion," *Ieee Sensors Journal*, vol. 6, pp. 28-38, Feb 2006.
45. S.C.L. Yuen, J.M.H. Lee, M.H.M. Luk, G.M.H. Chan, K.F. Lei, P.H.W. Leong, W.J. Li, and Y. Yam, "AA size micro power conversion cell for wireless applications," *Proceedings of the 5th World Congress on Intelligent Control and Automation*, June 15-19, 2004, Hangzhou, P.R. China.
46. M. Duffy and D. Carroll, "Electromagnetic generators for power harvesting," *Power Electronics Specialists Conference, 2004. PESC 04. 2004 IEEE 35th Annual Volume 3*, pp. 2075-2081, 2004.
47. W.J. Li, T.C.H. Ho, G.M.H. Chan, P.H.W. Leong, and H.Y. Wong, "Infrared signal transmission by a laser-micromachined, vibration-induced power generator," *Circuits and Systems, Proceedings of the 43rd IEEE Midwest Symposium*, vol. 1, pp. 236-239, 2000.
48. N. N. H. Ching, H. Y. Wong, W. J. Li, P. H. W. Leong, and Z. Y. Wen, "A laser-micromachined multi-modal resonating power transducer for wireless sensing systems," *Sensors and Actuators a-Physical*, vol. 97-8, pp. 685-690, Apr 1 2002.
49. R. Amirtharajah and A. P. Chandrakasan, "Self-powered signal processing using vibration-based power generation," *Ieee Journal of Solid-State Circuits*, vol. 33, pp. 687-695, May 1998.
50. Product specifications, Parylene knowledge, Specialty Coating Systems, Inc. IN, USA, 1-800-356-8260.

51. I. Sari, T. Balkan, and H. Kulah, "A wideband electromagnetic micro power generator for wireless microsystems," *Transducers 2007*, vol.1, pp. 275-278, June 2007.
52. I. Sari, T. Balkan and H. Kulah, "An Electromagnetic Micro Power Generator for Wideband Environmental Vibrations," *Sensors and Actuators A: Physical*, doi: 10.1016/j.sna.2007.11.021, vol. 145-146 (2008), pp. 405-413.
53. I. Sari, T. Balkan, and H. Kulah, "An energy harvesting MEMS frequency detector," *6th IEEE Conference on Sensors (IEEE SENSORS 2007)*, Atlanta, USA, October 28-31, 2007, pp. 1460-1463.
54. H. Hosaka, K. Itao, and S. Kuroda, "Evaluation of energy dissipation mechanisms in vibrational microactuators," *Micro Electro Mechanical Systems, 1994, MEMS '94, Proceedings, IEEE Workshop on*, Oiso, Japan, 1994, pp. 193-198.
55. S.G. Kelly, *Fundamentals of Mechanical Vibrations*, McGraw-Hill, New York, International Edition, 1993.
56. C. Serre, A. Perez-Rodriguez, N. Fondevilla, E. Martincic, S. Martinez, J. R. Morante, J. Montserrat, and J. Esteve, "Design and implementation of mechanical resonators for optimized inertial electromagnetic microgenerators," *Microsystem Technologies-Micro-and Nanosystems-Information Storage and Processing Systems*, vol. 14, pp. 653-658, Apr 2008.
57. S. Roundy, "On the effectiveness of vibration-based energy harvesting," *Journal of Intelligent Material Systems and Structures*, vol. 16, pp. 809-823, Oct 2005.
58. R.F. Fung, Y.T. Liu, and C.C. Wang, "Dynamic model of an electromagnetic actuator for vibration control of a cantilever beam with a tip mass," *Journal of Sound and Vibration*, vol. 288, pp. 957-980, Dec 20 2005.
59. L. Mateu and F. Moll, "Review of energy harvesting techniques and applications for microelectronics," *Proceedings of SPIE - The International*

- Society for Optical Engineering, v 5837 PART I, VLSI Circuits and Systems II, 2005, p 359-373.
60. E. Koukharenko, S.P. Beeby, M.J. Tudor, N.M. White, T. O'Donnell, C. Saha, S. Kulkarni, and S. Roy, "Microelectromechanical systems vibration powered electromagnetic generator for wireless sensor applications," Microsystem Technologies-Micro-and Nanosystems-Information Storage and Processing Systems, vol. 12, pp. 1071-1077, Sep 2006.
 61. N.G. Stephen, "On energy harvesting from ambient vibration," Journal of Sound and Vibration, vol. 293, pp. 409-425, May 30 2006.
 62. S. Roundy and Y. Zhang, "Toward self-tuning adaptive vibration based micro-generators," Smart Structures, Devices, and Systems II, Poceedings of SPIE Vol. 5649, pp. 373-384.
 63. D. Spreemann, Y. Manoli, B. Folkmer, and D. Mintenbeck, "Non-resonant vibration conversion," Journal of Micromechanics and Microengineering, vol. 16, pp. S169-S173, Sep 2006.
 64. S.G. Adams, F.M. Bertsch, K.A. Shaw, P.G. Hartwell, F.C. Moon, and N.C. MacDonald, "Capacitance based tunable resonators," Journal of Micromechanics and Microengineering, vol. 8, pp. 15-23, Mar 1998.
 65. E.S. Leland and P.K. Wright, "Resonance tuning of piezoelectric vibration energy scavenging generators using compressive axial preload," Smart Materials & Structures, vol. 15, pp. 1413-1420, Oct 2006.
 66. R.F.M. Marcal, M. Negreiros, A.A. Susin, and J.L. Kovaleski, "Detecting faults in rotating machines," IEEE Instrumentation & Measurement Magazine, vol. 3, pp. 24-26, Dec 2000.
 67. G.K. Singh and S.A.S.A. Kazzaz, "Induction machine drive condition monitoring and diagnostic research - a survey," Electric Power Systems Research, vol. 64, pp. 145-158, Feb 2003.

68. S. Kumar, N. Roy, and R. Ganguli, "Monitoring low cycle fatigue damage in turbine blade using vibration characteristics," *Mechanical Systems and Signal Processing*, vol. 21, pp. 480-501, Jan 2007.
69. S.D. Senturia, *Microsystem Design*, Kluwer Academic Publishers, 2001.
70. N. Maluf, and K. Williams, *Introduction to Microelectromechanical Systems Engineering*, Artech House, 2004.
71. C. B. Williams, C. Shearwood, M. A. Harradine, P. H. Mellor, T. S. Birch, and R. B. Yates, "Development of an electromagnetic micro-generator," *IEE Proceedings-Circuits Devices and Systems*, vol. 148, pp. 337-342, Dec 2001.

APPENDIX A

LAYOUT DRAWINGS

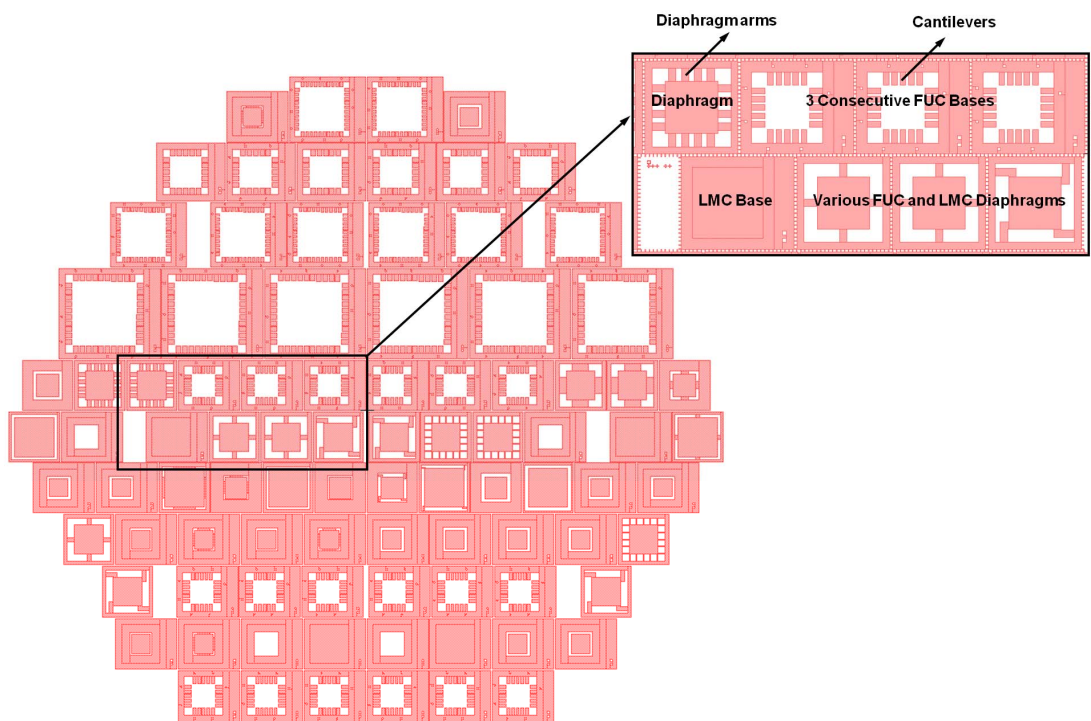


Figure A.1. Layouts of the 1st mask to fabricate cantilevers from parylene.

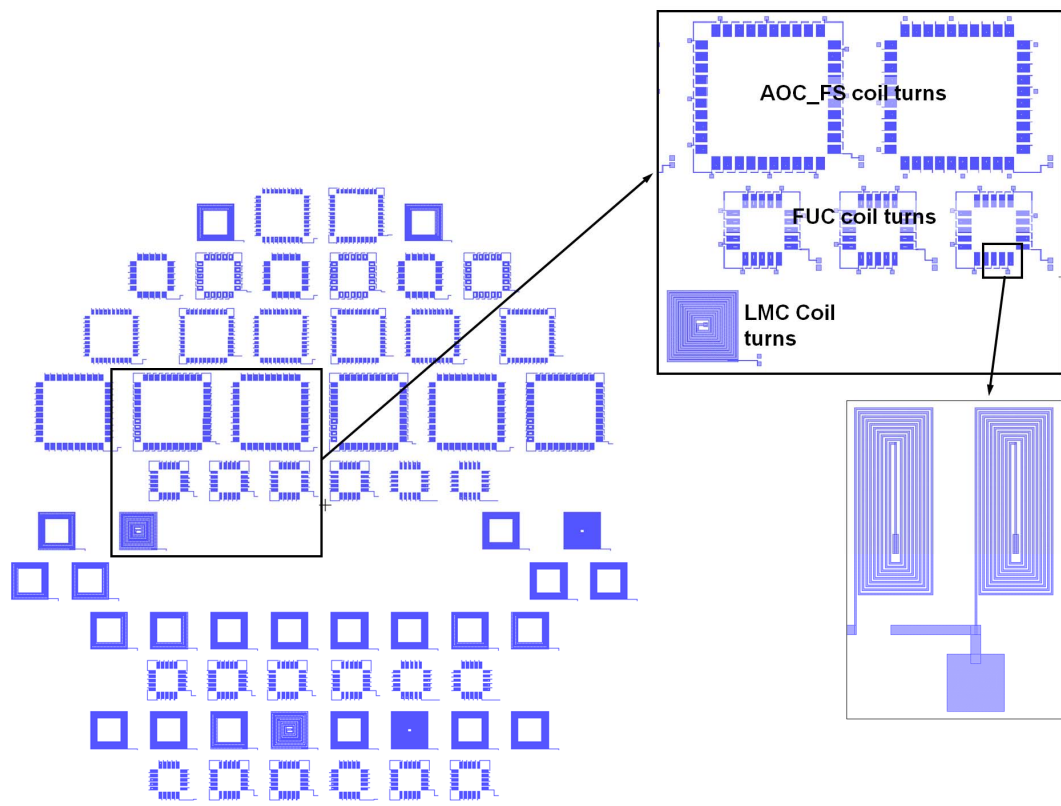


Figure A.2. Layouts of the 2nd mask to fabricate the coil turns from titanium-gold (Ti/Au).

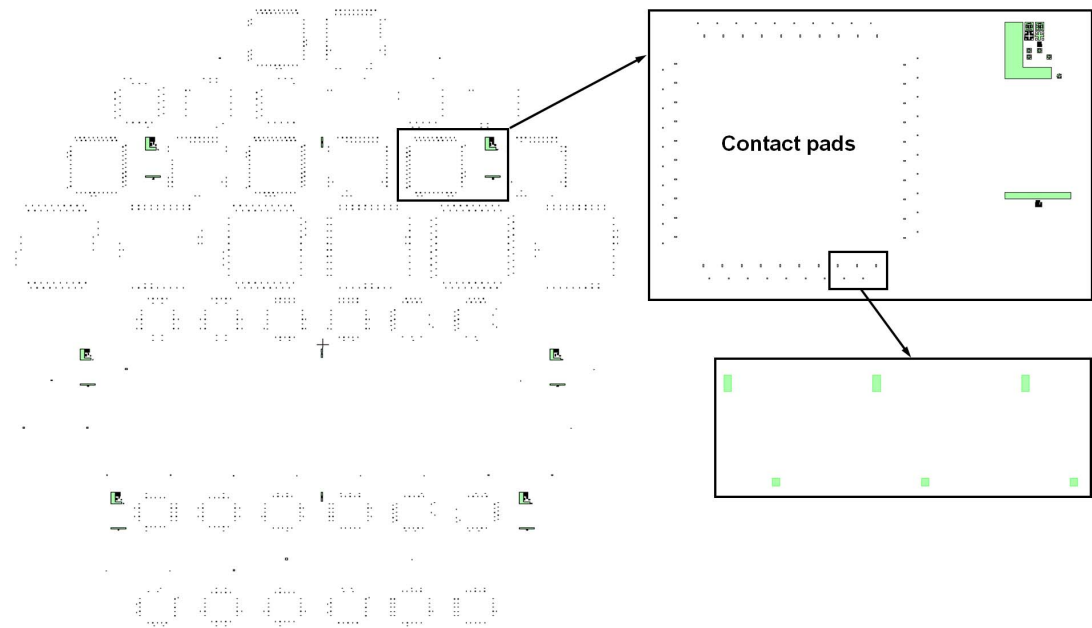


Figure A.3. Layouts of the 3rd mask to form the contact pads parylene cantilevers.

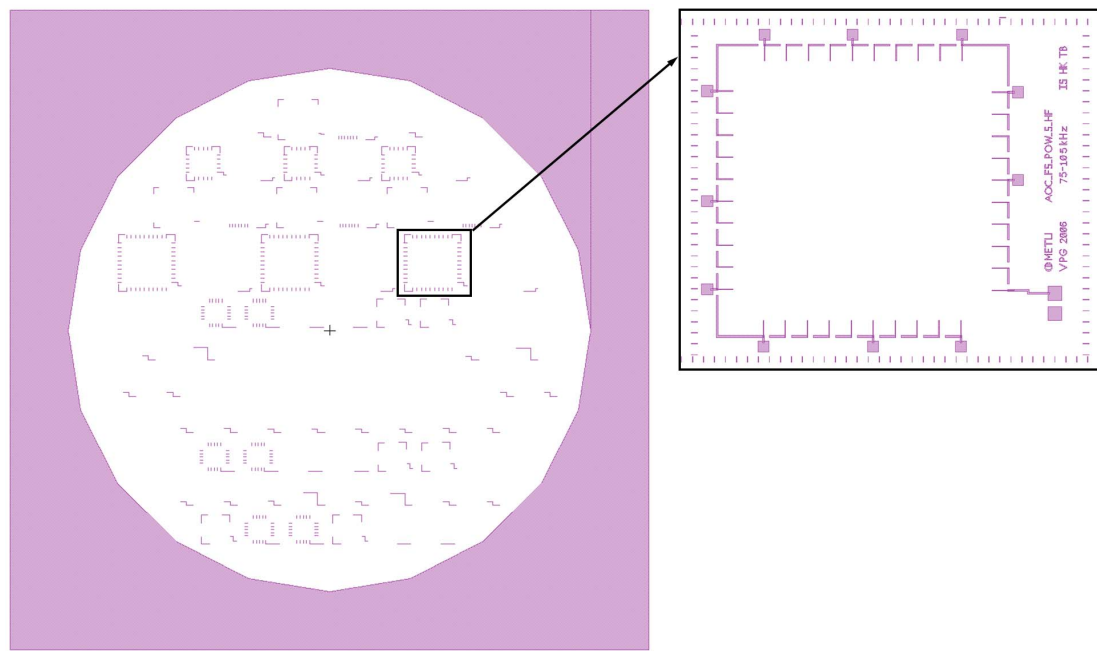


Figure A.4. Layouts of the 4th mask to fabricate the metal routes from titanium-gold (Ti/Au).

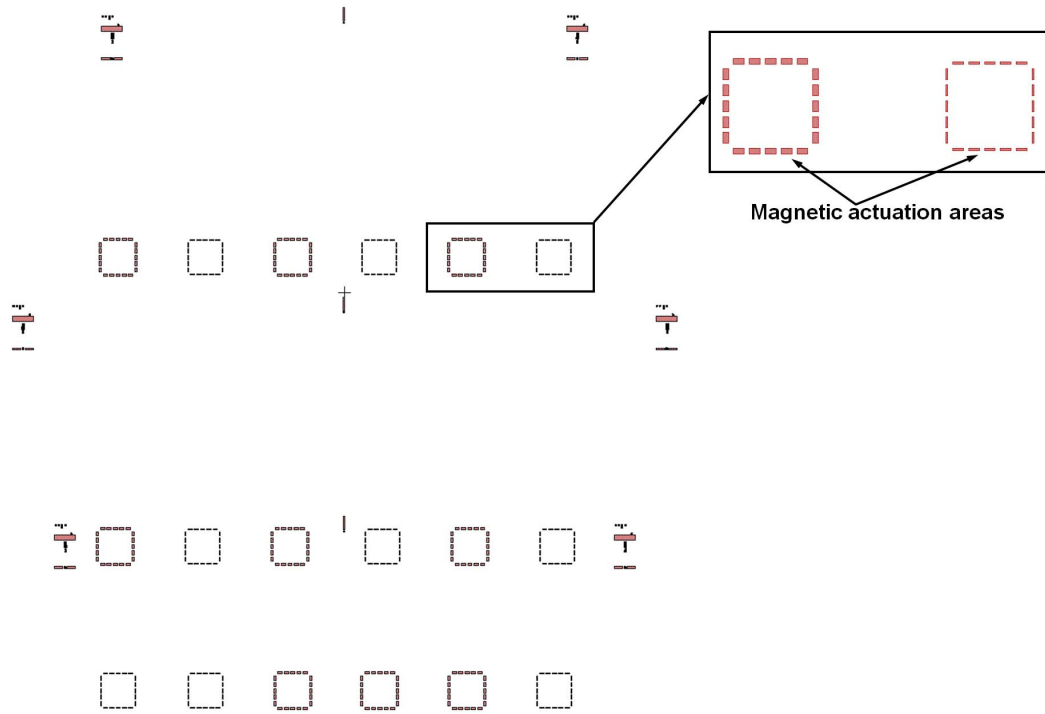


Figure A.5. Layouts of the 5th mask to fabricate the magnetic actuation areas from nickel (Ni).

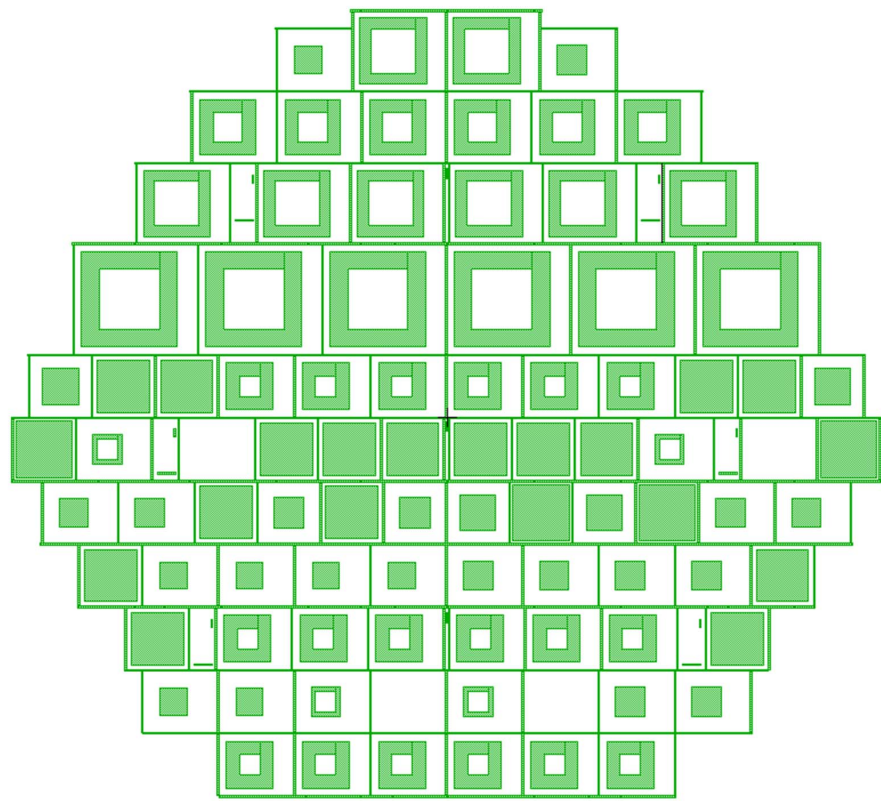


Figure A.6. Layouts of the 6th mask for through etch of the wafers from the backside by deep reactive ion etching (DRIE) to release the devices.

APPENDIX B

FABRICATION PROCESS OUTLINE

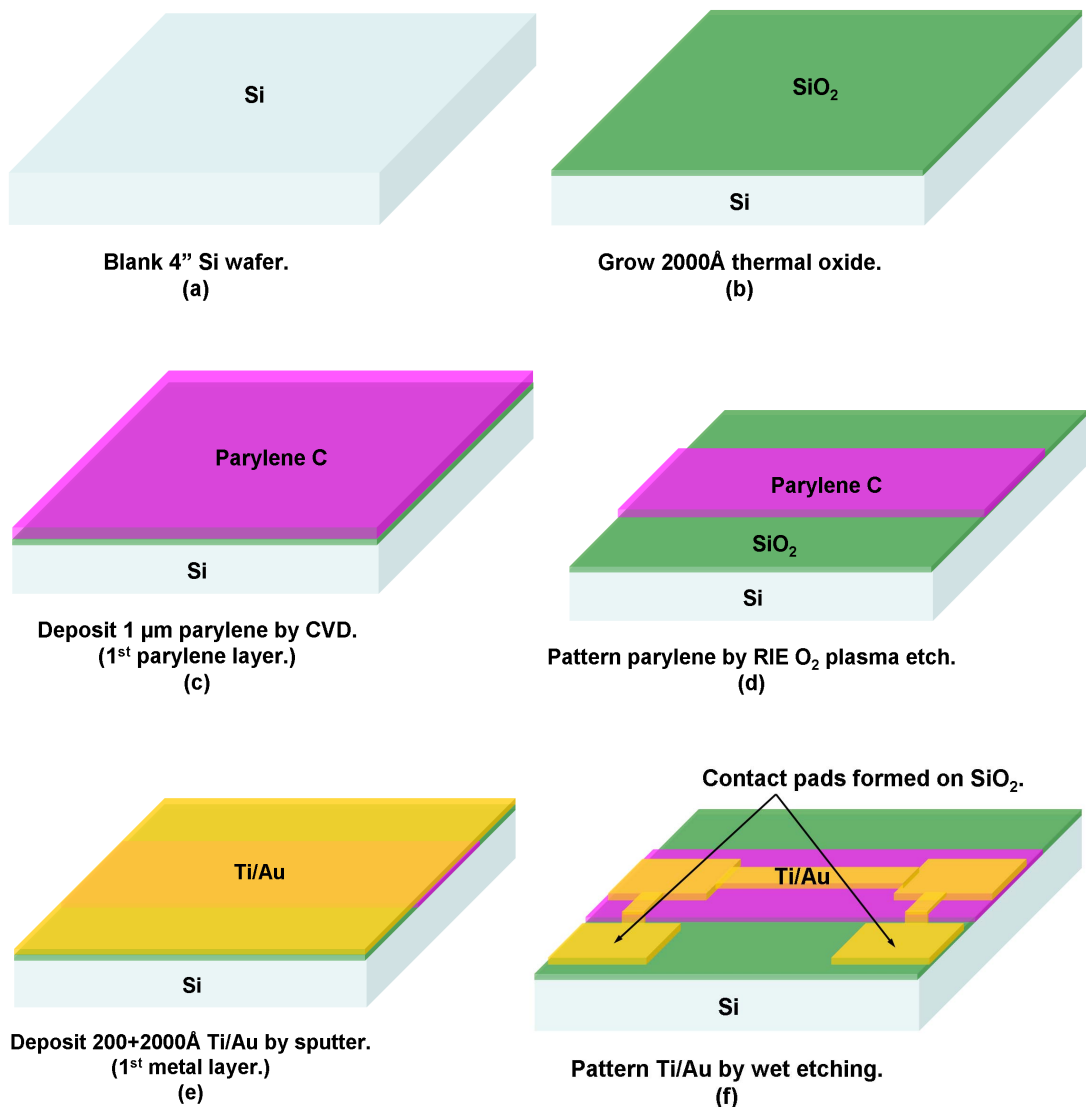


Figure B.1. Fabrication process outline of the micro generators.

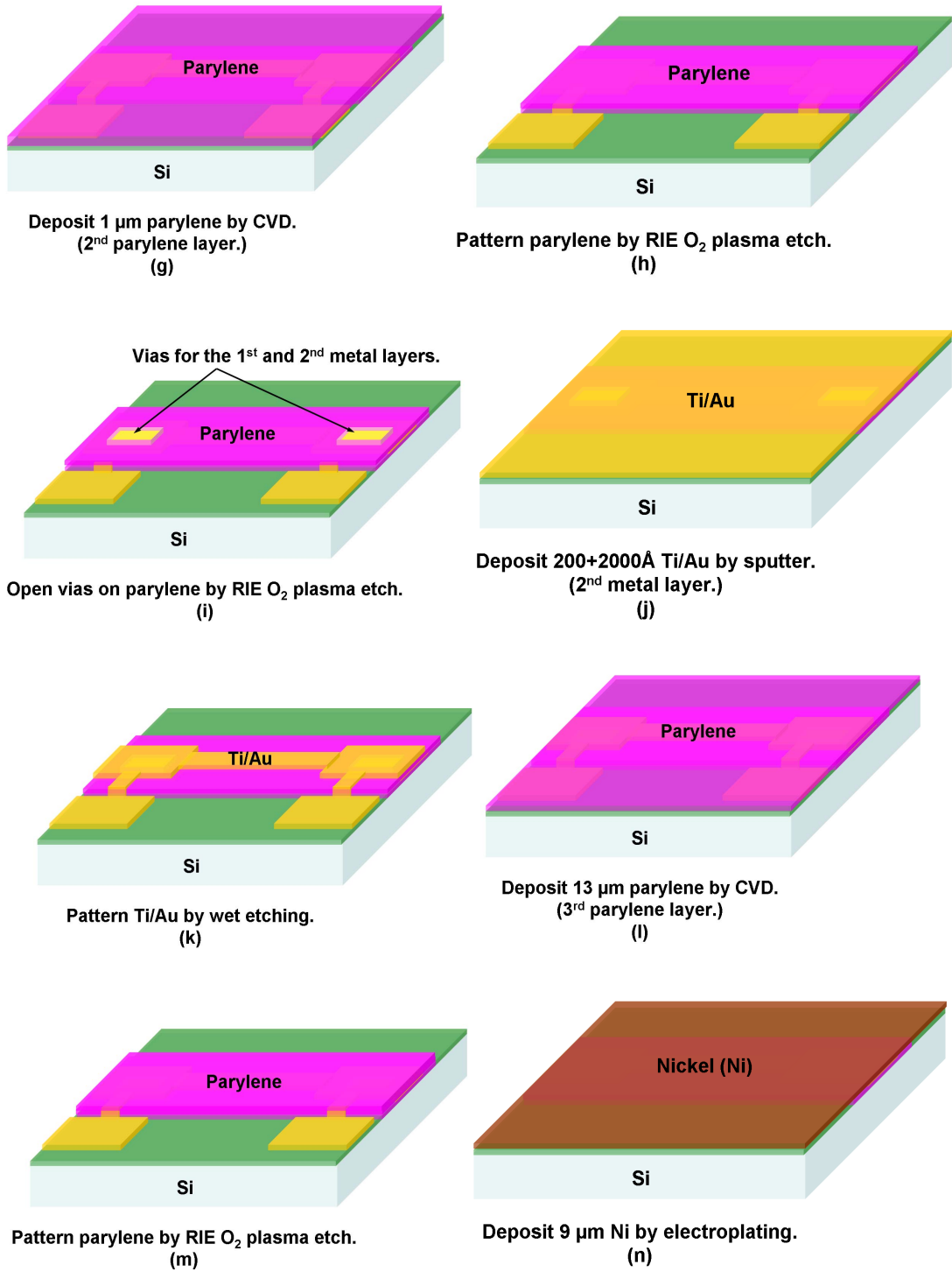


Figure B.1. (cont'd).

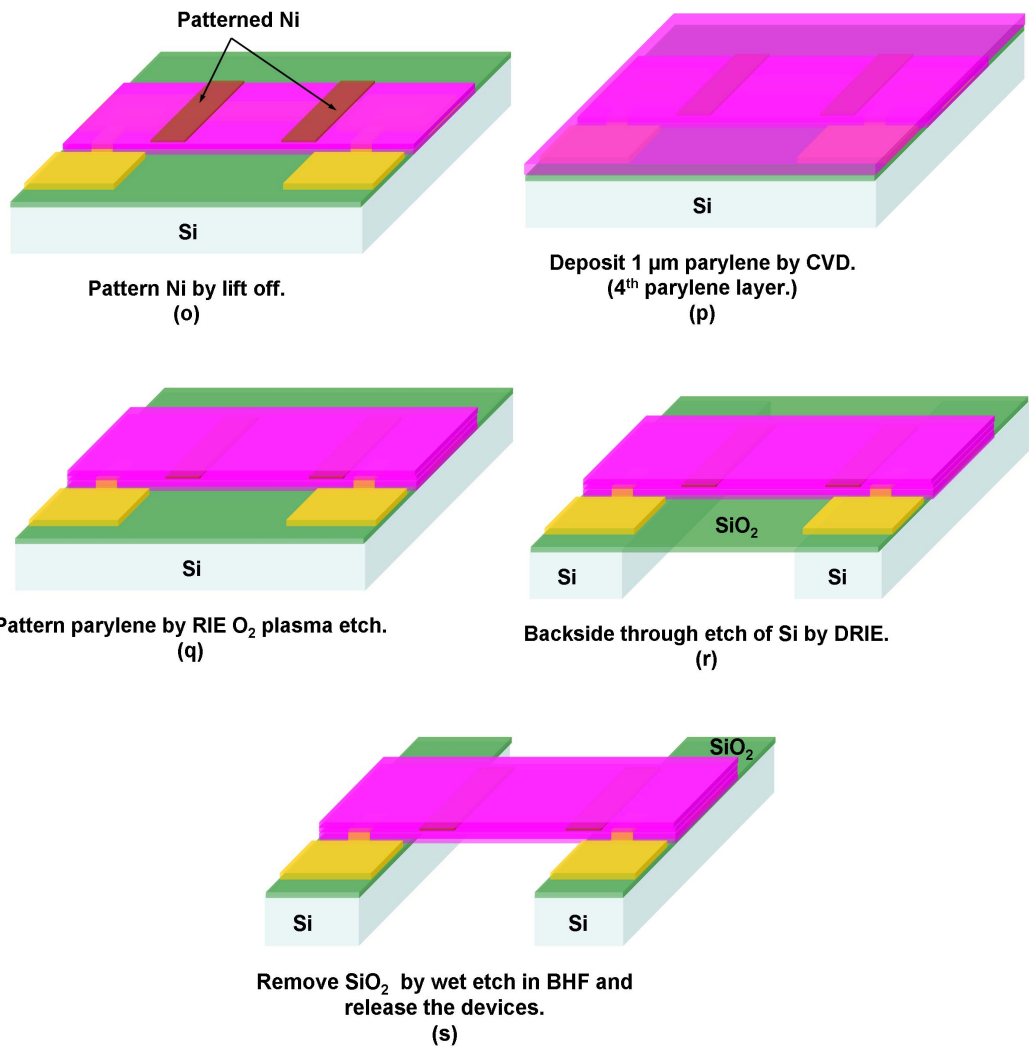


Figure B.1. (cont'd).

APPENDIX C

FABRICATION PROCESS FLOW

Table C.1. Process steps of the 1st parylene layer.

Cantilever Mask	A1	Parylene Deposition (1 μm)	SP:15, PLA1:10, use A174-Silane (Protect backside by tape.)
	A2	Lithography	
	A2.1	Dehydration	Dehydrate 10 mins. in oven @120°C. Cool down in desiccator for 5 mins.
	A2.2	PR Spin	SPR 220-3 @2500rpm, t=30 s (3.5 μm aimed)
	A2.3	Softbake	Softbake t=90s over contact hotplate @T=115°C
	A2.4	Expose	Expose 7 sec. (Vacuum contact)
	A2.5	Rehydration	Rehydrate 30 mins. prior to develop with 1 pipette full of water in closed box
	A2.6	Develop	MF24A, 40-50 sec.
	A3	Parylene Etch by RIE	~5 mins. (~0.33-0.43 $\mu\text{m}/\text{min}$), O ₂ Plasma, 100 sccm, 100 mTorr, 100 Watt
	A4	PR Strip	Acetone + IPA + DI Water

Table C.2. Deposition and patterning of the 1st metal layer.

Coil Turn (Metal 1) Mask	B1	Dehydration	Right before sputter, dehydrate 10 mins. in oven @120°C, cool down in desiccator for 5 mins.
	B2	Ti sputter (200 Å)	Endpoint thickness=75Å, MFC1=2 sccm
	B3	Au Sputter (2000 Å)	Timer 2=180s (will be used), MFC1=6.2 sccm
	B4	Lithography	
	B4.1	Dehydration	Dehydrate 10 mins. in oven @120°C, Cool down in desiccator for 5 mins.
	B4.2	PR Spin	SPR 220-3 @2500rpm, t=30 s (3.5 µm aimed)
	B4.3	Softbake	Softbake t=90s over contact hotplate @T=115°C
	B4.4	Expose	Expose 7 sec. (Vacuum contact)
	B4.5	Rehydration	Rehydrate 30 mins. prior to develop with 1 pipette full of water in closed box
	B4.6	Develop	MF24A, 40-50 sec.
	B4.7	O ₂ Plasma	O ₂ Plasma @ 0.2-0.3 Torr for 1-2 mins. (Remove exposed, but undeveloped PR specially between 10 µm lines)
	B4.8	Hardbake	Hardbake (for Metal etch) @120°C for 10 mins., Cool down in desiccator 5 mins.
	B5	Au Wet Etch	Au etchant 25-32 s.
	B6	Ti Wet Etch	Ti etchant, prepare 100 ml (80% H ₂ O+10% HF+10% H ₂ O ₂), 25 ml Ti etchant + 1575 ml DI H ₂ O, ~80 sec.
	B7	PR Strip	Try Acetone + IPA, else use SVC

Table C.3. Process steps of the 2nd parylene layer.

Cantilever Mask	C1	Parylene Deposition (1 μm)	SP:15, PLA1:10, use A174-Silane (Protect backside by tape.)
	C2	Lithography	
	C2.1	Dehydration	Dehydrate 10 mins. in oven @120°C. Cool down in desiccator for 5 mins.
	C2.2	PR Spin	SPR 220-3 @2500rpm, t=30 s (3.5 μm aimed)
	C2.3	Softbake	Softbake t=90s over contact hotplate @T=115°C
	C2.4	Expose	Expose 7 sec. (Vacuum contact)
	C2.5	Rehydration	Rehydrate 30 mins. prior to develop with 1 pipette full of water in closed box
	C2.6	Develop	MF24A, 40-50 sec.
	C3	Parylene Etch by RIE	~5 mins. (~0.33-0.43 $\mu\text{m}/\text{min}$), O ₂ Plasma, 100 sccm, 100 mTorr, 100 Watt
	C4	PR Strip	Acetone + IPA + DI Water

Table C.4. Process steps of contact opening on 2nd parylene layer.

Contact Mask	D2	Lithography	
	D2.1	Dehydration	Dehydrate 10 mins. in oven @120°C. Cool down in desiccator for 5 mins.
	D2.2	PR Spin	SPR 220-3 @2500rpm, t=30 s (3.5 µm aimed)
	D2.3	Softbake	Softbake t=90s over contact hotplate @T=115°C
	D2.4	Expose	Expose 7 sec. (Vacuum contact)
	D2.5	Rehydration	Rehydrate 30 mins. prior to develop with 1 pipette full of water in closed box
	D2.6	Develop	MF24A, 40-50 sec.
	D3	Parylene Etch by RIE	~5 mins. (~0.33-0.43 µm/min), O ₂ Plasma, 100 sccm, 100 mTorr, 100 Watt
	D4	PR Strip	Acetone + IPA + DI Water

Table C.5. Deposition and patterning of the 2nd metal layer.

Metal Routing (Metal 2) Mask	E1	Dehydration	Right before sputter, dehydrate 10 mins. in oven @120°C, cool down in desiccator for 5 mins.
	E2	Ti sputter (200 Å)	Endpoint thickness=75A, MFC1=2 sccm
	E3	Au Sputter (2000 Å)	Timer 2=180s (will be used), MFC1=6.2 sccm
	E4	Lithography	
	E4.1	Dehydration	Dehydrate 10 mins. in oven @120°C, Cool down in desiccator for 5 mins.
	E4.2	PR Spin	SPR 220-3 @2500rpm, t=30 s (3.5 µm aimed)
	E4.3	Softbake	Softbake t=90s over contact hotplate @T=115°C
	E4.4	Expose	Expose 7 sec. (Vacuum contact)
	E4.5	Rehydration	Rehydrate 30 mins. prior to develop with 1 pipette full of water in closed box
	E4.6	Develop	MF24A, 40-50 sec.
	E4.7	O ₂ Plasma	O ₂ Plasma @ 0.2-0.3 Torr for 1-2 mins. (Remove exposed, but undeveloped PR specially between 10 µm lines)
	E4.8	Hardbake	Hardbake (for Metal etch) @120°C for 10 mins., Cool down in desiccator 5 mins.
	E5	Au Wet Etch	Au etchant 25-32 s.
	E6	Ti Wet Etch	Ti etchant, prepare 100 ml (80% H ₂ O+10% HF+10% H ₂ O ₂), 25 ml Ti etchant + 1575 ml DI H ₂ O, ~80 sec.
	E7	PR Strip	Try Acetone + IPA, else use SVC

Table C.6. Process steps of the 3rd parylene layer.

Cantilever Mask	F1	Parylene Deposition (13 µm)	SP:15, PLA1:10, use A174-Silane (Protect backside by tape.)
	F2	Lithography	
	F2.1	Dehydration	Dehydrate 10 mins. in oven @120°C. Cool down in desiccator for 5 mins.
	F2.2	PR Spin	AZ9260 @900 rpm, , t=30 s (18 µm aimed) + EBR with the same settings.
	F2.3	Relaxation	Keep in desiccator in horizontal position for t=10 min.
	F2.4	Softbake	Softbake t=18 min. over contact hotplate @T=100°C
	F2.5	Expose	Expose 55 sec. (Vacuum contact)
	F2.6	Rehydration	Rehydrate 60 mins. prior to develop with 5 pipette full of water in closed box.
	F2.7	Develop	AZ826 MIF, 15 min.
	F3	Parylene Etch by RIE	30 + 30 mins. (~22 µm/min), O ₂ Plasma, 100 sccm, 100 mTorr, 100 Watt
	F4	PR Strip	Acetone + IPA + DI Water

Table C.7. Process steps of Ni electroplating.

Nickel Mask	G1	Dehydration	Right before sputter, dehydrate 10 min. in oven @120°C Cool down in desiccator for 5 min.
	G2	Ti sputter (200 Å)	Endpoint thickness=75A, MFC1=2 sccm
	G3	Au Sputter (2000 Å)	Timer 2=180s (will be used), MFC1=6.2 sccm
	G4	Lithography	
	G4.1	Dehydration	Dehydrate 10 mins. in oven @120°C Cool down in desiccator for 5 mins.
	G4.2	PR Spin	AZ 9260 @900 rpm, t=30 s spin, (~18 µm aimed) + EBR with same settings
	G4.3	Air Dry	Dry in desiccator for 15 min. in horizontal position
	G4.4	Softbake	Softbake t=20 min. @100°C
	G4.5	Rehydration (relaxation)	Rehydrate 60 mins prior to develop with 5 pipette full of water in closed box (Humidity should be at least 50%)
	G4.6	Expose	Expose 55 s in vacuum contact
	G4.7	Develop	AZ 826 MIF, 15 min.
	G4.8	Hardbake	No
	G5	Ni Electroplating (9 µm)	T=50°C, I _d =8.1 A/dm ² , A=0.0033 dm ² (FUC Series Ni mask), duty=0.04, T _{on} =0.1 ms, T _{off} =2.4 ms, I _{avg} =0.012 A
	G6	Au Wet Etch	Au etchant 25-32 s.
	G7	Ti Wet Etch	Ti etchant, prepare 100 ml (80% H ₂ O+10% HF+10% H ₂ O ₂), 25 ml Ti etchant + 1575 ml DI H ₂ O, ~80 sec.
	G8	PR Strip	Acetone + IPA +DI Water.

Table C.8. Process steps of the 4th parylene layer.

Cantilever Mask	H1	Parylene Deposition (1 μm)	SP:25, PLA1:10, use A174-Silane (Protect backside by tape.)
	H2	Lithography	
	H2.1	Dehydration	Dehydrate 10 mins. in oven @120°C. Cool down in desiccator for 5 mins.
	H2.2	PR Spin	AZ9260 @900 rpm, , t=30 s (18 μm aimed) + EBR with the same settings.
	H2.3	Relaxation	Keep in desiccator in horizontal position for t=10 min.
	H2.4	Softbake	Softbake t=18 min. over contact hotplate @T=100°C
	H2.5	Expose	Expose 55 sec. (Vacuum contact)
	H2.6	Rehydration	Rehydrate 60 mins. prior to develop with 5 pipette full of water in closed box.
	H2.7	Develop	AZ826 MIF, 15 min.
	H3	Parylene Etch by RIE	30 + 30 mins. (~22 $\mu\text{m}/\text{min}$), O ₂ Plasma, 100 sccm, 100 mTorr, 100 Watt
	H4	PR Strip	Acetone + IPA + DI Water

Table C.9. Process steps backside through etch of Si.

DRIE Mask	J1	Backside lithography	
	J1.1	Dehydration	Dehydrate 10 min. in oven @120°C, Cool down in desiccator for 5 min.
	J1.2	PR Spin	AZ 9260 @900 rpm, t=30 s spin, (~20 µm aimed)
	J1.3	Relaxation	Dry in desiccator for 15 min. in horizontal position
	J1.4	Softbake	Softbake 20 min. @100°C
	J1.5	Rehydration	Rehydrate 60 mins prior to develop with 5 pipette full of water in closed box.
	J1.6	Expose	Expose 65 s in vacuum contact
	J1.7	Develop	AZ 826 MIF, 15 min.
	J1.8	Reconstruct EB at the backside	Reconstruct edge bead at the back with AZ9260 @750 rpm (spin PR to the edge only), wait 5 mins., softbake @100°C, t=5 mins., cool down in desiccator
	J2	Attachment of handle wafer	Attach handle wafer to the process wafer by thermal gress over hot plate @115°C
	J3	Backside SiO ₂ etch by RIE	Use the DRIE mask, 100 mTorr, 300 W, Chiller Temp.=20°C, CF ₄ =12 sccm, CHF ₃ =38 sccm, t=~6 mins.
	J4	Backside Si etch by DRIE	About 100 mins.
	J5	Frontside SiO ₂ etch by RIE	Use the DRIE mask, 100 mTorr, 300 W, Chiller Temp.=20°C, CF ₄ =12 sccm, CHF ₃ =38 sccm, t=~6 mins.
	J6	Frontside SiO ₂ wet etch	Buffered HF (BHF), 5:1 (500 ml NH ₄ F + 100 ml HF), ~10 mins.
	J7	Release	Keep the wafer in acetone about one day.

CURRICULUM VITAE

PERSONAL INFORMATION

Surname, Name: Sari, İbrahim

Nationality: Turkish (TC)

Date and Place of Birth: 18 July 1976 , Mersin

Marital Status: Married

Phone: +44 23 8059 3278

Fax: +44 23 8059 3029

email: is2@ecs.soton.ac.uk

EDUCATION

Degree	Institution	Year of Graduation
M.Sc.	METU Mechanical Engineering	2002
B.Sc.	METU Mechanical Engineering	1999
High School	Tarsus American High School, Mersin	1994

WORK EXPERIENCE

Year	Place	Enrollment
2008-Present	University of Southampton, UK	Postdoctoral Research Fellow
2006-2008	METU, Dept. of Electrical and Electronics Eng.	Research Assistant
1999-2006	METU, Dept. of Mechanical Engineering	Teaching Assistant
1998 Summer	Anadolu Cam Sanayii, Mersin	Intern Engineering Student
1997 Summer	Anadolu Cam Sanayii, Mersin	Intern Engineering Student

FOREIGN LANGUAGES

Advanced English, Basic German and Japanese

PUBLICATIONS

Conference Papers

1. I. Sari, T. Balkan and H. Kulah, "An Electromagnetic Micro Power Generator for Low Frequency Environmental Vibrations Based on the Frequency up-Conversion Technique," 22nd IEEE Conference on Micro Electro Mechanical Systems (MEMS 2009), Sorrento, Italy, January 25-29, 2009.
2. I. Sari, T. Balkan and H. Kulah, "A Micro Power Generator with Planar Coils on Parylene Cantilevers," IEEE Prime 2008, 4th Conference on Ph.D. Research in Microelectronics and Electronics, Istanbul, Turkey, June 22-25, 2008, pp. 133-136.
3. I. Sari, T. Balkan and H. Kulah, "Design and Optimization of an Electromagnetic Micro Energy Scavenger with Parylene Cantilevers," PowerMEMS 2007, Freiburg, Germany, November 28-29, 2007, pp. 81-84.
4. I. Sari, T. Balkan and H. Kulah, "An Energy Harvesting MEMS Frequency Detector," 6th IEEE Conference on Sensors (IEEE SENSORS 2007), Atlanta, USA, October 28-31, 2007, pp. 1460-1463.
5. I. Sari, T. Balkan and H. Kulah, "A Wideband Electromagnetic Micro Power Generator for Wireless Microsystems," The 14th International Conference on Solid-State Sensors, Actuators and Microsystems (TRANSDUCERS'07 & EUROSENSORS XXI), Lyon, France, vol. 1, pp. 275-278, June 10-14, 2007.
6. O. Kokturk, I. Sari and T. Balkan, "Real-Time Control of a Hydraulic Servo Valve-Cylinder System," 4th National Hydraulics and Pneumatics Congress and Exhibition, pp. 65-77, December 2005, Izmir, Turkey, (in Turkish).
7. I. Sari, B. Platin and T. Balkan, "Design, Construction and Performance Testing of a Ball-Beam Balancing Experimental Set-up," TOK 2002, Automatic Control National Meeting, Middle East Technical University, Ankara, Turkey, pp. 39-48, September 2002, (in Turkish).
8. I. Sari, C. Okwudire, H. Ipek and O. Ilkgun, "Discrete-time modeling, control and simulation of a powered wheelchair by Matlab® Simulink®," Mechanical Engineering Department, Middle East Technical University, Ankara, Turkey.

Journal Articles

1. I. Sari, T. Balkan and H. Kulah, "An Electromagnetic Micro Power Generator for Wideband Environmental Vibrations," Sensors and Actuators A: Physical, doi: 10.1016/j.sna.2007.11.021, vol. 145-146 (2008), pp. 405-413.

HOBBIES

Traveling, gourmet, outdoor sports, movies, computers and internet.